CISLUNAR TRAJECTORY DESIGN METHODOLOGIES INCORPORATING QUASI-PERIODIC STRUCTURES WITH APPLICATIONS

by

Brian McCarthy

A Dissertation

Submitted to the Faculty of Purdue University

In Partial Fulfillment of the Requirements for the degree of

Doctor of Philosophy

School of Aeronautics and Astronautics

West Lafayette, Indiana

May 2022

THE PURDUE UNIVERSITY GRADUATE SCHOOL
STATEMENT OF COMMITTEE APPROVAL

Dr. Kathleen C. Howell, Chair

School of Aeronautics and Astronautics

Dr. Carolin Frueh

School of Aeronautics and Astronautics

Dr. Martin Corless

School of Aeronautics and Astronautics

Dr. Diane C. Davis

a.i. solutions, Inc

Approved by:

Dr. Gregory A. Blaisdell

To Mom

Lucy I. W. McCarthy

September 27, 1957 - February 21, 2012

ACKNOWLEDGMENTS

First, I would like to thank my fiancé, Holly. You are my rock and I am truly lucky to have met you through this grad school experience. Thank you for always supporting me and sticking with me through all the highs and lows. Your encouragement to have healthier life habits have help me achieve my goals. You inspire me every day and I am so excited for our next chapter together. I could not have asked for a better partner in life.

Second, I would like to thank my family. Dad, you have always been an inspiration ever since I can remember. You taught me to always pursue my passions and to do what makes me happy, regardless of how many people say it will be too hard or how long it will take. You have instilled a work ethic in me that I take great pride in. Without your encouragement, I would not have pushed myself to give up my full time job and move hundreds of miles away to pursue my passion. To my brother, E.J., you have always been a role model in my life as an older brother. Your dedication to your loved ones in unparalleled. Thank you for always checking in on me and sending me Chris Farley memes to cheer me up. Also, I would like to thank my Midwest family, Phil and Carin Reinckens as well as Jimmy and Kathryn Purcell. I am so grateful for all of your love and support since moving out here.

Next, I would like to thank my friends from back home, Dan Valcicak, Bas Welsh, Jason Webber, Nick Bambino, Ryan Chandler, Alex Whittemore, Cameron Cummings, Marty McGowan, Juan Ojeda Romero and the rest of the guys, you all have had a tremendous effect on my life. You have always kept me grounded and have been there to support me through some of my darkest days. I am forever grateful.

I would also like to thank my friends I met through my internships at NASA JSC, Brian Robinson, Jon Webb, Michael Porter, and many others. You all have always been encouraging when the grind of graduate school was getting me down and you have made my summer experiences unforgettable. I am looking forward to many more upon moving down to Houston. I would also like to thank my mentors at the Johns Hopkins Applied Physics Lab, Marty Ozimek, Wayne Schlei, Jacob Englander, Chris Scott and Fouad Khoury. I was able to learn so much from you all in a short time and I am incredible grateful I had the opportunity to work with such an amazing group of people.

I would like to also thank Diane Davis and Sean Phillips. Both of you have been instrumental in th development of my academic and professional career. I am forever grateful that you gave me the opportunity to join the DSTE project and brought me into the world of multi-body astrodynamics. Sean, your passion for your work, your business savvy, and your endless sense of humor made is truly unique. I am incredibly grateful for your encouragement and support during my experiences before grad school and during my short time at APL. Diane, I am deeply indebted to you for the opportunities that you helped provide for me and the doors you have helped open professionally and academically. There are few people in my life that I have been lucky enough to come across that inspire me as much as you have. Thank you for not only being a great mentor, but also an incredible friend.

To my friends I have made at Purdue, and specifically those from the Multi-Body Dynamics Research Group. You all inspire me be the best I can be and thank you for putting up with all of my antics day in and day out here at Purdue. Thank you for all the insightful discussions, valuable feedback, and constant encouragement during my time out here at Purdue. I am lucky to have worked with such an incredible group of individuals.

I would like to thank my committee members, Dr. Martin Corless, Dr. Carolin Frueh, and Dr. Diane Davis, for taking the time to review this dissertation and provide valuable feedback. I would also like to thank the School of Aeronautics and Astronautics, the College of Engineering, and the Rune and Barbara Eliasen Visualization Laboratory for financial support of my studies here at Purdue.

Lastly, I would like to extend my immense gratitude to my advisor, Dr. Kathleen Howell. Thank you for the opportunity to be a part of your research group and believing in me, even when I doubted myself. Your passion for your work is infectious and I have felt truly inspired every day under your guidance and support. Thank you for always taking the time to listen, provide insight, and teaching me to be a better engineer. I hope that I have the opportunity to continue to learn from you through my professional career and look forward to continued collaboration.

TABLE OF CONTENTS

LIST OF TABLES

LIST OF FIGURES

ABSTRACT

In the coming decades, numerous missions plan to exploit multi-body orbits for operations. Given the complex nature of multi-body systems, trajectory designers must possess effective tools that leverage aspects of the dynamical environment to streamline the design process and enable these missions. In this investigation, a particular class of dynamical structures, quasi-periodic orbits, are examined. This work summarizes a computational framework to construct quasi-periodic orbits and a design framework to leverage quasi-periodic motion within the path planning process. First, quasi-periodic orbit computation in the Circular Restricted Three-Body Problem (CR3BP) and the Bicircular Restricted Four-Body Problem (BCR4BP) is summarized. The CR3BP and BCR4BP serve as preliminary models to capture fundamental motion that is leveraged for end-to-end designs. Additionally, the relationship between the Earth-Moon CR3BP and the BCR4BP is explored to provide insight into the effect of solar acceleration on multi-body structures in the lunar vicinity. Characterization of families of quasi-periodic orbits in the CR3BP and BCR4BP is also summarized. Families of quasi-periodic orbits prove to be particularly insightful in the BCR4BP, where periodic orbits only exist as isolated solutions. Computation of three-dimensional quasi-periodic tori is also summarized to demonstrate the extensibility of the computational framework to higher-dimensional quasi-periodic orbits. Lastly, a design framework to incorporate quasi-periodic orbits into the trajectory design process is demonstrated through a series of applications. First, several applications were examined for transfer design in the vicinity of the Moon. The first application leverages a single quasi-periodic trajectory arc as an initial guess to transfer between two periodic orbits. Next, several quasi-periodic arcs are leveraged to construct transfer between a planar periodic orbit and a spatial periodic orbit. Lastly, transfers between two quasi-periodic orbits are demonstrated by leveraging heteroclinic connections between orbits at the same energy. These transfer applications are all constructed in the CR3BP and validated in a higher-fidelity ephemeris model to ensure the geometry persists. Applications to ballistic lunar transfers are also constructed by leveraging quasi-periodic motion in the BCR4BP. Stable manifold trajectories of four-body quasi-periodic orbits supply an initial guess to generate families of ballistic lunar transfers

to a single quasi-periodic orbit. Poincaré mapping techniques are used to isolate transfer solutions that possess a low time of flight or an outbound lunar flyby. Additionally, impulsive maneuvers are introduced to expand the solution space. This strategy is extended to additional orbits in a single family to demonstrate "corridors" of transfers exist to reach a type of destination motion. To ensure these transfers exist in a higher fidelity model, several solutions are transitioned to a Sun-Earth-Moon ephemeris model using a differential corrections process to show that the geometries persist.

1. INTRODUCTION

NASA's future exploration plans beyond Low Earth Orbit (LEO) are significant for both robotic and human spaceflight. In robotic spaceflight, the Europa Clipper and Dragonfly mission plans include exploration of the ocean worlds Europa and Titan, respectively, for origins of life [1], [2]. In human spaceflight, the Artemis and Gateway programs are structured to establish and maintain a human presence in cislunar space and to deliver facilities that can serve as a proving ground for extended mission operations in support of the exploration of Mars and beyond [3], [4]. Improving a fundamental understanding of the gravity environments for such missions and enhancing analysis capabilities to enable informed trajectory design decisions that leverage these environments are crucial to achieving the science objectives at these increasingly exotic destinations.

1.1 Motivation

Many design options for trajectories within the context of the relative two-body model are enabled due to the close-form, analytical nature of the solutions in this model. The two-body model is frequently successful for preliminary design of LEO and low lunar orbit (LLO) missions, and the analytical solutions enable a patched-conic approach for interplanetary spacecraft pathways throughout the solar system. However, in more complex scenarios, where spacecraft behavior is significantly influenced by more than one massive body, the two-body model is inadequate. Moreover, the inclusion of additional bodies into the force model introduces new dynamical structures that do not exist within the context of the two-body model. For example, the baseline operational orbit for the lunar NASA Gateway facility is a southern L_2 Near Rectilinear Halo Orbit (NRHO) that exists in a regime where neither the gravitational influence of the Earth nor the Moon can be neglected [5]. It has also been demonstrated that disposal from the Gateway orbit to heliocentric space relies upon the combined gravity of the Sun, Earth, and Moon to successfully achieve escape [6]. Similarly, trajectory planning for logistics modules and resupply vehicles from Earth to be delivered to the Gateway facility includes options to exploit ballistic lunar transfers (BLTs) that reduce propellant costs; the Sun, Earth, and Moon all play significant roles [7]. For

these scenarios, a four-body problem is required and the preliminary design is particularly challenging since all three of these gravitational bodies are incorporated. Neither the three- and four-body models possess analytical solutions and inherently reflect chaotic dynamical systems; however, understanding the types of structured motion in each of these models aids design in these regimes. One such type of dynamical structure is a set of sample behaviors, e.g., a wide array of quasi-periodic orbits. Quasi-periodic orbits present challenges in computational efficiency and the availability of flexible tools to analyze the associated motion. However, exploiting quasi-periodic motion significantly expands the solution space as compared to a narrower definition of a solution space that incorporates only periodic structures.

1.2 Objectives

The overarching goal of this research is to develop a computational framework and an effective design process to incorporate quasi-periodic orbits into the multi-body trajectory design process. The specific objectives to enable both an effective computational structure and a design scheme that incorporates quasi-periodic orbits as important building blocks are as follows:

1. *Develop an effective computational algorithm for quasi-periodic orbits in the three- and four-body problems.* The computational algorithm provides solutions of families in the three- and four-body problems. In these models, quasi-periodic orbits are characterized by a set of parameters. This straightforward set of parameters to characterize complex quasi-periodic motion allows for these orbits to be reduced to a simpler representation.

2. *Quantify stability and develop computational methods to represent hyperbolic quasi-periodic orbit manifolds.* Variational methods and linear stability informs the type of motion that exists in the vicinity of an orbit. By characterizing the stability into a single metric, or stability index, quasi-periodic orbits are assessed for natural flow that approaches and departs the orbit. Exploiting these natural pathways provides sufficient quality initial guesses for transfer trajectories into and out of quasi-periodic orbits.

3. *Establish a framework to encompass quasi-periodic motion as a natural element in the trajectory design process.* Given the complex behavior associated with quasi-periodic motion, a decision process is necessary to evaluate and select the various paths for design applications. As such, Poincaré mapping techniques and differential corrections schemes are presented to identify solutions of interest, and to construct solutions that satisfy desirable constraints.

4. *Demonstrate the framework and utility of quasi-periodic motion through applications in the three- and four-body problems.* To validate and verify the elements of the framework, sample scenarios are constructed and the design strategy is applied. First, transfer trajectory design scenarios for various types of departure and destination orbits are considered in the three-body problem. Second, low-energy, ballistic lunar transfer scenarios are considered in the four-body problem to demonstrate the design of end-to-end transfers from trans-lunar injection to arrival into various destination orbits.

The applications are focused on trajectory design in cislunar space; however, the orbit and transfer construction process is extendable to other regimes. The three- and four-body models are formulated using non-dimensional parameters, offering ease of extension to other planet-moon, Sun-planet, or Sun-planet-moon systems.

1.3 Previous Contributions

1.3.1 Multi-Body Dynamics

In 1687, Sir Isaac Newton released his seminal work, *Principia*, with the laws of motion and a framework for classical mechanics [8]. The three-volume *Principia* sparked a search for the solution to the N-body problem. Shortly after, Leonhard Euler introduced a formulation of the restricted three-body problem using a rotating reference frame. In Euler's formulation, two massive bodies move in circular orbits around their mutual barycenter and a third body possesses negligible mass. Euler also demonstrated the locations of the collinear equilibrium solutions in the three-body problem [9]. In 1772, Joseph Louis Lagrange identified the triangular equilibrium solutions, located at one vertex of equilateral triangles with

the two massive bodies as the remaining vertices [10]. A single integral of motion emerged in the three-body problem in 1836, recognized by Carl Gustav Jacob Jacobi, and commonly denoted the Jacobi Constant [11]. American astronomer and mathematician George Hill focused the search for periodic solutions and introduced the limiting regions of motion in the three-body problem, i.e., the zero velocity surfaces [12]. Inspired by Hill's work, Henri Poincaré proved the existence of an infinite number of periodic solutions in the three-body problem and acknowledged chaotic behavior, as published in *Les Méthodes Nouvelles de la Mécanique Céleste* [13]. Furthermore, Poincaré is credited with framing the foundations of modern dynamical systems theory. Emerging from Poincaré's work, dynamical systems theory evolved, with a direct link to the KAM theory associated with quasi-periodic motion by Kolmogorov, Arnold, and Moser between 1954 and 1963 [14]–[16]. In 1967, Szebehely published a modern, comprehensive treatment of the three-body problem, *Theory of Orbits: The Restricted Problem of Three Bodies* [17].

1.3.2 Quasi-Periodic Orbits

One of the challenges associated with leveraging quasi-periodic orbits for trajectory and transfer design is the computational difficulties, specifically in astrodynamics applications. Prior to the significant computational advancements in the last few decades, numerical construction of quasi-periodic orbits leveraged semi-analytical methods as developed, for example, by Farquhar and Kamel, Richardson and Cary, as well as Gomez, Masdemont, and Simó [18]–[20]. Such approaches were frequently based on a Lindstedt-Poincaré technique; thus, such strategies are sometimes valid only in close proximity to the underlying periodic orbit that possesses a center mode. Jorba and Masdemont exploited reduction to the center manifold and represented the quasi-periodic orbit as a truncated Fourier series. With the advancement of computing technology, numerical methods have also significantly improved. Goméz and Noguera developed a predictor-corrector method to compute families of periodic orbits in the vicinity of the triangular libration points in 1985 [21]. Howell and Pernicka also developed a differential corrections scheme to compute Lissajous trajectories in the three-body problem in 1988 [22]. More recent developments focused on the direct computation of a

torus associated with quasi-periodic motion. Schilder, Osinga, and Vogt developed a method to solve the partial differential equations that represent the full torus [23]. In 2009, Jorba and Olmedo as well as Kolemen, Kasdin, and Gurfil exploit Poincaré sections and a Fourier series to compute tori in a perturbed three-body problem [24]. Within the last decade, Gómez and Mondelo as well as Olikara and Scheeres, develop a stroboscopic mapping technique, using a Fourier series to represent an invariant curve on a torus [25], [26]; Olikara also explores computation of quasi-periodic orbits within the context of the Hill Restricted Four-Body Problem (HR4BP) using collocation [27]. Baresi et al. provide a performance comparison between current numerical methods to compute quasi-periodic tori [28]. Similarly, Haro et al. explore methods for computing invariant tori for a broader class of problems [29]. In 2020, Anderson, Easton, and Lo explore computing quasi-periodic orbits leveraging isolating blocks [30]. Further, Kumar et al. summarize a numerical method to compute the stable, unstable, and center manifolds of tori in the planar perturbed CR3BP [31]. While computational efficiency is accomplished through the use of analytical and semi-analytical methods, these methods typically are limited in their regions of convergence. While demanding computational resources and time, fully numerical simulations offer access to a wider range of solutions.

Quasi-periodic orbits have been exploited for various applications in the past, both for proposed missions and operations. In 1978, the ISEE-3 mission was the first mission to leverage a halo orbit at the Sun-Earth L_1 point [32]. Since then, the Sun-Earth L_1 point has served as an advantageous location for solar observatories due to its constant line of sight with the Earth and the Sun. NASA's ACE, WIND, and SOHO missions and NOAA's DSCOVR mission currently operate in quasi-periodic orbits in the vicinity of the Sun-Earth L_1 point to provide improved solar event warnings [33], [34]. The James Webb Space Telescope also operates in a Sun-Earth L_2 quasi-halo orbit [35]. Beyond the Earth region, Restrepo, Russell, and Lo explore the use of Lissajous trajectories at Europa as staging orbits for a lander in the Jupiter-Europa system [36]; Baresi and Scheeres examine the use of 3-dimensional tori for small body explorations [37]. Additionally, quasi-periodic orbits are explored for use in formation flying by Barden and Howell, Baresi and Scheeres, and, most recently, Henry and Scheeres [38]–[40]. Quasi-periodic orbits for solar sail trajectories have also been examined

by Guzzetti et al., Mora and Heiligers, as well as Farrés and Jorba [41]–[43]. Quasi-periodic orbits offer design alternatives for a wide range of applications. While earlier missions employed quasi-periodic orbits, they were not designed as such. With more capability to plan the use of quasi-periodic orbits early in the design process and a better understanding of the fundamental behaviors, designs can be more efficient and flexible.

2. DYNAMICAL MODELS AND NUMERICAL METHODS

Many preliminary trajectory design concepts within the context of the relative model are enabled due to the analytical, closed-form solution to the problem. This model is frequently successful for preliminary mission design for low-Earth orbiting spacecraft. For interplanetary spacecraft, the patched-conics approach also offers insightful concepts for many missions; however, in more complex mission scenarios, where spacecraft are significantly influenced, possibly over long time intervals, by more than one massive body, the two-body model is not adequate. Perturbations from other bodies render a Keplerian approximation of the motion inaccurate for practical applications and new types of structured motion appear when more gravitational bodies are introduced. The inclusion of a third and fourth gravitational body expands the design options in a multi-body dynamical environment.

2.1 Circular Restricted Three-Body Problem

Although there is no known solution to the problem of three bodies, the simplified Circular Restricted Three-Body Problem (CR3BP) is introduced to understand the fundamental behaviors. Assumptions in the CR3BP are introduced such that the derivation of the equations of motion becomes straightforward. First, three centrobaric bodies are defined in this model, denoted P_1, P_2, and P_3, and, assuming point masses, are denoted m_1, m_2, and m_3, respectively. An inertial reference frame, I, denoted $\hat{X}$-$\hat{Y}$-$\hat{Z}$, is defined relative to the barycenter, B, of P_1 and P_2, as illustrated in Figure 2.1. Second, the mass of P_3 is assumed as significantly less than the masses of P_1 and P_2 ($m_3 << m_1, m_2$) and, subsequently, the motion of P_1 and P_2 is not influenced by P_3. Thus, the motion of P_1 and P_2 is Keplerian and remains on a closed path. For simplicity, and a reasonable approximation to many Sun-planet and planet-moon systems, let the Keplerian motion be circular. Third, the plane of motion of the bodies P_1 and P_2 is assumed to be the $\hat{X}$-$\hat{Y}$ plane. Conveniently, the $\hat{Z}$-direction in the inertial coordinate frame aligns with the angular momentum of P_1 and P_2. The third body, P_3, is then free to move anywhere in three-dimensional space. While these assumptions simplify the dynamics in the system, the results offer insight into more complex multi-body regimes.

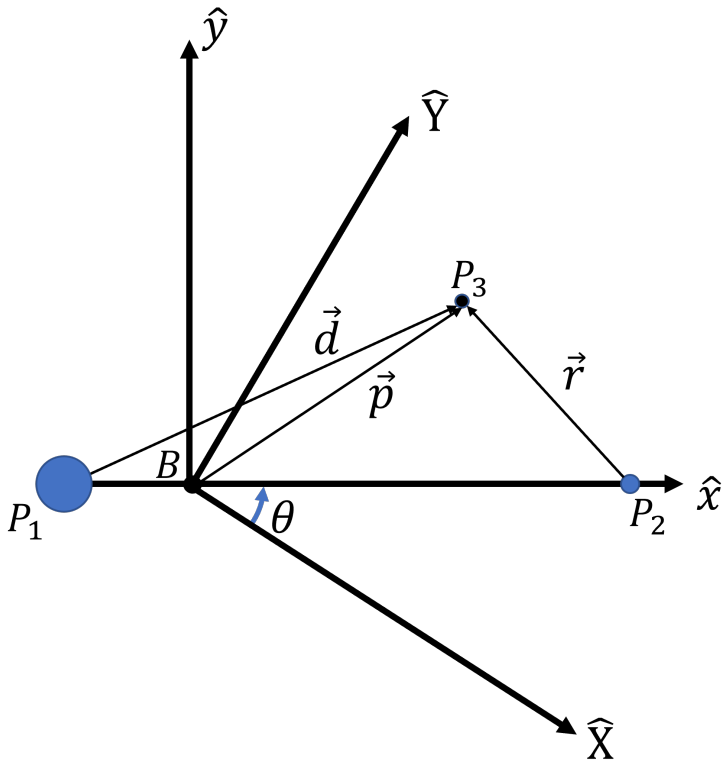

Figure 2.1. Geometry in the three body systems; definition of inertial and rotating reference frames.

Given the set of assumptions, the associated equations of motion in the CR3BP are formulated to model the behavior of the infinitesimal mass P_3. Beginning with the formulation of the N-body problem using Newton's Second Law, the equations of motion are first formulated in the inertial frame for $N = 3$. Subsequently, these equations are non-dimensionalized using a set of characteristic quantities to mitigate numerical difficulties for a broad range of applications. Finally, the non-dimensional equations of motion are expressed in a rotating frame, defined as $\hat{x}$-$\hat{y}$-$\hat{z}$ in Figure 2.1. The $\hat{x}$ direction is defined from the barycenter towards P_2, the $\hat{z}$ direction is in the same direction as $\hat{Z}$ and $\hat{y}$ completes the orthonormal triad. A thorough derivation of the equations of motion and the characteristic quantities for the CR3BP is found in Appendix A. The derivation found in Appendix A is formulated in a similar manner to McCarthy as well as Szebehely [17], [44]. The scalar non-dimensional position and velocity states for P_3, relative to the barycenter in the rotating frame, are

defined as $\vec{x} = \begin{bmatrix} x & y & z & \dot{x} & \dot{y} & \dot{z} \end{bmatrix}^T$, where the first three and the last three elements are the position and velocity components, respectively, and the T operator corresponds to the transpose. The non-dimensional position of P_3 is represented in Figure 2.1 by the vector $\vec{p}$. The equations of motion for the CR3BP are a set of three, second-order scalar differential equations, that is,

$$\ddot{x} - 2\dot{y} = x - \frac{(1-\mu)(x+\mu)}{d^3} - \frac{\mu(x-1+\mu)}{r^3} \tag{2.1}$$

$$\ddot{y} + 2\dot{x} = y - \frac{(1-\mu)y}{d^3} - \frac{\mu y}{r^3} \tag{2.2}$$

$$\ddot{z} = -\frac{(1-\mu)z}{d^3} - \frac{\mu z}{r^3} \tag{2.3}$$

where $\ddot{x}$, $\ddot{y}$, and $\ddot{z}$ are the scalar acceleration components with respect to nondimensional time in the rotating frame, μ is the CR3BP mass parameter, $\mu = M_2/(M_1 + M_2)$, $d = \sqrt{(x+\mu)^2 + y^2 + z^2}$ and $r = \sqrt{(x-1+\mu)^2 + y^2 + z^2}$ represent the distances of P_3 relative to P_1 and P_2, respectively. Alternatively, the equations of motion are written in terms of the pseudo potential function, U^*,

$$\ddot{x} - 2\dot{y} = \frac{\partial U^*}{\partial x} \tag{2.4}$$

$$\ddot{y} + 2\dot{x} = \frac{\partial U^*}{\partial y} \tag{2.5}$$

$$\ddot{z} = \frac{\partial U^*}{\partial z} \tag{2.6}$$

where the pseudo-potential function takes the form,

$$U^* = \frac{x^2 + y^2}{2} + \frac{\mu}{r} + \frac{1-\mu}{d} \tag{2.7}$$

No analytical solution is available for the equations of motion and numerical integration is of Equations (2.3) determines the time history of the path for a given set of initial states.

2.1.1 First-Order Variational Equations of Motion

The first-order variations for the six-dimensional state are an essential element of trajectory analysis in any model. Not only are they useful in differential corrections strategies, it crucial for many spacecraft guidance, navigation, and control applications as well. For a given reference solution, the state transition matrix (STM) offers information concerning the impact of the deviations of an initial state on the deviations in a final state downstream. In the general case, the first-order variational matrix, defined $\mathbf{A}$, is time-varying and is exploited to compute the differential equations associated with the STM. This STM is derived from a first-order Taylor series expansion, which is summarized in Appendix C. For the CR3BP, the matrix $\mathbf{A}$ defines the first-order variational equations of motion, $\dot{\mathbf{\Phi}} = \mathbf{A}\mathbf{\Phi}$,

$$\mathbf{A}(t) = \begin{bmatrix} 0 & 0 & 0 & 1 & 0 & 0 \\ 0 & 0 & 0 & 0 & 1 & 0 \\ 0 & 0 & 0 & 0 & 0 & 1 \\ U^*_{xx} & U^*_{xy} & U^*_{xz} & 0 & 2 & 0 \\ U^*_{yx} & U^*_{yy} & U^*_{yz} & -2 & 0 & 0 \\ U^*_{zx} & U^*_{zy} & U^*_{zz} & 0 & 0 & 0 \end{bmatrix} \tag{2.8}$$

where the notation for the pseudo-potential partial derivatives is $\frac{\partial^2 U^*}{\partial \mathrm{i} \partial \mathrm{j}} = U^*_{\mathrm{ij}}$. The partial derivatives of the pseudo-potential are defined,

$$U_{xx} = 1 - \frac{1-\mu}{d^3} - \frac{\mu}{r^3} + \frac{3(1-\mu)(x+\mu)^2}{d^5} + \frac{3\mu(x-1+\mu)^2}{r^5} \tag{2.9}$$

$$U_{yy} = 1 - \frac{1-\mu}{d^3} - \frac{\mu}{r^3} + \frac{3(1-\mu)y^2}{d^5} + \frac{3\mu y^2}{r^5} \tag{2.10}$$

$$U_{zz} = -\frac{1-\mu}{d^3} - \frac{\mu}{r^3} + \frac{3(1-\mu)z^2}{d^5} + \frac{3\mu z^2}{r^5} \tag{2.11}$$

$$U_{xy} = \frac{3(1-\mu)(x+\mu)y}{d^5} + \frac{3\mu(x-1+\mu)y}{r^5} \tag{2.12}$$

$$U_{xz} = \frac{3(1-\mu)(x+\mu)z}{d^5} + \frac{3\mu(x-1+\mu)z}{r^5} \tag{2.13}$$

$$U_{yz} = \frac{3(1-\mu)yz}{d^5} + \frac{3\mu yz}{r^5} \tag{2.14}$$

where d and r are the distances to P_1 and P_2, respectively, as previously noted. These first-order variations are numerically integrated because there is no analytical solution. Along with the state equations of motion in the CR3BP, the first-order variational equations of motion are numerically integrated to provide the elements of the STM from an initial to a final time. Generally, the STM supplies sensitivity information for many applications in dynamical systems analysis as well as problems in guidance and control.

2.1.2 Equilibrium Solutions

Without an analytical solution to the equations of motion in the CR3BP, the search for equilibrium solutions expands the understanding of the dynamical environment. In any familiar system modeled as a CR3BP, there exist five equilibrium solutions, denoted L_{i}. The collinear libration points, L_1, L_2, and L_3, reside along the $\hat{x}$-axis in the rotating frame. The triangular libration points, L_4 and L_5, are located off of the $\hat{x}$ axis and are equidistant from P_1 and P_2. The triangular libration points form an equilateral triangle with the two primaries in the $\hat{x}$-$\hat{y}$ plane. The representative locations of the equilibrium points in the rotating frame appear in Figure 2.2 as viewed in the rotating frame. While the solution for the collinear points requires iteration in any system, the locations of the triangular points are analytical, i.e., $(x_{L4}, y_{L4}) = (\frac{1}{2} - \mu, \frac{\sqrt{3}}{2})$, $(x_{L5}, y_{L5}) = (\frac{1}{2} - \mu, -\frac{\sqrt{3}}{2})$. The geometry for the five equilibrium points is defined for any system modeled as a CR3BP where the collinear points exist along the $\hat{x}$-axis and the triangular points are located equidistant from the primaries in the $\hat{x}$-$\hat{y}$ plane.

2.1.3 Integral of Motion

Although there is no analytical solution to the governing differential equations in the CR3BP, a single integral of motion does exist. This quantity is labeled the Jacobi Integral or Jacobi Constant (JC) and supplies significant insight into the problem by bounding the

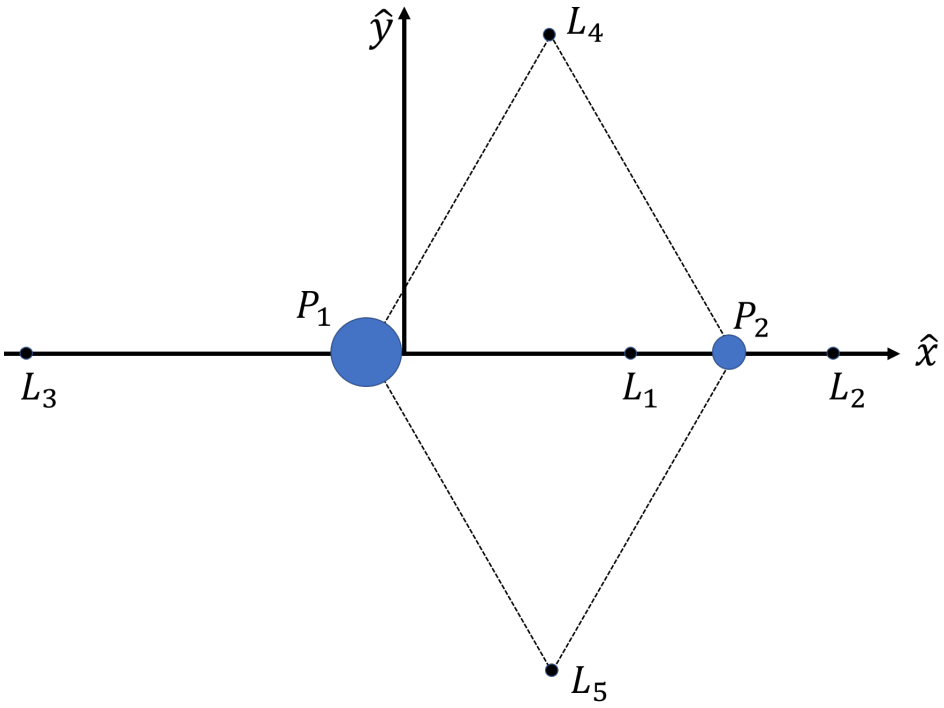

Figure 2.2. Relative locations of the five libration points as viewed in the rotating frame

solution space [45]. The Jacobi Constant is evaluated using the pseudo-potential function and the velocity magnitude as viewed in the rotating frame, i.e.,

$$JC = 2U^* - (\dot{x}^2 + \dot{y}^2 + \dot{z}^2) \tag{2.15}$$

where U^* is the pseudo-potential, defined in Equation (2.7). The Jacobi Constant is frequently denoted an energy-like quantity because it is defined using the pseudo-potential function. The pseudo-potential is not a potential in the sense of mechanical energy as derived in an inertial frame; the sum of the forces in the system do not equal the gradient of the pseudo-potential function. Rather, the pseudo-potential is derived by operating on the equations of motion in Equations (2.4)-(2.6). Equation (2.15) is rewritten to define the square of the velocity magnitude,

$$\dot{x}^2 + \dot{y}^2 + \dot{z}^2 = 2U^* - JC \tag{2.16}$$

where the relative velocity magnitude is defined $\sqrt{\dot{x}^2 + \dot{y}^2 + \dot{z}^2}$. It is apparent that the velocity squared term in Equation (2.16) must be positive. By equating the velocity magnitude to zero, an inequality defines the condition that must be satisfied for a real-valued velocity magnitude,

$$JC \leq 2U^* \tag{2.17}$$

The boundary that defines the imaginary and real-valued velocity magnitude is determined by defining the velocity squared term in Equation (2.16) as zero and, for a given value of JC, solving for the corresponding position components in the pseudo-potential function,

$$0 = 2U^* - JC \tag{2.18}$$

The position locations in the rotating frame that satisfy Equation (2.18) bound the region of the space where motion is allowed.

First, consider only planar motion, where $z = 0$. The solution to Equation (2.18) yields a set of points representing a continuous curve that defines the boundary. A more thorough discussion to compute this boundary is found in Szebehely [17]. The curves in the $\hat{x}\hat{y}$-plane in the rotating frame are labeled the Zero Velocity Curves (ZVCs) and sample ZVCs appear as plotted in Figure 2.3 for two representative values of Jacobi Constant. The "forbidden region" in Figure 2.3 defines the region where the velocity magnitude that solves Equation (2.18) is imaginary at a given JC value and, thus, it is not a physically realizable location. It is notable that the forbidden regions in Figure 2.3 contract around the L_1 and L_2 gateways. By decreasing the JC value to be less than the JC associated with L_2 (JC_{L2}), Figure 2.3b demonstrates that the ZVCs now enclose the Earth-Moon region and there is no longer access to the exterior region of the space. Increasing the Jacobi Constant such that $JC > JC_{L1}$, the gateway near L_1 closes, restricting access between the Earth and Moon regions. Similarly, decreasing the Jacobi constant such that $JC_{L4,5} < JC < JC_{L3}$ will open the L_3 gateway. Under this condition, P_3 is no longer restricted from traversing between the interior and exterior regions through the L_2 gateway, the L_3 gateway provides access to those regions as well. When $JC < JC_{L4,5}$, the ZVCs vanish in the plane and motion is available anywhere in

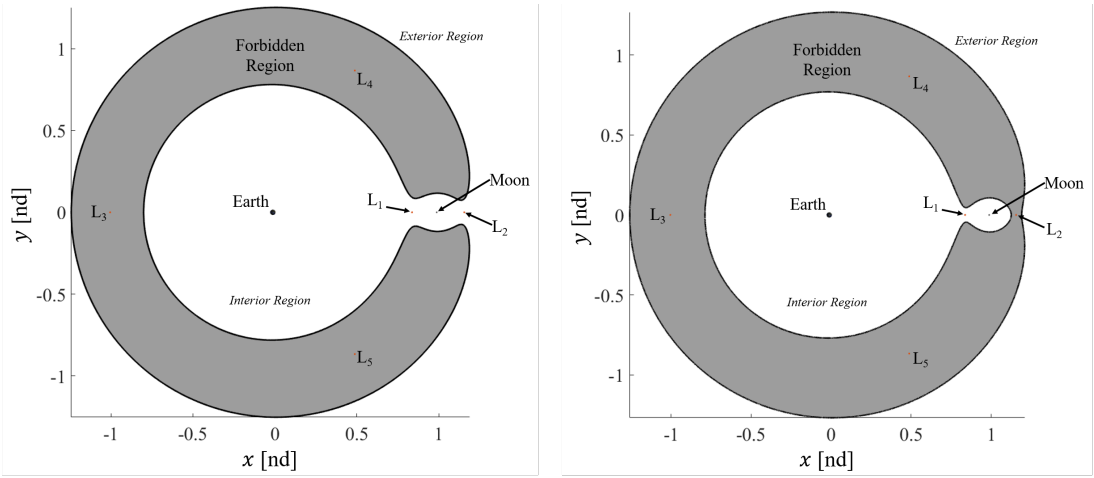

a b

Figure 2.3. Zero-Velocity Curves in the Earth-Moon system for (a) $JC = 3.16$ and (b) $JC = 3.18$.

the $\hat{x}\hat{y}$ plane. Considering the spatial scenario satisfying Equation (2.18), a three-dimensional surface bounds the motion for a given value of JC, denoted the Zero Velocity Surface (ZVS). An example of the ZVS in the Earth-Moon system is rendered in Figure 2.4 for a specific value of the JC, i.e., $JC = 3.16$. In the three-dimensional spatial problem, the forbidden region includes any position between the interior spherical structure and the exterior cylindrical structure. In the image in Figure 2.4, note that the L_1 and L_2 gateways are open. Figure 2.5 illustrates the in-plane ZVCs for different systems given the JC value $JC = \frac{JC_{L2}+JC_{L1}}{2}$, a value consistently evaluated across systems. This condition ensures that the Jacobi Constant is halfway between the Jacobi Constant value associated with L_1 and L_2, ensuring the L_1 gateway is open while the L_2 gateway is closed. Note that the difference in the size of the forbidden region as the mass ratio, μ, decreases. Szebehely provides a more thorough discussion of the ZVCs across a range of mass parameters as well [17]. The ZVCs define the regions where motion is allowable in the $\hat{x}\hat{y}$-plane for a given value of the Jacobi Constant. As the Jacobi Constant changes, regions of the space become available via the gateways defined by the collinear libration points.

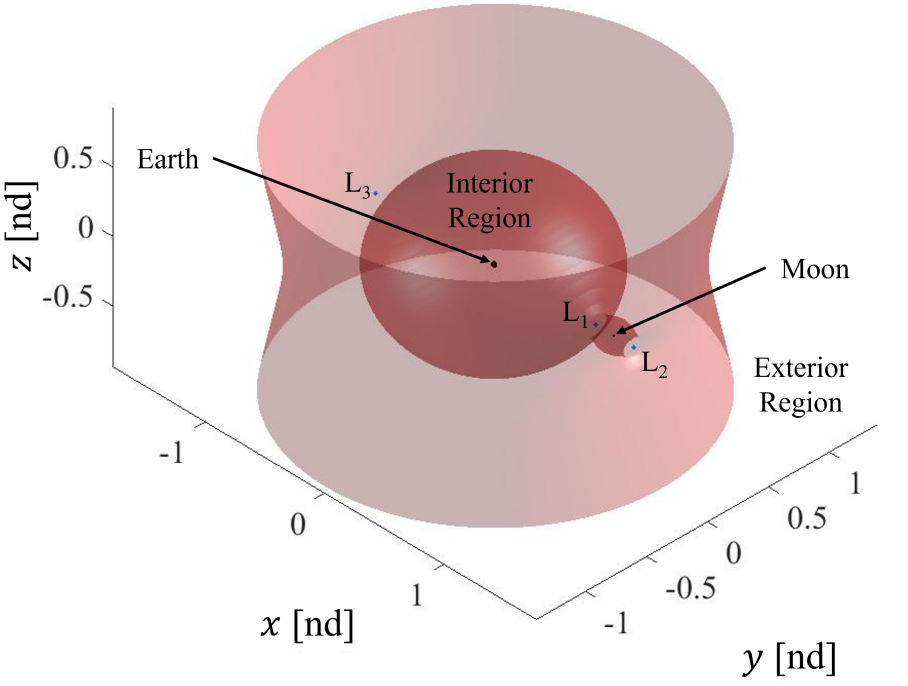

Figure 2.4. Zero-Velocity Surface (ZVS) in the Earth-Moon system, $JC = 3.16$.

2.2 Bicircular Restricted Four-Body Problem

Similar to the three-body problem, there is no solution to the problem of four bodies. However, several researchers have developed four-body models to capture the fundamental behavior. In 1960, Huang developed a model including the Sun, Earth, and Moon, denoted the very restricted four-body problem [46]. In this model, it was assumed that Sun and the Earth-Moon barycenter follow a circular Keplerian path about the Earth-Moon-Sun barycenter, while the Earth and Moon followed a circular Keplerian path about their mutual barycenter. Musen and Carpenter further developed a method to create a coherent Sun-Earth-Moon four-body problem using a geometric series [47]. More recently, Andreu formulated the quasi-bicircular problem, an attempt to more accurately capture the motion in the vicinity of the Sun-perturbed Earth-Moon L_2 point[48]. This investigation relies on the Earth-Moon-Sun bicircular restricted four-body problem (BCR4BP), which possesses the same formulation as the very restricted four-body problem developed by Huang. A set

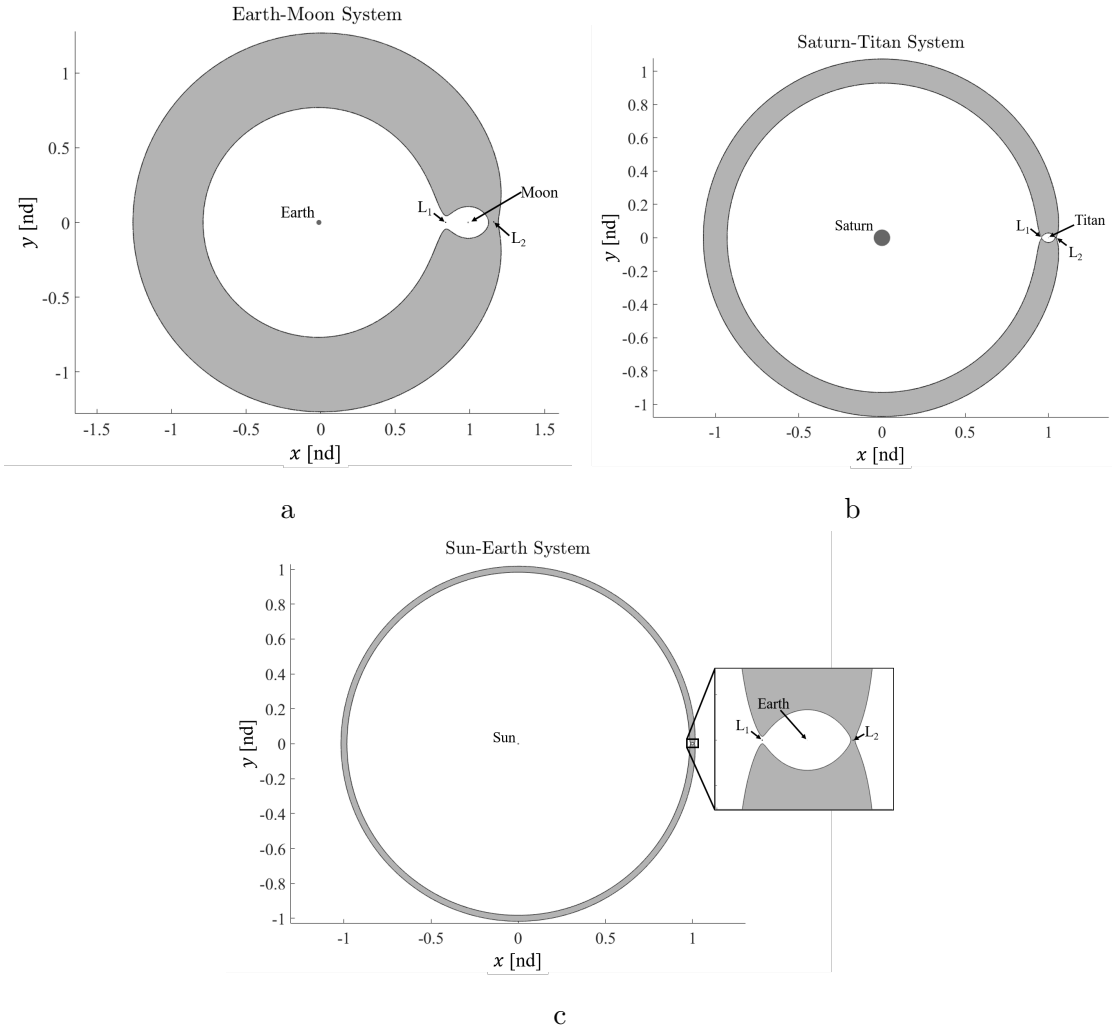

Figure 2.5. ZVCs for $JC = \frac{JC_{L2}+JC_{L1}}{2}$ in the (a) Earth-Moon system ($\mu = 0.1215$), (b) Saturn-Titan system ($\mu = 0.0002366$), and (c) Sun-Earth system($\mu = 3.0035 \times 10^{-6}$).

of assumptions for this model are first explored. Four centrobaric bodies are defined in this model, P_1, P_2, P_3, and P_4, with masses m_1, m_2, m_3, and m_4, respectively. Since this investigation concerns only the Earth-Moon-Sun bicircular problem, P_1, P_2, P_3, and P_4 correspond to the Earth, Moon, spacecraft and Sun, respectively. Similar to the CR3BP, it is assumed that the mass of P_3 is considered to be significantly less than the other three bodies ($m_3 << m_1, m_2, m_4$) and, subsequently, the motions of P_1, P_2 and P_4 are not influenced by P_3. Additionally, it is assumed that only the P_1-P_2 barycenter (denoted B_1) is influenced by P_4, i.e., the motion of P_1 and P_2 are not independently affected by the gravitational force

of P_4. This final assumption implies that the model is not coherent, but it is a sufficient approximation in the Sun-perturbed Earth-Moon region. It is also assumed that P_4 and B_1 move in circular, Keplerian paths about their mutual barycenter, denoted B_2, as well as the fact that P_1 and P_2 move in circular, Keplerian motions about B_1. Lastly, it is assumed in this work that the motion of the three massive bodies occurs in the same plane; again, assuming the Sun moves in the Earth-Moon plane is not necessary, but adequate for the purpose of this investigation. These assumptions allow the BCR4BP to be derived in a P_1-P_2 rotating frame, similar to the CR3BP.

The BCR4BP is a time-periodic system, where the location of the Sun in the Earth-Moon rotating frame is defined by a single angle θ_s. The Sun moves in a clockwise direction about B_1 (i.e., $\dot{\theta}_s$ is negative), as illustrated in Figure 2.6a. The equations of motion that describe the motion of P_3 in the Earth-Moon rotating frame are nondimensionalized and derived as,

$$\ddot{x} = 2\dot{y} + x - \frac{(1-\mu)(x+\mu)}{r_{13}^3} - \frac{\mu(x-1+\mu)}{r_{23}^3} - \frac{m_4(x - a_4\cos\theta_s)}{r_{43}^3} - \frac{m_4\cos\theta_s}{a_4^2} \tag{2.19}$$

$$\ddot{y} = -2\dot{x} + y - \frac{(1-\mu)y}{r_{13}^3} - \frac{\mu y}{r_{23}^3} - \frac{m_4(y - a_4\sin\theta_s)}{r_{43}^3} - \frac{m_4\sin\theta_s}{a_4^2} \tag{2.20}$$

$$\ddot{z} = -\frac{(1-\mu)z}{r_{13}^3} - \frac{\mu z}{r_{23}^3} - \frac{m_4 z}{r_{43}^3} \tag{2.21}$$

where r_{ij} is the distance of P_{i} relative to P_{j}, m_4 is the non-dimensional mass of P_4, i.e., $m_4 = \frac{M_4}{M_1+M_2}$, a_4 is the non-dimensional semi-major axis of the circular orbit reflecting the Sun-B_1 motion, and μ is the P_1-P_2 mass parameter, $\mu = \frac{M_2}{M_1+M_2}$. The term M_{i} is defined as the mass of P_{i}. Additionally, the rotation rate of the Sun about B_1, θ_s, is a function of a_4 and m_4, $\dot{\theta}_s = 1 - \sqrt{\frac{1+m_4}{a_4^3}}$. A complete derivation of the equation of motion describing the BCR4BP are summarized by Scheuerle [49]. As noted and consistent with the CR3BP, the BCR4BP is formulated using non-dimensional units. The dimensionalizing quantities for the BCR4BP, as represented in the Earth-Moon rotating frame, are listed in Table 2.1. Similarly, analyzing the motion in a Sun-B_1 rotating frame is advantageous. In this frame, the $\hat{x}'$-axis is directed from the Sun to B_1. The $\hat{z}'$-direction is defined parallel to the Sun-B_1

orbit angular momentum vector; the $\hat{y}'$-direction completes the triad. The Sun-B_1 rotating frame is illustrated in Figure 2.6b. The equations of motion for the Sun-B_1 rotating frame,

$$\ddot{x}' = 2\dot{y}' + x' - \frac{(1-\mu')(x'+\mu')}{r_{43}'^3} - \frac{\mu'(1-\mu)(x'-x_E')}{r_{13}'^3} - \frac{\mu'\mu(x'-x_M')}{r_{23}'^3} \tag{2.22}$$

$$\ddot{y}' = -2\dot{x}' + y' - \frac{(1-\mu')y'}{r_{43}'^3} - \frac{\mu'(1-\mu)(y'-y_E')}{r_{13}'^3} - \frac{\mu'\mu(y'-y_M')}{r_{23}'^3} \tag{2.23}$$

$$\ddot{z}' = -\frac{(1-\mu')z'}{r_{43}'^3} - \frac{\mu'(1-\mu)z'}{r_{13}'^3} - \frac{\mu'\mu z'}{r_{23}'^3} \tag{2.24}$$

where $\dot{x}'$, $\dot{y}'$, and $\dot{z}'$ are the non-dimensional relative velocity components in the Sun-B_1 rotating frame, $\ddot{x}'$, $\ddot{y}'$, and $\ddot{z}'$ are the non-dimensional relative acceleration components as viewed in the Sun-B_1 rotating frame, x_E' and y_E' are the position components of the Earth to an observer in the Sun-B_1 rotating frame, x_M' and y_M' are the position components of the Moon in the Sun-B_1 rotating frame, μ is the P_1-P_2 mass parameter, r_{ij}' is the distance of P_i relative to P_j in the Sun-B_1 rotating frame, and $\mu' = \frac{M_1+M_2}{M_1+M_2+M_4}$ is the Sun-B_1 mass parameter. The non-dimensionalizing quantities in the Sun-B_1 frame are again listed in Table 2.1. It is useful to visualize motion in this frame to add insight into the influence of solar gravity on trajectories with excursions beyond the Earth-Moon vicinity.

Table 2.1. Non-dimensional quantities for the Earth-Moon and Sun-B_1 rotating frame formulations of the BCR4BP. $\tilde{G}$ represents the Universal Gravitational Constant, M_i represents the mass of body P_i, and a_{12} and a_{4B1} are the semi-major axes of the Moon relative to the Earth and the Earth-Moon barycenter relative to the Sun, respectively

	Earth-Moon Rotating Frame	Sun-B_1 Rotating Frame
Length	$l_{EM}^* = a_{12} = 384747.992$ km	$l_{SB1}^* = a_{4B1} = 149597894$ km
Mass	$m_{EM}^* = \sum_{i=1,2} M_i = 6.04564 \times 10^{24}$ kg	$m_{SB1}^* = \sum_{i=1,2,4} M_i = 1.9884 \times 10^{30}$ kg
Time	$t_{EM}^* = \sqrt{\frac{{l_{EM}^*}^3}{\tilde{G}m_{EM}^*}} = 375699.859$ s	$t_{SB1}^* = \sqrt{\frac{{l_{SB1}^*}^3}{\tilde{G}m_{SB1}^*}} = 5022636.4$ s

To interpret the behavior within the context of both the Earth-Moon and Sun-B_1 rotating frames, a transformation between the frames is necessary. The transformation for position

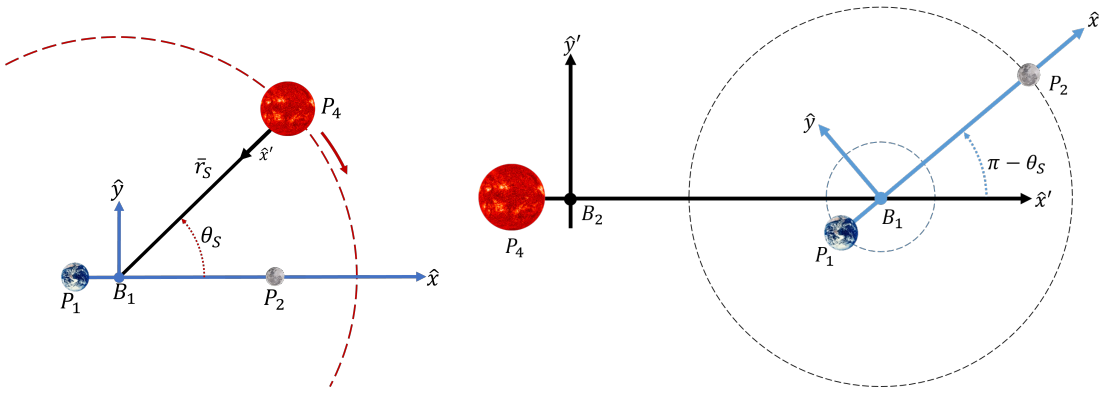

Figure 2.6. Earth-Moon rotating frame (left) and Sun-B_1 rotating frame (right) as defined in the BCR4BP.

and velocity, from the Earth-Moon rotating frame to the Sun-B_1 rotating frame is defined from Boudad [50],

$$\bar{x}' = \begin{bmatrix} 1-\mu' \\ 0 \\ 0 \\ 0 \\ 0 \\ 0 \end{bmatrix} + \bar{x}\frac{l^*_{EM}}{l^*_{SB1}} \begin{bmatrix} -\cos(\theta_s) & -\sin(\theta_s) & 0 & 0 & 0 & 0 \\ \sin(\theta_s) & -\cos(\theta_s) & 0 & 0 & 0 & 0 \\ 0 & 0 & 1 & 0 & 0 & 0 \\ -\dot{\theta}_s\sin(\theta_s) & \dot{\theta}_s\cos(\theta_s) & 0 & -\cos(\theta_s)\frac{t^*_{SB1}}{t^*_{EM}} & -\sin(\theta_s)\frac{t^*_{SB1}}{t^*_{EM}} & 0 \\ -\dot{\theta}_s\cos(\theta_s) & -\dot{\theta}_s\sin(\theta_s) & 0 & \sin(\theta_s)\frac{t^*_{SB1}}{t^*_{EM}} & -\cos(\theta_s)\frac{t^*_{SB1}}{t^*_{EM}} & 0 \\ 0 & 0 & 0 & 0 & 0 & \frac{t^*_{SB1}}{t^*_{EM}} \end{bmatrix} \tag{2.25}$$

where θ_s is the Sun angle, $\dot{\theta}_s$ is the rotation rate of the Sun about B_1 in the Earth-Moon rotating frame, $\bar{x} = \begin{bmatrix} x & y & z & \dot{x} & \dot{y} & \dot{z} \end{bmatrix}^T$ is the state vector in the Earth-Moon rotating frame and $\bar{x}' = \begin{bmatrix} x' & y' & z' & \dot{x}' & \dot{y}' & \dot{z}' \end{bmatrix}^T$ is a state vector in the Sun-B_1 rotating frame. This transformation process is simply reversed to transition states from the Sun-B_1 rotating frame to the Earth-Moon rotating frame.

2.2.1 First-Order Variational Equations of Motion

For analysis of behaviors in the vicinity of any reference solution in any model, understanding the first-order variations is necessary and also is a key capability in the BCR4BP.

Since a state in the BCR4BP is a function of θ_s, as well as position and velocity, the variational matrix, $\mathbf{A}$, for the BCR4BP is defined,

$$\mathbf{A}(t) = \begin{bmatrix} 0 & 0 & 0 & 1 & 0 & 0 & 0 \\ 0 & 0 & 0 & 0 & 1 & 0 & 0 \\ 0 & 0 & 0 & 0 & 0 & 1 & 0 \\ \Upsilon_{xx} & \Upsilon_{xy} & \Upsilon_{xz} & 0 & 2 & 0 & \Upsilon_{x\theta_s} \\ \Upsilon_{yx} & \Upsilon_{yy} & \Upsilon_{yz} & -2 & 0 & 0 & \Upsilon_{y\theta_s} \\ \Upsilon_{zx} & \Upsilon_{zy} & \Upsilon_{zz} & 0 & 0 & 0 & \Upsilon_{z\theta_s} \\ 0 & 0 & 0 & 0 & 0 & 0 & 0 \end{bmatrix} \tag{2.26}$$

where Υ is the pseudo-potential function in the BCR4BP formulated in the Earth-Moon rotating frame, defined,

$$\Upsilon = \frac{1-\mu}{r_{13}} + \frac{\mu}{r_{23}} + \frac{x^2+y^2}{2} + \frac{m_4}{r_{43}} - \frac{m_4(x\cos\theta_s + y\sin\theta_s)}{a_4^2} \tag{2.27}$$

where $\Upsilon_{ij} = \frac{\partial^2 \Upsilon}{\partial i \partial j}$ are the second partial derivatives of the pseudo potential function. These are evaluated as follows,

$$\Upsilon_{xx} = 1 - \frac{1-\mu}{d^3} - \frac{\mu}{r^3} + \frac{3(1-\mu)(x+\mu)^2}{d^5} + \frac{3\mu(x-1+\mu)^2}{r^5} + \frac{3m_4(x - a_4\cos\theta_s)^2}{r_{34}^5} \tag{2.28}$$

$$\Upsilon_{yy} = 1 - \frac{1-\mu}{d^3} - \frac{\mu}{r^3} + \frac{3(1-\mu)y^2}{d^5} + \frac{3\mu y^2}{r^5} + \frac{3m_4(y - a_4\sin\theta_s)^2}{r_{34}^5} \tag{2.29}$$

$$\Upsilon_{zz} = -\frac{1-\mu}{d^3} - \frac{\mu}{r^3} + \frac{3(1-\mu)z^2}{d^5} + \frac{3\mu z^2}{r^5} + \frac{3m_4 z^2}{r_{34}^5} \tag{2.30}$$

$$\Upsilon_{xy} = \frac{3(1-\mu)(x+\mu)y}{d^5} + \frac{3\mu(x-1+\mu)y}{r^5} + \frac{3m_4(x - a_4\cos\theta_s)y}{r_{34}^5} \tag{2.31}$$

$$\Upsilon_{xz} = \frac{3(1-\mu)(x+\mu)z}{d^5} + \frac{3\mu(x-1+\mu)z}{r^5} + \frac{3m_4(x - a_4\cos\theta_s)y}{r_{34}^5} \tag{2.32}$$

$$\Upsilon_{yz} = \frac{3(1-\mu)yz}{d^5} + \frac{3\mu yz}{r^5} + \frac{3m_4(y - a_4\sin\theta_s)z}{r_{34}^5} \tag{2.33}$$

$$\Upsilon_{x\theta_s} = \frac{-a_4 m_4 \sin\theta_s}{r_{34}^3} + \frac{m_4\sin\theta_s}{a_4^2} + \frac{3m_4 a_4(x - a_4\cos\theta_s)(\sin\theta_s(x - a_4\cos\theta_s) - \cos\theta_s(y - a_4\sin\theta_s))}{r_{34}^5} \tag{2.34}$$

$$\Upsilon_{y\theta_s} = \frac{a_4 m_4\cos\theta_s}{r_{34}^3} - \frac{m_4\cos\theta_s}{a_4^2} - \frac{3m_4 a_4(y - a_4\sin\theta_s)(\cos\theta_s(y - a_4\sin\theta_s) - \sin\theta_s(x - a_4\cos\theta_s))}{r_{34}^5} \tag{2.35}$$

$$\Upsilon_{z\theta_s} = \frac{3m_4 a_4 z(\sin\theta_s(x - a_4\cos\theta_s) + \cos\theta_s(y - a_4\sin\theta_s))}{r_{34}^5} \tag{2.36}$$

where $r_{34} = \sqrt{(x - a_4\cos\theta_s)^2 + (y - a_4\sin\theta_s)^2 + z^2}$ is the distance from the spacecraft to the Sun. Note that these variational equations of motion are formulated in the Earth-Moon rotating frame and a set of equations is also defined for the Sun-B_1 rotating frame. As in the CR3BP, these first-order variational equations of motion are numerically integrated along with the six-dimensional state equations of motion.

2.2.2 Equilibrium Solutions

There are no constant equilibrium solutions in the BCR4BP; however, instantaneous equilibrium solutions do exist in the BCR4BP. The first and second derivatives are equated to zero and then solving for the position, an instantaneous equilibrium solution exists for each θ_s value. A continuation process to solve for the equilibrium solutions in the BCR4BP is detailed by Boudad [50]. Since the continuum of points that represents the equilibrium solutions is dependent on the Sun angle, a particle initialized at these locations will not remain there for all time. The particle immediately departs since the location of the Sun changes with

time. These curves are denoted E_i, consistent with the definition by Boudad [50]. The continuum of E_1 and E_2 equilibrium solutions in the Earth-Moon rotating frame are plotted in Figure 2.7a and 2.7b. Note that the Earth-Moon CR3BP libration points are included in Figures 2.7a and 2.7b for reference. For an alternative view, both equilibrium solutions are plotted in the Sun-B_1 rotating frame in Figure 2.7c. There are three additional equilibrium solutions, denoted E_3, E_4, and E_4 in the Earth-Moon vicinity. But, this investigation focuses on motion in the lunar vicinity and, as such, an understanding of the dynamics in this region is critical.

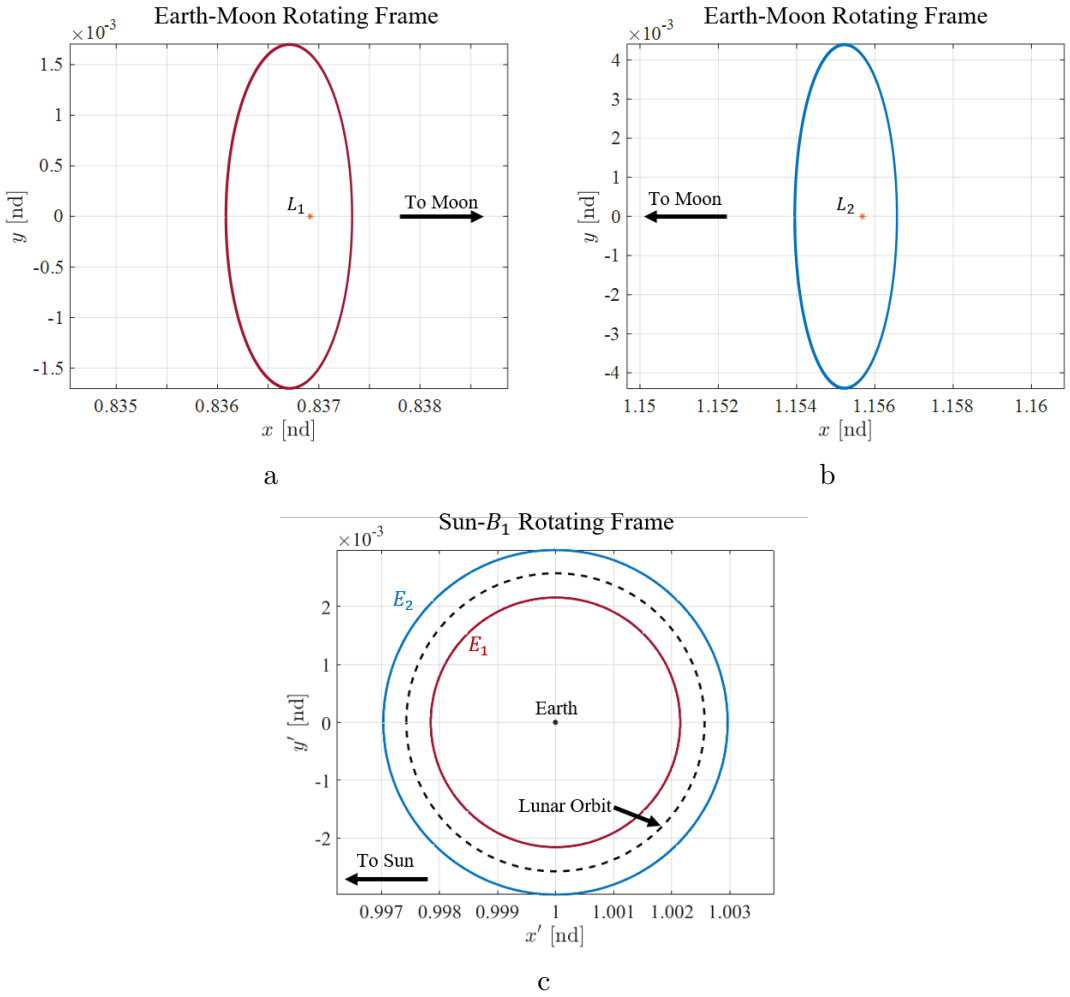

Figure 2.7. (a) The E_1 equilibrium solution from the BCR4BP in the Earth-Moon rotating frame. (b) The E_2 equilibrium solution from the BCR4BP in the Earth-Moon rotating frame. (c) E_1 and E_2 represented in the Sun-B_1 rotating frame.

2.2.3 BCR4BP Hamiltonian

In the CR3BP, an integral of the motion exists and is termed the Jacobi Constant. This is an energy-like quantity that emerges from the equations of motion. An energy-like quantity also exists in the BCR4BP, and is denoted the Hamiltonian, by previous investigators [49], [50]. In this analysis, the Hamiltonian as formulated in the BCR4BP Earth-Moon rotating frame is denoted H. Then, the quantity is labeled H' as formulated in the Sun-B_1 rotating frame. These quantities are a function of the pseudo-potential and the relative velocity magnitude, i.e.,

$$H = 2\Upsilon - (\dot{x}^2 + \dot{y}^2 + \dot{z}^2) \tag{2.37}$$

$$H' = 2\Upsilon' - (\dot{x}'^2 + \dot{y}'^2 + \dot{z}'^2) \tag{2.38}$$

where Υ is the pseudo-potential function defined in Equation (2.27) and Υ' is the pseudo-potential as defined for the BCR4BP in the Sun-B_1 rotating frame. The Sun-B_1 Hamiltonian is defined similarly using the pseudo-potential relative to the Sun-B_1 formulation of the BCR4BP. The quantities H and H' are not "Hamiltonian" functions in the classical sense of Hamiltonian mechanics, since the equations of motion cannot be directly derived from Equations (2.37) and (2.38). Rather, the quantities H and H' are defined as such for a more direct comparison to the Jacobi Constant in the CR3BP. The symbols H and H' are retained in this investigation due to the links to the broader range of models.

2.3 Ephemeris Model

The ephemeris force model offers a higher-fidelity gravity force representation on a spacecraft by incorporating the ephemeris states of various celestial bodies. In this model, the motion of a massless spacecraft, s, is described relative to an inertial frame. The path of the spacecraft is influenced by the gravity of a central body (c) and the number (p) of perturbing bodies. The relative equations of motion for the ephemeris model are formulated as three scalar, second-order differential equations,

$$\ddot{x}_{c,s} = -\frac{GM_c x_{c,s}}{r_{c,s}^3} - G\sum_{\mathrm{i}=1}^{p} M_{\mathrm{i}} \left(\frac{x_{c,s} - x_{c,\mathrm{i}}}{|\vec{r}_{c,s} - \vec{r}_{c,\mathrm{i}}|^3} + \frac{x_{c,\mathrm{i}}}{r_{c,\mathrm{i}}^3} \right) \tag{2.39}$$

$$\ddot{y}_{c,s} = -\frac{GM_c y_{c,s}}{r_{c,s}^3} - G\sum_{\mathrm{i}=1}^{p} M_{\mathrm{i}} \left(\frac{y_{c,s} - y_{c,\mathrm{i}}}{|\vec{r}_{c,s} - \vec{r}_{c,\mathrm{i}}|^3} + \frac{y_{c,\mathrm{i}}}{r_{c,\mathrm{i}}^3} \right) \tag{2.40}$$

$$\ddot{z}_{c,s} = -\frac{GM_c z_{c,s}}{r_{c,s}^3} - G\sum_{\mathrm{i}=1}^{p} M_{\mathrm{i}} \left(\frac{z_{c,s} - z_{c,\mathrm{i}}}{|\vec{r}_{c,s} - \vec{r}_{c,\mathrm{i}}|^3} + \frac{z_{c,\mathrm{i}}}{r_{c,\mathrm{i}}^3} \right) \tag{2.41}$$

where $x_{c,s}$, $y_{c,s}$, and $z_{c,s}$ are the position components of the spacecraft relative to the central body, c, G is the Universal Gravitational Constant, M_{i} is the mass of the i^{th} perturbing body, M_c is the mass of the central body, $\vec{r}_{c,\mathrm{i}}$ is the position of the i^{th} perturbing body relative to the central body. The relative equations of motion are defined using dimensional quantities; however, nondimensionalization is typically performed to mitigate challenges associated with numerical integration. The interpolated position and velocity states that correspond to the bodies are extracted from the ephemerides on the JPL NAIF server [51]. Similar to the CR3BP and BCR4BP, it is also useful to obtain information about the first-order variations in the ephemeris model. The variational matrix for the ephemeris model is defined,

$$\mathbf{A}(t) = \begin{bmatrix} 0 & 0 & 0 & 1 & 0 & 0 \\ 0 & 0 & 0 & 0 & 1 & 0 \\ 0 & 0 & 0 & 0 & 0 & 1 \\ U_{xx} & U_{xy} & U_{xz} & 0 & 0 & 0 \\ U_{yx} & U_{yy} & U_{yz} & 0 & 0 & 0 \\ U_{zx} & U_{zy} & U_{zz} & 0 & 0 & 0 \end{bmatrix} \tag{2.42}$$

where $U_{\mathrm{ij}} = \frac{\partial^2 U}{\partial \mathrm{i} \partial \mathrm{j}}$ are the partial derivatives of the potential function for the ephemeris model, defined as,

$$U_{xx} = GM_c \left(\frac{3x_{c,s}^2}{r_{c,s}^5} - \frac{1}{r_{c,s}^3} \right) + \sum_{\mathrm{i}=1}^{p} GM_{\mathrm{i}} \left(\frac{3(x_{c,\mathrm{i}} - x_{c,s})^2}{|\vec{r}_{c,\mathrm{i}} - \vec{r}_{c,s}|^5} - \frac{1}{|\vec{r}_{c,\mathrm{i}} - \vec{r}_{c,s}|^3} \right) \tag{2.43}$$

$$U_{yy} = GM_c \left(\frac{3y_{c,s}^2}{r_{c,s}^5} - \frac{1}{r_{c,s}^3} \right) + \sum_{\mathrm{i}=1}^{p} GM_{\mathrm{i}} \left(\frac{3(y_{c,\mathrm{i}} - y_{c,s})^2}{|\vec{r}_{c,\mathrm{i}} - \vec{r}_{c,s}|^5} - \frac{1}{|\vec{r}_{c,\mathrm{i}} - \vec{r}_{c,s}|^3} \right) \tag{2.44}$$

$$U_{zz} = GM_c \left(\frac{3z_{c,s}^2}{r_{c,s}^5} - \frac{1}{r_{c,s}^3} \right) + \sum_{\mathrm{i}=1}^{p} GM_{\mathrm{i}} \left(\frac{3(z_{c,\mathrm{i}} - z_{c,s})^2}{|\vec{r}_{c,\mathrm{i}} - \vec{r}_{c,s}|^5} - \frac{1}{|\vec{r}_{c,\mathrm{i}} - \vec{r}_{c,s}|^3} \right) \tag{2.45}$$

$$U_{xy} = GM_c \left(\frac{3x_{c,s}y_{c,s}}{r_{c,s}^5} - \frac{1}{r_{c,s}^3} \right) + \sum_{\mathrm{i}=1}^{p} GM_{\mathrm{i}} \frac{3(x_{c,\mathrm{i}} - x_{c,s})(y_{c,\mathrm{i}} - y_{c,s})}{|\vec{r}_{c,\mathrm{i}} - \vec{r}_{c,s}|^5} \tag{2.46}$$

$$U_{xz} = GM_c \left(\frac{3x_{c,s}z_{c,s}}{r_{c,s}^5} - \frac{1}{r_{c,s}^3} \right) + \sum_{\mathrm{i}=1}^{p} GM_{\mathrm{i}} \frac{3(x_{c,\mathrm{i}} - x_{c,s})(z_{c,\mathrm{i}} - z_{c,s})}{|\vec{r}_{c,\mathrm{i}} - \vec{r}_{c,s}|^5} \tag{2.47}$$

$$U_{yz} = GM_c \left(\frac{3y_{c,s}z_{c,s}}{r_{c,s}^5} - \frac{1}{r_{c,s}^3} \right) + \sum_{\mathrm{i}=1}^{p} GM_{\mathrm{i}} \frac{3(y_{c,\mathrm{i}} - y_{c,s})(z_{c,\mathrm{i}} - z_{c,s})}{|\vec{r}_{c,\mathrm{i}} - \vec{r}_{c,s}|^5} \tag{2.48}$$

Note that the ephemeris problem is also a function of the epoch since the epoch determines the vector locations of the perturbing bodies relative to the central body, $\vec{r}_{c,\mathrm{i}}$. Subsequently, the first-order variations on the spacecraft state with respect to the initial epoch are a specific focus. Thus, if the dimensional epoch time is defined as τ, then the first-order variational equations of motion for epoch time are expressed,

$$\frac{d}{dt} \frac{\partial \vec{r}_{c,s}}{\partial \tau} = \mathbf{A} \frac{\partial \vec{r}_{c,s}}{\partial \tau} + \sum_{\mathrm{i}=1}^{p} \frac{\partial \dot{\vec{r}}_{c,s}}{\partial \vec{r}_{c,\mathrm{i}}} \vec{v}_{c,\mathrm{i}} \tag{2.49}$$

where $\mathbf{A}$ for an ephemeris model is defined in Equation (2.42), $\vec{v}_{c,\mathrm{i}}$ is the velocity of the i^{th} perturbing body relative to the central body, $\frac{\partial \vec{r}_{c,s}}{\partial \tau} = \begin{bmatrix} \frac{\partial x_{c,s}}{\partial \tau} & \frac{\partial y_{c,s}}{\partial \tau} & \frac{\partial y_{c,s}}{\partial \tau} & \frac{\partial \dot{x}_{c,s}}{\partial \tau} & \frac{\partial \dot{y}_{c,s}}{\partial \tau} & \frac{\partial \dot{z}_{c,s}}{\partial \tau} \end{bmatrix}^T$ is

the vector reflecting state derivatives with respect to epoch time. Then, the partial derivative of $\dot{\vec{r}}_{c,s}$ with respect to the position of the i$^{\text{th}}$ perturbing body, $\vec{r}_{c,\text{i}}$, is written,

$$\frac{\partial \dot{\vec{r}}_{c,s}}{\partial \vec{r}_{c,\text{i}}} = \begin{bmatrix} 0 & 0 & 0 \\ 0 & 0 & 0 \\ 0 & 0 & 0 \\ \frac{\partial \ddot{x}_{c,s}}{\partial x_{c,\text{i}}} & \frac{\partial \ddot{x}_{c,s}}{\partial y_{c,\text{i}}} & \frac{\partial \ddot{x}_{c,s}}{\partial z_{c,\text{i}}} \\ \frac{\partial \ddot{y}_{c,s}}{\partial x_{c,\text{i}}} & \frac{\partial \ddot{y}_{c,s}}{\partial y_{c,\text{i}}} & \frac{\partial \ddot{y}_{c,s}}{\partial z_{c,\text{i}}} \\ \frac{\partial \ddot{z}_{c,s}}{\partial x_{c,\text{i}}} & \frac{\partial \ddot{z}_{c,s}}{\partial y_{c,\text{i}}} & \frac{\partial \ddot{z}_{c,s}}{\partial z_{c,\text{i}}} \end{bmatrix} \tag{2.50}$$

where each component in the lower half of the matrix is expressed,

$$\frac{\partial \ddot{x}_{c,s}}{\partial x_{c,\text{i}}} = GM_{\text{i}} \left(\frac{1}{|\vec{r}_{c,\text{i}} - \vec{r}_{c,s}|^3} - \frac{3(x_{c,\text{i}} - x_{c,s})^2}{|\vec{r}_{c,\text{i}} - \vec{r}_{c,s}|^5} - \frac{1}{r_{c,\text{i}}^3} + \frac{3x_{c,\text{i}}^2}{r_{c,\text{i}}^5} \right) \tag{2.51}$$

$$\frac{\partial \ddot{y}_{c,s}}{\partial y_{c,\text{i}}} = GM_{\text{i}} \left(\frac{1}{|\vec{r}_{c,\text{i}} - \vec{r}_{c,s}|^3} - \frac{3(y_{c,\text{i}} - y_{c,s})^2}{|\vec{r}_{c,\text{i}} - \vec{r}_{c,s}|^5} - \frac{1}{r_{c,\text{i}}^3} + \frac{3y_{c,\text{i}}^2}{r_{c,\text{i}}^5} \right) \tag{2.52}$$

$$\frac{\partial \ddot{z}_{c,s}}{\partial z_{c,\text{i}}} = GM_{\text{i}} \left(\frac{1}{|\vec{r}_{c,\text{i}} - \vec{r}_{c,s}|^3} - \frac{3(z_{c,\text{i}} - z_{c,s})^2}{|\vec{r}_{c,\text{i}} - \vec{r}_{c,s}|^5} - \frac{1}{r_{c,\text{i}}^3} + \frac{3z_{c,\text{i}}^2}{r_{c,\text{i}}^5} \right) \tag{2.53}$$

$$\frac{\partial \ddot{x}_{c,s}}{\partial y_{c,\text{i}}} = \frac{\partial \ddot{y}_{c,s}}{\partial x_{c,\text{i}}} = -3GM_{\text{i}} \left(\frac{(x_{c,\text{i}} - x_{c,s})(y_{c,\text{i}} - y_{c,s})}{|\vec{r}_{c,\text{i}} - \vec{r}_{c,s}|^5} - \frac{3x_{c,\text{i}} y_{c,\text{i}}}{r_{c,\text{i}}^5} \right) \tag{2.54}$$

$$\frac{\partial \ddot{x}_{c,s}}{\partial z_{c,\text{i}}} = \frac{\partial \ddot{z}_{c,s}}{\partial x_{c,\text{i}}} = -3GM_{\text{i}} \left(\frac{(x_{c,\text{i}} - x_{c,s})(z_{c,\text{i}} - z_{c,s})}{|\vec{r}_{c,\text{i}} - \vec{r}_{c,s}|^5} - \frac{3x_{c,\text{i}} z_{c,\text{i}}}{r_{c,\text{i}}^5} \right) \tag{2.55}$$

$$\frac{\partial \ddot{y}_{c,s}}{\partial z_{c,\text{i}}} = \frac{\partial \ddot{z}_{c,s}}{\partial y_{c,\text{i}}} = -3GM_{\text{i}} \left(\frac{(y_{c,\text{i}} - y_{c,s})(z_{c,\text{i}} - z_{c,s})}{|\vec{r}_{c,\text{i}} - \vec{r}_{c,s}|^5} - \frac{3y_{c,\text{i}} z_{c,\text{i}}}{r_{c,\text{i}}^5} \right) \tag{2.56}$$

These additional six, scalar differential equations are integrated along with the state and the STM equations of motion. The variational relationships are useful in gradient-based targeting problems in the ephemeris model to satisfy realistic mission constraints.

2.4 Differential Corrections

Initial conditions for arbitrary trajectory arcs are selected through a variety of methods. However, rarely do such initial conditions meet all constraints for a given design, especially in multi-body regimes. Numerical strategies, such as differential corrections, are required to determine solutions that meet all of the constraints for a particular scenario. The STM provides the basis for various differential corrections strategies that are successful in this regime. Using the relationships based on the STM, one available type of multi-dimensional Newton differential corrections method is introduced that is straightforward to apply in many scenarios.

Generally in trajectory design problems, a differential corrections algorithm is employed to solve a two-point boundary value problem. A more extensive summary of different types of differential corrections methods is provided by Spreen [52]. While many methods exist to solve two-point boundary value problems, a constraint/free variable Newton method is employed in this investigation. The free variable vector $\vec{X}$ is defined,

$$\vec{X} = \begin{bmatrix} X_1 \\ \vdots \\ X_n \end{bmatrix} \tag{2.57}$$

where n is the number of free variables. Within a trajectory design application, sample free variables might typically include time-of-flight (TOF), state vector elements, epoch times, altitudes, as well as line-of-sight angles and other physical parameters. For a given design concept, there are then a set of m scalar constraints to be satisfied,

$$\vec{F}(\vec{X}) = \begin{bmatrix} F_1(\vec{X}) \\ \vdots \\ F_m(\vec{X}) \end{bmatrix} = \vec{0} \tag{2.58}$$

that are a function of the free variables. In this strategy, constraints are always defined such that they are equal to zero for a satisfactory solution, $\vec{X}^*$. Given an initial free variable

vector, $\vec{X}_0$, a first-order Taylor series expansion defines the constraint vector based on a final set of free variables $\vec{X}_f$,

$$\vec{F}(\vec{X}_f) = \vec{F}(\vec{X}_0) + \boldsymbol{DF}(\vec{X}_0)(\vec{X}_f - \vec{X}_0) \tag{2.59}$$

where $\boldsymbol{DF}(\vec{X}_0)$ is the $m \times n$ Jacobian matrix of partial derivatives of the constraints with respect to the free variables,

$$\boldsymbol{DF}(\vec{X}_0) = \frac{\partial \vec{F}}{\partial \vec{X}_0} = \begin{bmatrix} \frac{\partial F_1}{\partial X_1} & \cdots & \frac{\partial F_1}{\partial X_n} \\ \cdots & \ddots & \cdots \\ \frac{\partial F_m}{\partial X_1} & \cdots & \frac{\partial F_m}{\partial X_n} \end{bmatrix} \tag{2.60}$$

When satisfied, the constraint vector is equal to zero, so Equation (2.59) is rewritten,

$$\vec{F}(\vec{X}_\mathrm{j}) + \boldsymbol{DF}(\vec{X}_\mathrm{j})(\vec{X}_{\mathrm{j}+1} - \vec{X}_\mathrm{j}) = \vec{0} \tag{2.61}$$

where $\vec{X}_\mathrm{j}$ and $\vec{X}_{\mathrm{j}+1}$ are the free variable vectors for the j^{th} iteration and $\mathrm{j}+1^{\mathrm{th}}$ iteration, respectively. From linear algebra, the solution for Equation (2.61) depends on the relative sizes of the vectors $\vec{X}$ and $\vec{F}(\vec{X})$. First, the condition $n = m$ is considered, where the number of free variables is equal to the number of constraints. An update equation for the iterative Newton scheme is defined for the free variables by rearranging Equation (2.61) such that each iteration delivers an update to the design variable vector, i.e.,

$$\vec{X}_{\mathrm{j}+1} = \vec{X}_\mathrm{j} - (\boldsymbol{DF}(\vec{X}_\mathrm{j}))^{-1}\vec{F}(\vec{X}_\mathrm{j}) \tag{2.62}$$

The second condition, where the number of free variables is greater than the number of constraints or $n > m$, yields a Jacobian that is a non-square matrix. In this scenario, an infinite number of solutions exist. While there are several methods to solve an underdetermined

system, a minimum norm approach provides a solution that remains closest to the initial guess, $\vec{X}_0$. The minimum norm solution to the underdetermined system is formulated as,

$$\vec{X}_{\mathrm{j}+1} = \vec{X}_{\mathrm{j}} - \mathbf{DF}(\vec{X}_{\mathrm{j}})^T[\mathbf{DF}(\vec{X}_{\mathrm{j}})\mathbf{DF}(\vec{X}_{\mathrm{j}})^T]^{-1}\vec{F}(\vec{X}_{\mathrm{j}}) \tag{2.63}$$

where $\mathbf{DF}(\vec{X}_{\mathrm{j}})^T$ is the transpose of the Jacobian matrix evaluated on $\vec{X}_{\mathrm{j}}$. The minimum norm solution provides an update to the next iteration of the free variable vector, $\vec{X}_{\mathrm{j}+1}$, which minimizes the difference between the free variable vector of the current iteration, $\vec{X}_{\mathrm{j}}$ and the next iteration, $\vec{X}_{\mathrm{j}+1}$. Retaining the minimum difference between iteration attempts keeps the solution as close as possible to the initial guess supplied in the differential corrections scheme. The third scenario, an overdetermined system, occurs when the number of constraints is greater than the number of free variables or $n < m$. For this condition, there are no solutions to Equation (2.61). However, a least-squares approach delivers a free variable vector that minimizes $\vec{F}(\vec{X}_{\mathrm{j}}) + \mathbf{DF}(\vec{X}_{\mathrm{j}})(\vec{X}_{\mathrm{j}+1} - \vec{X}_{\mathrm{j}})$ in Equation (2.61). The least squares solution is computed

$$\vec{X}_{\mathrm{j}+1} = \vec{X}_{\mathrm{j}} - [\mathbf{DF}(\vec{X}_{\mathrm{j}})^T\mathbf{DF}(\vec{X}_{\mathrm{j}})]^{-1}\mathbf{DF}(\vec{X}_{\mathrm{j}})^T\vec{F}(\vec{X}_{\mathrm{j}}) \tag{2.64}$$

Differential corrections is a numerical algorithm, so the solution to Equation (2.61) cannot typically be solved to yield absolute zero. Therefore, a free variable vector is computed such that the magnitude of the constraint vector is below a small tolerance, ϵ,

$$||\vec{F}(\vec{X}^*)|| < \epsilon \tag{2.65}$$

where $\vec{X}^*$ is the free variable vector that satisfies the constraints. While a solution is not guaranteed, differential corrections reliably delivers a solution using a "good" initial guess.

2.4.1 Single Shooting

A single shooting differential corrections scheme is a simple application of a multi-dimensional Newton method for trajectory design. Consider a single trajectory arc in Figure 2.8, whose initial condition is defined by the state vector $\vec{x}(t_0)$ where the initial time is de-

fined t_0. The trajectory is propagated for a time, $t = t_0 + T$, such that the final state along the arc is $\vec{x}(t) = \vec{x}(t_0 + T)$. Further consider a desired location, $\vec{r}^* = \begin{bmatrix} x^* & y^* & z^* \end{bmatrix}^T$, achieved by modifying the time of flight and the initial velocity vector. A free variable vector, $\vec{X}$, is

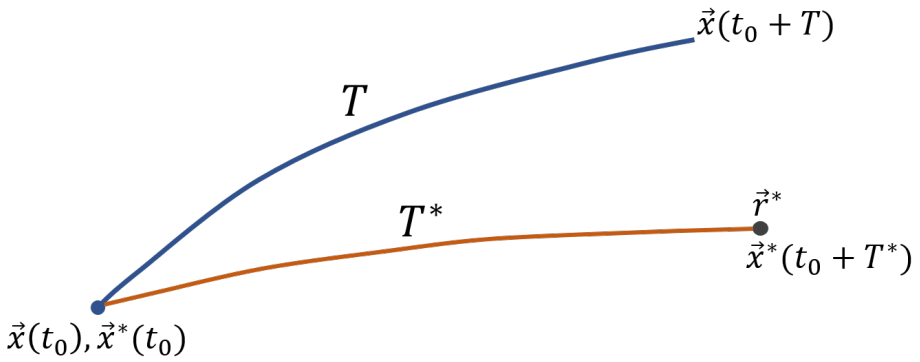

Figure 2.8. Single shooting differential corrections targeting scheme

developed for this scenario, such that,

$$\vec{X} = \begin{bmatrix} \dot{x}(t_0) \\ \dot{y}(t_0) \\ \dot{z}(t_0) \\ T \end{bmatrix} \tag{2.66}$$

where $\dot{x}(t_0)$, $\dot{y}(t_0)$, and $\dot{z}(t_0)$ are the velocity components at the initial state, and T is the non-dimensional time of flight. The constraint vector is then defined as,

$$\vec{F}(\vec{X}) = \begin{bmatrix} x(t_0 + T) - x^* \\ y(t_0 + T) - y^* \\ z(t_0 + T) - z^* \end{bmatrix} \tag{2.67}$$

such that the final position is achieved when $\vec{F}(\vec{X}) = \vec{0}$. The Jacobian matrix is formulated, using Equation (2.60) as follows,

$$\mathbf{DF}(\vec{X}) = \begin{bmatrix} \frac{\partial(x(t_0+T)-x^*)}{\partial \dot{x}(t_0)} & \frac{\partial(x(t_0+T)-x^*)}{\partial \dot{y}(t_0)} & \frac{\partial(x(t_0+T)-x^*)}{\partial \dot{z}(t_0)} & \frac{\partial(x(t_0+T)-x^*)}{\partial T} \\ \frac{\partial(y(t_0+T)-y^*)}{\partial \dot{x}(t_0)} & \frac{\partial(y(t_0+T)-y^*)}{\partial \dot{y}(t_0)} & \frac{\partial(y(t_0+T)-y^*)}{\partial \dot{z}(t_0)} & \frac{\partial(y(t_0+T)-y^*)}{\partial T} \\ \frac{\partial(z(t_0+T)-z^*)}{\partial \dot{x}(t_0)} & \frac{\partial(z(t_0+T)-z^*)}{\partial \dot{y}(t_0)} & \frac{\partial(z(t_0+T)-z^*)}{\partial \dot{z}(t_0)} & \frac{\partial(z(t_0+T)-z^*)}{\partial T} \end{bmatrix} \tag{2.68}$$

Notice that the final desired position, $\vec{r}^*$, is independent of the free variables. Then, the Jacobian matrix is rewritten in terms of the elements of the STM and the time derivative of position at the final state,

$$\mathbf{DF}(\vec{X}) = \begin{bmatrix} \frac{\partial x(t)}{\partial \dot{x}(t_0)} & \frac{\partial x(t)}{\partial \dot{y}(t_0)} & \frac{\partial x(t)}{\partial \dot{z}(t_0)} & \frac{\partial x(t)}{\partial T} \\ \frac{\partial y(t)}{\partial \dot{x}(t_0)} & \frac{\partial y(t)}{\partial \dot{y}(t_0)} & \frac{\partial y(t)}{\partial \dot{z}(t_0)} & \frac{\partial y(t)}{\partial T} \\ \frac{\partial z(t)}{\partial \dot{x}(t_0)} & \frac{\partial z(t)}{\partial \dot{y}(t_0)} & \frac{\partial z(t)}{\partial \dot{z}(t_0)} & \frac{\partial z(t)}{\partial T} \end{bmatrix} = \begin{bmatrix} \Phi_{1,4}(t,t_0) & \Phi_{1,5}(t,t_0) & \Phi_{1,6}(t,t_0) & \dot{x}(t) \\ \Phi_{2,4}(t,t_0) & \Phi_{2,5}(t,t_0) & \Phi_{2,6}(t,t_0) & \dot{y}(t) \\ \Phi_{3,4}(t,t_0) & \Phi_{3,5}(t,t_0) & \Phi_{3,6}(t,t_0) & \dot{z}(t) \end{bmatrix} \tag{2.69}$$

where $t = t_0 + T$, and $\Phi_{\mathrm{i,j}}(t, t_0)$ is element i, j of the STM, propagated from time t_0 to time t. Infinitely many solutions exist since there are more free variables than constraints or $n > m$, thus, the system is underdetermined. However, given a reasonable initial guess, iterating using the minimum norm formulation in Equation (2.63), a solution, $\vec{x}^*(t_0)$, is determined to within some acceptable tolerance.

2.4.2 Multiple Shooting

The single shooting algorithm is straightforwardly extended to multiple shooting by linking several single shooting problems using the same free variable/constraint formulation. The multiple shooting algorithm is valuable for trajectory design by linking trajectory segments for various applications, including the computation of periodic orbits. Consider a set of discontinuous trajectory arcs as illustrated in Figure 2.9. Such a set of discontinuous arcs serve as an initial guess for some scenario. The initial state at the beginning of each arc, or patch point state, is defined $\vec{x}_{\mathrm{i}} = \begin{bmatrix} x(t_{\mathrm{i}}) & y(t_{\mathrm{i}}) & z(t_{\mathrm{i}}) & \dot{x}(t_{\mathrm{i}}) & \dot{y}(t_{\mathrm{i}}) & \dot{z}(t_{\mathrm{i}}) \end{bmatrix}^T$, where i is the index corresponding to the patch point. The i^{th} patch point state, $\vec{x}_{\mathrm{i}}$ is propagated for time T_{i} and the final state at the end of the propagation arc, at time $t_{\mathrm{i}} + T_{\mathrm{i}}$, is defined as

$\vec{x}^t_{i+1}$. A free variable vector is developed using the state vectors corresponding to each patch

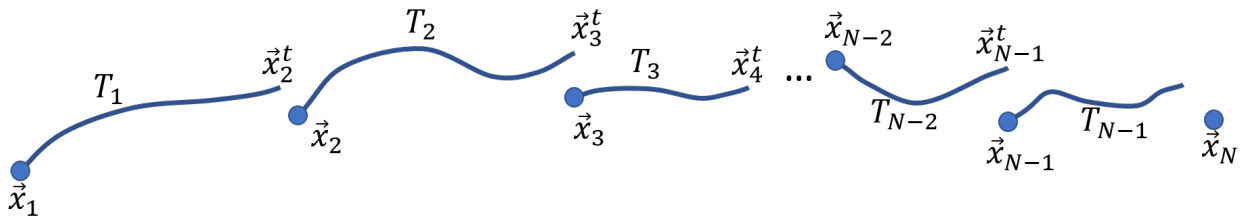

Figure 2.9. Trajectory arcs in multiple shooting scheme

point, including the propagation time for each trajectory arc; the resulting vector possesses a dimension $7N - 1$,

$$\vec{X} = \begin{bmatrix} \vec{x}_1 \\ \vec{x}_2 \\ \vec{x}_3 \\ \vdots \\ \vec{x}_{N-2} \\ \vec{x}_{N-1} \\ \vec{x}_N \\ T_1 \\ T_2 \\ T_3 \\ \vdots \\ T_{N-2} \\ T_{N-1} \end{bmatrix} \tag{2.70}$$

Thus, the initial conditions and the time-of-flight for each of the arcs are allowed to vary within the differential corrections scheme. A continuous trajectory is the goal, so the constraint vector is defined by state continuity between all of the arcs. The continuity is mathematically represented in the form of patch points. The constraint is expressed as the

difference between the initial patch point and the final state along the previous arc. The constraint vector includes $6N-6$ elements and is written

$$\vec{F}(\vec{X}) = \begin{bmatrix} \vec{x}_2^t - \vec{x}_2 \\ \vec{x}_3^t - \vec{x}_3 \\ \vdots \\ \vec{x}_{N-1}^t - \vec{x}_{N-1} \\ \vec{x}_N^t - \vec{x}_N \end{bmatrix} \tag{2.71}$$

The Jacobian is decomposed into two submatrices for organizational purposes during computation. The first submatrix includes the partial derivatives of the constraints with respect to the patch point state vectors

$$\mathbf{DF}_1 = \begin{bmatrix} \mathbf{\Phi}(t_1+T_1,t_1) & -\mathbf{I_{6\times 6}} & \mathbf{0_{6\times 6}} & \cdots & \mathbf{0_{6\times 6}} & \mathbf{0_{6\times 6}} \\ \mathbf{0_{6\times 6}} & \mathbf{\Phi}(t_2+T_2,t_2) & -\mathbf{I_{6\times 6}} & \cdots & \mathbf{0_{6\times 6}} & \mathbf{0_{6\times 6}} \\ \vdots & \vdots & \vdots & \ddots & & \\ \mathbf{0_{6\times 6}} & \mathbf{0_{6\times 6}} & \mathbf{0_{6\times 6}} & & \mathbf{\Phi}(t_{N-1}+T_{N-1},t_{N-1}) & -\mathbf{I_{6\times 6}} \end{bmatrix} \tag{2.72}$$

where $\mathbf{\Phi}(t_\mathrm{i}+T_\mathrm{i},t_\mathrm{i})$ is the STM from time t_i to $t_\mathrm{i}+T_\mathrm{i}$, $\mathbf{I}_{6\times 6}$ is a 6×6 identity matrix, and $\mathbf{0}_{6\times 6}$ is a 6×6 matrix of zeros. The second submatrix contains the partial derivatives of the constraints with respect to the times-of-flight

$$\mathbf{DF}_2 = \begin{bmatrix} \dot{\vec{x}}_2^t & \vec{0}_{6\times 1} & \cdots & \vec{0}_{6\times 1} \\ \vec{0}_{6\times 1} & \dot{\vec{x}}_3^t & \cdots & \vec{0}_{6\times 1} \\ \vdots & \vdots & \ddots & \\ \vec{0}_{6\times 1} & \vec{0}_{6\times 1} & & \dot{\vec{x}}_N^t \end{bmatrix} \tag{2.73}$$

Combining the submatrices in Equation (2.72) and Equation (2.73) into one matrix yields the final Jacobian,

$$\mathbf{DF}(\vec{X}) = \begin{bmatrix} \mathbf{DF}_1 & \mathbf{DF}_2 \end{bmatrix} \tag{2.74}$$

Since infinitely many solutions exist, i.e., there are more free variables than constraints, the minimum norm formulation from Equation (2.63) delivers a solution. The process converges when the norm of the constraint vector is below a specified tolerance, ϵ. Given a reasonable initial guess, the multiple shooting scheme provides a continuous trajectory from the initial discontinuous trajectory segments.

2.4.3 Continuation

The previous section included a summary of strategies to compute single periodic orbits, but it is typically more beneficial to analyze a family of solutions during any design process. A family of solutions supplies a broader understanding of the dynamical environment. There are many different approaches to enable a continuation process, but two common continuation methods are exploited frequently in this investigation to compute families of solutions: natural parameter continuation and pseudo-arclength continuation. A simple illustration comparing the basic concept in each of the two techniques appears in Figure 2.10. Both natural parameter and pseudo-arclength continuation methods supply initial guesses to the differential corrections procedure to converge each solution within the family. In natural parameter continuation, a physical parameter characterizes the family, p, and it is selected to "continue" the family from one member to the next. By stepping some distance δp along the parameter p direction, the initial guess for the next member of the family, represented as the black dot in Figure 2.10a, is input to the Newton algorithm that then proceeds in an attempt to converge to a new solution. Natural parameter continuation is simple to implement, however, difficulties arise when the slope of the p parameter curve, as represented in Figure 2.10, becomes steep or reaches a cusp. The Newton method requires a close initial guess to converge on a solution so, as the slope of the curve of p increases, smaller steps, i.e., δp, are required, increasing the computation time. Furthermore, natural parameter continuation requires some knowledge of the evolution of the elements in the free variable vector throughout the family. In contrast, a pseudo-arclength continuation scheme uses the nullspace of the Jacobian matrix from the previously converged orbit in the family to construct an initial guess in the direction tangent to the family. Figure 2.10b, adapted

from Bosanac [53], depicts the initial guess delivered by the pseudo-arclength scheme; observe that the initial guess is closer to the converged solution. The pseudo-arclength strategy

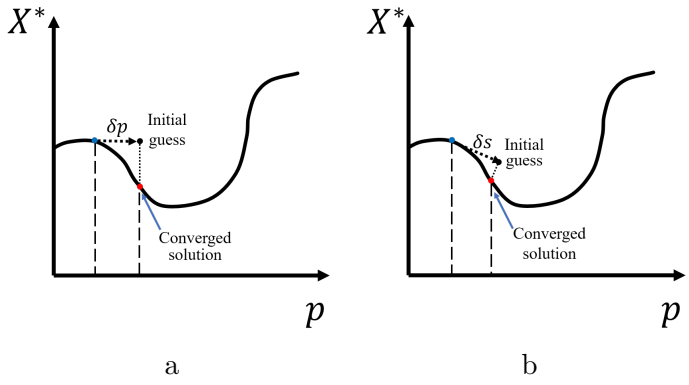

Figure 2.10. (a) Natural parameter continuation and (b) pseudo-arclength continuation schemes[53].

introduces an additional constraint on the step δs as the process moves along the family in a higher-dimensional space. The Jacobian matrix, **DF**, is constructed such that it is defined by a one-dimensional nullspace. Consider a free variable vector from a previously converged orbit in the family, defined as $\vec{X}^*_{\mathrm{i}-1}$. Additionally, consider the one-dimensional nullspace of the Jacobian matrix from the previous solution, defined as $\Delta\vec{X}^*_{\mathrm{i}-1}$. The new initial guess for the free variable vector representing the next member of the family is then defined

$$\vec{X}_{\mathrm{i}} = \vec{X}^*_{\mathrm{i}-1} + \delta s(\Delta\vec{X}^*_{\mathrm{i}-1}) \tag{2.75}$$

where $\vec{X}_{\mathrm{i}}$ is the initial guess for the i^{th} member of the family. The pseudo-arclength constraint is defined by the scalar expression,

$$(\vec{X}_{\mathrm{i}} - \vec{X}^*_{\mathrm{i}-1})^T \Delta\vec{X}^*_{\mathrm{i}-1} - \delta s = 0 \tag{2.76}$$

where $\vec{X}_{\mathrm{i}}$ is the free variable vector for the current iteration in the differential corrections process and δs is the non-physical step size. Appending the pseudo-arclength constraint to the end of the constraint vector yields an augmented constraint vector, $\vec{G}(\vec{X}_{\mathrm{i}})$,

$$\vec{G}(\vec{X}_{\mathrm{i}}) = \begin{bmatrix} \vec{F}(\vec{X}_{\mathrm{i}}) \\ (\vec{X}_{\mathrm{i}} - \vec{X}^*_{\mathrm{i}-1})^T \Delta \vec{X}^*_{\mathrm{i}-1} - \delta s \end{bmatrix} = \vec{0} \tag{2.77}$$

Subsequently, an augmented Jacobian is constructed using the partial derivatives from the pseudo-arclength constraint with respect to the free variables. The partial derivatives are equal to the nullspace of the previously converged solution. The nullspace vector is appended to the last row of the Jacobian matrix, producing the square Jacobian matrix,

$$\mathbf{DG} = \frac{\partial \vec{G}(\vec{X}_{\mathrm{i}})}{\partial \vec{X}_{\mathrm{i}}} = \begin{bmatrix} \mathbf{DF} \\ \Delta \vec{X}^*_{\mathrm{i}-1}{}^T \end{bmatrix} \tag{2.78}$$

The augmented Jacobian matrix is now full-rank, so a unique periodic solution exists if the constraints are satisfied. Pseudo-arclength continuation, while more complex, requires no a priori knowledge of the family evolution. The strategy ensures that the initial guess for each orbit in the family is in the direction tangent to the family and that a unique solution emerges when all the constraints are satisfied. However, when a priori knowledge of the solution space is known, natural parameter continuation is much simpler to implement and sometimes more intuitive. Both continuation strategies have strengths and drawbacks, and the application dictates the most effective method.

2.5 Computing Periodic Solutions in the CR3BP

As in the two-body model, an infinite number of periodic solutions also exists within the CR3BP. A simple single shooting differential corrections strategy is developed to demonstrate the computation of periodic solutions associated with the collinear libration points given a

reasonable initial guess. Consider a state vector that lies along the $\hat{x}$-axis, such that the only component of velocity is perpendicular to the $\hat{x}\hat{z}$-plane. Such a state vector is defined

$$\vec{x}_0 = \begin{bmatrix} x_0 & 0 & 0 & 0 & \dot{y}_0 & 0 \end{bmatrix}^T \tag{2.79}$$

Note that the initial state $\vec{x}_0$ includes a zero $\hat{z}$-component of position and velocity, resulting in purely planar motion when the state is propagated in the CR3BP. A differential corrections strategy is developed that ensures that the next crossing of the $\hat{x}\hat{z}$-plane is perpendicular. By constraining a second perpendicular crossing, symmetry is guaranteed across the $\hat{x}\hat{z}$-plane by the Mirror Theorem [54]. The trajectory thus returns to the appropriate initial condition and a periodic trajectory results. An initial guess to deliver as input to the corrections strategy is determined from the linear variations near one of the libration points, as summarized in Appendix A.0.1. Figure 2.11 depicts the initial guess (red) and the converged solution (blue) for a planar Lyapunov orbit near L_2 in the Earth-Moon system, using a differential corrections strategy based on perpendicular crossings. Only two elements in the state vector

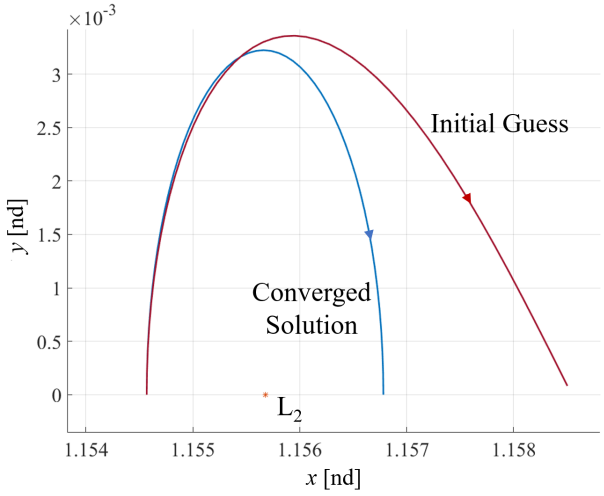

Figure 2.11. Initial guess (red) and converged solution (blue) in a perpendicular crossing differential corrections scheme for an Earth-Moon L_2 Lyapunov orbit

are varied to guarantee a perpendicular crossing. Consequently, the free variable vector is defined

$$\vec{X} = \begin{bmatrix} x_0 \\ \dot{y}_0 \\ T \end{bmatrix} \tag{2.80}$$

where T is the time of flight to the plane crossing (note that the period of the converged orbit is $2T$). The constraint vector is defined for a perpendicular crossing as follows

$$\vec{F}(\vec{X}) = \begin{bmatrix} y^t \\ \dot{x}^t \end{bmatrix} = \vec{0} \tag{2.81}$$

where y^t and $\dot{x}^t$ are the $\hat{y}$-component of position and $\hat{x}$-component of velocity at the $\hat{x}\hat{z}$-plane crossing at time $t_0 + T$, respectively. The Jacobian matrix for the corrections scheme is constructed from elements of the STM and the derivatives of the state vector

$$\mathbf{DF} = \begin{bmatrix} \Phi_{2,1} & \Phi_{2,5} & \dot{y}^t \\ \Phi_{4,1} & \Phi_{4,5} & \ddot{x}^t \end{bmatrix} \tag{2.82}$$

where $\Phi_{\mathrm{i,j}}$ is the (i, j) element of STM, propagated from the initial time, t_0, to the final time $t_0 + T$. The elements in the last column of the Jacobian are from the derivative of the state vector at time $t_0 + T$. A half period of the converged orbit is depicted in blue in Figure 2.11. A single shooting scheme is very effective when computing simple periodic orbits, however, a more robust strategy is typically required when it is not possible to leverage symmetries or when the path involves more dynamically sensitive regions.

Various types of periodic orbits exist in the CR3BP and some of these orbits possess long periods or close encounters with one or both primaries. By incorporating a multiple shooting strategy into the periodic orbit corrections scheme, a generally more robust algorithm is

available. By discretizing an initial guess for a periodic orbit into arcs bounded by patch points, or node points, the free variable vector is defined

$$\vec{X} = \begin{bmatrix} \vec{x}_1 \\ \vec{x}_2 \\ \vdots \\ \vec{x}_{N-1} \\ T \end{bmatrix} \tag{2.83}$$

where $\vec{x}_{\mathrm{i}}$ is the state vector at patch point i and T is the integration time along each trajectory arc. The constraint vector is defined

$$\vec{F}(\vec{X}) = \begin{bmatrix} \vec{x}_2^t - \vec{x}_2 \\ \vec{x}_3^t - \vec{x}_3 \\ \vdots \\ \vec{x}_{N-1}^t - \vec{x}_{N-1} \\ x_N^t - x_1 \\ y_N^t - y_1 \\ z_N^t - z_1 \\ \dot{x}_N^t - \dot{x}_1 \\ \dot{z}_N^t - \dot{z}_1 \\ y_1 \end{bmatrix} \tag{2.84}$$

The last continuity constraint is formulated differently since one of the dimensions of the six-dimensional state is implicitly defined by the Jacobi constant. In this formulation, the difference between the $\hat{y}$-component of velocity at the end of the last trajectory arc and the

first patch point is unconstrained and the $\hat{y}$-component of the first patch points is constrained to be zero. Using the constraint and free variable vectors, the Jacobian matrix is defined

$$\mathbf{DF} = \begin{bmatrix} \mathbf{\Phi}(t_1+T,t_1) & -\mathbf{I_{6\times 6}} & \mathbf{0_{6\times 6}} & \dots & \mathbf{0_{6\times 6}} & \dot{\vec{x}}_2^t \\ \mathbf{0_{6\times 6}} & \mathbf{\Phi}(t_2+T,t_2) & -\mathbf{I_{6\times 6}} & \dots & \mathbf{0_{6\times 6}} & \dot{\vec{x}}_3^t \\ \vdots & \vdots & \vdots & \ddots & & \\ \mathbf{J} & \mathbf{0_{6\times 6}} & \mathbf{0_{6\times 6}} & & \mathbf{R} & \vec{q} \end{bmatrix} \tag{2.85}$$

where the submatrices $\mathbf{J}$ and $\mathbf{R}$ are defined

$$\mathbf{J} = \begin{bmatrix} -1 & 0 & 0 & 0 & 0 & 0 \\ 0 & -1 & 0 & 0 & 0 & 0 \\ 0 & 0 & -1 & 0 & 0 & 0 \\ 0 & 0 & 0 & -1 & 0 & 0 \\ 0 & 0 & 0 & 0 & 0 & -1 \\ 0 & 1 & 0 & 0 & 0 & 0 \end{bmatrix} \tag{2.86}$$

$$\mathbf{R} = \begin{bmatrix} \Phi_{1,1} & \Phi_{1,2} & \Phi_{1,3} & \Phi_{1,4} & \Phi_{1,5} & \Phi_{1,6} \\ \Phi_{2,1} & \Phi_{2,2} & \Phi_{2,3} & \Phi_{2,4} & \Phi_{2,5} & \Phi_{2,6} \\ \Phi_{3,1} & \Phi_{3,2} & \Phi_{3,3} & \Phi_{3,4} & \Phi_{3,5} & \Phi_{3,6} \\ \Phi_{4,1} & \Phi_{4,2} & \Phi_{4,3} & \Phi_{4,4} & \Phi_{4,5} & \Phi_{4,6} \\ \Phi_{6,1} & \Phi_{6,2} & \Phi_{6,3} & \Phi_{6,4} & \Phi_{6,5} & \Phi_{6,6} \\ 0 & 0 & 0 & 0 & 0 & 0 \end{bmatrix} \tag{2.87}$$

and where $\Phi_{\mathrm{i,j}}$ is the (i,j) element of the STM at time $t_{N-1}+T$ from t_{N-1}. The vector $\vec{q}$ is a six-element vector, comprised of the derivatives of the last six elements of the constraint vector in Equation (2.84) with respect to time-of-flight

$$\vec{q} = \begin{bmatrix} \dot{x}(t_N+T) & \dot{y}(t_N+T) & \dot{z}(t_N+T) & \ddot{x}(t_N+T) & \ddot{z}(t_N+T) & 0 \end{bmatrix}^T \tag{2.88}$$

where $\dot{x}(t_N+T)$, $\dot{y}(t_N+T)$, and $\dot{z}(t_N+T)$ are the velocity components of the state at the end of the final patch point propagation, $\ddot{x}(t_N+T)$ and $\ddot{z}(t_N+T)$ are the $\hat{x}$- and $\hat{z}$-components

of acceleration at the end the final propagation arc. Representative orbits from three orbit families are plotted in Figure 2.12 including the L_2 Lyapunov, northern halo, and vertical orbit families in the Jupiter-Europa system, computed using a multiple shooting differential corrections strategy coupled with a pseudo-arclength continuation strategy. This differential corrections strategy is more complex than a single shooting algorithm, however, it is more robust for periodic solutions that exist in dynamically sensitive regions.

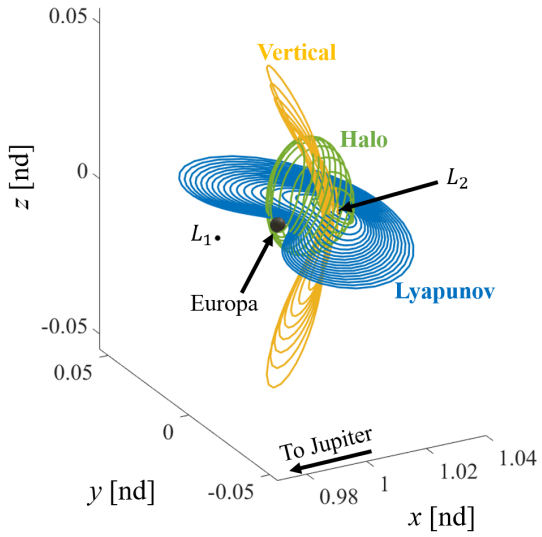

Figure 2.12. L_2 Lyapunov, halo and vertical orbits in the Jupiter-Europa system ($\mu = 2.528 \times 10^{-5}$), constructed using pseudo-arclength continuation

2.6 Computing Periodic Solutions in the BCR4BP

Periodic orbits are known to exist only as isolated solutions in the BCR4BP. Since the system itself is time-periodic, the orbital period of a periodic orbit in the BCR4BP must be commensurate with the synodic period, i.e., the period of the Earth-Moon-Sun system in the BCR4BP. A α:β synodic resonance is defined such that α periods of the spacecraft orbit are completed or every β revolutions of the Earth-Moon-Sun system, where the period of the system is approximately 29.5 days. The Sun returns to the original angle relative to the Earth-Moon line in the BCR4BP after this interval, as illustrated in Figure 2.6a in the

Earth-Moon rotating frame. In this investigation, four-body periodic orbits are examined within the BCR4BP model formulated as a periodically perturbed Earth-Moon CR3BP. Motion within the vicinity of the libration points is first examined by gradually introducing the perturbative effect of the Sun. Second, identification and computation of periodic orbits in the BCR4BP leveraging resonant periodic orbits from the Earth-Moon CR3BP is summarized. Transitioning these dynamical structures from the Earth-Moon CR3BP to the BCR4BP provides greater insight into how solar acceleration affects motion in the Earth-Moon neighborhood.

To gradually introduce the Sun's effect on a particular trajectory, the BCR4BP is formulated with an additional parameter to scale the solar acceleration. The equations of motion for the BCR4BP in the Earth-Moon rotating frame are formulated with the inclusion of the additional parameter, ε,

$$\ddot{x} = 2\dot{y} + x - \frac{(1-\mu)(x+\mu)}{r_{13}^3} - \frac{\mu(x-1+\mu)}{r_{23}^3} - \varepsilon m_4 \left(\frac{x - a_4\cos\theta_s}{r_{43}^3} + \frac{\cos\theta_s}{a_4^2} \right) \tag{2.89}$$

$$\ddot{y} = -2\dot{x} + y - \frac{(1-\mu)y}{r_{13}^3} - \frac{\mu y}{r_{23}^3} - \varepsilon m_4 \left(\frac{y - a_4\sin\theta_s}{r_{43}^3} + \frac{\sin\theta_s}{a_4^2} \right) \tag{2.90}$$

$$\ddot{z} = -\frac{(1-\mu)z^3}{r_{13}} - \frac{\mu z}{r_{23}^3} - \varepsilon m_4 \frac{z}{r_{43}^3} \tag{2.91}$$

where the ε term is a scaling parameter for the Sun mass; $\varepsilon = 0$ reflects an Earth-Moon CR3BP with no solar gravity and $\varepsilon = 1$ for the BCR4BP. The terms in blue in Equations (2.89)-(2.89) represent the contributions from the Sun and the terms in black reflect the acceleration as modeled in the CR3BP. Subsequently, this model represents the same dynamics as Equations (2.19)-(2.21) whenever $\varepsilon = 1$. Formulating the BCR4BP with the parameter ε provides a means to gradually scale the impact of the Sun and evolve the dynamical structures from the CR3BP to the BCR4BP.

Sun-perturbed periodic motion is first examined in the vicinity of the Earth-Moon libration points. These periodic structures differ from the instantaneous equilibrium solutions computed in Section 2.2.2; in contrast to the instantaneous equilibrium solutions, a spacecraft initialized on the Sun-perturbed periodic orbit remains on this path for all time. Using a differential corrections process and a pseudo-arclength continuation scheme, the libration

points in the Earth-Moon CR3BP are transitioned to a periodic orbit in the BCR4BP. To complete this transition, a multiple shooting differential corrections procedure is formulated using the free variable vector defined as follows,

$$\vec{X} = \begin{bmatrix} x_1 & y_1 & z_1 & \dots & \dot{x}_m & \dot{y}_m & \dot{z}_m & \varepsilon \end{bmatrix}^T \tag{2.92}$$

where m is the number of arcs in the multiple shooting scheme and ε is the parameter that scales the equations of motion from the CR3BP to the BCR4BP. The constraint vector is defined,

$$\vec{F} = \begin{bmatrix} x_1^t - x_2 & y_1^t - y_2 & \dots & \dot{y}_m^t - \dot{y}_1 & \dot{z}_m^t - \dot{z}_1 \end{bmatrix}^T \tag{2.93}$$

such that the position and velocity continuity is constrained between each of the trajectory arcs, where x_{i}^t, y_{i}^t, z_{i}^t, $\dot{x}_{\mathrm{i}}^t$, $\dot{y}_{\mathrm{i}}^t$, and $\dot{z}_{\mathrm{i}}^t$ are the position and velocity components of segment i after propagating for the segment time, T. For targeting periodic orbits in the BCR4BP, there is no integral of the motion; thus, full state continuity between the initial and final state on the orbit is required for periodicity. Additionally, time is not included as a free variable, since the period of the orbit must be equal to the synodic period of the system. Lastly, the gradient of the constraints is constructed using the elements of first-order state variations and ε. The gradient matrix thus appears as,

$$\mathbf{DF} = \begin{bmatrix} \mathbf{\Phi}(t_1 + T, t_1) & -\mathbf{I_{6\times 6}} & \mathbf{0_{6\times 6}} & \dots & \mathbf{0_{6\times 6}} & \frac{\partial \vec{x}_1^t}{\partial \varepsilon} \\ \mathbf{0_{6\times 6}} & \mathbf{\Phi}(t_2 + T, t_2) & -\mathbf{I_{6\times 6}} & \dots & \mathbf{0_{6\times 6}} & \frac{\partial \vec{x}_2^t}{\partial \varepsilon} \\ \vdots & \vdots & \vdots & \ddots & & \\ -\mathbf{I_{6\times 6}} & \mathbf{0_{6\times 6}} & \mathbf{0_{6\times 6}} & & \mathbf{\Phi}(t_m + T, t_m) & \frac{\partial \vec{x}_m^t}{\partial \varepsilon} \end{bmatrix} \tag{2.94}$$

where T is a fraction of the synodic period, T_{syn}/m and $\frac{\partial \vec{x}_1^t}{\partial \varepsilon}$ reflects the variations of the state with respect the Sun mass scaling parameter. Numerical experience has demonstrated that finite-differencing is particularly sensitive to the size of a perturbation for the derivatives with respect to ε. Consequently, the computation of the partial derivatives leveraging finite-differencing is not sufficiently accurate to exploit pseudo-arclength continuation, as the nullspace of the Jacobian matrix is required. To avoid introducing such errors into the

nullspace calculation, the non-linear variational equations of motion are numerically integrated. The differential equations associated with the variations of the states with respect to ε are defined by augmenting the BCR4BP state variational equations,

$$\mathbf{A} = \begin{bmatrix} 0 & 0 & 0 & 1 & 0 & 0 & 0 \\ 0 & 0 & 0 & 0 & 1 & 0 & 0 \\ 0 & 0 & 0 & 0 & 0 & 1 & 0 \\ \Upsilon^*_{xx} & \Upsilon^*_{xy} & \Upsilon^*_{xz} & 0 & 2 & 0 & \Upsilon^*_{x\varepsilon} \\ \Upsilon^*_{yx} & \Upsilon^*_{yy} & \Upsilon^*_{yz} & -2 & 0 & 0 & \Upsilon^*_{y\varepsilon} \\ \Upsilon^*_{zx} & \Upsilon^*_{zy} & \Upsilon^*_{zz} & 0 & 0 & 0 & \Upsilon^*_{z\varepsilon} \\ 0 & 0 & 0 & 0 & 0 & 0 & 0 \end{bmatrix} \tag{2.95}$$

where Υ^* is the augmented pseudo-potential function for the BCR4BP that includes ε,

$$\Upsilon^* = \frac{1-\mu}{r_{13}} + \frac{\mu}{r_{23}} + \frac{x^2+y^2}{2} + \varepsilon\left(\frac{m_4}{r_{43}} - \frac{m_4(x\cos\theta_s + y\sin\theta_s)}{a_4^2}\right) \tag{2.96}$$

and $\Upsilon^*_{x\varepsilon}$, $\Upsilon^*_{y\varepsilon}$, and $\Upsilon^*_{z\varepsilon}$ are the second partial derivatives of the augmented pseudo-potential function defined, that is,

$$\Upsilon^*_{x\varepsilon} = -m_4\left(\frac{x - a_4\cos\theta_s}{r_{43}^3} + \frac{\cos\theta_s}{a_4^2}\right) \tag{2.97}$$

$$\Upsilon^*_{y\varepsilon} = -m_4\left(\frac{y - a_4\sin\theta_s}{r_{43}^3} + \frac{\sin\theta_s}{a_4^2}\right) \tag{2.98}$$

$$\Upsilon^*_{z\varepsilon} = \frac{-m_4 z}{r_{43}^3} \tag{2.99}$$

The remaining second partial derivatives in the $\mathbf{A}$ matrix are defined with the Sun mass terms scaled by ε in Equations (2.28)-(2.33). Using a pseudo-arclength continuation strategy aids in evolving from the CR3BP ($\varepsilon = 0$) to the BCR4BP ($\varepsilon = 1$); notably, the orbit in the BCR4BP may not retain the same stability characteristics as the solution in the CR3BP. To add insight into the possible stability changes, a hodograph that includes two parameters associated with the transition of the L_1 and L_2 libration points in the CR3BP to the BCR4BP are plotted in Figure 2.13. The colored segments in the hodograph indicate the stability properties across

the continuation process. The horizontal axis is the pseudo-arclength step size, δs. The pseudo-arclength step size is selected as the parameter for the horizontal axis because it is monotonically increasing throughout the continuation process. Blue indicates that there is a single saddle mode and two center modes, and the red line implies two saddle nodes and a single center mode. The L_1 continuation procedure produces consistent stability properties throughout the entire transition and reaches a unique solution in the BCR4BP ($\varepsilon = 1$). However, the L_2 continuation process in step size initially transitions to $\varepsilon < 0$, then crosses back over $\varepsilon = 0$. The solution at this second location where $\varepsilon = 0$ corresponds to the L_2 2:1 synodic resonant Lyapunov orbit in the CR3BP; the resonance corresponds to an orbit with 2 orbital periods for a single revolution of the Sun in the Earth-Moon rotating frame. Therefore, the orbits in the vicinity of the L_2 libration point do not necessarily transition to yield a unique structure in the BCR4BP, rather the process resets to produce the equivalent to the 2:1 synodic resonant Lyapunov orbit. Additionally, there are stability changes along the transition from the CR3BP 2:1 Lyapunov orbit to the BCR4BP 2:1 Lyapunov orbit. The stability change at $\varepsilon \approx 0.287$ introduces a bifurcation in the L_2 halo orbit family in the CR3BP and, ultimately, a 2:1 halo orbit in the BCR4BP emerges. This investigation focuses on the behaviors in the vicinity of the Earth-Moon L_1 and L_2 points in the BCR4BP that result from these transitions.

Periodic orbits are also potentially computed directly from periodic orbits in the CR3BP that possess a commensurate period with the synodic period in the BCR4BP. To determine the locations at which periodic orbits exist in the BCR4BP, the orbital period of any CR3BP periodic orbits in the Earth-Moon system is examined. For a representative example, the ratio of the synodic period to the orbital period, $P_{\text{syn}}/P_{\text{orbital}}$ for a subset of the L_1 and L_2 halo families in the Earth-Moon CR3BP is plotted in Figure 2.14a and 2.14b, respectively. This representation of the resonances is also used by Boudad et al. [55]. Four resonant L_1 halo orbits are transitioned to the BCR4BP and then plotted in Figure 2.15. Transitioning orbits into the BCR4BP using this method adds insight into any shifts in the geometry when solar perturbations are introduced in cislunar space.

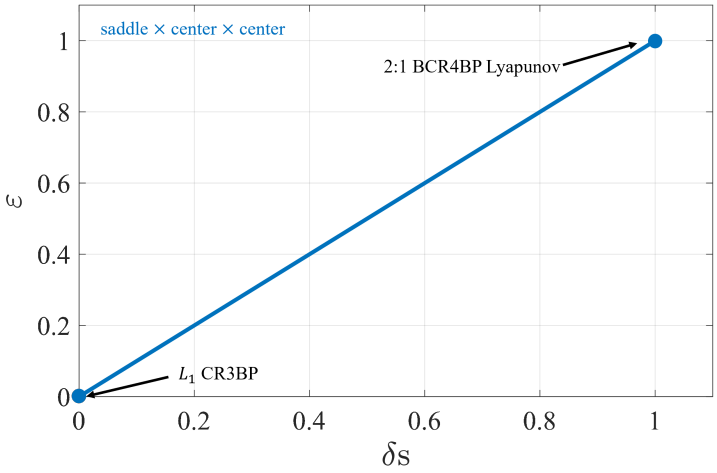

a

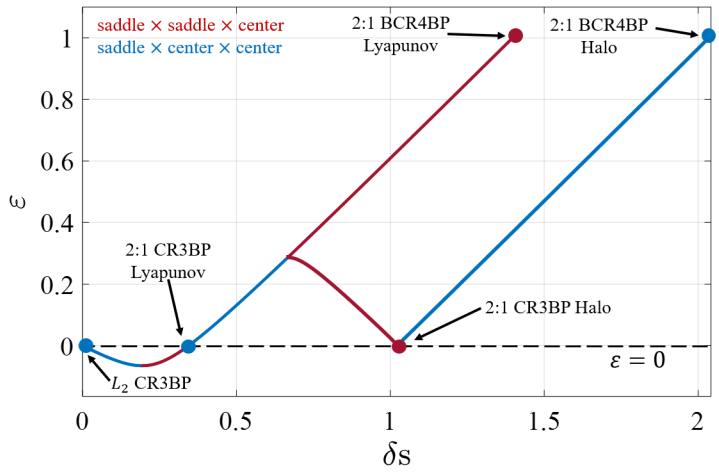

b

Figure 2.13. Sun mass scaling parameter as a function of the pseudo-arclength step, δs, from the initial libration point at $\varepsilon = 0$ for (a) L_1 and (b) L_2. Note that the stability properties of the L_2 point change during the continuation process.

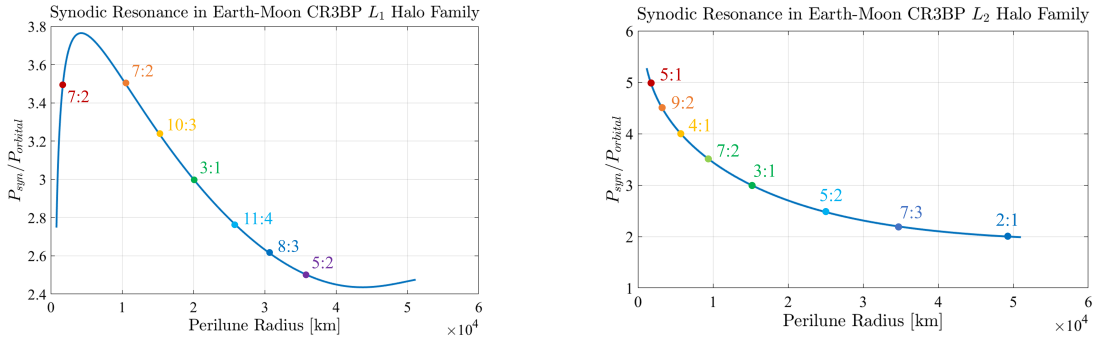

a b

Figure 2.14. (a) Resonances in L_1 halo family in the Earth-Moon CR3BP. (b) Resonances in L_2 halo family in the Earth-Moon CR3BP.

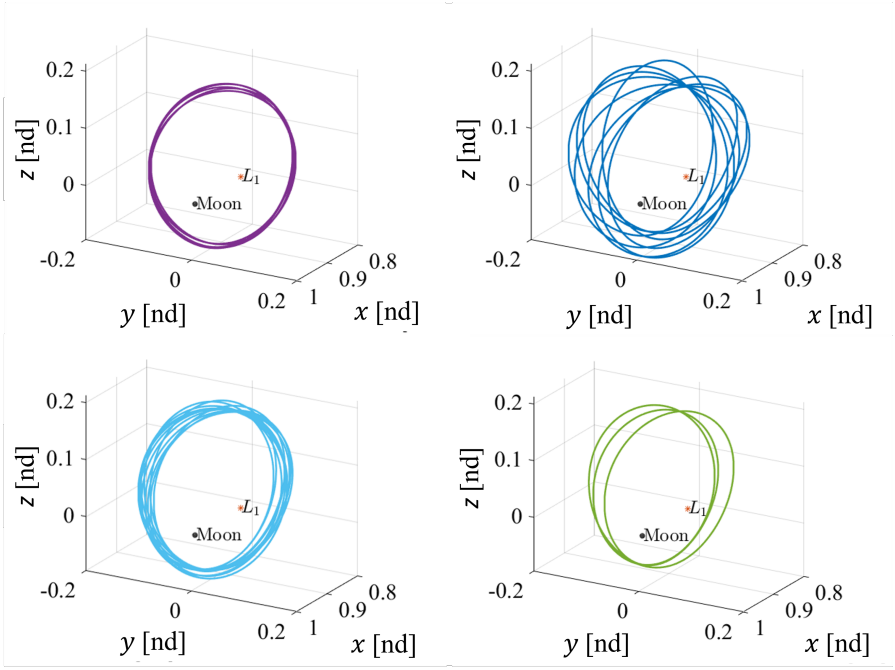

Figure 2.15. Periodic Earth-Moon L_1 halo orbits in the BCR4BP: 5:2 resonance (purple), 8:3 resonance (blue), 11:4 resonance (light blue), 3:1 resonance (green).

2.7 Stability and Invariant Manifolds

Just as the stability evaluation of an equilibrium point is examined using linear variations, the stability of a periodic orbit is also quantified through linearization. The stability of a periodic orbit is determined by reducing the periodic orbit to a fixed point on a stroboscopic map. Reducing the periodic orbit to a fixed point allows the characteristics of the orbit to be analyzed as a discrete time system. If a fixed point is defined at any location along the path of a periodic orbit as $\vec{x}(t)$, the path returns to the same location after one revolution of the orbit

$$\vec{x}(t+T) = \vec{x}(t) \tag{2.100}$$

where T is the time to complete one period of the orbit. Expanding this concept to n revolutions, the periodic orbit is represented in terms of the state vector as

$$\vec{x}(nT) = \vec{x}((n+1)T) = \vec{x}^* \tag{2.101}$$

where $\vec{x}^*$ is the fixed point. The differential of the variations on the stroboscopic map relative to the fixed point are defined for each iteration of the map using the STM

$$\delta\vec{x}(nT) = \mathbf{\Phi}(nT, 0)\delta\vec{x}(0) \tag{2.102}$$

where n represents the number of revolutions around the orbit, $\mathbf{\Phi}(nT, 0)$ is the STM propagated from time $t = 0$ to time $t = nT$. Using the property of the STM in Equation (C.7) found in Appendix C, Equation (2.102) is rewritten using the STM over one revolution, also denoted the monodromy matrix, $\mathbf{M}$, to the appropriate power, i.e.,

$$\delta\vec{x}(nT) = \mathbf{M}^n\delta\vec{x}(0) \tag{2.103}$$

The system in Equation (2.103) is transformed into a discrete time system by defining k as an integer iterate of the stroboscopic map. The continuous time system in Equation (2.103) is rewritten as the discrete time system,

$$\delta\vec{x}(k+1) = \mathbf{M}\delta\vec{x}(k) \tag{2.104}$$

where k an integer iterate of the map. The general solution of the discrete time system in Equation (2.104) is defined with the eigenvalues and eigenvectors of $\mathbf{M}$

$$\delta\vec{x}(k) = A_1\lambda_1^k\vec{v}_1 + A_2\lambda_2^k\vec{v}_2 + A_3\lambda_3^k\vec{v}_3 + A_4\lambda_4^k\vec{v}_4 + A_5\lambda_5^k\vec{v}_5 + A_6\lambda_6^k\vec{v}_6 \tag{2.105}$$

where λ_i is the ith eigenvalue of $\mathbf{M}$, $\vec{v}_\mathrm{i}$ is the corresponding eigenvector, and A_i is a coefficient of the general solution. It is apparent that variations from the fixed point are governed by the magnitude of the λ_i relative to one. However, information about the eigenstructure of the monodromy matrix is gathered by exploiting some properties of the monodromy matrix in the CR3BP and the BCR4BP. Since the CR3BP and BCR4BP are both Hamiltonian systems, the eigenvalues of the STM exist in reciprocal pairs. Furthermore, the monodromy matrix for a periodic orbit in a Hamiltonian system requires that two unity eigenvalues exist when a single integral of motion exists for that problem [56]. Thus, there is always a unity pair of eigenvalues for periodic orbits in the CR3BP. Stability information is available from the remaining reciprocal pairs of eigenvalues.

For periodic orbits that possess stable and unstable subspaces, invariant manifolds exist that define asymptotically approaching and departing motion to the periodic orbit. If the monodromy matrix has an eigenvalue associated with the unstable subspace, i.e., $Re(\lambda_U) > 1$, then there exists a reciprocal eigenvalue associated with the stable subspace, $\lambda_S = \frac{1}{\lambda_U}$. The eigenvectors associated with the stable ($\vec{v}_S$) subspace and the unstable subspace ($\vec{v}_S$) represent the local hyperbolic manifolds that asymptotically approach and depart the periodic orbit, respectively. The global invariant hyperbolic manifolds are computed by perturbing

states along the periodic orbit by some small value ϵ in the stable/unstable direction and integrating backwards/forwards,

$$\vec{x}_U^* = \vec{x}^* \pm \epsilon \frac{\vec{v}_U}{|\vec{v}_U|} \tag{2.106}$$

$$\vec{x}_S^* = \vec{x}^* \pm \epsilon \frac{\vec{v}_S}{|\vec{v}_S|} \tag{2.107}$$

where $\vec{x}^*$ is the location on the periodic orbit, and $\vec{x}_U^*$ and $\vec{x}_S^*$ are the perturbed state in the unstable and stable directions, respectively. Eigenvectors do not have a unique direction, thus, to generate the full global manifold trajectory for a particular location, the trajectory is perturbed in both positive and negative directions. Recall, a fixed point along a periodic orbit is independent of the location along the orbit. To produce the stable and unstable directions at different locations around the periodic orbit, the STM, $\mathbf{\Phi}(t, 0)$, transforms the eigenvectors calculated from the monodromy matrix, where t is the time relative to the location of the fixed point on the periodic orbit. A set of trajectories that represent the stable (blue) and the unstable (red) manifolds for an Earth-Moon L_1 Lyapunov orbit is plotted in Figure 2.16. The stable and unstable hyperbolic manifolds provide transfer trajectories into and out of unstable periodic orbits without deterministic maneuvers. A periodic orbit possesses a center subspace when reciprocal pairs of complex eigenvalues of the monodromy matrix exist on the unit circle. The center manifold indicates bounded, quasi-periodic motion in the vicinity of the periodic orbit. An infinite number of quasi-periodic orbits exist for periodic orbits that have center modes. The center modes and their relationship to existence of quasi-periodic motion on higher-dimensional invariant tori are discussed further in later chapters.

2.7.1 Stability Index

The stability of a periodic orbit is determined from the eigenvalues of the monodromy matrix. However, a single value to quantify the stability is conveniently defined. If a pair of eigenvalues exist that include real parts, $(\lambda_\mathrm{i}, \frac{1}{\lambda_\mathrm{i}})$, then the orbit is unstable if the real part of

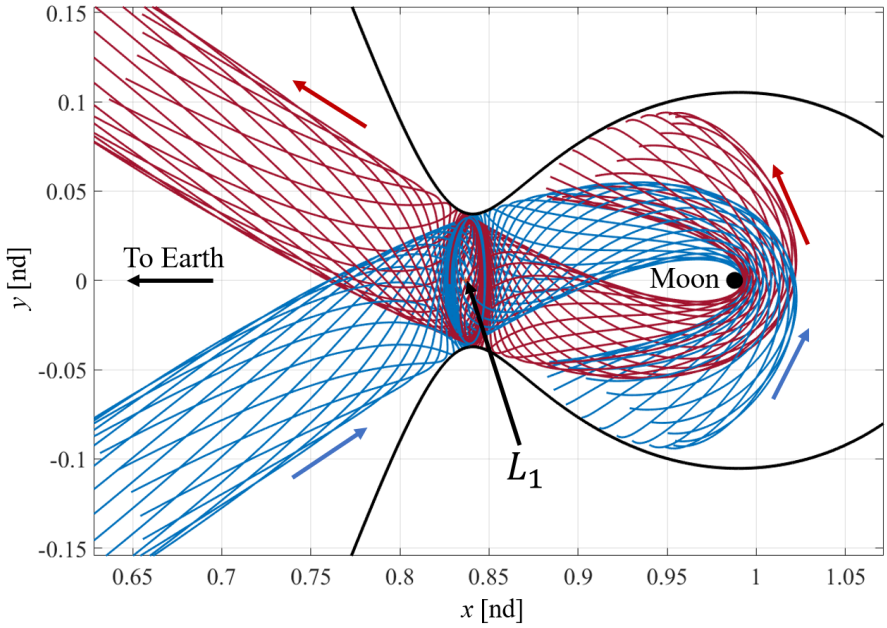

Figure 2.16. Stable (blue) and unstable (red) manifold trajectories from an L_1 Lyapunov orbit. The ZVCs for the Jacobi Constant ($JC = 3.1827$) of this orbit are defined by the black curve.

one of the eigenvalues is greater than one. The orbit is considered stable if the real part of both eigenvalues are equal to one. Subsequently, a stability index is defined

$$\nu = \frac{1}{2}(|\lambda_{max}| + \frac{1}{|\lambda_{max}|}) \tag{2.108}$$

where λ_{max} corresponds to the eigenvalue with the maximum real part. Linearly stable orbits are identified by stability indices $\nu = 1$, while linearly unstable orbits yield stability indices $\nu > 1$. The stability index for the Earth-Moon L_2 halo family is plotted in Figure 2.17 as it evolves along the family. A stability index provides a single, convenient parameter to characterize stability of orbits along a family.

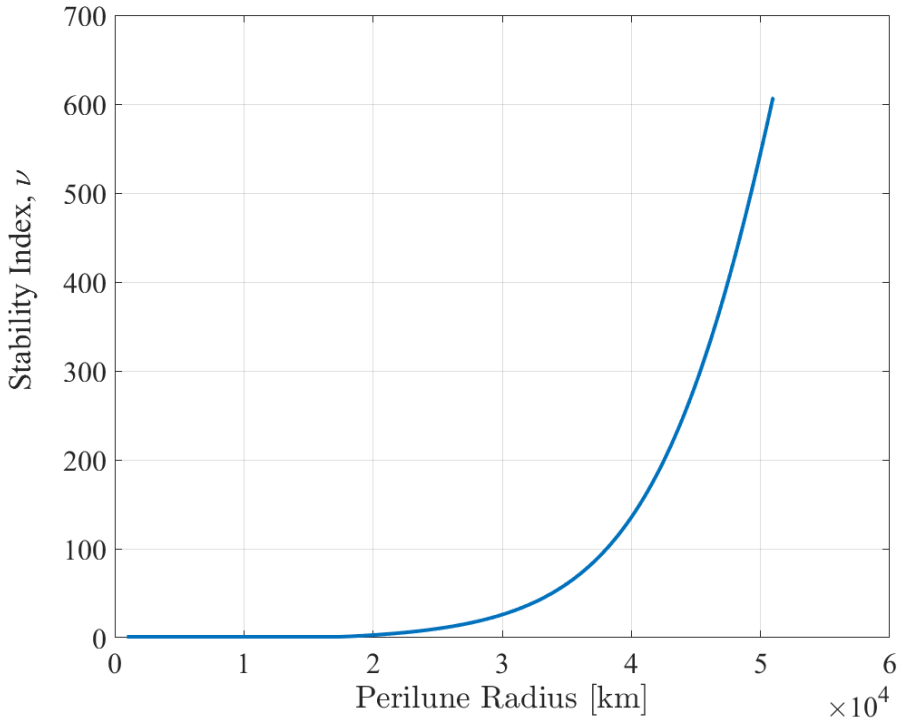

Figure 2.17. Stability index for a subset of the Earth-Moon L_2 halo family

3. MULTI-BODY QUASI-PERIODIC ORBITS

In the CR3BP and BCR4BP, an infinite number of quasi-periodic orbits exist. To assess the behavior in the vicinity of these periodic orbits, a periodic orbit is reduced to a fixed point on a stroboscopic map. The eigenvalues from the STM over a single period of the orbit (i.e., the monodromy matrix) provide information concerning the linear stability properties as well. Because the CR3BP and the BCR4BP are Hamiltonian systems, the eigenstructure is symmetric across the real and imaginary axes in the complex plane. A periodic orbit with a complex value of unit magnitude indicates the existence of a center subspace and quasi-periodic motion in the vicinity of the orbit. In fact, an infinite number of quasi-periodic solutions exist as families of invariant tori in the vicinity of the periodic orbit.

Invariant tori are defined by their dimensionality, where an n-dimensional torus possesses n fundamental frequencies that characterize the motion or flow. Equilibrium solutions in the CR3BP and periodic orbits in the CR3BP and BCR4BP are examples of 0- and 1-dimensional (1D) tori, since the equilibrium solutions remain fixed (i.e., no fundamental frequency exists, and the periodic orbits possess a single fundamental frequency associated with the period of the orbit). Quasi-periodic orbits exist on tori in which two or more frequencies define the motion, that is, $n > 1$. This investigation explores computation of both 2-dimensional (2D) and 3-dimensional (3D) quasi-periodic tori based on the strategy described by Gómez and Mondelo and by Olikara and Scheeres [25], [26].

3.1 Computation of 2-D Quasi-Periodic Tori

Quasi-periodic orbits that exist as 2D tori possess one more frequency compared to a periodic orbit. By increasing the dimension to two for a torus, the motion is bounded on a surface defined by two fundamental frequencies, as opposed to a curve for a 1D torus. These two frequencies are denoted longitudinal and latitudinal frequencies and define the motion on the torus. Consider the 2D torus rendered in configuration space as shown in Figure 3.1a. The longitudinal and latitudinal frequencies are represented by the blue and red circles, respectively. Then, any location on the 2D torus is defined by two angles, θ_0 and θ_1. The rate of change of each of these angles $\dot{\theta}_0$ and $\dot{\theta}_1$ are the longitudinal and latitudinal frequen-

cies, respectively. Given that the motion is bounded to a surface, quasi-periodic trajectories associated with 2D tori offer a wide variety of alternatives in the trajectory design process while avoiding the requirement for extensive computational resources. In addition, 2D tori are straightforward to visualize in configuration space for a more visual design approach. The algorithm to compute 2D tori as described by Gómez and Mondelo and by Olikara and Scheeres is first summarized. However, the approach in this investigation formulates the construction of the discrete Fourier transform and rotation operator as matrix operations instead of summation notation representation. Using a matrix approach simplifies the implementation of the computation algorithm and facilitates extensions to higher-dimensional tori.

3.1.1 Correction Algorithm

To compute 2D tori, a stroboscopic mapping technique is employed, where a discretized invariant circle or invariant curve is produced for use in a differential corrections scheme. The time associated with the stroboscopic map, T_0, is defined by the period of the longitudinal frequency associated with a particular quasi-periodic orbit (i.e., the blue circle in Figure 3.1a). The invariant curve is a representation of the flow on a 2D torus. However, given the difficulty of propagating the full representation of the flow, individual trajectories are numerically integrated as a discretization of the flow. A simple representation of the flow through a single latitudinal cycle and an invariant curve (blue) is plotted in Figure 3.1b. A single trajectory segment (gold) with an initial state located on the invariant curve is integrated for time T_0, where the trajectory path first returns to the stroboscopic map, as reflected in Figure 3.1b by the blue circle. The integration time is the period associated with the longitudinal frequency $\dot{\theta}_0$ such that

$$T_0 = \frac{2\pi}{\dot{\theta}_0} \tag{3.1}$$

The state at the first return to the invariant curve on the stroboscopic map rotates by a unique angle (defined as ρ in Figure 3.1b) relative to the initial state along the invariant curve. The rotation angle is defined by

$$\rho = \frac{2\pi\dot{\theta}_1}{\dot{\theta}_0} = T_0\dot{\theta}_1 \tag{3.2}$$

where $\dot{\theta}_1$ is the latitudinal frequency. This rotation angle is a property of the torus; for each return through the stroboscopic map, the state at each return rotates by ρ. Then, at the m^{th} return through the stroboscopic map, the initial state rotates by $m\rho$. In addition, if a single quasi-periodic trajectory arc is propagated for $t \to \infty$, then the full invariant curve is represented on the stroboscopic map when the frequencies are not commensurate. However, for computation, the invariant curve is discretized into N states, $\vec{u}_{\text{i}}(\theta_0, \theta_{1\text{i}})$, where $\text{i} = 1, 2, ..., N$, as illustrated in Figure 3.2 in which θ_0 and $\theta_{1\text{i}}$ are the longitudinal and latitudinal angles, respectively, for the i^{th} discretized state. When the location of the stroboscopic map at θ_0 is defined, the locations of the states around the invariant curve are associated with the latitudinal angle $\theta_{1\text{i}}$. When the discretized states are propagated for the time associated with the longitudinal frequency, T_0, all the states rotate by ρ such that

$$\vec{u}_{\text{i}}(\theta_0, \theta_{1\text{i}}) = \vec{u}_{\text{i}}(\theta_0 + 2\pi, \theta_{1\text{i}} - \rho) \tag{3.3}$$

where the longitudinal angle θ_0 also represents time along a trajectory arc. Equation (3.3) is then rewritten as a function of time,

$$\vec{u}_{\text{i}}(0, \theta_{1\text{i}}) = \vec{u}_{\text{i}}(T_0, \theta_{1\text{i}} - \rho) \tag{3.4}$$

where T_0 is the stroboscopic mapping time. Given this property, an invariance constraint is developed for a 2D torus, that is,

$$\boldsymbol{R}_{-\rho}\vec{u}_{\text{i}}(T_0, \theta_{1\text{i}}) - \vec{u}_{\text{i}}(0, \theta_{1\text{i}}) = \mathbf{0} \tag{3.5}$$

where $\boldsymbol{R}_{-\rho}$ is the rotation operator that removes the rotation around the invariant curve by ρ at the first return to the stroboscopic map. When the invariance constraint is enforced, 2D toroidal motion is ensured.

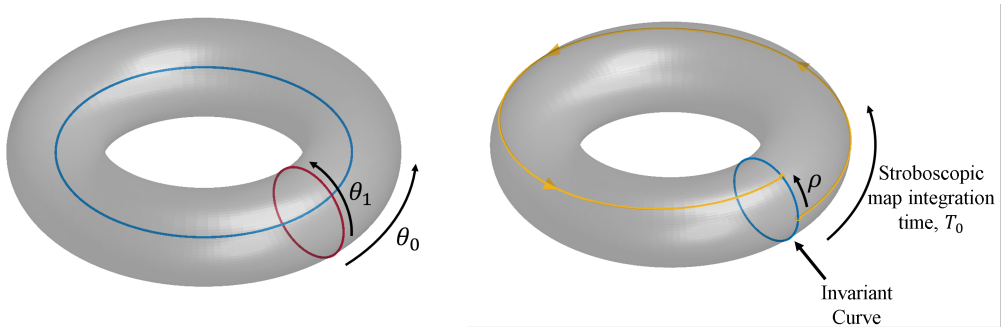

a b

Figure 3.1. (a) Longitudinal and latitudinal frequency representations on a 2D torus in configuration space. (b) A 2D torus with the invariant curve (blue), the rotation angle ρ, and a single trajectory (gold) propagated to the first return to the invariant curve.

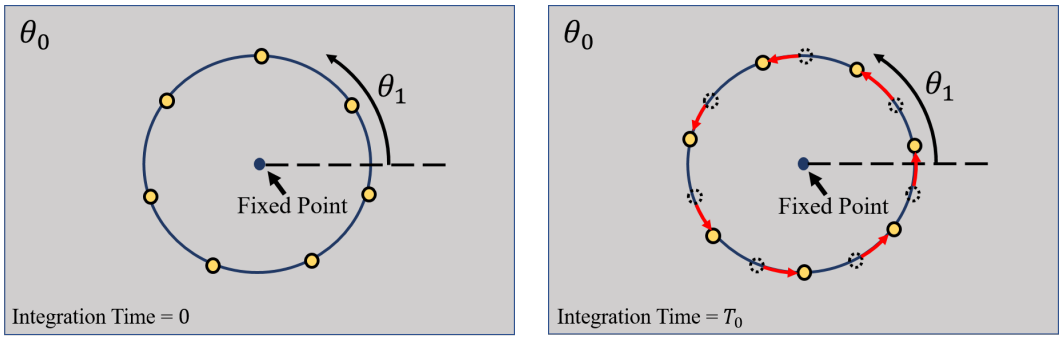

a b

Figure 3.2. Periodic orbit is represented by the fixed point (blue dot) on the map. A set of seven discretized states (yellow) on the invariant curve are represented along the blue circle. The invariant curve is associated with the stroboscopic map defined at θ_0. The initial location of the states is represented in (a). The first return to the map (i.e., at time T_0) is represented in (b), where the states have all rotated by ρ.

The invariance constraint is the basis from which a corrections algorithm is constructed to compute families of quasi-periodic orbits. However, a reasonably accurate initial guess is required to seed a free-variable and constraint differential corrections scheme [57]. Quasi-

periodic motion exists in the vicinity of a periodic orbit whose monodromy matrix possesses complex eigenvalues on the unit circle. To construct an initial guess for the states around the invariant curve, the eigenvector associated with the center mode for the periodic orbit, $\vec{v}_C$, is exploited. Perturbing in the direction of the center subspace yields states with nearly quasi-periodic motion:

$$\vec{x}_{\mathrm{i}}^{0} = \vec{x}^{*} + \epsilon(\mathrm{Re}[\vec{v}_C]\cos(\theta_{1\mathrm{i}}) - \mathrm{Im}[\vec{v}_C]\sin\theta_{1\mathrm{i}}) \tag{3.6}$$

where $\vec{x}^{*}$ represents the 6-element fixed point on the stroboscopic map associated with the periodic orbit, $\mathrm{Re}[\vec{v}_C]$ and $\mathrm{Im}[\vec{v}_C]$ are the real and imaginary parts of the center manifold eigenvector, respectively, and ϵ is a small quantity. The position and velocity states are transformed from a basepoint at the barycenter to a basepoint relative to the nearby periodic orbit, defined,

$$\vec{u}_{\mathrm{i}}^{0} = \vec{x}_{\mathrm{i}}^{0} - \vec{x}^{*} \tag{3.7}$$

The initial guess for the i^{th} discretized position and velocity state, $\vec{u}_{\mathrm{i}}^{0}$, is located near the invariant curve and is parameterized by the latitudinal location $\theta_{1\mathrm{i}} = \frac{2\pi(\mathrm{i}-1)}{N}$. When each of these angles is arranged into a matrix of size $1 \times N$, the set of parameterizing latitudinal angles yields a row vector of the form

$$\vec{\theta}_1 = \begin{bmatrix} 0 & \frac{2\pi}{N} & \frac{4\pi}{N} & \cdots & \frac{2\pi(N-2)}{N} & \frac{2\pi(N-1)}{N} \end{bmatrix} \tag{3.8}$$

such that latitudinal angles are evenly spaced between zero and 2π. The period of the fundamental orbit is employed as the initial guess for the integration time T_0^0 or the longitudinal period. An initial guess for the rotation angle is generated using the angular location of the center subspace eigenvalue on the unit circle in the complex plane, that is,

$$\rho^0 = \tan^{-1}\left(\frac{\mathrm{Im}[\lambda_C]}{\mathrm{Re}[\lambda_C]}\right) \tag{3.9}$$

where $\mathrm{Re}[\lambda_C]$ and $\mathrm{Im}[\lambda_C]$ are the real and imaginary parts, respectively, of the eigenvalue associated with the center subspace. For small values of ϵ, the approximations ρ^0, T_0^0 ,

and the states $\vec{u}_{\mathrm{i}}^{0}$ supply an initial guess for the elements of the free-variable vector that successfully converges in the differential corrections scheme.

A single-shooting differential corrections scheme is formulated using an invariance constraint based on Equation (3.5). The shooting scheme relies on a free-variable vector, a constraint vector, and a Jacobian matrix (i.e., the partial derivatives of the constraints with respect to the free variables). Given the approximations in Equations (3.7) and (3.9) as well as T_0^0, the free-variable vector for the differential corrections method is then defined as

$$\boldsymbol{X} = \begin{bmatrix} \vec{u}_1 \\ \vec{u}_2 \\ \vdots \\ \vec{u}_{N-1} \\ \vec{u}_N \\ T_0 \\ \rho \end{bmatrix} \tag{3.10}$$

where $\vec{u}_{\mathrm{i}} = \begin{bmatrix} u_{x,\mathrm{i}} & u_{y,\mathrm{i}} & u_{z,\mathrm{i}} & u_{\dot{x},\mathrm{i}} & u_{\dot{y},\mathrm{i}} & u_{\dot{z},\mathrm{i}} \end{bmatrix}^T$ is the i^{th} discretized 6-element state vector around the invariant curve. The free-variable vector is sized $6N + 2 \times 1$. The constraint vector is constructed such that the initial states discretized on the invariant curve match the final states after the longitudinal period, with the rotation around the invariant curve removed:

$$\boldsymbol{F} = \begin{bmatrix} \vec{u}_1^{t,R} - \vec{u}_1 \\ \vec{u}_2^{t,R} - \vec{u}_2 \\ \vdots \\ \vec{u}_{N-1}^{t,R} - \vec{u}_{N-1} \\ \vec{u}_N^{t,R} - \vec{u}_N \\ JC_{\mathrm{avg}} - JC_d \end{bmatrix} \tag{3.11}$$

where $\vec{u}_{\mathrm{i}}^{t,R}$ represents the i^{th} discretized state around the invariant curve after the first return on the stroboscopic map is propagated and the rotation angle ρ is removed. The last constraint in the $\boldsymbol{F}$ vector is a constraint on Jacobi Constant for quasi-periodic orbits in

the CR3BP. The term JC_{avg} is the average of the Jacobi constant values over each of the discretized states on the invariant curve:

$$JC_{\text{avg}} = \frac{1}{N}\sum_{\text{i}=1}^{N} JC_{\text{i}} \tag{3.12}$$

where JC_{i} is the Jacobi Constant associated with the i^{th} state on the invariant curve. The value JC_d is the desired Jacobi constant value for the torus. When the Jacobi Constant is included as a constraint, a family of quasi-periodic orbits is generated whose members possess the same Jacobi Constant. In the BCR4BP, the Jacobi Constant constraint is removed, since the BCR4BP model does not possess an integral of the motion.

The invariance constraint given in Equation (3.5) is formulated using a rotation operator $\boldsymbol{R}_{-\rho}$. The rotation operator removes the rotation about the invariant curve after the first return to the stroboscopic map and is constructed using a discrete Fourier transform. First, a single state located at some latitudinal angle θ_1 along the invariant curve is defined using a truncated 1D Fourier series:

$$\boldsymbol{u}(\theta_1) = \text{e}^{\text{i}\theta_1\vec{k}}\boldsymbol{C}_0 \tag{3.13}$$

where $\text{i} = \sqrt{-1}$ and $\vec{k}$ is defined as

$$\vec{k} = \begin{bmatrix} -\frac{N-1}{2} & \dots & -1 & 0 & 1 & \dots & \frac{N-1}{2} \end{bmatrix} \tag{3.14}$$

for odd valued N. The matrix $\boldsymbol{C}_0$ consists of complex Fourier series coefficients sized as $N \times 6$. To compute the coefficients in $\boldsymbol{C}_0$, a discrete Fourier transform operator, $\boldsymbol{D}$, is leveraged:

$$\boldsymbol{C}_0 = \boldsymbol{D}\boldsymbol{U} \tag{3.15}$$

where $\boldsymbol{U}$ is the matrix of state vectors on the invariant circle:

$$\boldsymbol{U} = \begin{bmatrix} \vec{u}_1^T \\ \vec{u}_2^T \\ \vec{u}_3^T \\ \vdots \\ \vec{u}_N^T \end{bmatrix} = \begin{bmatrix} u_{x,1} & u_{y,1} & u_{z,1} & u_{\dot{x},1} & u_{\dot{y},1} & u_{\dot{z},1} \\ u_{x,2} & u_{y,2} & u_{z,2} & u_{\dot{x},2} & u_{\dot{y},2} & u_{\dot{z},2} \\ u_{x,3} & u_{y,3} & u_{z,3} & u_{\dot{x},3} & u_{\dot{y},3} & u_{\dot{z},3} \\ \vdots & \vdots & \vdots & \vdots & \vdots & \vdots \\ u_{x,N} & u_{y,N} & u_{z,N} & u_{\dot{x},N} & u_{\dot{y},N} & u_{\dot{z},N} \end{bmatrix} \tag{3.16}$$

where each row of the $\boldsymbol{U}$ matrix is a 6-element state defined on the invariant curve. The discrete Fourier transform operator $\boldsymbol{D}$ is an $N \times N$ matrix, defined by

$$\boldsymbol{D} = \frac{1}{N} \mathrm{e}^{-\mathrm{i}\vec{k}^T\vec{\theta}_1} \tag{3.17}$$

$$= \frac{1}{N} \begin{bmatrix} \mathrm{e}^{-\mathrm{i}(-\frac{N-1}{2})0} & \mathrm{e}^{-\mathrm{i}(-\frac{N-1}{2})\frac{2\pi}{N}} & \mathrm{e}^{-\mathrm{i}(-\frac{N-1}{2})\frac{4\pi}{N}} & \dots & \mathrm{e}^{-\mathrm{i}(-\frac{N-1}{2})\frac{2\pi(N-1)}{N}} \\ \vdots & \vdots & \vdots & & \vdots \\ \mathrm{e}^{-\mathrm{i}(-1)0} & \mathrm{e}^{-\mathrm{i}(-1)\frac{2\pi}{N}} & \mathrm{e}^{-\mathrm{i}(-1)\frac{4\pi}{N}} & \dots & \mathrm{e}^{-\mathrm{i}(-1)\frac{2\pi(N-1)}{N}} \\ \mathrm{e}^{-\mathrm{i}(0)0} & \mathrm{e}^{-\mathrm{i}(0)\frac{2\pi}{N}} & \mathrm{e}^{-\mathrm{i}(0)\frac{4\pi}{N}} & \dots & \mathrm{e}^{-\mathrm{i}(0)\frac{2\pi(N-1)}{N}} \\ \mathrm{e}^{-\mathrm{i}(1)0} & \mathrm{e}^{-\mathrm{i}(1)\frac{2\pi}{N}} & \mathrm{e}^{-\mathrm{i}(1)\frac{4\pi}{N}} & \dots & \mathrm{e}^{-\mathrm{i}(1)\frac{2\pi(N-1)}{N}} \\ \vdots & \vdots & \vdots & & \vdots \\ \mathrm{e}^{-\mathrm{i}(\frac{N-1}{2})0} & \mathrm{e}^{-\mathrm{i}(\frac{N-1}{2})\frac{2\pi}{N}} & \mathrm{e}^{-\mathrm{i}(\frac{N-1}{2})\frac{4\pi}{N}} & \dots & \mathrm{e}^{-\mathrm{i}(\frac{N-1}{2})\frac{2\pi(N-1)}{N}} \end{bmatrix}$$

where $\vec{k}$ is constructed in Equation (3.14) and $\vec{\theta}_1$ is evaluated in Equation (3.8). The rotation matrix $\boldsymbol{R}_{-\rho}$ is defined using the matrix equation

$$\boldsymbol{R}_{-\rho} = \boldsymbol{D}^{-1}\boldsymbol{Q}_{-\rho}\boldsymbol{D} \tag{3.18}$$

where $\boldsymbol{Q}_{-\rho}$ is an $N \times N$ diagonal matrix and a function of the rotation angle ρ:

$$\boldsymbol{Q}_{-\rho} = \mathrm{diag}[\mathrm{e}^{-\mathrm{i}\vec{k}\rho}] = \begin{bmatrix} \mathrm{e}^{-\mathrm{i}(-\frac{N-1}{2})\rho} & 0 & \dots & 0 \\ 0 & \mathrm{e}^{-\mathrm{i}(-\frac{N-1}{2}+1)\rho} & \dots & 0 \\ \vdots & \vdots & \ddots & \vdots \\ 0 & 0 & \dots & \mathrm{e}^{-\mathrm{i}(\frac{N-1}{2})\rho} \end{bmatrix} \tag{3.19}$$

where diag[$\bullet$] transforms a vector into a diagonal matrix with the elements of the vector on the diagonal. The rotation operator removes the rotation around the invariant circle for each cycle to yield each vector element $\vec{u}_{\mathrm{i}}^{t,R}$ in the constraint vector in Equation (3.11). The $N \times 6$ matrix of states with the rotation removed, that is, $\boldsymbol{U}^{t,R}$, is then evaluated as

$$\boldsymbol{U}^{t,R} = \boldsymbol{R}_{-\rho}\boldsymbol{U}^{t} \tag{3.20}$$

where the matrix $\boldsymbol{U}^{t}$ is an $N \times 6$ matrix; each row is a state vector at the time of the first return to the stroboscopic map. This invariance constraint supplies the basis for the torus corrections algorithm used to compute 2D tori.

Finally, the Jacobian matrix is constructed. For a free variable and constraint differential corrections method, the elements of the Jacobian matrix consist of partial derivatives for the constraints with respect to the free variables. First, the partial derivatives for the invariance constraints in response to variations in the initial states on the invariant curve are evaluated, that is,

$$\frac{\partial(\boldsymbol{u}^{t,R} - \boldsymbol{u})}{\partial \boldsymbol{u}} = \frac{\partial \boldsymbol{u}^{t,R}}{\partial \boldsymbol{u}} - \frac{\partial \boldsymbol{u}}{\partial \boldsymbol{u}} = (\boldsymbol{R}_{-\rho} \otimes \boldsymbol{I})\tilde{\boldsymbol{\Phi}} - \tilde{\boldsymbol{I}} = \boldsymbol{DG} - \tilde{\boldsymbol{I}} \tag{3.21}$$

where $\boldsymbol{u}$ is a vector composed of the first $6N$ elements of the free-variable vector from Equation (3.10), $\boldsymbol{R}_{-\rho}$ is the rotation operator defined in Equation (3.18), $\boldsymbol{I}$ is a 6×6 identity matrix, $\tilde{\boldsymbol{I}}$ is a $6N \times 6N$ identity matrix, $\otimes$ is the Kronecker product operator, and $\tilde{\boldsymbol{\Phi}}$ is a block diagonal matrix that incorporates the state transition matrices (STMs) from the initial states along the invariant circle and are propagated to the first return of the map, yielding the following form:

$$\tilde{\boldsymbol{\Phi}} = \begin{bmatrix} \boldsymbol{\Phi}_1(T_0, 0) & \mathbf{0_{6\times 6}} & \mathbf{0_{6\times 6}} & \dots & \mathbf{0_{6\times 6}} \\ \mathbf{0_{6\times 6}} & \boldsymbol{\Phi}_2(T_0, 0) & \mathbf{0_{6\times 6}} & \dots & \mathbf{0_{6\times 6}} \\ \mathbf{0_{6\times 6}} & \mathbf{0_{6\times 6}} & \boldsymbol{\Phi}_3(T_0, 0) & \dots & \mathbf{0_{6\times 6}} \\ \vdots & \vdots & \vdots & \ddots & \vdots \\ \mathbf{0_{6\times 6}} & \mathbf{0_{6\times 6}} & \mathbf{0_{6\times 6}} & \dots & \boldsymbol{\Phi}_N(T_0, 0) \end{bmatrix} \tag{3.22}$$

where $\mathbf{\Phi}_{\mathrm{i}}(T_0, 0)$ is the STM from the i$^{\text{th}}$ initial state on the invariant circle propagated to the first return of the map after time T_0. Similarly, the invariance constraint with respect to the stroboscopic mapping time is defined as the time derivative of the final propagated states with the rotation removed, that is,

$$\frac{\partial \boldsymbol{u}^{t,R}}{\partial T_0} = \dot{\boldsymbol{u}}^{t,R} = \begin{bmatrix} \dot{\bar{u}}_1^{t,R} \\ \dot{\bar{u}}_2^{t,R} \\ \dot{\bar{u}}_3^{t,R} \\ \vdots \\ \dot{\bar{u}}_N^{t,R} \end{bmatrix} \tag{3.23}$$

where $\dot{\bar{u}}_{\mathrm{i}}^{t,R} = \begin{bmatrix} \dot{x}^R(T_0) & \dot{y}^R(T_0) & \dot{z}^R(T_0) & \ddot{x}^R(T_0) & \ddot{y}^R(T_0) & \ddot{z}^R(T_0) \end{bmatrix}^T$ is the derivative of the 6-dimensional state of the i$^{\text{th}}$ discretized point on the first return to the stroboscopic map and $\boldsymbol{u}^{t,R}$ is a vector of length $6N$ corresponding to those time derivatives. Finally, the partial derivatives for the invariance constraints with respect to the rotation angle ρ are defined by

$$\frac{\partial \boldsymbol{u}^{t,R}}{\partial \rho} = \boldsymbol{D}^{-1} \frac{\partial \boldsymbol{Q}_{-\rho}}{\partial \rho} \boldsymbol{D} \boldsymbol{U}^t \tag{3.24}$$

where $\boldsymbol{D}$ is defined in Equation (3.17), $\boldsymbol{U}^t$ is a $6 \times N$ matrix whose rows are the states from the initial invariant curve propagated to the first return on the stroboscopic map, and the partial derivative of the matrix $\boldsymbol{Q}_{-\rho}$ with respect to the rotation angle is defined by

$$\begin{aligned} \frac{\partial \boldsymbol{Q}_{-\rho}}{\partial \rho} &= \mathrm{diag}[\vec{k}]\mathrm{diag}[-\mathrm{i}\mathrm{e}^{-\mathrm{i}\vec{k}\rho}] \\ &= \begin{bmatrix} (\frac{N-1}{2})\mathrm{i}\mathrm{e}^{-\mathrm{i}(-\frac{N-1}{2})\rho} & 0 & \dots & 0 \\ 0 & (\frac{N-1}{2}-1)\mathrm{i}\mathrm{e}^{-\mathrm{i}(-\frac{N-1}{2}+1)\rho} & \dots & 0 \\ \vdots & \vdots & \ddots & \vdots \\ 0 & 0 & \dots & (-\frac{N-1}{2})\mathrm{i}\mathrm{e}^{-\mathrm{i}(\frac{N-1}{2})\rho} \end{bmatrix} \end{aligned} \tag{3.25}$$

where $\mathrm{diag}[\vec{k}]$ indicates a square diagonal matrix with the elements of the vector $\vec{k}$ from Equation (3.14) as the diagonal elements. The matrix $\boldsymbol{D}^{-1}\frac{\partial \boldsymbol{Q}_{-\rho}}{\partial \rho}\boldsymbol{D}\boldsymbol{U}^t$ is dimension $N \times 6$

but is rearranged to produce a $6N \times 1$ column vector that occupies elements of the Jacobian matrix. Thus, the matrix $\boldsymbol{D}^{-1}\frac{\partial \boldsymbol{Q}_{-\rho}}{\partial \rho}\boldsymbol{D}\boldsymbol{u}^t$ is defined,

$$\frac{\partial \mathbf{u}^{t,R}}{\partial \rho} = \begin{bmatrix} \left(\frac{\partial \vec{u}_1^{t,R}}{\partial \rho}\right)^T \\ \left(\frac{\partial \vec{u}_2^{t,R}}{\partial \rho}\right)^T \\ \vdots \\ \left(\frac{\partial \vec{u}_N^{t,R}}{\partial \rho}\right)^T \end{bmatrix} \tag{3.26}$$

where $\frac{\partial \vec{u}_{\mathrm{i}}^{t,R}}{\partial \rho}$ is the i^{th} row of the $\mathbf{D}^{-1}\frac{\partial \mathbf{Q}}{\partial \rho}\mathbf{D}\mathbf{u}^t$ matrix. Finally, for quasi-periodic orbits in the CR3BP, the scalar Jacobi constant constraint with respect to the initial states on the invariant curve are defined. Note that these derivatives are omitted from the corrections process for quasi-periodic orbits in the BCR4BP. The Jacobi constant is not explicitly dependent on the stroboscopic mapping time or the rotation angle. Therefore, the partial derivatives of the Jacobi constant constraint are only non-zero with respect to the initial state free variables:

$$\frac{\partial JC_{\mathrm{avg}}}{\partial \boldsymbol{u}} = \frac{1}{N}\begin{bmatrix} \frac{\partial JC_1}{\partial \boldsymbol{u}_1} & \frac{\partial JC_2}{\partial \boldsymbol{u}_2} & \frac{\partial JC_3}{\partial \boldsymbol{u}_3} & \cdots & \frac{\partial JC_N}{\partial \boldsymbol{u}_N} \end{bmatrix} \tag{3.27}$$

where $\frac{\partial JC_{\mathrm{i}}}{\partial \boldsymbol{u}_{\mathrm{i}}}$ is constructed as

$$\frac{\partial JC_{\mathrm{i}}}{\partial \boldsymbol{u}_{\mathrm{i}}} = \begin{bmatrix} 2U^*_{x,\mathrm{i}} & 2U^*_{y,\mathrm{i}} & 2U^*_{z,\mathrm{i}} & -2\dot{x}_{\mathrm{i}} & -2\dot{y}_{\mathrm{i}} & -2\dot{z}_{\mathrm{i}} \end{bmatrix} \tag{3.28}$$

and $U^*_{x,\mathrm{i}}$, $U^*_{y,\mathrm{i}}$, and $U^*_{z,\mathrm{i}}$ are the partial derivatives of the pseudo-potential function with respect to the x, y, and z positions in the barycentered rotating frame, respectively, evaluated at the i^{th} state along the invariant curve. The Jacobian matrix $\boldsymbol{DF}$ is constructed using the submatrices defined in Equations (3.21), (3.23), (3.24), and (3.27) for a single-shooting torus corrections scheme:

$$\boldsymbol{DF} = \begin{bmatrix} \frac{\partial(\boldsymbol{u}^{t,R}-\boldsymbol{u})}{\partial \boldsymbol{u}} & \frac{\partial \boldsymbol{u}^{t,R}}{\partial T_0} & \frac{\partial \boldsymbol{u}^{t,R}}{\partial \rho} \\ \frac{\partial JC_{\mathrm{avg}}}{\partial \boldsymbol{u}} & 0 & 0 \end{bmatrix} \tag{3.29}$$

This results in a dense $(6N+1) \times (6N+2)$ Jacobian matrix. Using the free-variable vector, constraint vector, and Jacobian matrix defined in Equations (3.10), (3.11), and (3.29),

respectively, a linear system solver is employed to deliver an update to the free variables that represent a torus for each iteration of the corrections procedure.

During the trajectory design process, it is valuable to have a continuum or a family of solutions available for analysis. Families of solutions also illuminate the dominant type of motion in a particular region of space. In this investigation, a procedure for computing families of 2D tori is used to leverage pseudo-arclength continuation [58]. An additional set of constraints and partial derivatives are included to ensure that the pseudo-arclength continuation process "steps" in the proper direction. Without these additional constraints, the invariant circle can shift in the longitudinal and latitudinal directions during an attempt to "step" to a new family member in a pseudo-arclength continuation scheme. Rather than converging to a new member of the family, the algorithm might converge to a different invariant curve on the same torus. Olikara and Scheeres describe an additional set of phase constraints to ensure that the invariant curve is representative of a true new torus in the family [26], and the Jacobian matrix of the corrections procedure is defined such that it possesses a 1D nullspace. Using the previously converged torus along the family, the latitudinal and longitudinal phase constraints are defined as two scalars:

$$F_{\theta_0} = \langle \boldsymbol{U}, \frac{\partial \tilde{\boldsymbol{U}}}{\partial \theta_0} \rangle = 0 \qquad (3.30) \qquad\qquad F_{\theta_1} = \langle \boldsymbol{U}, \frac{\partial \tilde{\boldsymbol{U}}}{\partial \theta_1} \rangle = 0 \qquad (3.31)$$

where $\langle \bullet, \bullet \rangle$ is the inner product operator, and $\tilde{\boldsymbol{U}}$ is the matrix of initial states on the invariant circle from the previously converged member of the family. The partial derivatives for the previously converged invariant curve states with respect to the latitudinal angle θ_1 are first defined as the $N \times 6$ matrix:

$$\frac{\partial \tilde{\boldsymbol{U}}}{\partial \theta_1} = \mathrm{i} e^{\mathrm{i}\vec{\theta}_1^T \vec{k}} \mathrm{diag}[\vec{k}] \tilde{\boldsymbol{C}}_0 \qquad (3.32)$$

where $\tilde{\boldsymbol{C}}_0$ is a $N \times 6$ matrix of Fourier coefficients for the invariant curve corresponding to the previously converged family member, as defined in Equation (3.15). In addition, $\vec{\theta}_1$ is the row vector from Equation (3.8) and $\vec{k}$ is defined as a row vector in Equation (3.14).

The phase constraint associated with the longitudinal angle θ_0 is defined by a similar inner product. The right side of the inner product is computed using Equation (3.32):

$$\frac{\partial \tilde{\boldsymbol{U}}}{\partial \theta_0} = \frac{1}{\tilde{\omega}_0}\left(\frac{\partial \tilde{\boldsymbol{U}}}{\partial t} - \tilde{\omega}_1 \frac{\partial \tilde{\boldsymbol{U}}}{\partial \theta_1}\right) = \frac{\tilde{T}_0}{2\pi}\left(\dot{\tilde{\boldsymbol{U}}} - \frac{\tilde{\rho}}{\tilde{T}_0}\frac{\partial \tilde{\boldsymbol{U}}}{\partial \theta_1}\right) \tag{3.33}$$

where $\tilde{T}_0$ is the stroboscopic mapping time and $\tilde{\rho}$ is the rotation angle for the previously converged family member. Finally, the partial derivatives for the phase constraints with respect to the free variables are evaluated for the elements of the Jacobian matrix. Because the phase constraints are not dependent on the rotation angle or the mapping time, only the derivatives with respect to the initial states on the invariant curve are non-zero, that is,

$$\frac{\partial F_{\theta_0}}{\partial \boldsymbol{u}} = \frac{\partial \tilde{\boldsymbol{U}}}{\partial \theta_0} \tag{3.34}$$

$$\frac{\partial F_{\theta_1}}{\partial \boldsymbol{u}} = \frac{\partial \tilde{\boldsymbol{U}}}{\partial \theta_1} \tag{3.35}$$

Because Equations (3.34) and (3.35) yield $N \times 6$ matrices, they are rearranged to yield a row vector of length $6N$ that is inserted into the Jacobian matrix. The Jacobian matrix is augmented from Equation (3.29) such that it includes the two phasing constraints and takes the following form:

$$\boldsymbol{DF} = \begin{bmatrix} \frac{\partial(\boldsymbol{u}^{t,R} - \boldsymbol{u})}{\partial \boldsymbol{u}} & \frac{\partial \boldsymbol{u}^{t,R}}{\partial T_0} & \frac{\partial \boldsymbol{u}^{t,R}}{\partial \rho} \\ \frac{\partial JC_{avg}}{\partial \boldsymbol{u}} & 0 & 0 \\ \frac{\partial F_{\theta_0}}{\partial \boldsymbol{u}} & 0 & 0 \\ \frac{\partial F_{\theta_1}}{\partial \boldsymbol{u}} & 0 & 0 \end{bmatrix} \tag{3.36}$$

where the partial derivatives for Jacobi Constant are only included for quasi-periodic orbits in the CR3BP. The phasing constraints are also appended to the end of the constraint vector in Equation (3.11). By including the phase constraints, the rank of the $\boldsymbol{DF}$ matrix is not altered and, consequently, the nullspace for the $\boldsymbol{DF}$ matrix remains 1-dimensional. A pseudo-arclength continuation scheme is implemented to compute families of 2D tori, ensuring that the invariant curve representing each family member is unique during the continuation process.

Multiple Shooting Torus Correction

The single-shooting torus correction formulation is extendable to multiple-shooting and collocation schemes [27], [44], [59]. Similar to the multiple shooting procedure developed for periodic orbits, the scheme for quasi-periodic orbits is generally more robust for orbits with long mapping times or close encounters with the primaries. Figure 3.3 depicts how the torus is split into multiple invariant curves, or patch curves, in the multiple shooting correction scheme. Continuity constraints are enforced between the states that represent the patch curves, similar to continuity constraints outlined in Section 2.4.2. The invariance constraints are imposed between the initial invariant patch curve and the states from the last patch curve integrated to the first return of the stroboscopic map. The free variable

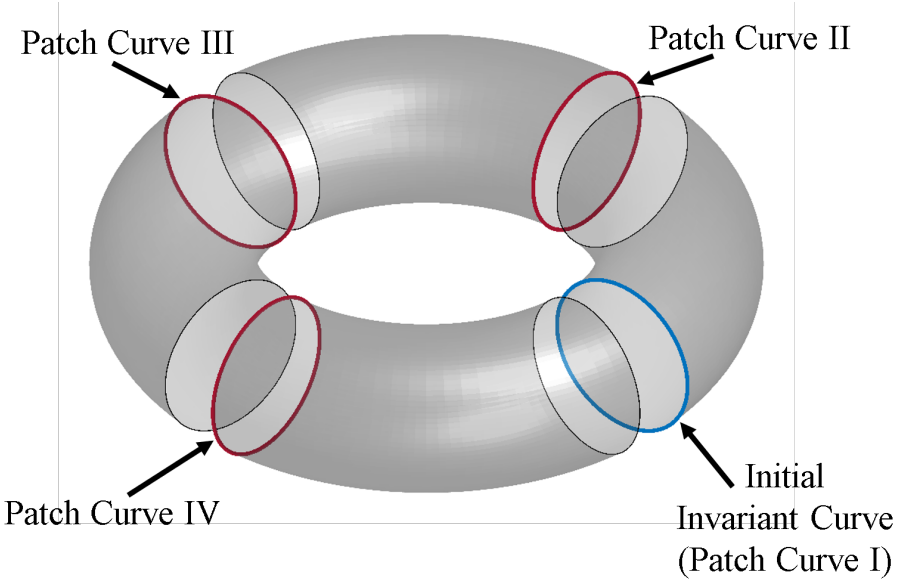

Figure 3.3. Representation of a patch curves along a torus used for a multiple shooting torus correction scheme

vector is defined, using M discretized patch curves

$$\boldsymbol{X} = \begin{bmatrix} \vec{u}_1^I \\ \vec{u}_2^I \\ \vec{u}_3^I \\ \vdots \\ \vec{u}_N^I \\ \vec{u}_1^{II} \\ \vec{u}_2^{II} \\ \vdots \\ \vec{u}_N^M \\ T_{seg} \\ \rho \end{bmatrix} \tag{3.37}$$

where $\vec{u}_{\mathrm{i}}^{\mathrm{j}} = \begin{bmatrix} u_{x,\mathrm{i}}^{\mathrm{j}} & u_{y,\mathrm{i}}^{\mathrm{j}} & u_{z,\mathrm{i}}^{\mathrm{j}} & u_{\dot{x},\mathrm{i}}^{\mathrm{j}} & u_{\dot{y},\mathrm{i}}^{\mathrm{j}} & u_{\dot{z},\mathrm{i}}^{\mathrm{j}} \end{bmatrix}$ and $\mathrm{i} = 1, 2, ..., N$ represents the index of the point on the invariant curve and $\mathrm{j} = I, II, III, ..., M$ represents the index of the patch curve

on the torus, and T_{seg} is the propagation time for the states on each invariant curve, such that $T_{seg} = \frac{T_0}{M}$. The constraint matrix is defined

$$\boldsymbol{F} = \begin{bmatrix} \vec{u}_1^{t,II} - \vec{u}_1^{II} \\ \vec{u}_2^{t,II} - \vec{u}_2^{II} \\ \vec{u}_3^{t,II} - \vec{u}_3^{II} \\ \vdots \\ \vec{u}_N^{t,II} - \vec{u}_N^{II} \\ \vec{u}_1^{t,III} - \vec{u}_1^{III} \\ \vdots \\ \vec{u}_N^{t,M} - \vec{u}_N^{M} \\ \vec{u}_1^{t,I,R} - \vec{u}_1^{I} \\ \vec{u}_2^{t,I,R} - \vec{u}_2^{I} \\ \vdots \\ \vec{u}_{N-1}^{t,I,R} - \vec{u}_{N-1}^{I} \\ \vec{u}_N^{t,I,R} - \vec{u}_N^{I} \\ JC_{avg} - JC_d \\ F_{\theta_0} \\ F_{\theta_1} \end{bmatrix} = \vec{0} \tag{3.38}$$

where the $\vec{u}_{\mathrm{i}}^{t,\mathrm{j}}$ is the end of the path associated with the i^{th} state on the $(\mathrm{j}-1)^{th}$ invariant curve. Note that for computing quasi-periodic orbits in the BCR4BP using a multiple

shooting scheme, the Jacobi Constant constraint is not included in the $\boldsymbol{F}$ vector. The Jacobian matrix for the multiple shooting formulation is defined,

$$\mathbf{DF} = \begin{bmatrix} \begin{bmatrix} \mathbf{DF}_{\Phi} \\ -\tilde{\mathbf{I}} \end{bmatrix} & \begin{bmatrix} \mathbf{0_{6N\times 6N(M-2)}} \end{bmatrix} & \begin{bmatrix} \frac{\partial(\vec{u}^{t,I,R}-\vec{u}^{I})}{\partial \vec{u}^{M}} \end{bmatrix} & \begin{bmatrix} \frac{\partial \vec{u}^{t}}{\partial T_{seg}} \\ \frac{\partial \vec{u}^{t,I,R}}{\partial T_{seg}} \end{bmatrix} & \begin{bmatrix} \mathbf{0_{6N(M-1)\times 1}} \\ \frac{\partial \vec{u}^{t,I,R}}{\partial \rho} \end{bmatrix} \\ \begin{bmatrix} \frac{\partial JC_{avg}}{\partial \vec{u}^{I}} \\ \frac{\partial\left(\vec{u}^{I}\cdot\frac{\partial \bar{\vec{u}}}{\partial \theta_0}\right)}{\partial \vec{u}^{I}} \\ \frac{\partial\left(\vec{u}^{I}\cdot\frac{\partial \bar{\vec{u}}}{\partial \theta_1}\right)}{\partial \vec{u}^{I}} \end{bmatrix} & \begin{bmatrix} \mathbf{0_{3\times 6N(M-1)+2}} \end{bmatrix} \end{bmatrix} \tag{3.39}$$

where the submatrix $\left[\mathbf{DF}_{\Phi}\right]$ is defined

$$\mathbf{DF}_{\Phi} = \begin{bmatrix} \tilde{\mathbf{\Phi}}^{I}(T_{seg},0) & -\tilde{\mathbf{I}} & \mathbf{0_{6N\times 6N}} & \dots & \mathbf{0_{6N\times 6N}} & \mathbf{0_{6N\times 6N}} \\ \mathbf{0_{6N\times 6N}} & \tilde{\mathbf{\Phi}}^{II}(T_{seg},0) & -\tilde{\mathbf{I}} & \dots & \mathbf{0_{6N\times 6N}} & \mathbf{0_{6N\times 6N}} \\ \vdots & \vdots & \vdots & \ddots & \vdots & \vdots \\ \mathbf{0_{6N\times 6N}} & \mathbf{0_{6N\times 6N}} & \mathbf{0_{6N\times 6N}} & \dots & \tilde{\mathbf{\Phi}}^{M-1}(T_{seg},0) & -\tilde{\mathbf{I}} \end{bmatrix} \tag{3.40}$$

and $\tilde{\mathbf{\Phi}}^{\mathrm{j}}(T_{seg},0)$ represents a block diagonal matrix of the STMs from the discretized states on the j^{th} patch curve, integrated from time $t=0$ to $t=T_{seg}$,

$$\tilde{\mathbf{\Phi}}^{\mathrm{j}} = \begin{bmatrix} \mathbf{\Phi_1}^{\mathrm{j}}(T_{seg},0) & \mathbf{0_{6\times 6}} & \mathbf{0_{6\times 6}} & \dots & \mathbf{0_{6\times 6}} \\ \mathbf{0_{6\times 6}} & \mathbf{\Phi_2}^{\mathrm{j}}(T_{seg},0) & \mathbf{0_{6\times 6}} & \dots & \mathbf{0_{6\times 6}} \\ \mathbf{0_{6\times 6}} & \mathbf{0_{6\times 6}} & \mathbf{\Phi_3}^{\mathrm{j}}(T_{seg},0) & \dots & \mathbf{0_{6\times 6}} \\ \vdots & \vdots & \vdots & \ddots & \vdots \\ \mathbf{0_{6\times 6}} & \mathbf{0_{6\times 6}} & \mathbf{0_{6\times 6}} & \dots & \mathbf{\Phi_N}^{\mathrm{j}}(T_{seg},0) \end{bmatrix} \tag{3.41}$$

The submatrix $\left[\frac{\partial \vec{u}^t}{\partial T_{seg}}\right]$ is defined as the invariant curve state partial derivatives with respect time along each arc

$$\left[\frac{\partial \vec{u}^t}{\partial T_{seg}}\right] = \begin{bmatrix} \dot{\vec{u}}_1^{t,II} \\ \dot{\vec{u}}_2^{t,II} \\ \vdots \\ \dot{\vec{u}}_N^{t,II} \\ \dot{\vec{u}}_1^{t,III} \\ \vdots \\ \dot{\vec{u}}_N^{t,M} \end{bmatrix} \tag{3.42}$$

where M is the number of patch curves used for the multiple shooting. The submatrices $\left[\frac{\partial \vec{u}^{t,I,R}}{\partial T_{seg}}\right]$ and $\left[\frac{\partial \vec{u}^{t,I,R}}{\partial \rho}\right]$ are computed from Equations (3.23) and (3.24), respectively; however, the partial derivatives are evaluated at the end of the propagation of the discretized states on patch curve M. The submatrix for the invariance condition partial derivatives with respect to the states on patch curve M is defined

$$\left[\frac{\partial(\vec{u}^{t,I,R} - \vec{u}^I)}{\partial \vec{u}^M}\right] = (\mathbf{R}(-\rho) \otimes \mathbf{I})\tilde{\mathbf{\Phi}}^M(T_{seg}, 0) \tag{3.43}$$

where $\tilde{\mathbf{\Phi}}^M(T_{seg}, 0)$ is defined in Equation (3.41) for j $= M$. Finally, the submatrices $\left[\frac{\partial JC_{avg}}{\partial \vec{u}^I}\right]$, $\left[\frac{\partial\left(\vec{u}^I \cdot \frac{\partial \bar{\vec{u}}}{\partial \theta_0}\right)}{\partial \vec{u}^I}\right]$, and $\left[\frac{\partial\left(\vec{u}^I \cdot \frac{\partial \bar{\vec{u}}}{\partial \theta_1}\right)}{\partial \vec{u}^I}\right]$ are defined in Equations (3.27), (3.34), and (3.35), evaluated at the states on the initial invariant curve. The remaining three submatrices consist of zero elements, where the dimension of the matrix is in the subscript in Equation (3.39). The multiple shooting formulation is more robust when encountering quasi-periodic orbits that have long propagation times or close approaches to primaries. Furthermore, the multiple shooting formulation is implemented with a pseudo-arclength continuation method to compute families of quasi-periodic orbits. The **DF** has a 1-dimensional null-space, and the pseudo-arclength constraint is appended to the end of the constraint vector.

3.1.2 QPO Families in the CR3BP

For a given periodic orbit in the CR3BP, three quasi-periodic orbit families are characterized in the vicinity. For the constraint vector defined in Equation (3.11), the Jacobi Constant is constrained such that each member of the family possesses the same value of JC. In this formulation, the rotation angle and mapping times vary over the family. However, constraining the mapping time or frequency ratio rather than the Jacobi constant yields different family structures. Figure 3.4 illustrates three members of three quasi-vertical families in the Earth-Moon CR3BP that originate from the same periodic vertical orbit. Quasi-periodic families in which the JC is constrained, as shown in Figure 3.4a, are useful for trajectory or transfer scenarios that require access to regions of space at a particular energy level. Members of a constant mapping time family share the same longitudinal period, which is equal to the orbital period of the central periodic orbit. With mapping time constrained, members of this family are useful for eclipse avoidance applications, specifically when the mapping time is in resonance with the eclipsing body [60].

The numerical continuation formulation in this investigation experiences difficulties for both consistent values of JC as well as constant mapping time families when integer values in the fundamental frequency ratios are encountered, as noted by Bosanac and Schilder et al. [23], [61]. When the fundamental frequencies are commensurate, the torus collapses to a period-g orbit, where g is the integer ratio, and the continuation scheme terminates. To avoid the difficulties associated with commensurate frequency ratios, a constant frequency ratio family is also generated and rendered in Figure 3.4c. The frequency ratio is defined as a function of only the rotation angle ρ for 2D tori, that is,

$$\frac{\dot{\theta}_0}{\dot{\theta}_1} = \frac{2\pi}{\rho} \tag{3.44}$$

Subsequently, constant frequency ratio families are also constant rotation angle families. When a constant frequency ratio family is initialized from a periodic orbit that does not exist near a period multiplying bifurcation, integer frequency ratios are avoided during the

continuation process for 2D tori in the CR3BP. Note that quasi-periodic orbit families are not limited to these three characterizations, but these types are suitable for this investigation.

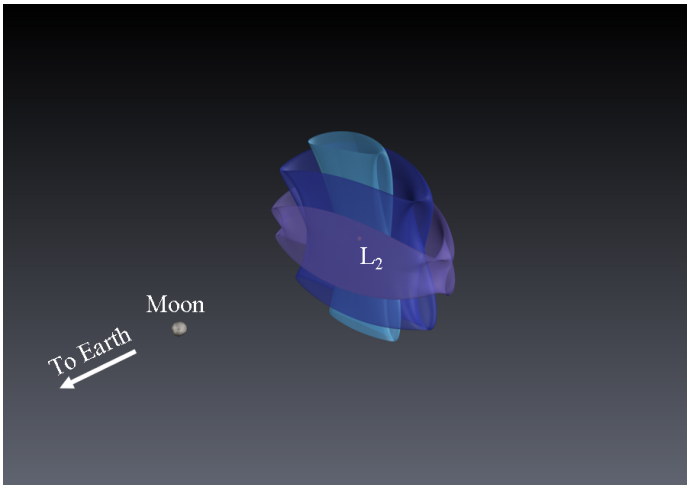

a

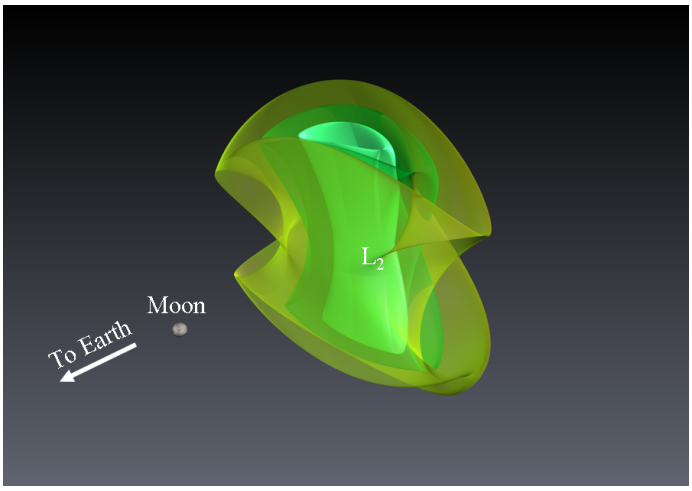

b

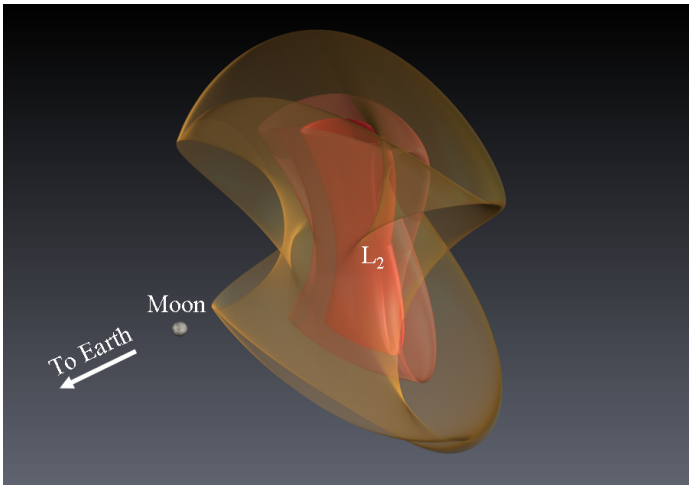

c

Figure 3.4. Given the same periodic vertical orbit: (a) constant energy quasi-vertical family, (b) constant mapping time quasi-vertical family, and (c) constant frequency ratio quasi-vertical family with the same underling periodic vertical orbit.

3.1.3 QPO Families in the BCR4BP

Quasi-periodic orbits are also known to exist in families in the BCR4BP. For non-autonomous Hamiltonian systems, one or more of the frequencies is typically constrained and the number of free variables to construct a family of invariant tori is reduced [62]. Since the BCR4BP is a periodically forced system, one of the fundamental frequencies, $\dot{\theta}_0$, is constrained to match the frequency of the system. As mentioned in Section 2.6, the orbital period of a periodic orbit must be commensurate with the synodic period of the system and exist as isolated solutions in the BCR4BP. Similarly, one of the frequencies reflecting a 2-dimensional quasi-periodic torus is constrained to be commensurate with the synodic period of the system and the second frequency, $\dot{\theta}_1$, is free; thus, a family of quasi-periodic orbits is defined along the frequency $\dot{\theta}_1$. Given that quasi-periodic orbits are known to exist in families in the BCR4BP, they provide a wider set of options for destinations in cislunar space, relaxing the constraint of a perfectly periodic orbit.

There are two methods in this investigation used seed an initial guess to construction these solutions in the BCR4BP. The first procedure involves using the center direction computed from the monodromy matrix of a periodic orbit in the BCR4BP, as discussed in Section 3.1.1. The second approach leverages a periodic orbit in the CR3BP that is transitioned using pseudo-arclength continuation from the CR3BP to the BCR4BP. Once the initial guess is constructed, the differential corrections strategy from Section 3.1.1 is employed to compute members of a family in the BCR4BP. The behavior of the families of tori provides a broader understanding of the local Sun-perturbed cislunar environment.

Method 1: Linear Approximation of Center Direction

Generating an initial guess using the center direction associated with a periodic orbit requires computation of the eigenvalues of the monodromy matrix associated with a periodic orbit. First, the eigenvalues of the monodromy matrix associated with the dynamically equivalent L_1 and L_2 orbits are computed and recorded in Table 3.1. The process to compute these dynamical equivalent orbits is summarized in Section 2.6. In the CR3BP, there are two center modes and one saddle mode for the L_1 and L_2 libration points; however, only

L_1 retains the saddle × center × center behavior for the dynamical equivalent orbit in the BCR4BP. The L_2 orbit possesses a saddle × saddle × center signature. The process to select an initial set of invariant curve states and rotation angle from Equations (3.7) and (3.9) and the initial guess for the mapping time is equal to the synodic period.

Table 3.1. Eigenvalues associated with the dynamically equivalent orbit associated with the Earth-Moon L_1 and L_2 libration points in the BCR4BP.

λ_{L_1}	λ_{L_2}
4.275×10^{8}	7.7667×10^{5}
3.859×10^{-7}	1.2877×10^{-6}
$-0.9937 + 0.1117\text{i}$	0.6023
$-0.9937 - 0.1117\text{i}$	1.6600
$-0.9508 + 0.3098\text{i}$	$0.8657 + 0.5005\text{i}$
$-0.9508 - 0.3098\text{i}$	$0.8657 - 0.5005\text{i}$

Method 2: Transitioning between the CR3BP and the BCR4BP

As discussed, the BCR4BP is formulated as an Earth-Moon CR3BP augmented with a periodic force from the Sun. By introducing a periodic forcing term to the problem, many of these CR3BP periodic orbits have a dynamically equivalent quasi-periodic orbit in the BCR4BP. To generate an initial guess, a periodic orbit in the CR3BP is transitioned to a quasi-periodic orbit by scaling up the Sun mass using the ε in the equations of motion, reflected in Equations (2.89)-(2.91). Consider an L_1 planar periodic Lyapunov orbit in the Earth-Moon CR3BP as plotted in Figure 3.5a. This periodic orbit delivers a quasi-periodic equivalent in the BCR4BP. First, the states along the invariant curve are parameterized. Since the periodic orbit represents the torus when $\varepsilon = 0$, the orbit is discretized uniformly in time to represent N discretized points along the invariant curve. These points represent the invariant curve for the torus when $\varepsilon = 0$. The L_1 Lyapunov orbit in Figure 3.5a is discretized into $N = 45$ states. The states along the periodic orbit are propagated forward for one synodic period, T_{syn} which is equal to the longitudinal period. The last parameter required to fully define the torus is the rotation angle. The rotation angle is computed by determining the angle between 0 and 2π that satisfies the invariance constraint in Equation (3.5) between

the initial states and the states propagated to the first return on the stroboscopic map, i.e., one synodic period. A root solving routine delivers a rotation angle, ρ, that resolves Equation (3.5) to zero. This rotation angle, satisfying the invariance constraint, defines the rotation on the torus when $\varepsilon = 0$, in the CR3BP. The torus is now fully defined for $\varepsilon = 0$ and a pseudo-arclength continuation process transitions the solution at $\varepsilon = 0$ to $\varepsilon = 1$. The continuation algorithm is formulated using a free-variable/constraint differential corrections method for each solution. The free variable vector is defined,

$$\boldsymbol{X} = \begin{bmatrix} \vec{u}_1 \\ \vec{u}_2 \\ \vdots \\ \vec{u}_N \\ \varepsilon \end{bmatrix} \tag{3.45}$$

where $\vec{u}_{\mathrm{i}}$ is the i^{th} 6-element state vector on the invariant curve and ε is the Sun mass scaling term included in Equations (2.89)-(2.91). The free variable vector contains $6N+1$ elements. Note that, in contrast to computing quasi-periodic orbits in the CR3BP, the rotation angle and the mapping time are not included as free variables for this transition process. The mapping time is constant for all 2-dimensional quasi-periodic orbits in the BCR4BP since it is tied to the synodic period of the system. The rotation angle remains constant when continuing a solutions from $\varepsilon = 0$ to $\varepsilon = 1$. The constraint vector is defined,

$$\boldsymbol{F} = \begin{bmatrix} \vec{u}_1^{t,R} - \vec{u}_1 \\ \vec{u}_2^{t,R} - \vec{u}_2 \\ \vdots \\ \vec{u}_{N-1}^{t,R} - \vec{u}_{N-1} \\ \vec{u}_N^{t,R} - \vec{u}_N \\ \vdots \\ F_{\theta_1} \end{bmatrix} \tag{3.46}$$

where the first $6N$ elements in the constraint vector represent the invariance constraint, defined in Equation (3.5) and F_{θ_1} is the scalar latitudinal phasing constraint to ensure that a new torus is computed rather than a phase shifted location around the current invariant curve. As Olikara and Scheeres note, there is no need for a phasing constraint on θ_0 since the system frequency equal to $\dot{\theta}_0$[26]. This differential corrections strategy is extendable to a multiple shooting formulation as well. Note that the constraint vector includes $6N + 1$ elements prior to inclusion of the pseudo-arclength constraint; however, the phase constraint is not a unique property of the torus. Consequently, including the phase constraint does not over-constrain the differential corrections problem. Also note that the partial derivative of the invariance constraint with respect to ε is evaluated as,

$$\frac{\partial \boldsymbol{F}_{\text{invar}}}{\partial \varepsilon} = \boldsymbol{R}_{-\rho} \frac{\partial \boldsymbol{U}^t}{\partial \varepsilon} \tag{3.47}$$

where the term $\frac{\partial \boldsymbol{U}^t}{\partial \varepsilon}$ is the partial derivative of the discretized states at the first return to the stroboscopic map with respect to ε. As mentioned in Section 2.6, evaluation of these partial derivatives relies on numerical integration of the variational equations of motion with respect to ε. The continuation process for the L_1 Lyapunov orbit in the BCR4BP is plotted as a grey surface and the invariant curve is plotted in blue in Figure 3.5b. It is possible to compute the same orbit using Method 1; however, not all periodic orbits in the CR3BP possess a unique, equivalent quasi-periodic analog in the BCR4BP.

Quasi-Periodic Orbits in the Vicinity of L_1

As noted by Jorba et al. and demonstrated in Section 2.6, there exists a unique orbit in the BCR4BP that is dynamically equivalent to the L_1 libration point from the CR3BP [63]. From Table 3.1, the dynamically equivalent L_1 orbit has two pairs of complex, unit magnitude eigenvalues. Subsequently, there are two unique families of quasi-periodic orbits that exist in the vicinity of this periodic orbit: a planar quasi-Lyapunov family and a spatial family of orbits denote the quasi-vertical family. A few members of the quasi-Lyapunov and quasi-vertical families are rendered in Figure 3.6. The quasi-vertical family retains a similar geometry to quasi-vertical orbits in the CR3BP. The stability index of these orbits is plotted

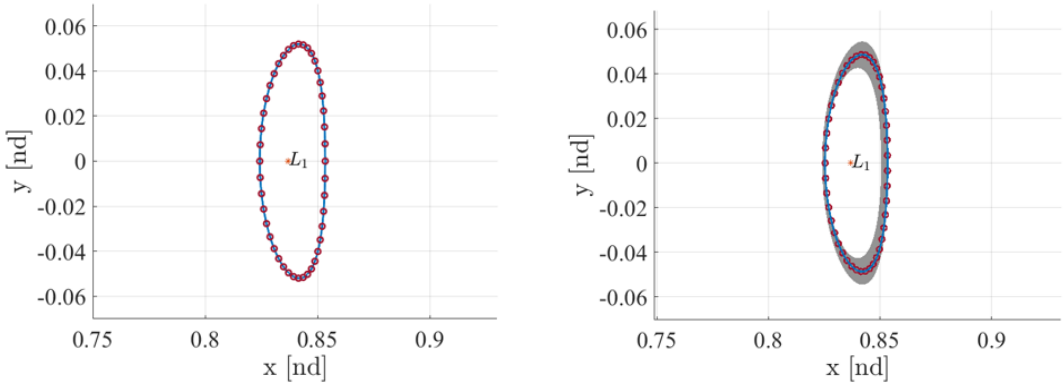

Figure 3.5. Torus representation of a planar periodic Lyapunov orbit when (a) $\varepsilon = 0$ and (b) $\varepsilon = 1$.

for each family in Figure 3.7. The members of both families are unstable since the stability index $\nu > 1$. The quasi-Lyapunov family includes a bifurcation to the L_1 quasi-halo family; The bifurcating orbit is highlighted in blue in Figure 3.6a. Similar to the CR3BP, there are northern and southern quasi-halo families in the BCR4BP. Members of the northern quasi-halo family are plotted in Figure 3.8a.

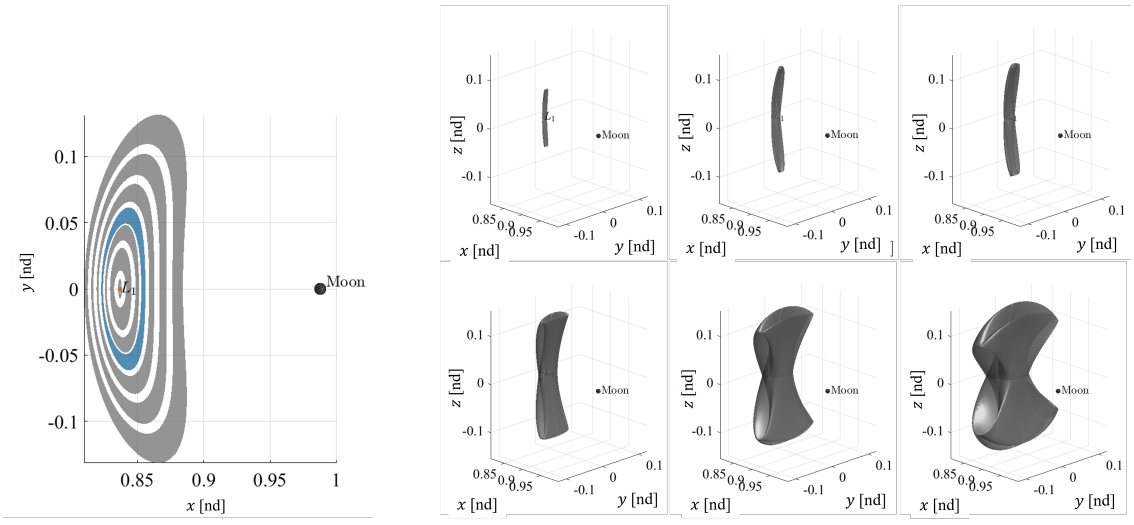

Figure 3.6. Members of the L_1 quasi-Lyapunov family (left) and the L_1 quasi-vertical family (right). The quasi-Lyapunov orbit highlighted in blue is the bifurcating orbit to the L_1 quasi-halo family.

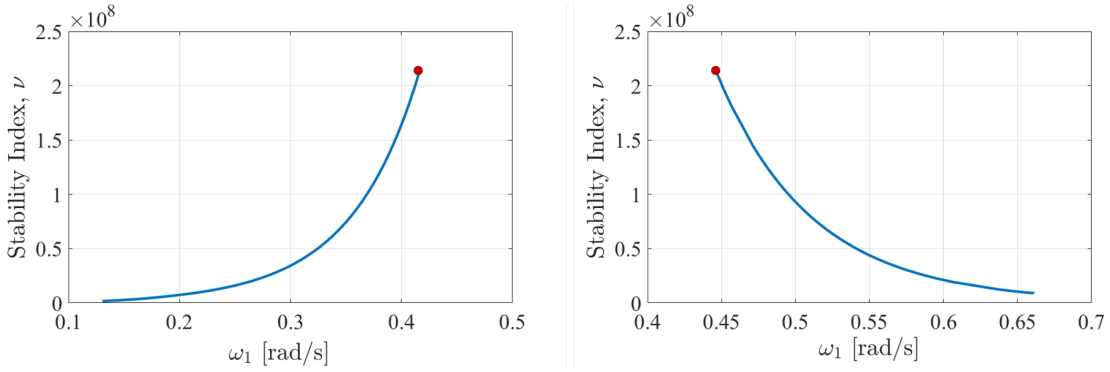

Figure 3.7. Stability index computed for the L_1 quasi-Lyapunov orbit family (left) and the L_1 quasi-vertical family (right). The red dot indicates the start of the family where it bifurcates from the dynamically equivalent L_1 orbit in the BCR4BP.

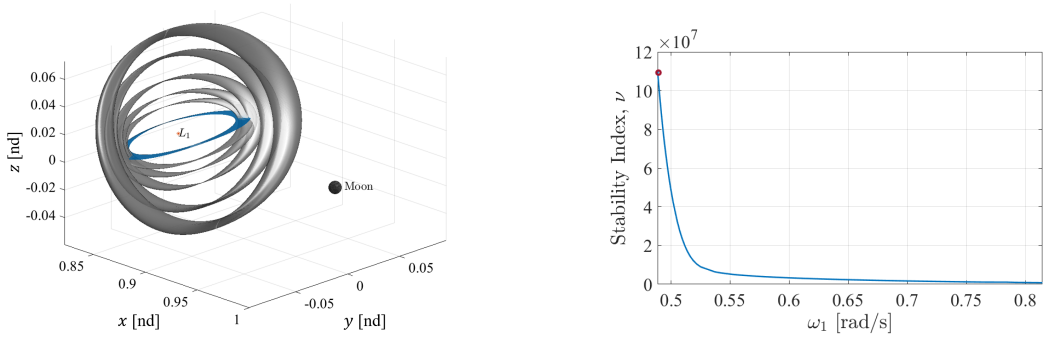

a b

Figure 3.8. (a) Members of the L_1 northern quasi-Lyapunov family; the bifurcating Lyapunov orbit is highlighted in blue (a). Stability index for the L_1 quasi-halo family as a function of latitudinal frequency (b). The origin of the family at the bifurcating quasi-Lyapunov orbit is indicated by the red dot.

Quasi-Periodic Orbits in the Vicinity of L_2

In contrast to the L_1 libration point, there is no unique dynamical equivalent for the L_2 point in the BCR4BP as the system evolves from the Earth-Moon CR3BP, as demonstrated in Section 2.6. The L_2 point is transitioned to a 2:1 resonant periodic Lyapunov orbit and the eigenvalues associated with this orbit are listed in Table 3.1. Note that, in contrast to the dynamically equivalent L_1 orbit, there is a single pair of complex, unit magnitude eigenvalues that correspond to the planar L_2 quasi-Lyapunov family. A few members of the

L_2 quasi-Lyapunov family are rendered in Figure 3.9. Note that members of the L_2 family appear to all overlap with one another and the y-amplitude of the torus in configuration space increases as ρ decreases, whereas the orbits in the L_1 quasi-Lyapunov family emanate from the dynamically equivalent L_1 orbit. Additionally, all of the members of the L_2 quasi-Lyapunov family are unstable.

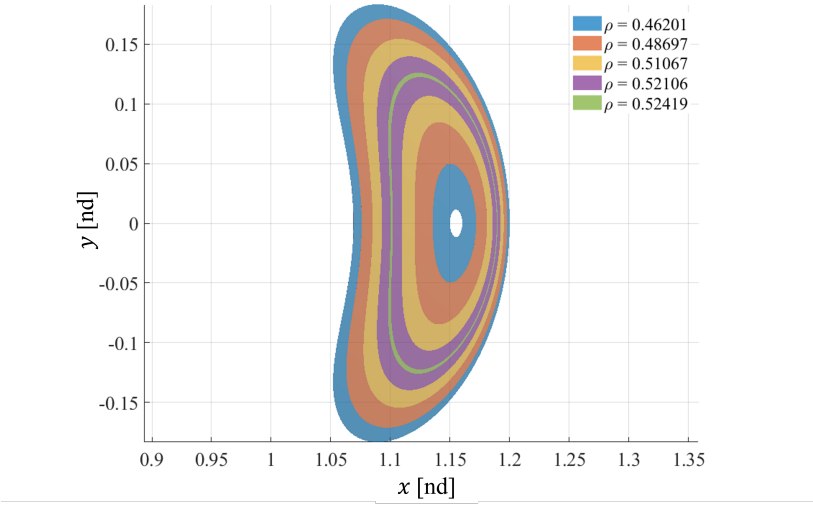

Figure 3.9. L_2 quasi-Lyapunov family.

Given that the stability changes during the continuation of the CR3BP L_2 point to the BCR4BP, as noted in Figure 2.13b, the precise locations of these bifurcations may be insightful. Consider the stability change where $\varepsilon \approx 0.287$, i.e., the stability transitions from a single saddle mode to two saddle modes. Following this bifurcation, ε returns to zero, $\varepsilon \to 0$, and the resultant dynamical structure is an L_2 halo orbit with a period equal to double the synodic period, indicating a 2:1 synodic resonance. Since the orbital period is in resonance with the synodic period, an equivalent periodic orbit in the BCR4BP ($\varepsilon = 1$) exists. After transitioning this 2:1 synodic resonant halo orbit to the BCR4BP using the same free variable/constraint method with Equations (2.92) and (2.93), the eigenvalues associated with the monodromy matrix of the orbit are examined. The monodromy matrix possesses two complex conjugate pairs of eigenvalues, all of unit magnitude. The two families of quasi-halo orbits associated with each pair are computed and a few members of each family are

plotted in Figure 3.10. Both quasi-halo orbit families bifurcate from the same periodic orbit, however, the characteristics of each family differ. The quasi-halo family rendered in Figure 3.10a appears similar to L_2 quasi-halo orbits in the CR3BP [60]. However, the quasi-halo family plotted in Figure 3.10b evolves to a different type of behavior than the quasi-halo motion in the Earth-Moon CR3BP. The hodograph of the rotation angle as a function of the x-component where $\theta_0 = \theta_1 = 0$ along the torus is plotted in Figure 3.11b; the red dot indicates the origin of the family. An example of a trajectory arc from one of the family members is plotted in Figure 3.11a; the torus associated with this trajectory is denoted by the gold dot on the plot in Figure 3.11b. Note that the behavior of the quasi-periodic trajectory in Figure 3.11a appears to include Lissajous motion combined with quasi-halo arcs since solar perturbations have been introduced. This is more apparent when the $\hat{z}$-component of position is plotted as a function of time in Figure 3.12. The smaller oscillations in the $\hat{z}$-component indicate the Lissajous-type motion and the larger oscillations indicate the traditional quasi-halo type motion. Subsequently, the dynamical environment near the Earth-Moon L_2 region, when perturbed by the Sun, possesses unique structured motion that can be leveraged for trajectory design.

As Rosales notes, the L_2 region is much more dynamically sensitive to solar perturbations in the BCR4BP; subsequently, solutions may be more challenging to compute by following bifurcations from the periodic 2:1 L_2 halo and Lyapunov orbits in the BCR4BP [64]. To examine other analogous structures from the CR3BP that evolve into the BCR4BP, continuation in Sun mass from the CR3BP to the BCR4BP is investigated. Consider a low amplitude L_2 periodic vertical orbit in the Earth-Moon CR3BP. Using the Sun mass continuation method, this periodic vertical orbit is transitioned from the CR3BP ($\varepsilon = 0$) to a quasi-periodic orbit in the BCR4BP ($\varepsilon = 1$). The periodic vertical orbit from the CR3BP (blue) and the corresponding quasi-vertical orbit (grey) in the BCR4BP are plotted together in the Earth-Moon rotating frame in Figure 3.13a. Additionally, ε is plotted as a function of the $\hat{x}$-position coordinate when $\theta_1 = \theta_0 = 0$. The red dot indicates the initial low-amplitude vertical orbit in the CR3BP. Note that the curve in ε follows a similar pattern to the L_2 point continuation from Figure 2.13b where ε initially decreases to become negative, before becoming positive and transitioning to the full BCR4BP. The yellow dot highlights the con-

tinuation process as it passes through the CR3BP again ($\varepsilon = 0$). The dynamical structure in this instance is a quasi-vertical torus in the CR3BP where one of the fundamental frequencies is equal to the synodic frequency. After computing this single quasi-vertical orbit in the BCR4BP, the pseudo-arclength continuation process begins using the GMOS algorithm. A few members of the quasi-vertical family are rendered in Figure 3.14. Note that the flat quasi-vertical orbit (left) in Figure 3.14 is near the bifurcation to the quasi-Lyapunov orbit

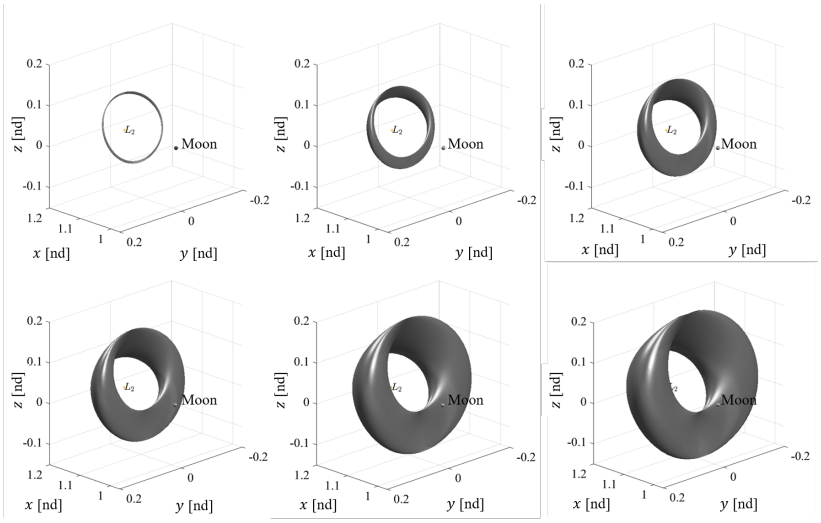

Figure 3.10. Members of two families of L_2 quasi-halo orbits that bifurcate from the 2:1 resonant L_2 halo orbit. The family rendered in (a) evolves toward the Moon, while the family rendered in (b) evolves away from the Moon.

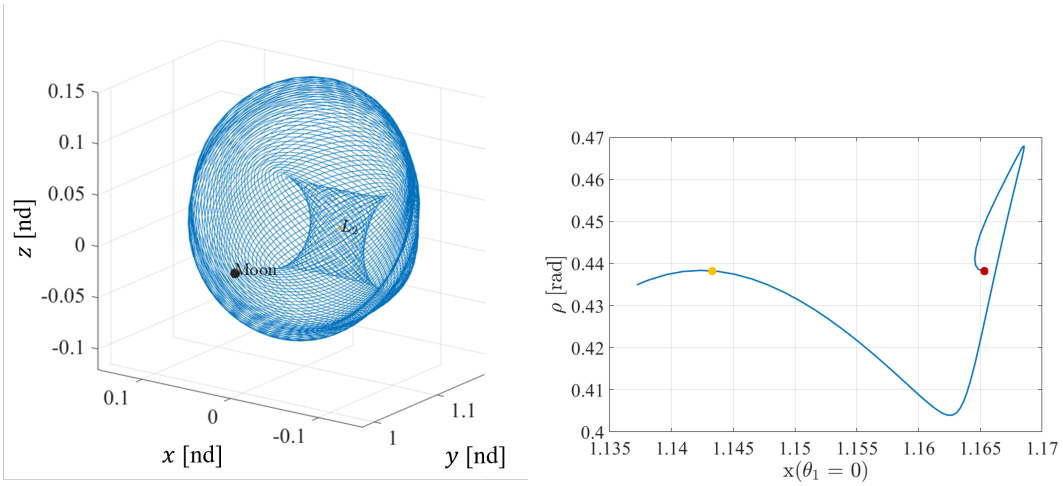

a b

Figure 3.11. (a) Trajectory arc propagated on an L_2 quasi-halo orbit with a rotation angle $\rho = 0.43814$. (b) Hodograph of the rotation angle vs the x-component of the torus where $\theta_0 = \theta_1 = 0$ for the quasi-halo family represented in Figure 3.10b.

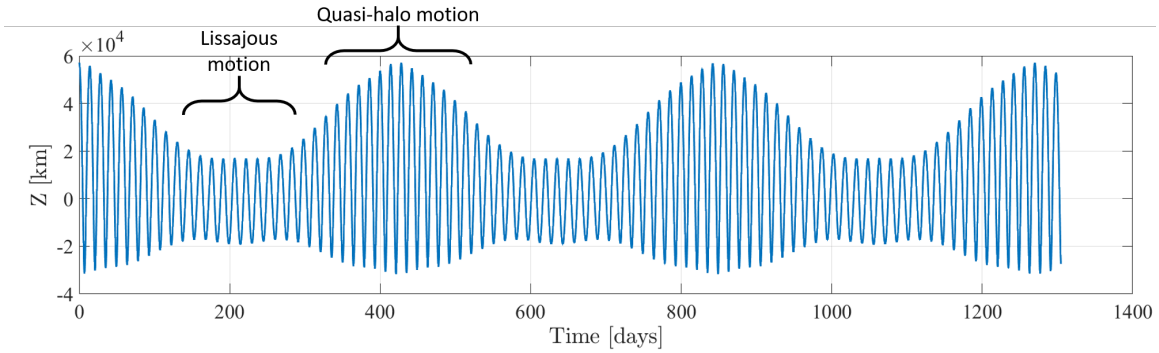

Figure 3.12. The $\hat{z}$-component of the trajectory from Figure 3.11a as a function of time. The trajectory is propagated for 1300 days.

family, as noted by Rosales [64]. Using the technique for the continuation in Sun mass reveals additional properties associated with the motion in the vicinity of the Sun-perturbed L_2 region.

Transitioning solutions through continuation in Sun mass supplies useful information concerning the dynamics in the cislunar region; however, challenges arise when attempting to transition some types of solutions. The GMOS algorithm relies on a Fourier series to represent the invariant curve and an assumption associated with the Fourier series is that a

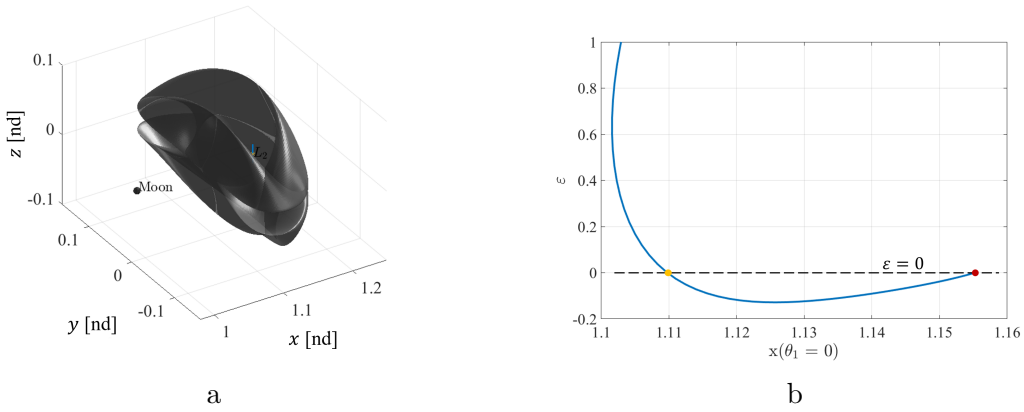

Figure 3.13. A low amplitude periodic vertical orbit from the CR3BP (blue) that is transitioned to a quasi-vertical orbit in the BCR4BP (grey) (a). The Sun mass scaling parameter, ε, plotted as a function of the x-component of each torus where $\theta_0 = \theta_1 = 0$ through the continuation process.

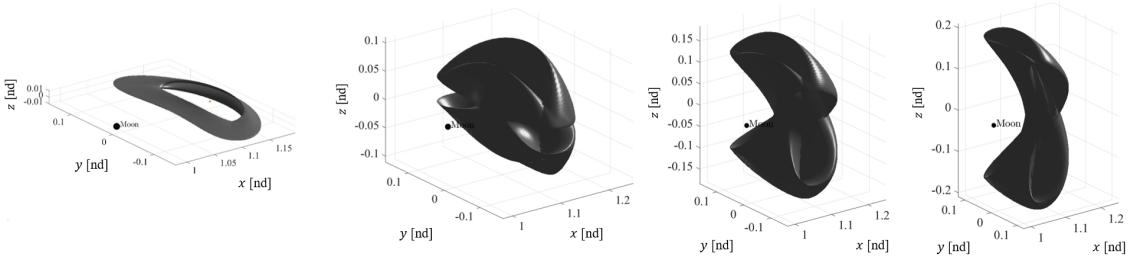

Figure 3.14. Members of the L_2 quasi-vertical family.

reasonable number of states can represent the invariant curve via a discrete Fourier transform. When the geometry of the invariant curve becomes too complex, the number of points required to accurately represent the curve becomes infeasible and the continuation process cannot proceed. This highlights the limitations of formulating the invariant curve using a Fourier series.

3.2 Computation of 3-D Quasi-Periodic Tori

Quasi-periodic motion that is characterized by a 3D torus possesses three fundamental frequencies. These three frequencies characterize the behavior on a higher-dimensional surface that bounds the motion. In the CR3BP, 3D tori bifurcate from the center subspace of a

2D torus or from periodic orbits possessing a 4-dimensional (4D) center subspace (i.e., two unique pairs of complex eigenvalues of unit magnitude). This investigation focuses on the latter but is directly applicable to the former. Challenges exist in rendering the projection of the torus in configuration space, since the initial condition set is a surface. In addition, computing 3D quasi-periodic tori is computationally intensive due to the number of elements of the Jacobian matrix in the differential corrections procedure and the number of numerical integrations required to sufficiently capture the flow of the torus. However, understanding the properties provided by 3D tori offers additional insight into motion in the lunar vicinity. In the following discussion, the algorithms of Gómez and Mondelo and of Olikara and Scheeres used to compute 3D tori are reviewed [25], [26]. This approach to computing 3D tori is also similar to the algorithm developed by Baresi and Scheeres to investigate 3D tori about a complex rotator asteroid [37].

3.2.1 Correction Algorithm

In a manner similar to computing 2D tori, a scheme for computing 3D tori is investigated using a stroboscopic mapping technique and formulated as a free-variable/constraint differential corrections scheme. The stroboscopic mapping time for 3D tori is defined in the same manner as for 2D tori in Equation (3.1). However, 3D tori are parameterized by the two rotation angles of ρ and η. The rotation angle ρ is defined exactly as for a 2D torus. Then, the additional angle η is defined as

$$\eta = \frac{2\pi\dot{\theta}_2}{\dot{\theta}_0} = T_0\dot{\theta}_2 \tag{3.48}$$

where $\dot{\theta}_2$ is the third fundamental frequency. In the same manner that states along the invariance curve for 2D tori are discretized, the initial set of states for a 3D torus is discretized into NM states on an invariant surface, since two angles of rotation exist, where i $= 1, 2, ..., N$ and j $= 1, 2, ..., M$. Figure 3.15 illustrates the basis for discretization of the states on a 3D

torus. For each return to the stroboscopic map, the two rotation angles are defined by ρ and η, and a single state is then parameterized by three angles such that

$$\boldsymbol{u}_{\mathrm{i,j}}(\theta_0, \theta_{1\mathrm{i}}, \theta_{2\mathrm{j}}) = \boldsymbol{u}_{\mathrm{i,j}}(\theta_0 + 2\pi, \theta_{1\mathrm{i}} - \rho, \theta_{2\mathrm{j}} - \eta) \tag{3.49}$$

which is rewritten using the stroboscopic mapping time in place of θ_0:

$$\vec{u}_{\mathrm{i,j}}(0, \theta_{1\mathrm{i}}, \theta_{2\mathrm{j}}) = \vec{u}_{\mathrm{i,j}}(T_0, \theta_{1\mathrm{i}} - \rho, \theta_{2\mathrm{j}} - \eta) \tag{3.50}$$

An invariance constraint is developed in a similar manner as the invariance constraint for a 2D torus, but the rotation operator is dependent on both rotation angles, that is,

$$\boldsymbol{R}_{-\rho,-\eta}\vec{u}_{\mathrm{i,j}}(T_0, \theta_{1\mathrm{i}}, \theta_{2\mathrm{j}}) - \vec{u}_{\mathrm{i,j}}(0, \theta_{1\mathrm{i}}, \theta_{2\mathrm{j}}) = \mathbf{0} \tag{3.51}$$

where $\boldsymbol{R}_{-\rho,-\eta}$ is the rotation operator that removes the rotations by both ρ and η at the first return to the stroboscopic map.

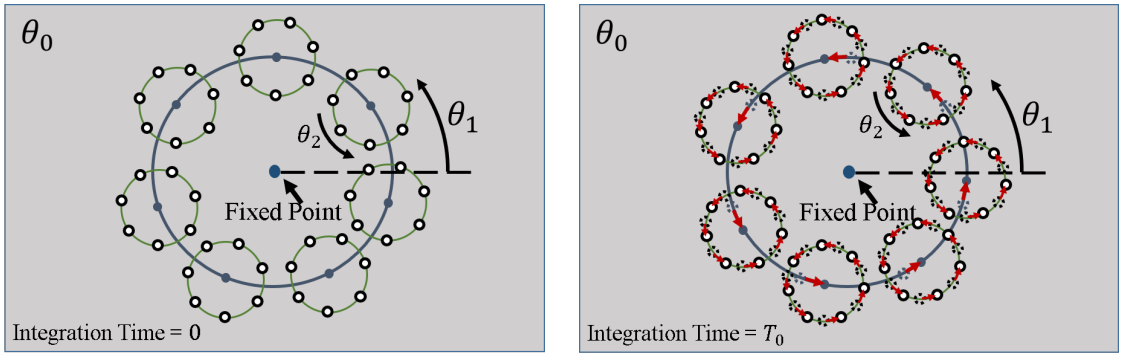

a b

Figure 3.15. Set of 49 discretized states (white) on the invariant curve, as represented by the blue circle. The invariant curve is associated with the stroboscopic map defined at θ_0. The initial location of the states is represented in (a). The first return to the map, at time T_0, is represented in (b), where the states have rotated by ρ. The nearby periodic orbit is represented by the fixed point on the map.

The computation of families for 3D tori is implemented by employing a free-variable and constraint method, where the eigenvectors and eigenvalues associated with the center

subspace are used to generate an initial guess. For periodic orbits whose monodromy matrix possesses two pairs of complex eigenvalues each of unit magnitude, an initial guess for the states on the invariant surface is evaluated as

$$\begin{aligned}\vec{u}^{0}_{\mathrm{i,j}} = \epsilon_1(\mathrm{Re}[\vec{v}_{C,1}]\cos(\theta_{1\mathrm{i}}) - \mathrm{Im}[\vec{v}_{C,1}]\sin\theta_{1\mathrm{i}}) \\ + \epsilon_2(\mathrm{Re}[\vec{v}_{C,2}]\cos(\theta_{2\mathrm{j}}) - \mathrm{Im}[\vec{v}_{C,2}]\sin\theta_{2\mathrm{j}})\end{aligned} \tag{3.52}$$

where $\vec{v}_{C,1}$ and $\vec{v}_{C,2}$ are two unique eigenvectors associated with the center subspace, $\mathrm{Re}[\,\bullet\,]$ and $\mathrm{Im}[\bullet]$ denote the real and imaginary parts, respectively, of the vector inside the brackets, and ϵ_1 and ϵ_2 are small values. Creating vectors for the set of angles that define each of the initial conditions takes the following form:

$$\vec{\theta}_1 = \begin{bmatrix} 0 & \frac{2\pi}{N} & \frac{4\pi}{N} & \dots & \frac{2\pi(N-2)}{N} & \frac{2\pi(N-1)}{N} \end{bmatrix} \tag{3.53}$$

$$\vec{\theta}_2 = \begin{bmatrix} 0 & \frac{2\pi}{M} & \frac{4\pi}{M} & \dots & \frac{2\pi(M-2)}{M} & \frac{2\pi(M-1)}{M} \end{bmatrix} \tag{3.54}$$

The period of the underlying periodic orbit is used as the stroboscopic mapping initial guess, T_0^0. The initial guess for each rotation angle is defined by the angular location of the unique center eigenvalues on the unit circles, that is, $\lambda_{C,1}$ and $\lambda_{C,2}$:

$$\rho^0 = \tan^{-1}\left(\frac{\mathrm{Im}[\lambda_{C,1}]}{\mathrm{Re}[\lambda_{C,1}]}\right) \tag{3.55}$$

$$\eta^0 = \tan^{-1}\left(\frac{\mathrm{Im}[\lambda_{C,2}]}{\mathrm{Re}[\lambda_{C,2}]}\right) \tag{3.56}$$

For small values of ϵ_1 and ϵ_2, the approximations for ρ^0, η^0, T_0^0, and $\vec{u}_{\mathrm{ij}}^0$ supply a sufficient initial guess for elements of the free-variable vector in the differential corrections scheme. The free-variable vector is defined as

$$\boldsymbol{X} = \begin{bmatrix} \vec{u}_{1,1} \\ \vec{u}_{1,2} \\ \vdots \\ \vec{u}_{1,M} \\ \vec{u}_{2,1} \\ \vdots \\ \vec{u}_{N,M} \\ T_0 \\ \rho \\ \eta \end{bmatrix} \tag{3.57}$$

where $\vec{u}_{\mathrm{i,j}} = \begin{bmatrix} u_{x,(\mathrm{i,j})} & u_{y,(\mathrm{i,j})} & u_{z,(\mathrm{i,j})} & u_{\dot{x},(\mathrm{i,j})} & u_{\dot{y},(\mathrm{i,j})} & u_{\dot{z},(\mathrm{i,j})} \end{bmatrix}^T$ is the $(\mathrm{i}^{\mathrm{th}}, \mathrm{j}^{\mathrm{th}})$ discretized 6-element state vector on the invariant surface. The free-variable vector is of size $6NM + 3$. The constraint vector is constructed with the invariance constraint for a 3D torus, a Jacobi constant constraint, and a final constraint on one of the three parameters that defines a 3D torus, that is, ρ, η, or T_0. For a representative example of a corrections problem in the CR3BP, the

mapping time is constrained to equal the period of the underlying periodic orbit T_{0d} such that the constraint vector is defined,

$$\boldsymbol{F} = \begin{bmatrix} \vec{u}_{1,1}^{t,R} - \vec{u}_{1,1} \\ \vec{u}_{1,2}^{t,R} - \vec{u}_{1,2} \\ \vdots \\ \vec{u}_{1,M}^{t,R} - \vec{u}_{1,M} \\ \vec{u}_{2,1}^{t,R} - \vec{u}_{2,1} \\ \vdots \\ \vec{u}_{N,M}^{t,R} - \vec{u}_{N,M} \\ JC_{\text{avg}} - JC_d \\ T_0 - T_{0d} \end{bmatrix} \tag{3.58}$$

where $\vec{u}_{\text{i,j}}^{t,R}$ represents the $(\text{i}^{\text{th}}, \text{j}^{\text{th}})$ discretized state on the invariant surface propagated to the first return of the stroboscopic map with the rotation removed. The term JC_{avg} is the average Jacobi constant value over the states on the invariant surface, defined by

$$JC_{\text{avg}} = \frac{1}{NM} \sum_{\text{i}=1}^{N} \sum_{\text{j}=1}^{M} JC_{\text{i,j}} \tag{3.59}$$

where $JC_{\text{i,j}}$ is the Jacobi constant for the $(\text{i}^{\text{th}}, \text{j}^{\text{th}})$ state on the invariant surface.

The rotation operator used in formulating the invariance constraint is constructed using a 2D Fourier series. First, the matrix D is constructed using a 2D Fourier series expression as follows:

$$\boldsymbol{D} = \frac{1}{NM} \left(\text{e}^{-\text{i}\vec{k}^T\vec{\theta}_1} \otimes \text{e}^{-\text{i}\vec{m}^T\vec{\theta}_2} \right) \tag{3.60}$$

where $\otimes$ is the Kronecker product operator, $\vec{\theta}_1$ and $\vec{\theta}_2$ are defined in Equations (3.53) and (3.54), respectively, and $\vec{k}$ and $\vec{m}$ are row vectors defined by

$$\vec{k} = \begin{bmatrix} -\frac{N-1}{2} & \dots & -1 & 0 & 1 & \dots & \frac{N-1}{2} \end{bmatrix} \tag{3.61}$$

$$\vec{m} = \begin{bmatrix} -\frac{M-1}{2} & \dots & -1 & 0 & 1 & \dots & \frac{M-1}{2} \end{bmatrix} \tag{3.62}$$

where N and M are odd-valued. The rotation operator for a 3D torus $\boldsymbol{R}_{-\rho,-\eta}$ is defined using the 2D discrete Fourier transform:

$$\boldsymbol{R}_{-\rho,-\eta} = \boldsymbol{D}^{-1}\boldsymbol{Q}_{-\rho,-\eta}\boldsymbol{D} \tag{3.63}$$

where the diagonal matrix $\boldsymbol{Q}_{-\rho,-\eta}$ is defined by

$$\boldsymbol{Q}_{-\rho,-\eta} = \text{diag}[\text{e}^{-\text{i}\vec{k}\rho}] \otimes \text{diag}[\text{e}^{-\text{i}\vec{m}\eta}] \tag{3.64}$$

The rotation matrix is dense and of size $NM \times NM$. When the states propagated from the initial invariant surface are arranged such that they reside in a $NM \times 6$ matrix, the rotations by ρ and η are removed using the rotation operator from Equation (3.63):

$$\boldsymbol{U}^{t,R} = \boldsymbol{R}_{-\rho,-\eta}\boldsymbol{U}^{t} \tag{3.65}$$

where $\boldsymbol{U}^{t}$ is the $NM \times 6$ matrix, and each row is a state vector from the invariant surface after being propagated to the first return of the stroboscopic map. The formulation of the invariance constraint provides the basis for numerically computing a 3D torus.

The Jacobian matrix is constructed in a manner similar to that for the 2D torus corrections scheme. First, the partial derivatives of the invariance constraints with respect to the initial states on the invariant surface are defined as

$$\frac{\partial(\boldsymbol{u}^{t,R} - \boldsymbol{u})}{\partial \boldsymbol{u}} = \frac{\partial \boldsymbol{u}^{t,R}}{\partial \boldsymbol{u}} - \frac{\partial \boldsymbol{u}}{\partial \boldsymbol{u}} = (\boldsymbol{R}_{-\rho,-\eta} \otimes \boldsymbol{I})\tilde{\tilde{\boldsymbol{\Phi}}} - \tilde{\tilde{\boldsymbol{I}}} \tag{3.66}$$

where $\tilde{\tilde{\boldsymbol{I}}}$ is an identity matrix of size $6NM \times 6NM$, $\otimes$ is the Kronecker product operator, and $\tilde{\tilde{\boldsymbol{\Phi}}}$ is a block diagonal matrix of the STMs of size $6NM \times 6NM$, which takes the following form:

$$\tilde{\tilde{\boldsymbol{\Phi}}} = \begin{bmatrix} \boldsymbol{\Phi}_{1,1}(T_0,0) & \mathbf{0_{6\times 6}} & \dots & \mathbf{0_{6\times 6}} & \mathbf{0_{6\times 6}} & \dots & \mathbf{0_{6\times 6}} \\ \mathbf{0_{6\times 6}} & \boldsymbol{\Phi}_{1,2}(T_0,0) & \dots & \mathbf{0_{6\times 6}} & \mathbf{0_{6\times 6}} & \dots & \mathbf{0_{6\times 6}} \\ \vdots & \vdots & \ddots & \vdots & \vdots & \vdots & \vdots \\ \mathbf{0_{6\times 6}} & \mathbf{0_{6\times 6}} & \dots & \boldsymbol{\Phi}_{1,M}(T_0,0) & \mathbf{0_{6\times 6}} & \dots & \mathbf{0_{6\times 6}} \\ \mathbf{0_{6\times 6}} & \mathbf{0_{6\times 6}} & \dots & \mathbf{0_{6\times 6}} & \boldsymbol{\Phi}_{2,1}(T_0,0) & \dots & \mathbf{0_{6\times 6}} \\ \vdots & \vdots & \vdots & \vdots & \vdots & \ddots & \vdots \\ \mathbf{0_{6\times 6}} & \mathbf{0_{6\times 6}} & \dots & \mathbf{0_{6\times 6}} & \mathbf{0_{6\times 6}} & \dots & \boldsymbol{\Phi}_{N,M}(T_0,0) \end{bmatrix} \tag{3.67}$$

where $\boldsymbol{\Phi}_{\mathrm{i,j}}(T_0,0)$ is the STM from the $(\mathrm{i^{th}}, \mathrm{j^{th}})$ initial state on the invariant surface propagated to the first return of the map at time T_0. The invariance constraint with respect to the mapping time is simply the time derivative of the states at the first return to the map with the rotation removed, as given in Equation (3.23). The partial derivatives of the invariance constraint with respect to the rotation angles are defined as

$$\frac{\partial \boldsymbol{u}^{t,R}}{\partial \rho} = \boldsymbol{D}^{-1} \frac{\partial \boldsymbol{Q}_{-\rho,-\eta}}{\partial \rho} \boldsymbol{D}\boldsymbol{U}^t \tag{3.68}$$

$$\frac{\partial \boldsymbol{u}^{t,R}}{\partial \eta} = \boldsymbol{D}^{-1} \frac{\partial \boldsymbol{Q}_{-\rho,-\eta}}{\partial \eta} \boldsymbol{D}\boldsymbol{U}^t \tag{3.69}$$

where the terms $\frac{\partial \boldsymbol{Q}_{-\rho,-\eta}}{\partial \rho}$ and $\frac{\partial \boldsymbol{Q}_{-\rho,-\eta}}{\partial \eta}$ are defined as

$$\frac{\partial \boldsymbol{Q}_{-\rho,-\eta}}{\partial \rho} = (\mathrm{diag}[\vec{k}]\mathrm{diag}[-\mathrm{i}e^{-\mathrm{i}\vec{k}\rho}]) \otimes \mathrm{diag}[e^{-\mathrm{i}\vec{m}\eta}] \tag{3.70}$$

$$\frac{\partial \boldsymbol{Q}_{-\rho,-\eta}}{\partial \eta} = \mathrm{diag}[e^{-\mathrm{i}\vec{k}\rho}] \otimes (\mathrm{diag}[\vec{m}]\mathrm{diag}[-\mathrm{i}e^{-\mathrm{i}\vec{m}\eta}]) \tag{3.71}$$

Just as the invariance constraints are rearranged from a $NM \times 6$ matrix to a $6NM$ vector, the partial derivatives are rearranged from a $NM \times 6$ matrix to a $6NM \times 1$ submatrix that is inserted into the Jacobian matrix. The Jacobian matrix takes the same form as Equation

(3.29) but now with size $6NM+2\times6NM+3$. However, phasing constraints are also required to ensure that the corrections algorithm converges on a unique torus for each family member.

For a 3D torus in the CR3BP, three phase constraints are required for θ_0, θ_1, and θ_2. Again, the phasing constraints emerge from the general form of the derivation in Olikara and Scheeres [26]. However, they are formulated in matrix notation for ease of implementation. The phase constraints for θ_0 and θ_1 are defined in Equations (3.30) and (3.31), whereas the phase constraint for θ_2 forms as an inner product between the states on the current invariant surface and the partial derivative for the set of states from the previous family member with respect to θ_2. However, the partial derivatives of the previous set of states $\tilde{\boldsymbol{U}}$ with respect to θ_0, θ_1, and θ_2 are defined as

$$\frac{\partial\tilde{\boldsymbol{U}}}{\partial\theta_0}=\frac{1}{\omega_0}\left(\frac{\partial\tilde{\boldsymbol{U}}}{\partial t}-\omega_1\frac{\partial\tilde{\boldsymbol{U}}}{\partial\theta_1}-\omega_2\frac{\partial\tilde{\boldsymbol{U}}}{\partial\theta_2}\right)=\frac{\tilde{T}_0}{2\boldsymbol{\pi}}\left(\dot{\tilde{\boldsymbol{U}}}-\frac{\tilde{\rho}}{\tilde{T}_0}\frac{\partial\tilde{\boldsymbol{U}}}{\partial\theta_1}-\frac{\tilde{\eta}}{\tilde{T}_0}\frac{\partial\tilde{\boldsymbol{U}}}{\partial\theta_2}\right) \tag{3.72}$$

$$\frac{\partial\tilde{\boldsymbol{U}}}{\partial\theta_1}=\left(\left(\mathrm{i}e^{\mathrm{i}\vec{\theta}_1^T\vec{k}}\mathrm{diag}[\vec{k}]\right)\otimes e^{\mathrm{i}\vec{\theta}_2^T\vec{m}}\right)\tilde{\boldsymbol{C}}_0 \tag{3.73}$$

$$\frac{\partial\tilde{\boldsymbol{U}}}{\partial\theta_2}=\left(e^{\mathrm{i}\vec{\theta}_1^T\vec{k}}\otimes\left(\mathrm{i}e^{\mathrm{i}\vec{\theta}_2^T\vec{m}}\mathrm{diag}[\vec{m}]\right)\right)\tilde{\boldsymbol{C}}_0 \tag{3.74}$$

where $\tilde{\rho}$ and $\tilde{\eta}$ are the rotation angles and $\tilde{T}_0$ is the mapping time from the previously converged family member. Next, $\tilde{\boldsymbol{C}}_0$ is the $NM\times6$ matrix of Fourier coefficients from the previously converged family member. The partial derivatives of the phase constraints for 3D tori are equal to the right side of the term for the inner product, as defined in Equations (3.72)-(3.74). Finally, the Jacobian matrix takes the following form:

$$\boldsymbol{DF}=\begin{bmatrix}\frac{\partial\boldsymbol{u}^{t,R}}{\partial\boldsymbol{u}} & \frac{\partial\boldsymbol{u}^{t,R}}{\partial T_0} & \frac{\partial\boldsymbol{u}^{t,R}}{\partial\rho} & \frac{\partial\boldsymbol{u}^{t,R}}{\partial\eta}\\ \frac{\partial JC_{avg}}{\partial\boldsymbol{u}} & 0 & 0 & 0\\ 0 & 1 & 0 & 0\\ \frac{\partial F_{\theta_0}}{\partial\boldsymbol{u}} & 0 & 0 & 0\\ \frac{\partial F_{\theta_1}}{\partial\boldsymbol{u}} & 0 & 0 & 0\\ \frac{\partial F_{\theta_2}}{\partial\boldsymbol{u}} & 0 & 0 & 0\end{bmatrix} \tag{3.75}$$

Note that the mapping time is a free variable and is included as a constraint in this formulation. The single-shooting formulation is also extendable to multiple shooting to aid in convergence when the torus passes close to a primary or when the stroboscopic mapping time is long. However, the numbers of free variables, constraints, and elements of the Jacobian matrix increase significantly when using a multiple-shooting algorithm. For example, in a single-shooting formulation where $N = 35$ and $M = 35$, the size of the Jacobian is 7352×7352. However, a multiple-shooting scheme that decomposes the torus into four segments increases the Jacobian size to 29402×29402. Jorba and Olmedo outlined challenges associated with computing higher-dimensional tori using a stroboscopic mapping technique [24].

3.2.2 3D Torus Families

In the CR3BP and the BCR4BP, periodic orbits exist over specified ranges in a family with two pairs of complex, unit magnitude eigenvalues. The Earth-Moon CR3BP L_2 halo orbit family includes a subset of orbits, with each possessing a 4-dimensional center subspace. Because a 3D quasi-periodic orbit in the CR3BP is uniquely defined by three parameters, a continuation scheme fixes two parameters and continues along the third. For example, a family of 3D quasi-periodic orbits with a fixed Jacobi Constant value and a fixed longitudinal period is computed from a halo orbit with a value of $JC = 3.0151782$ and orbit period of $T = 10.3288$ days, as plotted in the upper right corner in Figure 3.16. Because 3D tori are computed with a set of initial conditions that represent a surface, i.e., the invariant surface, they cannot be visualized in the same manner as 2D tori. To represent family members, initial conditions that represent the invariant surface are plotted for three members of a family in Figure 3.16, where the center blue dot represents the initial condition for the underlying periodic halo orbit. The arrow indicates the location in which the initial condition lies along the periodic orbit relative to the Moon in the Earth-Moon rotating frame. Similar to continuation for 2D torus families, 3D torus families experience complications when integer frequency ratios are encountered. However, three frequency ratios are examined during the continuation process: $\frac{\omega_0}{\omega_1}$, $\frac{\omega_0}{\omega_2}$, and $\frac{\omega_1}{\omega_2}$. If strong resonances (i.e., where the numerator

and denominator are close to 1) near any of these frequency ratios are encountered, the continuation algorithm halts. To avoid encountering integer frequency ratios, ρ and η are selected and constrained in the continuation algorithm. Fixed ρ and η values ensure that the frequency ratios remain constant for each member of the family, and integer ratios are avoided, provided that neither rotation angle is a multiple of 2π.

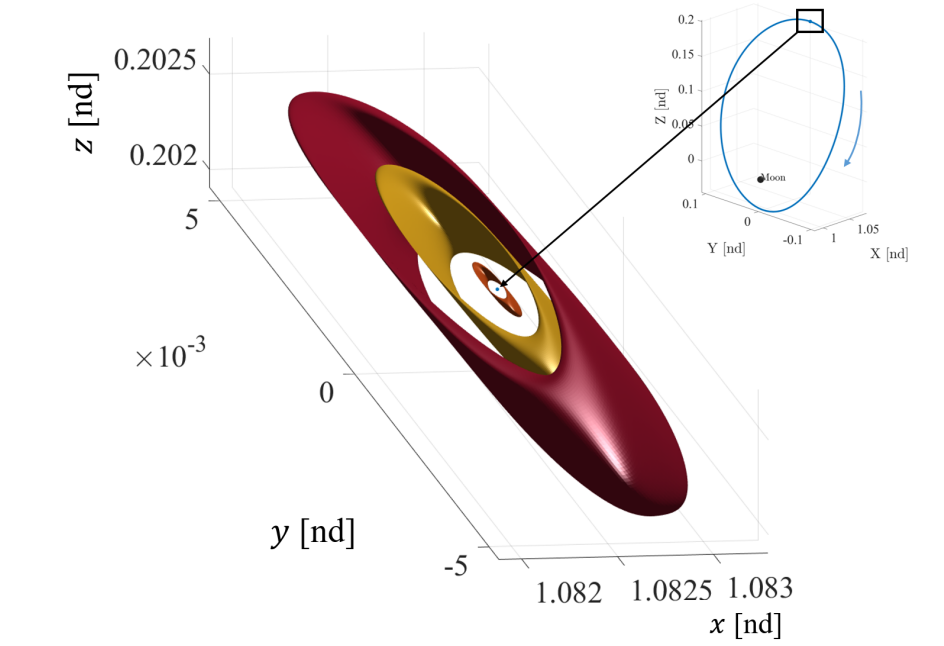

Figure 3.16. Initial invariant surfaces projected into configuration space representing three members of the 3D torus family, parameterized by $T_0 = 10.3288$ days and $JC = 3.0151782$. The blue arrow indicates the direction of motion.

In the BCR4BP, the dynamically equivalent L_1 orbit possesses two unique pairs of complex unit eigenvalues. A family of 3-dimensional tori exists in the vicinity of this structure as well. Since the BCR4BP does not possess an integral of the motion, the Jacobi Constant constraint is removed from the constraint vector from Equation (3.58). Additionally, since the system is periodically forced, the mapping time, T_0, is implicitly constrained. Thus, there are two parameters, i.e., $\dot{\theta}_1$ and $\dot{\theta}_2$, that define a member of a 3-dimensional torus family in the BCR4BP. To demonstrate a family of 3D tori in the BCR4BP, the average of the rotation angles is constrained, i.e., $\frac{\eta+\rho}{2} = 0$. A few of the invariant surfaces from the family

are rendered in Figure 3.17a as well as the underlying periodic orbit in blue. To further demonstrate the complexity of the motion, the state history for of a single trajectory for 430 days is rendered in Figure 3.17b. This type of toroidal motion captures the quasi-Lyapunov and quasi-vertical orbit motion found in the 2-dimensional tori in this region of space.

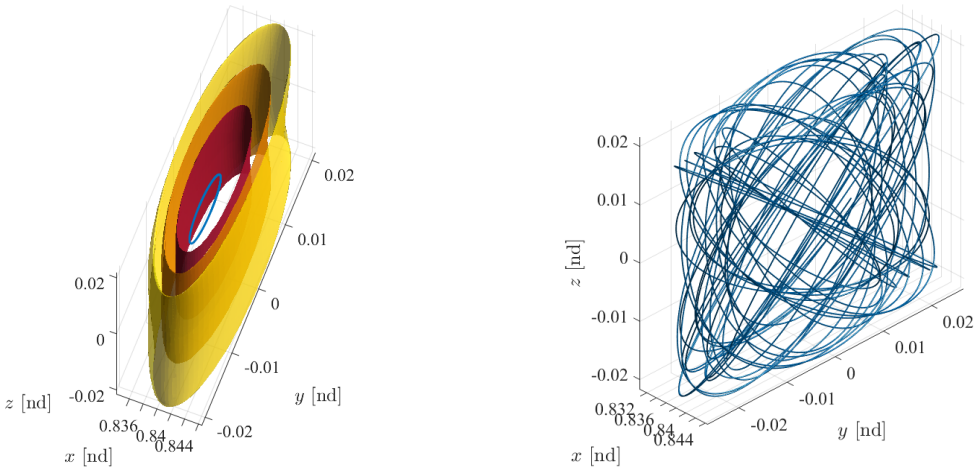

a b

Figure 3.17. (a) Initial invariant surfaces projected into configuration space representing three members of the 3D torus family in the L_1 region in the BCR4BP. (b) 3D torus trajectory propagated for 430 days in the BCR4BP.

3.3 Stability and Invariant Manifolds

Assessing the stability of orbits in the CR3BP and BCR4BP provides information on the motion in the vicinity of a given orbit and aids in discovering new types of solutions. Stability properties associated with quasi-periodic orbits are explored through the first order variations of the stroboscopic map. In particular, rather than assessing a fixed point (i.e., a periodic orbit), deviations from the invariant curve in the 2D-torus scenario and the invariant surface in the 3D-torus case are examined. In this investigation, a metric defined as a stability index is characterized for quasi-periodic orbits. For unstable quasi-periodic orbits, hyperbolic stable and unstable invariant manifolds exist that asymptotically approach and depart the torus corresponding to the given quasi-periodic orbit. Olikara and Scheeres previously examined stability and hyperbolic manifolds for 2D tori in the CR3BP, whereas

Baresi and Scheeres examined stability and hyperbolic manifolds for 3D tori in the vicinity of small bodies [26], [37]. This section characterizes stability, the stability index metric, and summarizes the computation of trajectories that represent stable and unstable hyperbolic manifolds.

Recall that the invariance constraint ensures that the initial states used to discretize the flow on a torus are equal to the states propagated over the mapping time after the rotation is removed. The partial derivative for the invariance constraint with respect to the states on the stroboscopic map yields

$$\boldsymbol{DG}_{2\mathrm{D}} = (\boldsymbol{R}_{-\rho} \otimes \boldsymbol{I})\tilde{\boldsymbol{\Phi}} \tag{3.76}$$

$$\boldsymbol{DG}_{3\mathrm{D}} = (\boldsymbol{R}_{-\rho,-\eta} \otimes \boldsymbol{I})\tilde{\tilde{\boldsymbol{\Phi}}} \tag{3.77}$$

where $\boldsymbol{R}_{-\rho}$ and $\boldsymbol{R}_{-\rho,-\eta}$ are the rotation operators for 2D and 3D tori, respectively, $\boldsymbol{I}$ is a 6×6 identity matrix, $\otimes$ is the Kronecker product operator, and $\tilde{\boldsymbol{\Phi}}$ and $\tilde{\tilde{\boldsymbol{\Phi}}}$ are defined in Equations (3.22) and (3.67), respectively. The resulting dense matrices represent the variations of the invariant curve on the stroboscopic map. The eigenstructure of $\boldsymbol{DG}$ offers information on the stability of the quasi-periodic orbit. Since the CR3BP and BCR4BP are reducible systems, as noted by Jorba, the eigenvalues of the $\boldsymbol{DG}$ matrix are related to a the eigenvalues of a transformation matrix [65]. The eigenvalues for 2D and 3D tori are related through the following relationships:

$$\boldsymbol{\lambda}_{2D} = \Lambda_r \mathrm{e}^{-\mathrm{i}\vec{k}\rho} \tag{3.78}$$

$$\boldsymbol{\lambda}_{3D} = \Lambda_r \left(\mathrm{e}^{-\mathrm{i}\vec{k}\rho} \otimes \mathrm{e}^{-\mathrm{i}\vec{m}\eta}\right) \tag{3.79}$$

where ρ and η are the rotation angles defined in Equations (3.2) and (3.48), and Λ_r is the r^{th} eigenvalue of the transformation matrix defined by Jorba in which $r = 1, 2, ..., 6$ [65]. The resulting $\boldsymbol{\lambda}$ are the eigenvalues of the matrix $\boldsymbol{DG}$, and $\vec{k}$ and $\vec{m}$ are defined in Equations (3.14) and (3.62), respectively.

Consider an L_2 quasi-halo orbit in the Earth-Moon CR3BP system, as rendered in Figure 3.18a. The eigenstructure for the $\boldsymbol{DG}$ matrix of the quasi-halo orbit is plotted on the complex

plane in Figure 3.18b. The eigenvalues exist on concentric circles about the origin in the complex plane. A circle with a radius greater than 1 is associated with the unstable mode of the torus, whereas a circle with a radius less than 1 reflects the stable mode. Furthermore, the stable mode radius is the reciprocal of the unstable mode radius, since the eigenvalues exist in reciprocal pairs for Hamiltonian systems [37], [56]. Given the concentric circle structure for the eigenvalues, a stability index ν is defined as

$$\nu = \frac{1}{2}\left(R_u + \frac{1}{R_u}\right) \tag{3.80}$$

where R_u is the radius of the circle associated with the unstable mode. Quasi-periodic orbits in which $\nu = 1$ are considered stable, whereas stability indices greater than 1 reflect an unstable orbit. The stability index for the quasi-halo orbit rendered in Figure 3.18a is $\nu = 1.3837$. The stability over the family of constant energy quasi-halo orbits ($JC = 3.1389$) is plotted as a function of mapping time in Figure 3.19. Note that the stability index appears linear across the mapping time for this family but is an artifact of the members of the family remaining in a region close to the underlying periodic orbit. The advantage of a scalar stability index is its appeal as a single, convenient metric to characterize linear stability for a given orbit. Stable and unstable quasi-periodic orbits are easily identified and the stability evolution across a family is represented as a single curve.

3.3.1 Hyperbolic Stable and Unstable Quasi-Periodic Manifolds

Hyperbolic stable and unstable invariant manifolds exist for quasi-periodic orbits that possess a stability index of $\nu > 1$. The stable and unstable hyperbolic manifolds asymptotically approach and depart the torus, respectively. To compute stable/unstable manifolds, the eigenvectors associated with the stable and unstable eigenvalues of $\boldsymbol{DG}$ are exploited. Selecting an eigenvalue on the stable/unstable circle with no imaginary components has a corresponding eigenvector that is purely real. The stable/unstable eigenvectors are denoted as $\vec{v}_{s,r}$ and $\vec{v}_{u,r}$, respectively. These eigenvectors are defined by $6N$ elements for a 2D torus

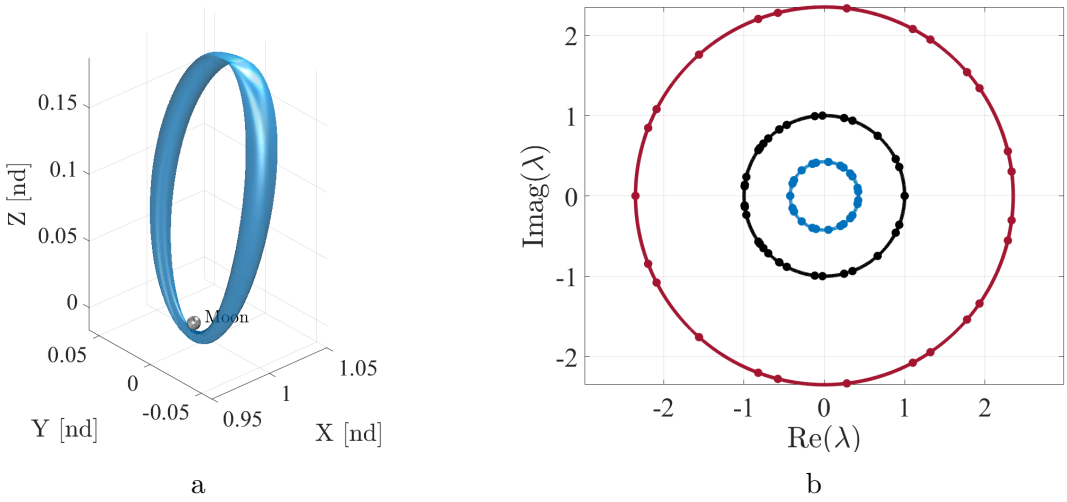

Figure 3.18. (a) Earth-Moon L_2 quasi-halo orbit in the CR3BP ($JC = 3.044$). (b) Eigenstructure of $\boldsymbol{DG}$ matrix corresponding to the quasi-halo orbit computed with $N = 25$.

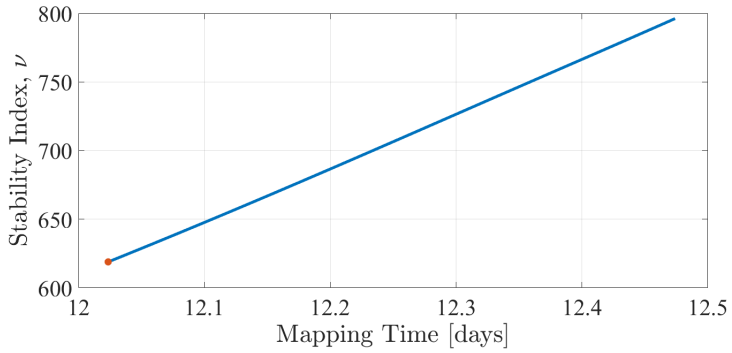

Figure 3.19. Stability index as a function of mapping time for an Earth-Moon L_1 constant energy quasi-halo family ($JC = 3.1389$) in the CR3BP. The red point represents the stability index of the periodic halo orbit associated with this quasi-halo orbit family.

and $6NM$ elements for a 3D torus. The elements of the eigenvectors are subdivided such that

$$\vec{v}_{s,r} = \begin{bmatrix} \vec{v}_{1,s,r} \\ \vec{v}_{2,s,r} \\ \vdots \\ \vec{v}_{N,s,r} \end{bmatrix}, \vec{v}_{u,r} = \begin{bmatrix} \vec{v}_{1,u,r} \\ \vec{v}_{2,u,r} \\ \vdots \\ \vec{v}_{N,u,r} \end{bmatrix} \tag{3.81}$$

for a 2D torus, where $\vec{v}_{\mathrm{i},s,r}$ and $\vec{v}_{\mathrm{i},u,r}$ correspond to the 6-element stable and unstable directions, respectively, for the i^{th} state on the invariant curve. The eigenvectors for a 3D torus are subdivided such that

$$\vec{v}_{s,r} = \begin{bmatrix} \vec{v}_{1,1,s,r} \\ \vec{v}_{1,2,s,r} \\ \vdots \\ \vec{v}_{1,M,s,r} \\ \vec{v}_{2,1,s,r} \\ \vdots \\ \vec{v}_{N,M,s,r} \end{bmatrix}, \vec{v}_{u,r} = \begin{bmatrix} \vec{v}_{1,1,u,r} \\ \vec{v}_{1,2,u,r} \\ \vdots \\ \vec{v}_{1,M,u,r} \\ \vec{v}_{2,1,u,r} \\ \vdots \\ \vec{v}_{N,M,u,r} \end{bmatrix} \tag{3.82}$$

where $\vec{v}_{\mathrm{i,j},s,r}$ and $\vec{v}_{\mathrm{i,j},u,r}$ correspond to the 6-element stable and unstable directions, respectively, for the $(\mathrm{i}^{\mathrm{th}}, \mathrm{j}^{\mathrm{th}})$ state on the invariant surface. Subsequently, the states from the stroboscopic map are perturbed by a small value ϵ in the stable/unstable directions and integrated backwards/forwards to generate a representation of the global stable/unstable manifolds,

$$\boldsymbol{x}_{\mathrm{i},s} = \boldsymbol{x}_{\mathrm{i}} + \epsilon \frac{\boldsymbol{v}_{\mathrm{i},s,r}}{|\boldsymbol{v}_{\mathrm{i},s,r}|} \tag{3.83}$$

$$\boldsymbol{x}_{\mathrm{i},u} = \boldsymbol{x}_{\mathrm{i}} + \epsilon \frac{\boldsymbol{v}_{\mathrm{i},u,r}}{|\boldsymbol{v}_{\mathrm{i},u,r}|} \tag{3.84}$$

where $\vec{x}_{\mathrm{i},s}$, $\vec{x}_{\mathrm{i},u}$, and $\vec{x}_{\mathrm{i}}$ represent the 6-element stable and unstable initial state vectors and the i^{th} state on the invariant curve in non-dimensional barycentered coordinates, respectively. The stable and unstable directions are constructed from the STM for states at other longitudinal locations along a torus. The same general form is used to generate the initial states for a 3D torus. A projection of a torus in configuration space for an unstable quasi-halo orbit appears in Figure 3.20. Figure 3.20 also shows snapshots at various times as the unstable manifold trajectory states evolve after departure from the quasi-halo orbit. The torus projection of the unstable manifolds as viewed in configuration space distorts as it is propagated forward in time towards the Moon. Similarly, the projection of the other unstable

half manifold in the direction of the Earth is rendered in Figure 3.21. The black trajectories rendered in Figures 3.20 and 3.21 represent a time history of some of the trajectories that exist on the unstable manifold.

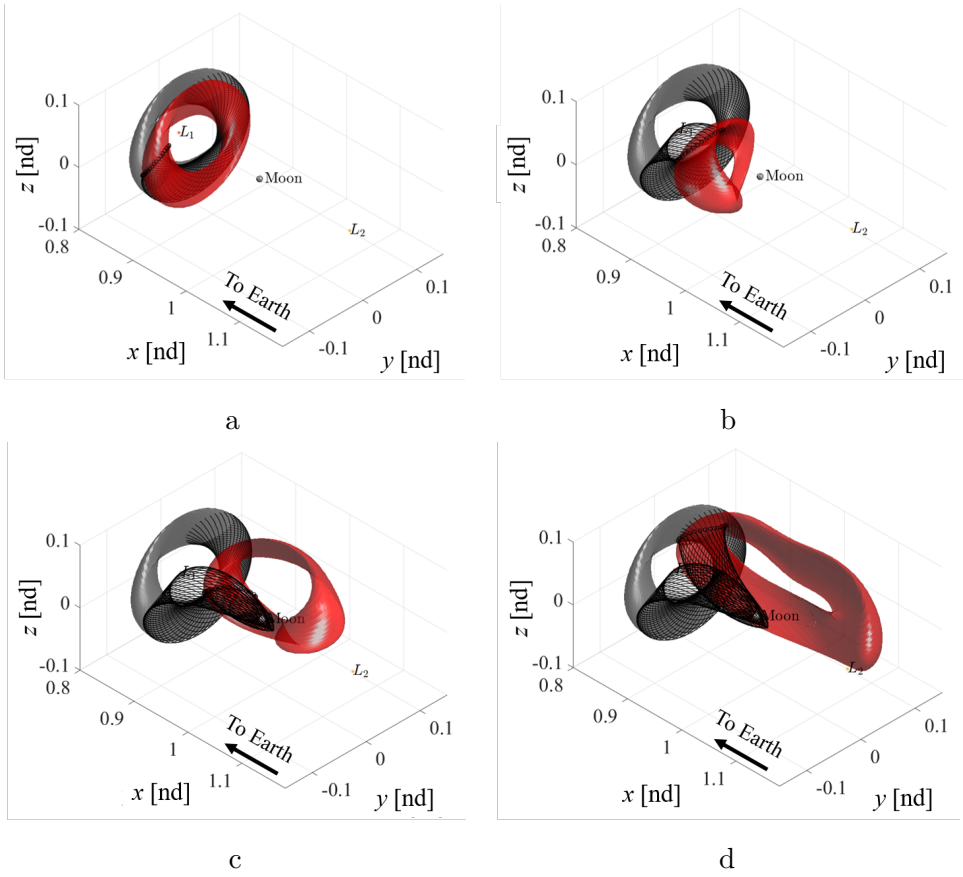

Figure 3.20. Unstable manifold in the $+x$ direction for an Earth-Moon L_1 quasi-halo orbit ($JC = 3.1389$). Trajectories associated with one invariant curve are plotted in black. A snapshot of the points comprising the corresponding manifold, shown in red, are recorded after (a) 7.79 days, (b) 9.75 days, (c) 11.39 days, and (d) 13.02 days.

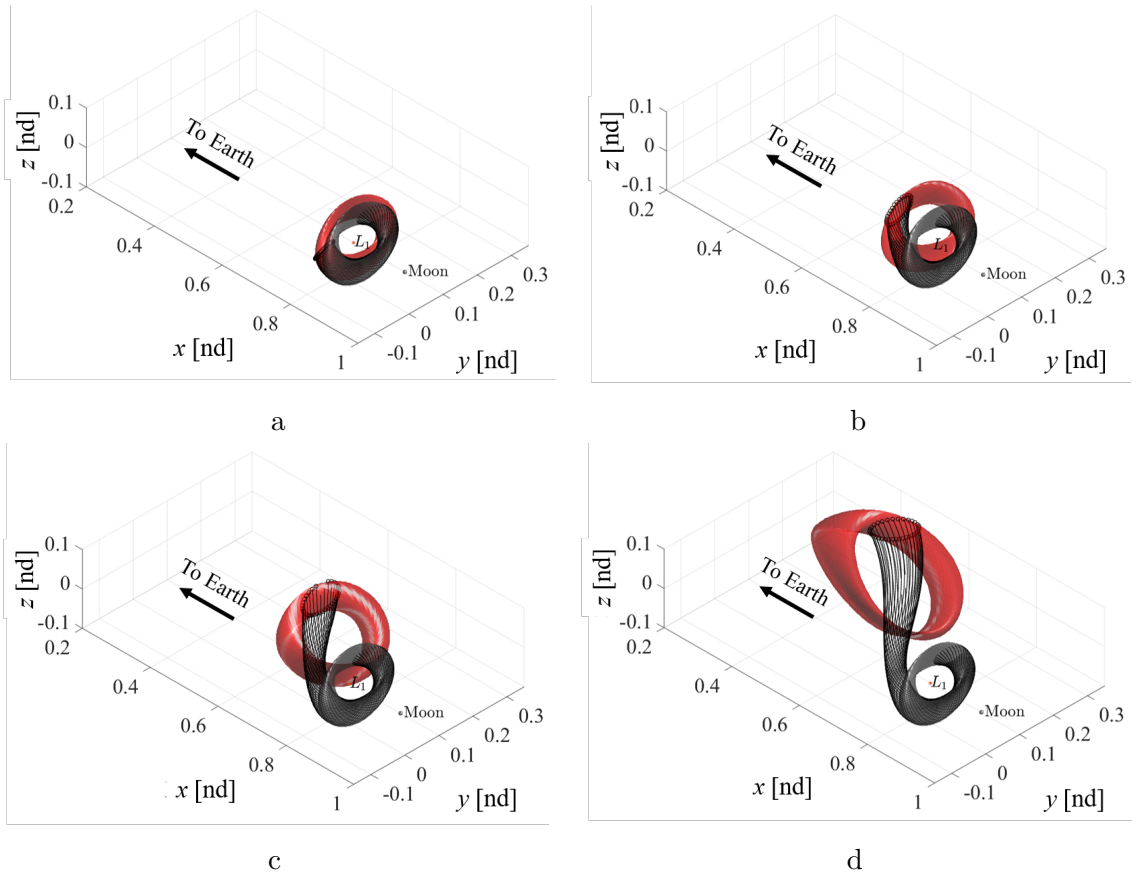

Figure 3.21. Unstable manifold in the -x direction for an Earth-Moon L_1 quasi-halo orbit ($JC = 3.1389$). Trajectories associated with one invariant curve are shown in black. A snapshot of the points comprising the corresponding manifold, shown in red, are recorded after (a) 7.79 days, (b) 9.75 days, (c) 11.39 days, and (d) 13.02 days.

4. APPLICATIONS

In 2020, NASA released the agency's lunar exploration program overview, including the Artemis and Gateway status as well as plans for additional extended lunar missions [4]. To enable such endeavors, an understanding of the cislunar multi-body dynamical environment is crucial to the success of the program. However, given the chaotic nature of multi-body systems, preliminary path planning in this environment is challenging. To meet these challenges, knowledge of the underlying dynamical structures available in cislunar space aid in creating viable mission options and in streamlining the trajectory design process. Quasi-periodic orbits provide alternatives for operation orbits to meet a variety of constraints as well as suitable initial guess transfer trajectories. This investigation demonstrates a framework to incorporate quasi-periodic orbits into the trajectory design process through a variety of applications.

4.1 Poincaré Mapping

Poincaré maps were first conceived by Henri Poincaré as a technique to understand the flow of a dynamical system and reduce the dimensionality of a given system [13]. In the trajectory design problem, Poincaré maps are useful in the identification of solutions of interest that are used as an initial guess. Poincaré maps are first constructed by selecting a hyperplane to examine the flow. Hyperplanes are defined by a condition, such as a plane crossing in physical space or defined by a characteristic of the path, such as an apse point. To visually understand this technique, consider the hyperplane Σ in Figure 4.1. Trajectories that pass through or satisfy the condition of the defined hyperplane along their path are recorded. Evolution of the states is observed between $\vec{x}_{R0}$ and $\vec{x}_{R1}$, as the trajectory moves forward in time. Additionally, trajectories that return to the same location on the map are considered periodic, exemplified by state $\vec{x}^*$ on the hyperplane in Figure 4.1. In this investigation, Poincaré maps are exploited in the CR3BP and BCR4BP to identify transfer trajectories between locations of interest.

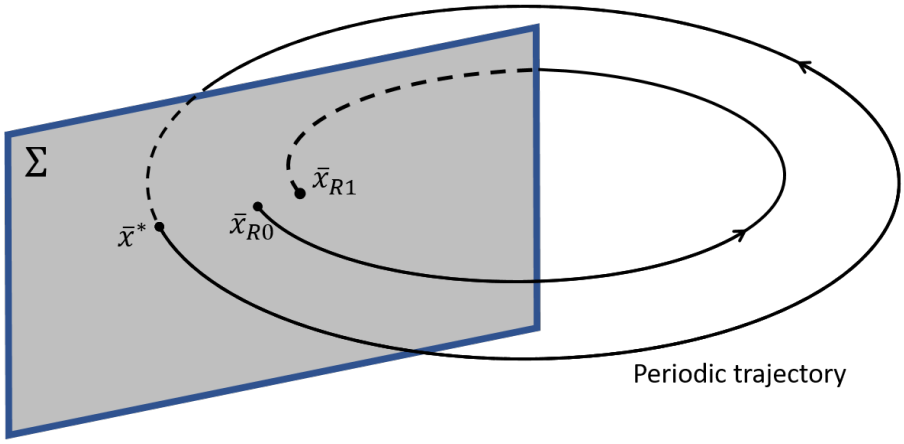

Figure 4.1. Diagram of Poincaré mapping technique.

4.2 Quasi-Periodic Orbit Trajectory Arcs

Comparing the torus surface projections in configuration space is valuable when assessing the shape and family evolution of quasi-periodic orbits. However, for mission applications, understanding the motion of individual trajectories that reside on the torus ultimately provides potential paths through space. Figure 4.2 depicts a single trajectory, residing on a torus projected in configuration space of a Sun-Earth L_1 quasi-vertical orbit in the CR3BP. The trajectory remains on the surface as the propagation time increases. Simply numerically integrating an initial state to create a time history of a trajectory along a quasi-periodic orbit causes the trajectory to considerably deviate from the torus due to accumulation of numerical error during the propagation. Leveraging properties of a torus, a strategy is developed to circumvent the numerical error build up for long propagation times. Consider an initial state, $\vec{u}(t)$, which is located on an invariant curve associated with a converged quasi-periodic orbit. For a 2D torus, the angles θ_0 and θ_1 correspond to longitudinal and latitudinal locations of the initial state on the torus at time t. Similarly, for a 3D torus, the angles θ_0, θ_1, and θ_2 correspond to a location on a 3D torus. As summarized in Section 3.1, the initial state returns to the invariant curve or invariant surface after propagating for the

stroboscopic mapping time. If n represents the iterate of the map, then the state on the n^{th} return to the map for a 2D torus and a 3D torus is defined, respectively,

$$\vec{u}(t + nT_0) = \vec{u}(\theta_0, \theta_1 + n\rho) = \mathrm{e}^{\mathrm{i}(\theta_1 + n\rho)\vec{k}}\mathbf{C_0} \tag{4.1}$$

$$\vec{u}(t + nT_0) = \vec{u}(\theta_0, \theta_1 + n\rho, \theta_2 + n\eta) = \left(\mathrm{e}^{\mathrm{i}(\theta_1 + n\rho)\vec{k}} \otimes \mathrm{e}^{\mathrm{i}(\theta_2 + n\eta)\vec{m}}\right)\mathbf{C_0} \tag{4.2}$$

where $\mathbf{C_0}$ is the matrix of Fourier coefficients for the invariant curve or surface, $\vec{k}$ is defined in Equation (3.14), $\vec{m}$ is defined in Equation (3.62) and $\otimes$ is the Kronecker product operator. Subsequently, individual numerical integration durations are limited, at most, to the stroboscopic mapping time. A single state is rotated about the invariant curve/surface and integrated for the stroboscopic mapping time to obtain a time history of states for a desired number of passes through the map.

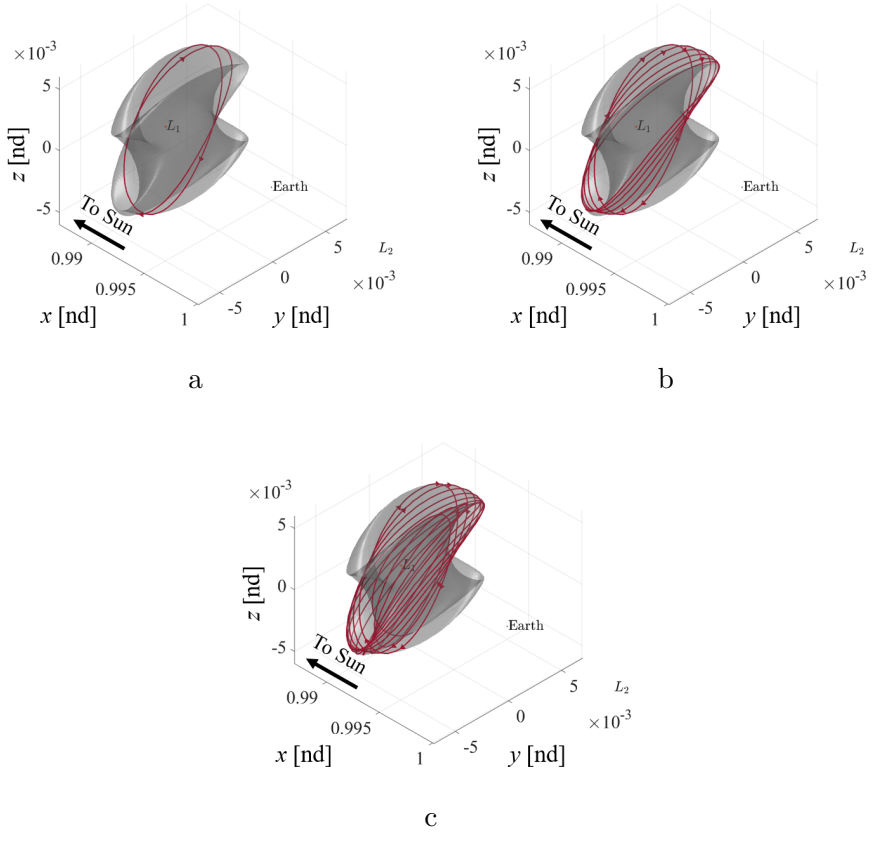

Figure 4.2. Single Sun-Earth L_1 quasi-vertical trajectory propagated for (a) 325 days, (b) 1,068 days, and (c) 2,182 days.

4.3 Transfer Trajectory Design in the Earth-Moon System

Any transfer between two periodic orbits requires that the periodic orbits intersect or that an intermediate transfer path intersects both the originating and destination orbits in position space. Maneuvers adjust the energy and/or flight path direction to achieve the desired destination orbit or transfer trajectory characteristics. In a conic model, various numerical and analytical methods are available to compute transfer trajectories that minimize various parameters (e.g., time of flight, required energy, or maneuver magnitude [66]). However, in regimes in which multiple bodies significantly influence the path of the spacecraft, the dynamics are more complex, necessitating innovative techniques to compute transfer trajectories. In addition, no known closed-form, analytical solutions exist for periodic orbits in the CR3BP. However, various strategies are effective at computing transfer trajectories between periodic orbits in multi-body regimes [67]–[74]. Incorporating quasi-periodic trajectory arcs into transfer trajectories between periodic orbits or quasi-periodic orbits has not been widely explored.

4.3.1 Transfer Design Leveraging a Single Quasi-Periodic Orbit Arc

One of the next significant steps in human spaceflight is the habitat concept as part of the Gateway program [3]. Plans for the Lunar Gateway facility include operation in an L_2 NRHO, which exists in a regime in which the gravitational influence of the Earth and Moon are both significant. Capabilities are required for excursions from the NRHO (near the Moon) to other halo orbit destinations (near the Earth-Moon L_2 libration point), to name one example. Difficulties exist in generating transfers between stable and nearly stable (i.e., a stability index near 1) periodic orbits, as they do not possess useful stable/unstable manifolds. These characteristics add complexity to the design process [75], [76]. The current baseline for the Lunar Gateway is a 9:2 lunar synodic resonant southern L_2 NRHO ($r_p = 3,200$ km). In addition, a 4:1 lunar synodic resonant southern L_2 NRHO ($r_p = 5,700$ km) delivers favorable eclipse avoidance properties [76], [77]. A constant frequency ratio quasi-NRHO is computed from a periodic NRHO with a lunar periapsis radius of $r_p = 4,680$ km. A single quasi-NRHO from the family is selected such that it is the first member of the

family to intersect both the 9:2 and 4:1 resonant periodic NRHOs in configuration space, as depicted in Figure 4.3a. At an intersection location along the 9:2 synodic resonant NRHO, a trajectory arc is propagated on the quasi-NRHO until it reaches the vicinity of the 4:1 synodic resonant NRHO. A differential corrections scheme permits impulsive departure and arrival maneuvers and constrains position continuity at the departure and arrival orbits. The corrections process converges on the solution rendered in Figure 4.3b. The departure $\Delta v_1 = 25.6$ m/s and the arrival $\Delta v_2 = 24.0$ m/s yield a total $\Delta v_{tot} = 49.6$ m/s for a feasible transfer. The time of flight from the 9:2 to the 4:1 synodic resonant NRHO is 11.4 days. Lunar synodic resonant NRHOs possess useful eclipse avoidance properties, and quasi-NRHOs offer trajectory arcs for applications as initial guesses for various types of transfers.

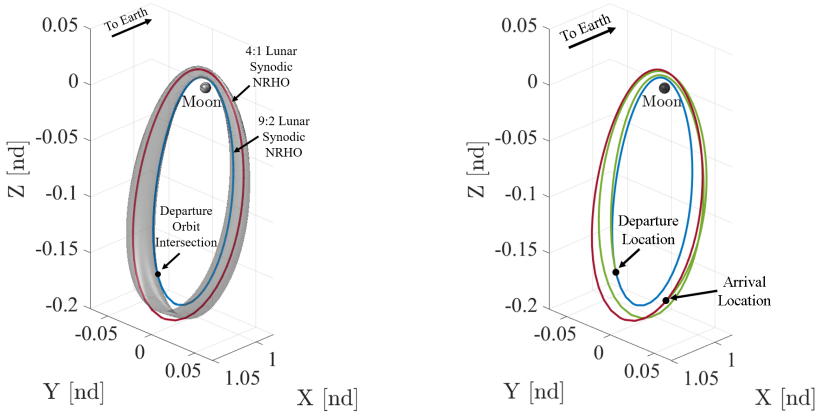

Figure 4.3. (a) Quasi-NRHO leveraged for transfer initial guess with departure orbit (blue) and arrival orbit (red). (b) Converged transfer trajectory (green) departing from a 9:2 lunar synodic resonant southern L_2 NRHO (blue) to a 4:1 lunar synodic resonant southern L_2 NRHO (red).

The NRHO transfer as shown in Figure 4.3 serves as a feasible solution to the CR3BP. However, a theoretical minimum Δv is available to assess feasible transfers for comparison. Recall that the Jacobi constant is a function of the pseudo-potential and the relative velocity magnitude from Equation (2.15). To accommodate only the energy difference between the departure and arrival orbits, a theoretical minimum Δv is constructed. Rearranging the

Jacobi-constant equation to solve for the velocity magnitude by simple computing the difference in magnitude between the departure velocity and arrival velocity derives the following:

$$\Delta v_{min} = \sqrt{2U^* - JC_2} - \sqrt{2U^* - JC_1} \tag{4.3}$$

where JC_2 is the desired Jacobi constant, JC_1 is the Jacobi constant corresponding to the departure location, and U^* is the pseudo-potential function from Equation (2.7). The pseudo-potential is evaluated at the departure location, as the equation supplies the minimum maneuver magnitude necessary to change energy at that departure location. The resulting Δv_{min} is the minimum velocity change required to achieve a Jacobi constant of JC_2 at the departure location. From Equation (4.3), the theoretical minimum energy change is 34.23 m/s. Although the feasible solution does not match the theoretical minimum, understanding the theoretical minimum for a given transfer trajectory frames a comparison for further optimization of the transfer.

4.3.2 Transfer Design Leveraging Multiple QPO Arcs

A single trajectory arc from a quasi-periodic orbit provides a sufficient initial guess for a transfer trajectory between two periodic NRHOs. However, multiple quasi-periodic and periodic orbit trajectory arcs can also be combined and leveraged to produce initial guesses for more complex itineraries to access more locations in cislunar space. Consider a sample planar L_2 Lyapunov orbit (black) and a northern L_2 NRHO (gold) in the Earth-Moon system as plotted in Figure 4.4a. Quasi-periodic orbits (red, purple, blue, and orange) and a single periodic orbit are shown in the figure to provide an initial guess that attempts to "slide" up from the Lyapunov orbit to the NRHO, thereby exploiting the natural motion in the region to generate the initial guess. When trajectory arcs are selected from the quasi-periodic orbits, an initial guess is constructed; this is plotted in Figure 4.4b. When a multiple-shooting differential corrections scheme is used while allowing for velocity discontinuities to simulate maneuvers at the end of each trajectory arc as shown in Figure 4.4b, a feasible solution is converged with a time of flight of 181 days and a total Δv equal to 450 m/s over six maneuvers. As a reference, the theoretical minimum Δv for this transfer is 220

m/s, as computed from Equation (4.3). The converged solution is plotted in Figure 4.5. To examine the change in energy over the transfer, the Jacobi constant is plotted as a function of the time along the transfer in Figure 4.6. The black circle indicates the Jacobi constant for the originating Lyapunov orbit, the gold circle denotes the Jacobi constant value of the destination NRHO, and the arrows highlight the locations of the six maneuvers. Most of the transfer duration is spent along the first segment after departing from the Lyapunov, and the first maneuver does not change the Jacobi constant significantly. The first four maneuvers decrease the Jacobi constant, whereas the last two maneuvers increase the Jacobi constant to ultimately match the Jacobi constant of the NRHO. Although alternate geometries are possible by exploiting periodic halo orbit manifolds, arcs from both periodic and quasi-periodic orbits provide a sufficient initial guess to retain a "sliding" geometry and converge a feasible solution for the CR3BP.

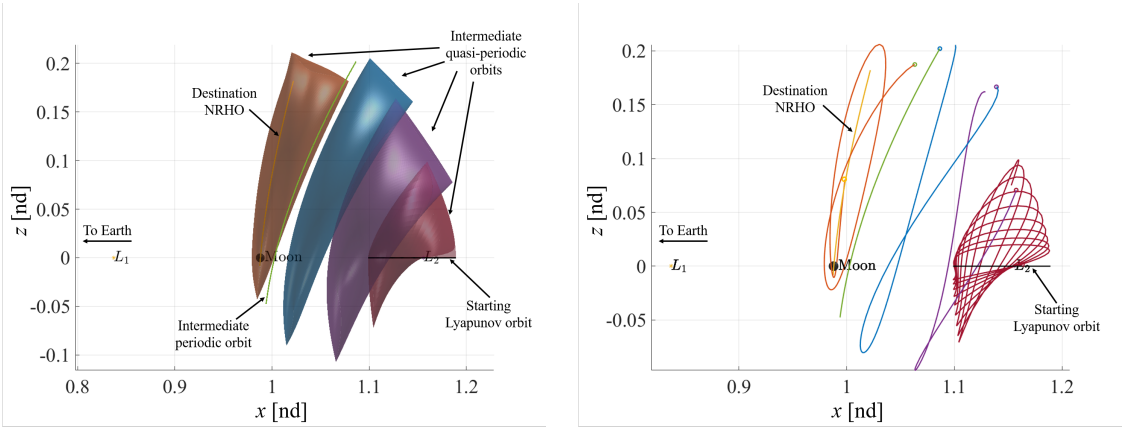

Figure 4.4. (a) Quasi-periodic and periodic orbits leveraged to generate an initial guess for "sliding" geometry transfer from planar L_2 Lyapunov orbit (black) to northern L_2 NRHO (gold). (b) Initial-guess arcs from periodic and quasi-periodic orbits.

Unstable quasi-periodic orbits also offer manifold trajectories that supply maneuver-free paths into and out of a quasi-periodic orbit. When manifold trajectories are used from a quasi-periodic orbit, initial guesses for alternative transfers from a planar L_2 Lyapunov orbit to a northern L_2 NRHO also emerge. First, a Poincaré map is generated on a hyperplane selected at the $\hat{z}$-component location where $\dot{y}_{NRHO} = 0$, as illustrated in grey in Figure 4.7.

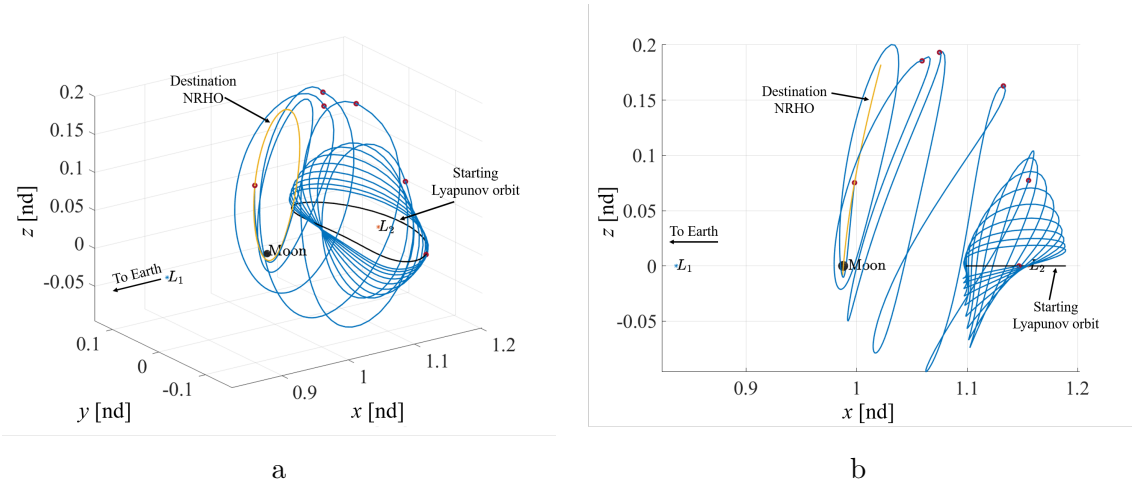

Figure 4.5. Feasible transfer from a planar L_2 Lyapunov orbit (black) to a northern L_2 NRHO (gold) using a "sliding" geometry initial guess plotted in (a) 3D view and (b) $\hat{x}\hat{z}$ projection. The red circles indicate the locations of the maneuvers.

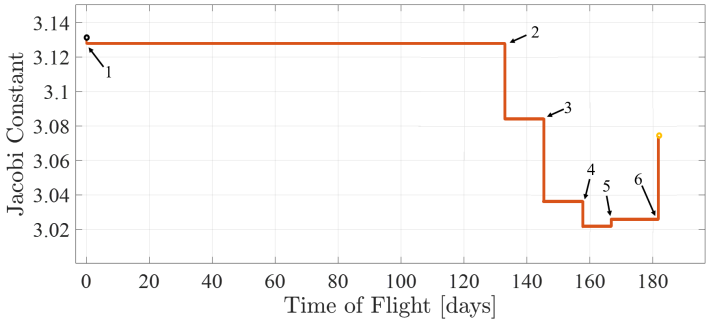

Figure 4.6. Jacobi constant as a function of time along the transfer trajectory for the "sliding" geometry transfer.

This location is selected because the velocity of the NRHO is directed nearly perpendicular to the hyperplane and avoids sensitivities associated with having a connection point near perilune. In addition, only certain returns are plotted on the map. For trajectories that intersect the map where $y > 0$, the $\hat{z}$ component of velocity must be positive, and where $y < 0$, the $\hat{z}$ component of velocity must be negative. The arrows in Figure 4.7 illustrate this direction constraint on the hyperplane. Including this constraint removes points that flow in the opposite direction as compared to the NRHO in any region of the map. Finally, the points on the map are colored by the angle between the velocity vector along the quasi-periodic

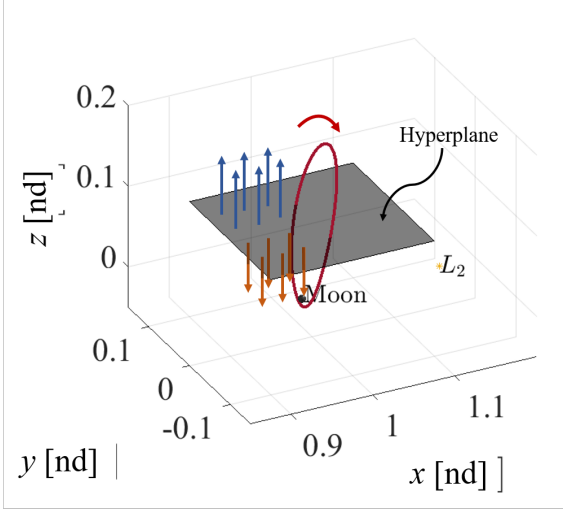

Figure 4.7. Poincaré map. The red arrow indicates the direction of motion along the NRHO.

manifold trajectory at the map crossing and the velocity vector along the NRHO where it crosses the map. A quasi-halo orbit, rendered in grey in Figure 4.8a, is selected, and the unstable manifolds are propagated and recorded on the map and plotted in Figure 4.8b. The cool colors on the map indicate that the direction of the velocity difference is small between the map point and the velocity vector for the NRHO, and the warmer colors represent a larger angle. Selecting a point with a cool color close to one of the NRHO intersections on the map yields a sufficient initial guess for a differential corrections scheme. When the departure and arrival locations are allowed to introduce a velocity discontinuity, a feasible transfer trajectory is converged requiring only two impulsive maneuvers; this is plotted in Figure 4.9. The transfer duration is 89 days and total $\Delta v = 282$ m/s with the theoretical minimum Δv computed using Equation (4.3) at 146 m/s. It should be noted that the theoretical minimum for the quasi-periodic manifold is different than the sliding geometry, as the departure and insertion locations are different in each application. The unstable manifold strategy offers a solution that requires only a departure and arrival maneuver as opposed to multiple intermediate maneuvers to achieve a complex itinerary. The transfer time of flight is also sufficiently reduced. In addition, the required Δv is reduced by exploiting the unstable manifolds.

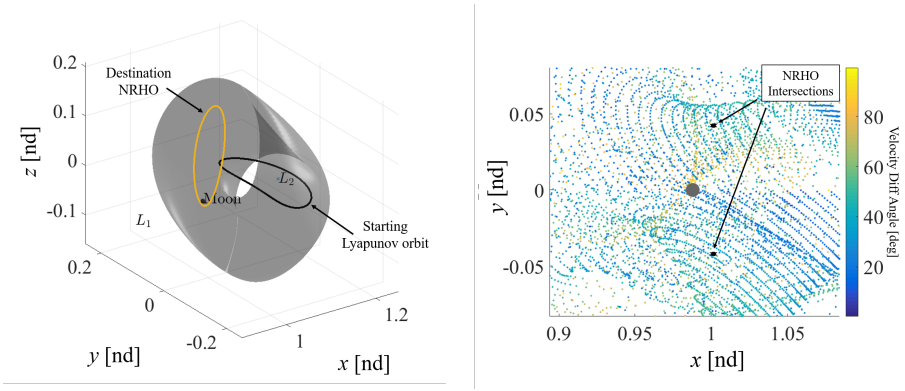

a b

Figure 4.8. (a) Starting planar L_2 Lyapunov orbit (black), destination northern L_2 NRHO, and quasi-halo orbit used to generate an initial guess for a transfer trajectory. (b) Poincaré map showing the crossings of unstable manifold trajectories from the quasi-halo orbit.

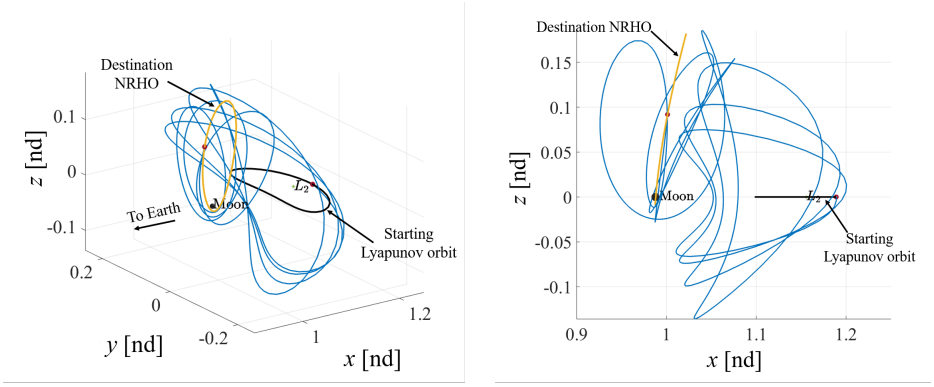

a b

Figure 4.9. Feasible transfer from planar L_2 Lyapunov orbit (black) to northern L_2 NRHO (gold) using trajectory arcs from a quasi-halo orbit and its associated unstable manifold plotted in (a) 3D view and (b) $\hat{x}\hat{z}$ projection. The red circles indicate the locations of the maneuvers.

4.3.3 Transfer Design Between Quasi-Periodic Orbits

Unstable quasi-periodic orbit manifolds are also be leveraged for transfers between quasi-periodic orbits. Heteroclinic connections between quasi-periodic orbits by several authors. Calleja et al. demonstrated an indirect method to compute heteroclinic connections between periodic and quasi-periodic orbits using collocation [78]. Goméz demonstrated connections using a large set of trajectories propagated from the semi-analytic center manifold [79].

Olikara expanded upon both of these methods to develop a boundary value problem to compute heteroclinic connections between quasi-periodic tori [27]. Given the higher dimensionality of the spatial problem as compared to the planar CR3BP, difficulties exist in finding an initial heteroclinic connection between two orbits. A method developed by Haapala and Howell is expanded upon to leverage glyphs to obtain an initial guess for a connection between two quasi-periodic orbits [69]. A differential corrections process is further developed to compute a continuous heteroclinic connection between two quasi-periodic orbits. Consider an L_1 and L_2 unstable quasi-halo orbit in the Earth-Moon CR3BP, rendered in Figure 4.11b. Both of these orbits are computed such that their $JC = 3.11$. Since both of these orbits exist at the same Jacobi Constant, it is possible that heteroclinic connections exist that provide maneuver-free paths between them. Trajectories representing the unstable manifolds are propagated in forward time from the L_2 quasi-halo orbit and recorded whenever they cross the $\hat{x}\hat{z}$ plane in the Earth-Moon rotating frame in red. Similarly, trajectories representing the stable manifolds of the L_1 quasi-halo are propagated in reverse time and the crossings are recorded in blue. From the recorded states, a Poincaré map is created using the position and velocity information. The position at the crossing of the plane is recorded as a point and the velocity information is represented as an arrow. The direction of the arrow indicates the direction of the $\hat{x}$ and $\hat{z}$ components of velocity at the plane crossing, while the length of the arrow indicates the magnitude of the $\hat{x}$ and $\hat{z}$ velocity components. Lastly, only states with $\dot{y} > 0$ are rendered on the map so that the direction of the flow through the map is consistent between the stable and unstable trajectories. Thus, a initial guess is selected such that two points that share a similar x- and z-position as well as possess an arrow in nearly the same direction and magnitude. While this does not guarantee a connection, it provides a sufficient initial guess to seed a differential corrections problem. The targeting problem to compute heteroclinic connections is an extension of the formulation by Haapala and Howell [69] and the scheme is illustrated in the diagram in Figure 4.10. The red oval indicates the initial torus and the blue oval indicates the destination torus. The states retrieved from the

Poincaré map are used to construct the initial guess for the black path in Figure 4.10. The constraint vector is then defined,

$$\boldsymbol{F} = \begin{bmatrix} \vec{x}_T - \left(\vec{x}^t_{M,u} + d_u \frac{\Phi_u \vec{v}_u}{|\Phi_u \vec{v}_u|} \right) \\ \vec{x}^t_T - \left(\vec{x}^t_{M,s} + d_s \frac{\Phi_s \vec{v}_s}{|\Phi_s \vec{v}_s|} \right) \end{bmatrix} \tag{4.4}$$

where $\vec{x}_T$ is the beginning of transfer segment and $\vec{x}^t_T$ is the transfer segment propagated for time T_T, d_u and d_s are scalars that define the small perturbation of the state on the unstable and stable manifold directions, respectively, $\vec{v}_u$ and $\vec{v}_s$ are the 6×1 stable and unstable eigenvectors at latitudinal angles of $\theta_{1,u}$ and $\theta_{1,s}$, respectively, on the invariant curve of their respective orbits, and Φ_u and Φ_s are the state transition matrices propagated from their initial states, $\vec{x}_{M,u}$ and $\vec{x}_{M,s}$, on the invariant curve of the initial and destination tori, respectively. Subsequently, a free variable vector is defined,

$$\boldsymbol{X} = \begin{bmatrix} \vec{x}_T \\ T_T \\ \tau_u \\ \tau_s \\ \theta_{1,u} \\ \theta_{1,s} \end{bmatrix} \tag{4.5}$$

where T_T is the time along the transfer segment, τ_u is time from invariant curve to the unstable perturbation location on the initial torus, τ_s is the time from arrival to the invariant curve of the destination torus, and $\theta_{1,u}$ and $\theta_{1,s}$ are the latitudinal angles along the invariant curve of the initial and destination tori, respectively. The Jacobian of the targeting problem is subsequently defined,

$$\boldsymbol{DF} = \begin{bmatrix} \boldsymbol{I}_{6\times 6} & \boldsymbol{0}_{6\times 1} & \frac{\partial(\vec{x}^t_{M,u} + d_u \frac{\Phi_u \vec{v}_u}{|\Phi_u \vec{v}_u|})}{\partial \tau_u} & \boldsymbol{0}_{6\times 1} & \frac{\partial(\vec{x}^t_{M,u} + d_u \frac{\Phi_u \vec{v}_u}{|\Phi_u \vec{v}_u|})}{\partial \theta_{1,u}} & \boldsymbol{0}_{6\times 1} \\ \boldsymbol{\Phi}(T_T, 0) & \dot{\vec{x}}^t_T & \boldsymbol{0}_{6\times 1} & \frac{\partial(\vec{x}^t_{M,s} + d_s \frac{\Phi_s \vec{v}_s}{|\Phi_s \vec{v}_s|})}{\partial \tau_s} & \boldsymbol{0}_{6\times 1} & \frac{\partial(\vec{x}^t_{M,s} + d_s \frac{\Phi_s \vec{v}_s}{|\Phi_s \vec{v}_s|})}{\partial \theta_{1,s}} \end{bmatrix} \tag{4.6}$$

where $\mathbf{\Phi}(T_T, 0)$ is the state transition matrix from $\vec{x}_T$ to $\vec{x}_T^t$. Note that there is one more constraint than free variable for this problem. However, since Jacobi Constant is implicitly constrained when solving for a heteroclinic connection in the CR3BP, one of the state constraints is removed. Subsequently, there are 11 constraints and 11 free variables and a unique solution between two quasi-periodic orbits at the same Jacobi Constant, given such a connection exist. This formulation is also extendable to a multiple shooting problem, where the transfer segment is decomposed into smaller segments. The initial guess from the map in Figure 4.11a supplied to the differential corrections procedure and the resulting converged heteroclinic connection is rendered in Figure 4.11b.

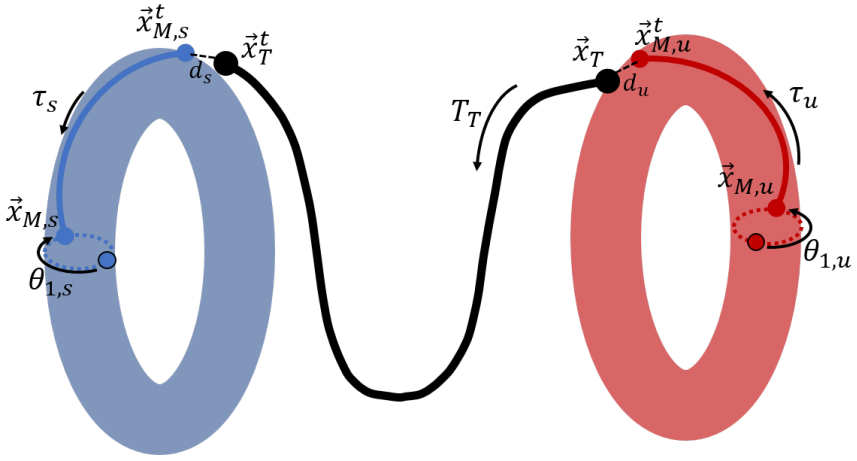

Figure 4.10. Heteroclinic targeting procedure diagram.

Given that the targeting problem defines a unique transfer solution, the process is extended to construct families of heteroclinic transfers. To construct families, a parameter to represent the destination orbit is included in the process. Since quasi-periodic orbits are uniquely defined by two parameters in the CR3BP and the Jacobi Constant is constrained between the initial and final orbits, the rotation angle is selected as the parameter to characterize the destination orbit within a family of heteroclinic connections. The initial converged transfer from Figure 4.11b is used to seed a natural parameter continuation process, where the destination orbit is changing for each member of the family. Members of the family of heteroclinic transfers where $JC = 3.11$ are rendered in Figure 4.12a. Note that the gaps

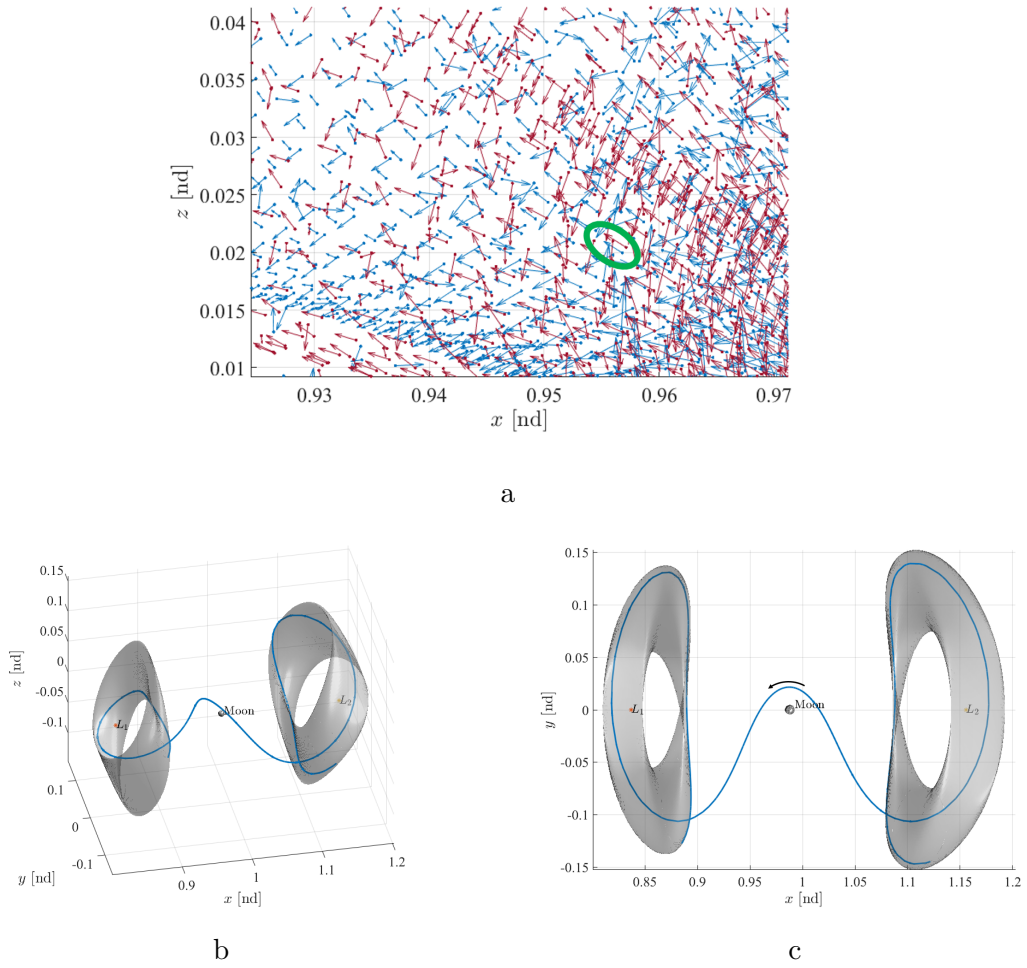

Figure 4.11. (a) Poincaré map with the stable manifold trajectory points (blue) from an L_1 quasi-halo orbit and the unstable manifold trajectory points (blue) from an L_2 quasi-halo orbit. (b) Converged heteroclinic connection between the two quasi-halo orbits with $JC = 3.11$. (c) $\hat{x}\hat{y}$ projection of the converged heteroclinic transfer. Arrows indicate the the direction of motion.

in the continuum of transfer solutions occurred where the frequency ratio of the departing orbit was commensurate.

Note that challenges exist when implementing a pseudo-arclength continuation process for this problem. The variations in the stable and unstable eigenvectors with respect to the rotation angle of the quasi-periodic orbit (i.e., the parameter representing the departing/destination orbit in the CR3BP) cannot be computed analytically. Based on numerical experiments, the accuracy of the finite difference partial derivatives with respect to the rota-

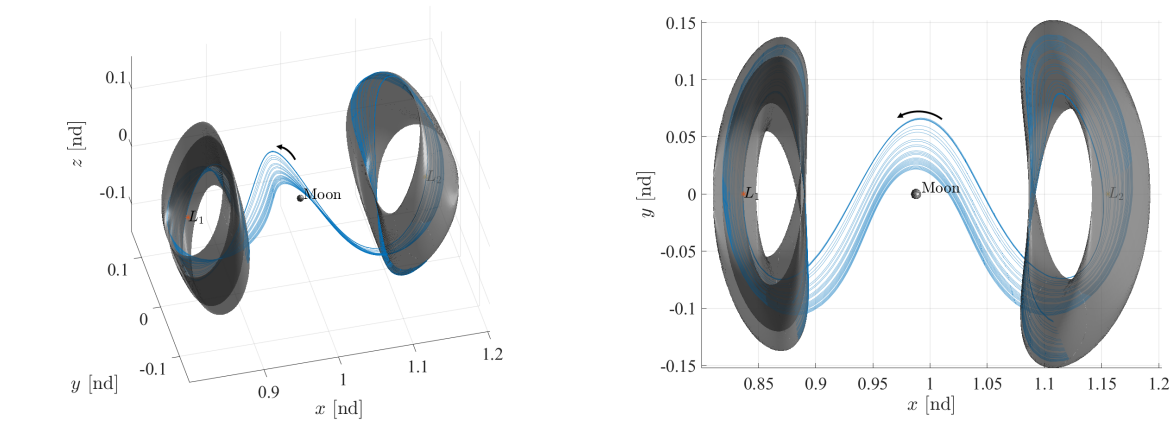

Figure 4.12. Family of heteroclinic transfer between an L_2 quasi-halo orbit with $\rho = 0.48882741$ and a range of L_1 quasi-halo orbits with $JC = 3.11$. Arrows indicate the direction of motion. The first and last L_1 quasi-halo orbits from the family are plotted in each projection.

tion angle are highly sensitive to the perturbation size. Thus, it is challenging to converge on a transfer such that the nullspace of the Jacobian can be computed accurately to construct the pseudo-arclength constraint. Additionally, the accuracy of the derivatives with respect to rotation angle is related to the accuracy of which the eigenvectors are computed for the departing/destination quasi-periodic orbit. Since the stable and unstable eigenvectors are a function of a converged quasi-periodic orbit, the quasi-periodic orbit computation must be decoupled from the heteroclinic transfer targeting problem. Subsequently, the rotation angle representing the departing orbit can be included as a free variable and can aid in computation of a heteroclinic connection, but the non-zero columns of the Jacobian that correspond to the variations with respect to the rotation angle must be computed numerically using finite differencing.

4.3.4 Ephemeris Validation

The CR3BP provides a good approximation of the dynamics in the vicinity of the Earth and Moon. However, ensuring that solutions from the simplified model are valid in a higher-fidelity ephemeris model is crucial. To transition these solutions from the CR3BP to the

ephemeris model, a multiple-shooting technique is employed. First, consider the transfer geometries from Section 4.3.2. Six revolutions of the initial Lyapunov orbit and destination NRHO are computed in the CR3BP and discretized into nodes to represent the trajectory path before and after the transfer. The transfer arc itself is also discretized into nodes in the CR3BP, and the velocity discontinuities are incorporated at the impulsive maneuver locations within the corrections scheme. The locations of the velocity discontinuities are constrained to have position and epoch continuity; all other nodes are constrained to have position, velocity, and epoch continuity. The free variables of the multiple-shooting scheme are position, velocity, and epoch at each node as well as time of flight along each propagated node. This method of ephemeris differential corrections is outlined in greater detail by Pavlak [80]. The transfers are converged in the Sun-Earth-Moon ephemeris model using an initial epoch for the initial state along the originating orbit for January 1, 2023; the transfers are plotted in Figure 4.13. Both transfers maintain their geometries after being transitioned to the ephemeris model. The Δv for the sliding and quasi-halo manifold geometries are 451 m/s and 272 m/s, respectively, which are consistent with the solutions computed for the CR3BP. In addition, the times of flight for each transfer type remain the same in the ephemeris model. A similar differential corrections process is used to transition heteroclinic

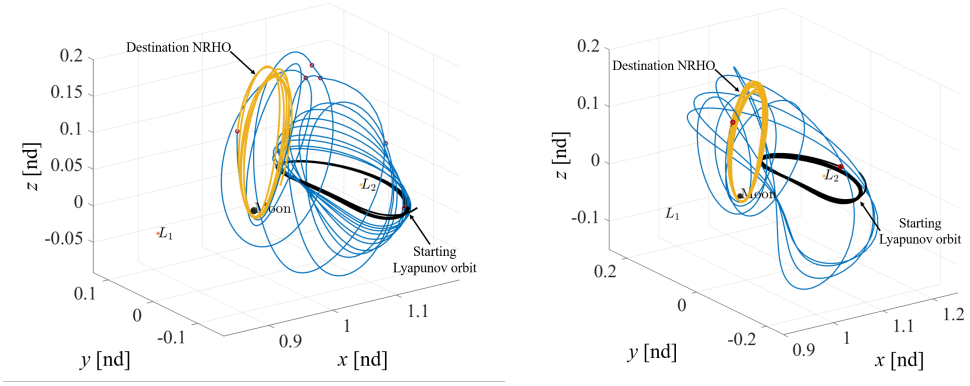

Figure 4.13. (a) Sliding geometry transfer and (b) quasi-halo manifold converged in the Sun-Earth-Moon ephemeris model using an initial epoch of January 1, 2023.

connections between quasi-periodic orbits; however, no impulsive maneuvers are allowed.

To demonstrate the transition, consider a transfer between two halo orbits from in Section 4.3.3. First, 130-day arcs from the departure L_2 quasi-halo and destination L_1 quasi-halo are constructed to represent the path before and after the transfer. Using the two 130-day segements, along with the transfer arc, the entire initial guess trajectory from the CR3BP is discretized into 200 nodes. Using a Sun-Earth-Moon ephemeris differential corrections process, the transfer is converged with an initial epoch at the initial state of the departure orbit of January 1, 2024. The converged ephemeris transfer (blue), along with the initial guess from the CR3BP (red), are plotted in Figure 4.14. This transition demonstrates that the geometry characteristics for the L_2 to L_1 quasi-halo transfer is maintained in a higher-fidelity ephemeris model. For all of these applications, the motion from the CR3BP provides a sufficient initial guess to transition to an ephemeris model.

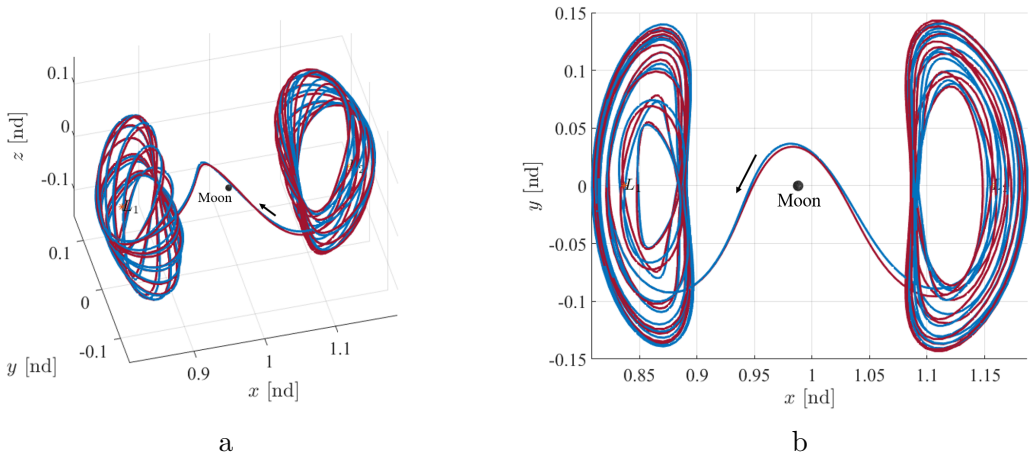

Figure 4.14. Maneuver-free transfer between an L_2 quasi-halo orbit and an L_1 quasi-halo orbit converged in the Sun-Earth-Moon ephemeris model using an initial epoch of January 1, 2024.

4.4 Ballistic Lunar Transfer Design

In the next decade, NASA plans to operate the lunar Gateway in an NRHO and leverage other orbits in cislunar space for Artemis program operations [4], [5]. The complex dynamics in these regimes presents difficulties in preliminary, efficient path planning from Earth. However, developing a framework leveraging dynamical structures that exploit the force from the

Sun aids in the trajectory design process. In this section, a process to design Ballistic Lunar Transfers (BLTs) that leverage the Sun, Earth, and Moon's gravity to access the lunar region is detailed. BLTs provide a more propellant efficient path from the Earth to the Moon by leveraging the gravitational force of the Sun at the expense of time of flight. To demonstrate the characteristics that define a BLT, consider a spacecraft departing the Earth into a highly eccentric orbit, as plotted in an arbitrary Earth-centered inertial frame in Figure 4.15a. Note that the apogee of the instantaneous conic orbit (red) is well beyond the lunar orbit radius. If the Earth departure is timed properly, as the spacecraft traverses out toward apogee, the perigee of the orbit begins to increase from the perturbing solar gravity force, as demonstrated in Figure 4.15b. Ultimately, as the spacecraft falls back towards perigee, the perigee radius matches the lunar orbit radius, illustrated in Figure 4.15c. While this demonstrates a simple case to match the lunar orbit radius, the same technique of leveraging lunar, solar, and Earth's gravity to reach multi-body orbits is possible. The framework to construct BLTs in this investigation focuses on quasi-periodic orbit destinations.

Several previous and upcoming missions are planning to leverage low energy transfers the exploit solar gravity in cislunar space. JAXA's Hiten spacecraft and NASA's GRAIL mission both leveraged solar gravity to reach the lunar vicinity [81], [82]. Upcoming, the CAPSTONE mission plans to leverage a BLT to reach an NRHO; logistics and cargo vehicles enroute to the Gateway are potentially leveraging these types of transfers as well [76], [83]. Additionally, the EQUULEUS and Lunar IceCube missions plan to exploit these types of transfers as piggyback missions on NASA's Artemis-1 mission [84], [85]. These low-energy transfers offer a reduced propellant cost alternative to direct lunar transfer trajectories studied for the Apollo program [86].

4.4.1 Ballistic Lunar Transfers

Various approaches have been previously examined to compute ballistic lunar transfers. Parker and Anderson explore BLTs using dynamical systems and numerical methods within the context of a patched three-body model as well as an ephemeris model [87]. Parrish et al. survey ballistic lunar transfer options to NRHOs completely within the context of an

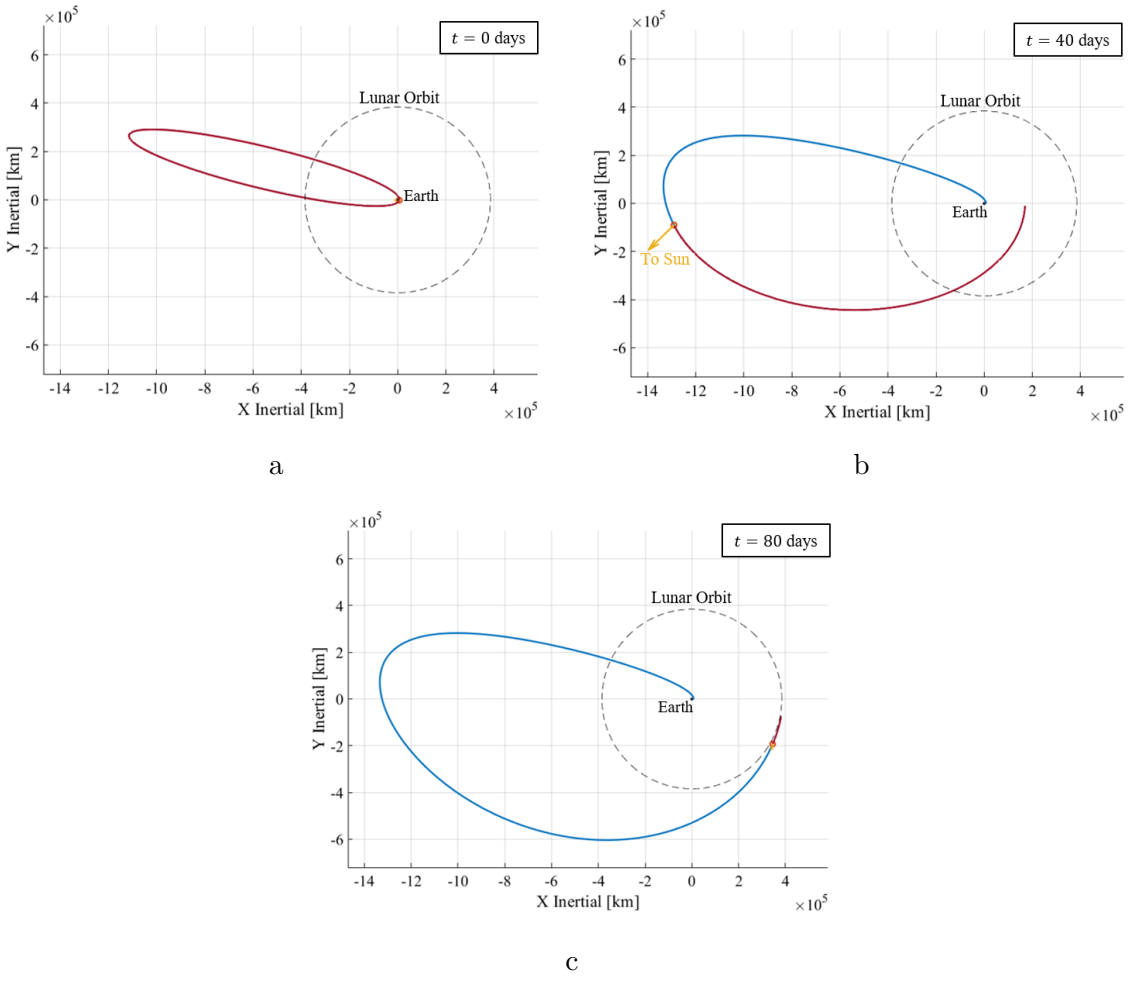

Figure 4.15. Evolution of a ballistic lunar transfer in an Earth-centered inertial frame. The instantaneous conic trajectory is plotted in red and the time history of the true trajectory is plotted in blue at (a) $t = 0$ days, (b) $t = 40$ days, and (c) $t = 80$ days. The gold arrow points in the direction of the Sun.

ephemeris model [7]. Additionally, Scheuerle et al. construct ballistic lunar transfers in the planar three- and four-body problems using dynamical systems techniques [88]. Scheuerle and Howell also examine families of ballistic lunar transfers to other cislunar orbits [89]. Rosales et al. as well as McCarthy and Howell also demonstrated techniques for computing BLTs to periodic and quasi-periodic orbits in the BCR4BP [90]–[93]. Oshima et al. summarize a global search for optimal BLTs as well as provide references for previous δv optimal ballistic lunar transfers [94]. This investigation examines construction of ballistic lunar transfers

within the context of a four-body problem, focusing specifically on quasi-periodic orbits in the BCR4BP.

Given that some of the resulting behaviors in the BCR4BP are chaotic and the problem does not possess an analytical solution, periapsis Poincaré maps are leveraged to understand the flow. Periapsis Poincaré maps are employed by numerous authors to offer insight into the various behaviors and expose structures in multi-body systems. Davis explores the use of periapsis maps in the CR3BP in the vicinity of the smaller primary to understand the flow in that region [95]. Haapala and Howell also leveraged periapsis maps and their relationships to invariant manifolds [96]. Further, Haapala and Howell exploit higher dimensional Poincaré maps to aid in trajectory design in the CR3BP [97]. Additionally, Paskowitz and Scheeres as well as Davis et al. adapt periapsis maps for use in the vicinity of icy moons of Saturn and Jupiter [98]–[100]. In the BCR4BP, Scheuerle et al., as well as McCarthy and Howell, employ periapsis maps to generate solutions for ballistic lunar transfers [88], [92], [93]. This investigation leverages these mapping techniques in the BCR4BP to construct BLTs.

There are two required conditions or a spacecraft to be located at a periapsis, or, more specifically, a point of closest approach along a path relative to a massive body. The first condition is based on the dot product between the position and velocity of a spacecraft relative to a primary and the determination that it is equal to zero,

$$\vec{r} \bullet \vec{v} = 0 \tag{4.7}$$

where $\vec{r}$ is the position of the spacecraft relative to a primary body and $\vec{v}$ is the relative rotating velocity of the spacecraft for differential equations formulated in the rotating frame. This first condition ensures that the spacecraft is at an apse relative to a primary body. The second condition is derived to ensure that the apse condition is a periapse, where the derivative of the first condition is greater than zero,

$$v^2 + \vec{r} \bullet \dot{\vec{v}} = 0 \tag{4.8}$$

where v is the mangitude of the spacecraft relative velocity in the rotating frame and $\dot{\vec{v}}$ is the time derivative of the relative velocity as observed in the rotating frame, i.e. the relative acceleration. The surface of section for the periapsis map is the appropriate hyperplane for assessment of these two conditions.

Poincaré maps enable construction of transfer trajectories in this investigation by providing an initial guess for the desired fundamental motion. Consider an unstable Earth-Moon L_2 quasi-halo orbit, from the quasi-halo Type A family in Figure 3.10a. Recording perigee points after 365 days of propagation backwards along the stable manifold, a periapsis map relative to the Earth is rendered in the Earth-Moon rotating frame in Figure 4.16a. Perigees that exist at altitudes near Low Earth Orbit (LEO) simulate a post-translunar injection (post-TLI) state along the trajectory. To further identify solutions of interest, each perigee point is colored by the time of flight from the perigee point to arrival into the destination orbit. A perigee point with a cooler color corresponds to a shorter time of flight. Additionally, points are filtered on the map such that the angular momentum vector (cross product between the Earth-centered position and velocity vectors) is in the positive $\hat{z}$-direction and any points associated trajectories incorporating more than 10 periapses are removed from the map. By filtering the perigee points using these criteria, the only map points that are rendered do not remain in the Earth-Moon neighborhood for a long time after Earth departure. The grey circle in the middle of the map in Figure 4.16a represents the Earth and the trajectory associated with the point indicated by the red arrow is plotted in Figure 4.16b.

Ballistic lunar transfers are available for destinations in the vicinity of the Earth-Moon L_1 region as well. Consider an unstable L_1 quasi-halo orbit rendered in Figure 4.17a. Trajectories associated with the stable manifold of the quasi-halo orbit are propagated in reverse time and a perigee map is again rendered, as illustrated in Figure 4.17b. A trajectory associated with a perigee near the Earth corresponds to a ballistic path to the L_1 quasi-halo orbit and such a transfer is plotted in Figure 4.18a. Note that the transfer geometry is similar to the L_2 quasi-halo transfer in Figure 4.16b. Using this mapping technique, transfers to destinations in the vicinity of L_1 and L_2 are achievable.

Ballistic lunar transfer solutions are known to exist that leverage lunar flybys; however, flexibility is necessary to plan a lunar encounter that reaches a particular destination.

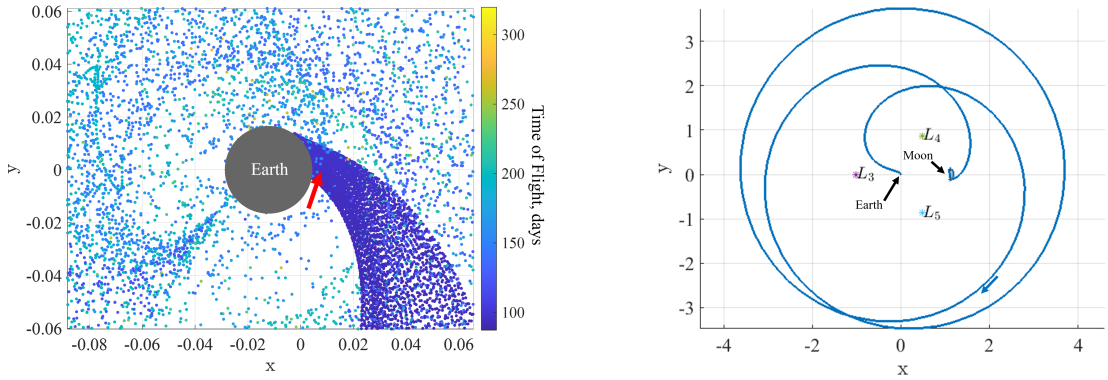

Figure 4.16. (a) Periapsis map for stable manifold trajectories of an L_2 quasi-halo Type A orbit (red arrow indicates selected point) (b) Transfer trajectory to L_2 quasi-halo associated with point selected on map plotted in the Earth-Moon rotating frame.

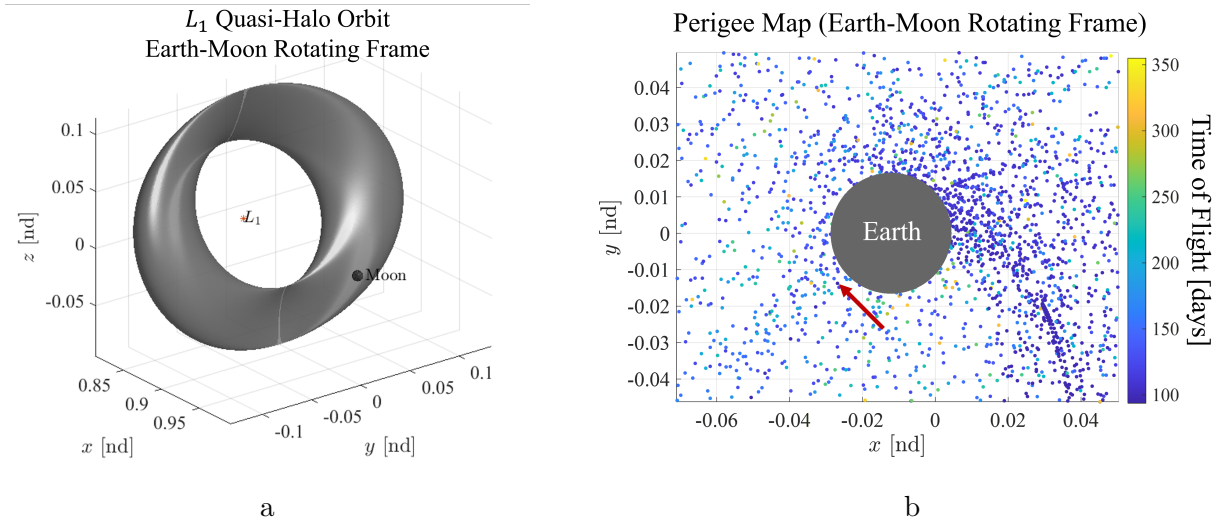

Figure 4.17. (a) Selected L_1 quasi-halo orbit in the BCR4BP. (b) Periapsis map for stable manifold trajectories of an L_1 quasi-halo orbit (red arrow indicates selected point).

Transfers that possess a leading side or trailing side lunar encounter demonstrate expanded flexibility. Consider a Type A L_2 quasi-halo orbit from Figure 3.10a and a perigee map populated from the stable manifold trajectories associated with the orbit in Figure 4.19a. The points on the map are colored by the next perilune altitude along the trajectory associated

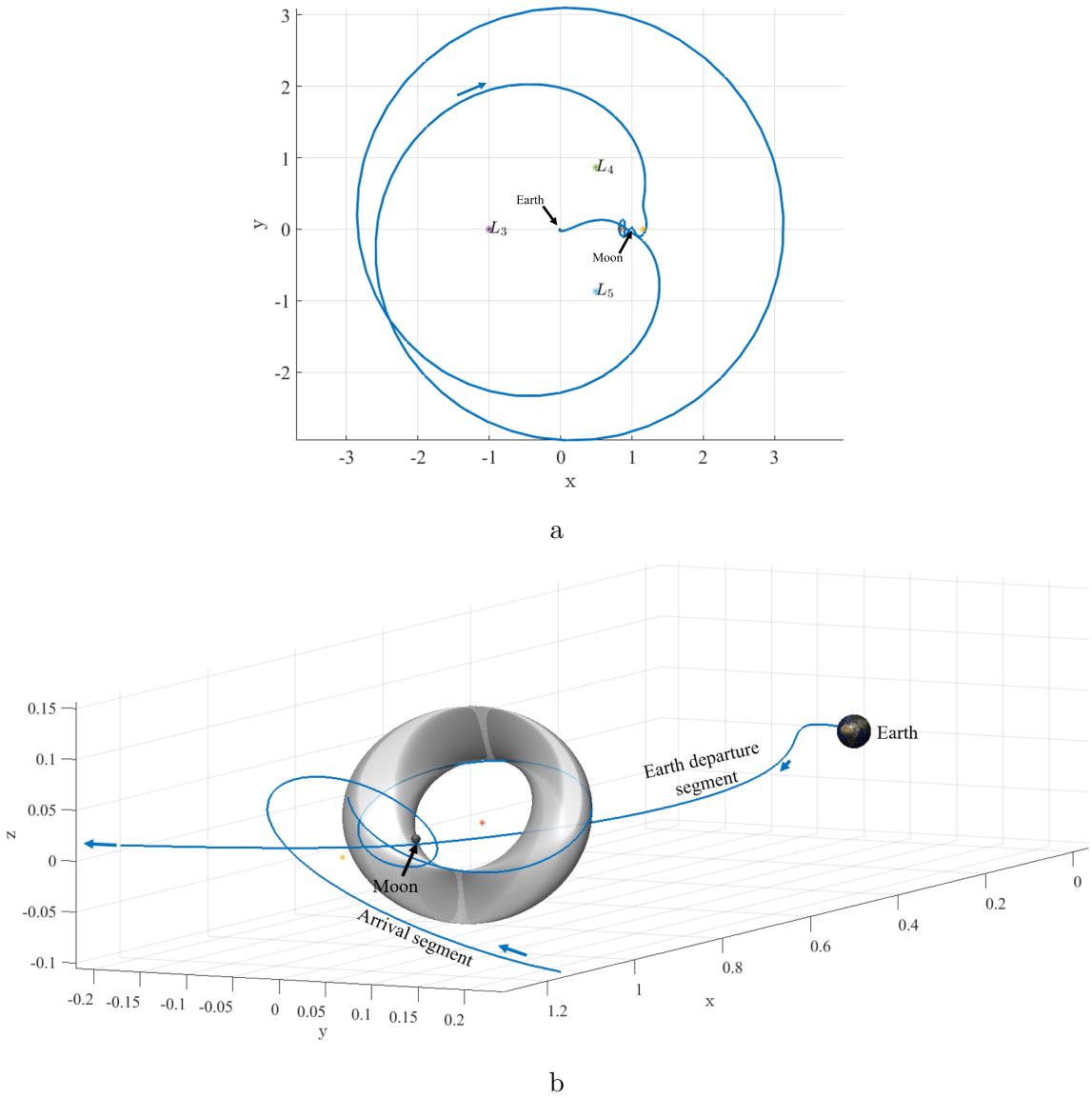

a

b

Figure 4.18. (a) Transfer trajectory to L_1 quasi-halo associated with point selected on map plotted in the Earth-Moon rotating frame. (b) Zoomed-in view of Earth departure and arrival to L_1 quasi-halo orbit. Blue arrows indicate the direction of motion.

with that point. By selecting points that are close to the Earth and possess a cooler color, the outbound lunar flyby is incorporated along the trajectory. The two arrows in Figure 4.19a indicate the points selected and both transfer trajectories are plotted in Figures 4.19b and 4.19c. The lunar flyby altitude is 1450 km for the leading side transfer and 30,000 km for the trailing side transfer. Leveraging leading or trailing side flybys into path planning for

a given destination orbit increases the overall flexibility and feasibility of a particular design.

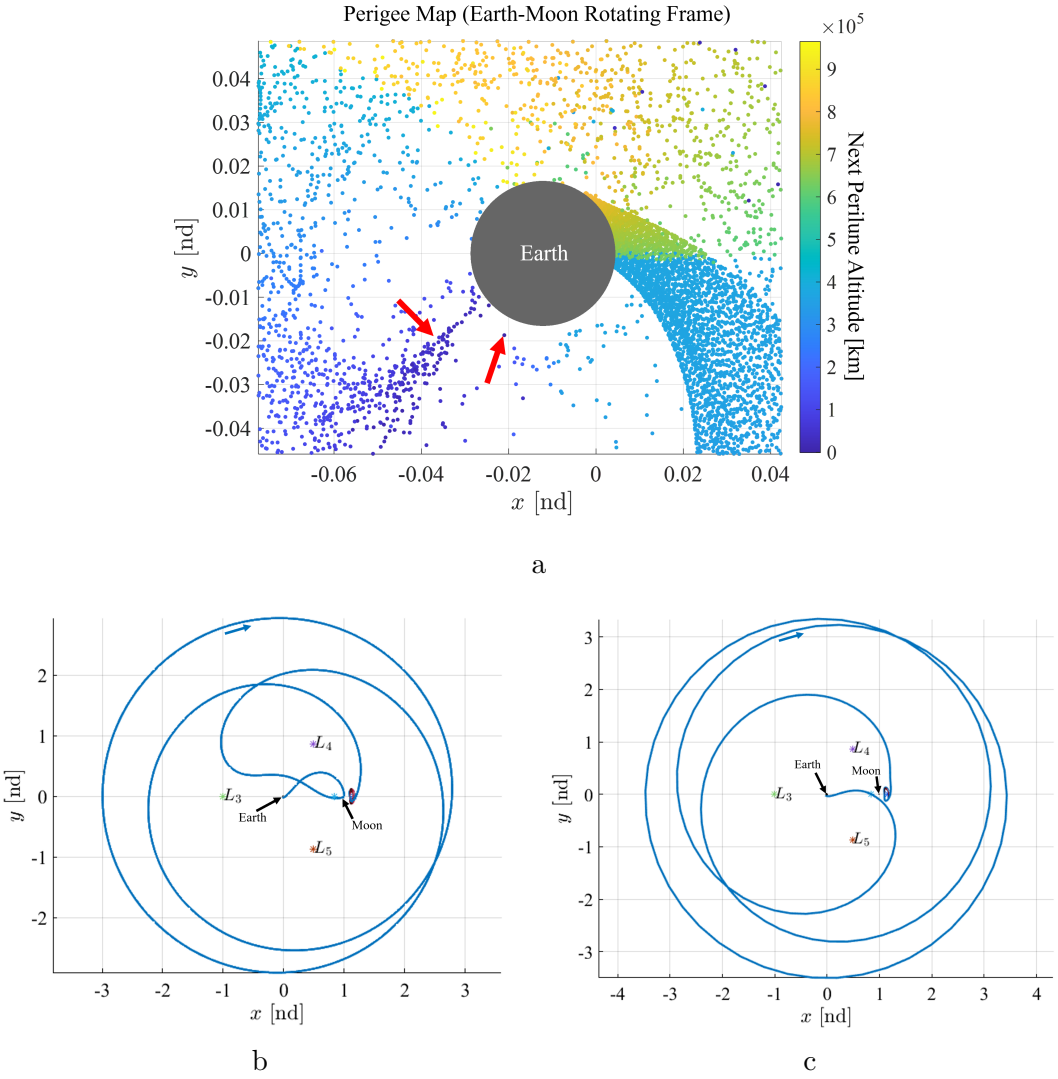

Figure 4.19. (a) Perigee map of L_2 quasi-halo orbit stable manifold trajectories. (b) Leading and (c) trailing lunar encounter ballistic lunar transfers to L_2 quasi-halo orbit. Blue arrows indicate the direction of motion.

4.4.2 Families of Ballistic Lunar Transfers

The point solutions selected from the periapsis maps in the previous section are useful for a single initial guess; however, a continuum, or family, of solutions provides more insight into

the fundamental behavior. McCarthy and Howell summarize a method to construct families of solutions to periodic orbits [92]. To produce families of solutions for quasi-periodic orbits, a free-variable/constraint vector differential corrections process is employed. The targeting problem is illustrated in Figure 4.20. There are an assigned set of nodes to minimally define the targeting problem in the illustration. The state of the first node, $\vec{x}_1$, is constrained to be located at a perigee with an altitude of 150 km and forward-shooting is employed to match the state at $\vec{x}_2$ after a time of flight T_1. Backward shooting is then implemented from $\vec{x}_3^-$ to match the state at $\vec{x}_2$ after a propagation time of $-T_1$. The state $\vec{x}_3^-$ at Node 3 is also constrained to be a perilune, where an impulsive maneuver can be placed. Lastly, a forward-shooting segment from $\vec{x}_3^+$ is constrained to match the manifold trajectory state $\vec{x}_M$ that ultimately flows into the quasi-periodic orbit. Enforcing the trajectory to be on the manifold of a quasi-periodic orbit is an extension of a similar constraint in the CR3BP by Ojeda-Romero and Howell [101]. Additionally, the forward and backward shooting scheme is implemented to more effectively converge solutions that possess low altitude perilunes. The constraint vector is thus defined,

$$\vec{F} = \begin{bmatrix} \vec{x}_1^t - \vec{x}_2 \\ \vec{x}_3^{t^-} - \vec{x}_2 \\ \vec{x}_3^{t^+} - \vec{x}_M \\ \vec{r}_3^- - \vec{r}_3^+ \\ \vec{d}_1 \cdot \vec{v}_1 \\ d_1 - d_{1,\text{desired}} \\ \vec{r}_3^- \cdot \vec{v}_3^- \\ \vec{v}_3^- + \Delta v \hat{v}_3^- - \vec{v}_3^+ \\ \Delta v \end{bmatrix} = \vec{0} \tag{4.9}$$

where $\vec{x}_\text{i}^t$ is a 6-element state vector at the end of the nonlinear propagation from state $\vec{x}_\text{i}$, $\vec{r}_3^-$ and $\vec{r}_3^+$ are the pre- and post-Δv position vectors at node 3, respectively, $\vec{d}_1$ is the position vector for node 1 relative to the Earth, $\bar{v}_\text{i}$ is the velocity vector at the i$^\text{th}$ node, $\vec{r}_3^-$ is the pre-maneuver position vector relative to the Moon at node 3, $\Delta v \hat{v}_3^-$ is vector representing

the maneuver, and Δv is the impulsive maneuver magnitude. Note that the maneuver is assumed to be implemented in the direction of $\vec{v}_3^-$. The free variable vector is then defined,

$$\vec{X} = \begin{bmatrix} \vec{x}_1 & \vec{x}_2 & \vec{x}_3^- & \vec{x}_3^+ & T_1 & T_2 & \tau & \Delta v & \theta_1 \end{bmatrix}^T \tag{4.10}$$

where T_1 is the time of flight between the states $\vec{x}_1$ and $\vec{x}_2$ as well as the backwards propagated segment $\vec{x}_2$ and $\vec{x}_3^-$, T_2 is the time of flight between $\vec{x}_3^+$ and $\vec{x}_M$, τ is the propagation time from the manifold trajectory arrival state to the final state on the invariant curve of the quasi-periodic orbit, θ_1 is the latitudinal angle on the invariant curve and Δv is the impulsive maneuver magnitude. Note that Δv is included in the free variable vector and the constraint vector; this formulation was chosen for ease of extensibility to include an outbound powered flyby by simply removing the last constraint on Δv. The constraint vector includes 28 elements and the free variable vector offers 29 elements for updates. Subsequently, a pseudo-arclength continuation scheme is employed to build a family of solutions since a 1-dimensional nullspace of the Jacobian exists for each solution. Lastly, the Jacobian of the problem is defined,

$$\boldsymbol{DF} = \begin{bmatrix} \boldsymbol{\Phi}_1(T_1) & -\boldsymbol{I}_{6\times6} & \boldsymbol{0}_{6\times6} & \boldsymbol{0}_{6\times6} & \frac{\partial \vec{x}_1^t}{\partial T_1} & \frac{\partial \vec{x}_1^t}{\partial T_2} & \frac{\partial \vec{x}_1^t}{\partial \tau} & \boldsymbol{0}_{6\times1} & \boldsymbol{0}_{6\times1} \\ \boldsymbol{0}_{6\times6} & -\boldsymbol{I}_{6\times6} & \boldsymbol{\Phi}_{3^-}(-T_1) & \boldsymbol{0}_{6\times6} & \frac{\partial \vec{x}_3^{t^-}}{\partial T_1} & \frac{\partial \vec{x}_3^{t^-}}{\partial T_2} & \frac{\partial \vec{x}_3^{t^-}}{\partial \tau} & \boldsymbol{0}_{6\times1} & \boldsymbol{0}_{6\times1} \\ \boldsymbol{0}_{6\times6} & \boldsymbol{0}_{6\times6} & \boldsymbol{0}_{6\times6} & \boldsymbol{\Phi}_{3^+}(T_2) & \frac{\partial \vec{x}_3^{t^+}}{\partial T_1} & \frac{\partial \vec{x}_3^{t^+}}{\partial T_2} & \frac{\partial (\vec{x}_3^{t^+} - \vec{x}_M)}{\partial \tau} & \boldsymbol{0}_{6\times1} & \frac{\partial(-\vec{x}_M)}{\partial \theta_1} \\ \boldsymbol{0}_{3\times6} & \boldsymbol{0}_{3\times6} & \begin{bmatrix} \boldsymbol{I}_{3\times3} & \boldsymbol{0}_{3\times3} \end{bmatrix} & \begin{bmatrix} \boldsymbol{I}_{3\times3} & \boldsymbol{0}_{3\times3} \end{bmatrix} & \boldsymbol{0}_{6\times1} & \boldsymbol{0}_{6\times1} & \boldsymbol{0}_{6\times1} & \boldsymbol{0}_{6\times1} & \boldsymbol{0}_{6\times1} \\ \begin{bmatrix} \vec{v}_1 & \vec{d}_1 \end{bmatrix} & \boldsymbol{0}_{1\times6} & \boldsymbol{0}_{1\times6} & \boldsymbol{0}_{1\times6} & 0 & 0 & 0 & 0 & 0 \\ \begin{bmatrix} \frac{\vec{d}_1}{d_1} & \boldsymbol{0}_{1\times3} \end{bmatrix} & \boldsymbol{0}_{1\times6} & \boldsymbol{0}_{1\times6} & \boldsymbol{0}_{1\times6} & 0 & 0 & 0 & 0 & 0 \\ \boldsymbol{0}_{1\times6} & \boldsymbol{0}_{1\times6} & \begin{bmatrix} \vec{v}_3^- & \vec{r}_3^- \end{bmatrix} & \boldsymbol{0}_{1\times6} & 0 & 0 & 0 & 0 & 0 \\ \boldsymbol{0}_{3\times6} & \boldsymbol{0}_{3\times6} & \frac{\partial(\vec{v}_3^- + \Delta v \hat{v}_3^- - \vec{v}_3^+)}{\partial \vec{x}_3^-} & \begin{bmatrix} \boldsymbol{0}_{3\times3} & -\boldsymbol{I}_{3\times3} \end{bmatrix} & \boldsymbol{0}_{3\times1} & \boldsymbol{0}_{3\times1} & \boldsymbol{0}_{3\times1} & \hat{v}_3^- & 0 \\ \boldsymbol{0}_{1\times6} & \boldsymbol{0}_{1\times6} & \boldsymbol{0}_{1\times6} & \boldsymbol{0}_{1\times6} & 0 & 0 & 0 & 1 & 0 \end{bmatrix} \tag{4.11}$$

where $\boldsymbol{\Phi}_1(T_1)$ is the state transition matrix associated with $\vec{x}_1$, propagated for time T_1, $\boldsymbol{\Phi}_{3^-}(-T_1)$ is the state transition matrix associated with $\vec{x}_3^-$, propagated for time $-T_1$, $\boldsymbol{\Phi}_{3^+}(T_2)$ is the state transition matrix associated with $\vec{x}_3^+$, propagated for time T_2, $\boldsymbol{I}_{3\times3}$

and $\boldsymbol{I}_{6\times6}$ are identity matrices and the partial derivatives with respect to T_1, T_2, and τ, are defined,

$$\frac{\partial \vec{x}_1^t}{\partial T_1} = \dot{\vec{x}}_1^t + 2\dot{\theta}_s \frac{\partial \vec{x}_1^t}{\partial \theta_s} \tag{4.12}$$

$$\frac{\partial \vec{x}_1^t}{\partial T_2} = \dot{\theta}_s \frac{\partial \vec{x}_1^t}{\partial \theta_s} \tag{4.13}$$

$$\frac{\partial \vec{x}_1^t}{\partial T_2} = -\dot{\theta}_s \frac{\partial \vec{x}_1^t}{\partial \theta_s} \tag{4.14}$$

where $\dot{\vec{x}}_1^t$ is the time derivative of the state vector at the end of the propagation segement $\vec{x}_1$, $\dot{\theta}_s$ is the frequency of the system, and the variations $\frac{\partial \vec{x}_1^t}{\partial \theta_s}$ are numerically integrated using the equations of motion from Section 2.2.1. The time derivatives of $\vec{x}_3^{t^-}$ are defined,

$$\frac{\partial \vec{x}_3^{t^-}}{\partial T_1} = -\dot{\vec{x}}_3^{t^-} + \dot{\theta}_s \frac{\partial \vec{x}_3^{t^-}}{\partial \theta_s} \tag{4.15}$$

$$\frac{\partial \vec{x}_3^{t^-}}{\partial T_2} = \dot{\theta}_s \frac{\partial \vec{x}_3^{t^-}}{\partial \theta_s} \tag{4.16}$$

$$\frac{\partial \vec{x}_3^{t^-}}{\partial \tau} = -\dot{\theta}_s \frac{\partial \vec{x}_3^{t^-}}{\partial \theta_s} \tag{4.17}$$

and the time derivatives of $\vec{x}_3^{t^+}$ are defined,

$$\frac{\partial \vec{x}_3^{t^+}}{\partial T_1} = \mathbf{0}_{6\times1} \tag{4.18}$$

$$\frac{\partial \vec{x}_3^{t^+}}{\partial T_2} = \dot{\vec{x}}_3^{t^-} + 2\dot{\theta}_s \frac{\partial \vec{x}_3^{t^+}}{\partial \theta_s} \tag{4.19}$$

$$\frac{\partial \vec{x}_3^{t^+}}{\partial \tau} = -\dot{\theta}_s \frac{\partial \vec{x}_3^{t^+}}{\partial \theta_s} \tag{4.20}$$

where $\mathbf{0}_{6\times1}$ is a 6 element vector of zeros. The derivative of the tangential maneuver constraint with respect to the backwards propagated state is defined,

$$\frac{\partial(\vec{v}_3^- + \Delta v \hat{v}_3^- - \vec{v}_3^+)}{\partial \vec{x}_3^-} = \begin{bmatrix} \mathbf{0}_{3\times3} & \frac{\partial(\vec{v}_3^- + \Delta v \hat{v}_3^- - \vec{v}_3^+)}{\partial \vec{v}_3^-} \end{bmatrix} \tag{4.21}$$

where

$$\frac{\partial(\vec{v}_3^- + \Delta v \hat{v}_3^- - \vec{v}_3^+)}{\partial \vec{v}_3^-} = \begin{bmatrix} 1 + \frac{\Delta v}{|\vec{v}_3^-|} & 0 & 0 \\ 0 & 1 + \frac{\Delta v}{|\vec{v}_3^-|} & 0 \\ 0 & 0 & 1 + \frac{\Delta v}{|\vec{v}_3^-|} \end{bmatrix} - \frac{\Delta v}{|\vec{v}_3^-|^3} \begin{bmatrix} \dot{x}_3^- & \dot{y}_3^- & \dot{z}_3^- \\ \dot{x}_3^- & \dot{y}_3^- & \dot{z}_3^- \\ \dot{x}_3^- & \dot{y}_3^- & \dot{z}_3^- \end{bmatrix} \tag{4.22}$$

where $\dot{x}_3^-$, $\dot{y}_3^-$, and $\dot{z}_3^-$ are the velocity components of the state vector $\vec{x}_3^-$, and Δv is the maneuver magnitude. The state vector at the "step-off" point on to the manifold, $\vec{x}_M$, is defined,

$$\vec{x}_M = \vec{x}_{\text{QPO}} + \delta \frac{\Phi \vec{v}}{|\Phi \vec{v}|} \tag{4.23}$$

where $\vec{x}_{\text{QPO}}$ is the state vector on the quasi-periodic orbit at the arrival location, δ is a small perturbation value, Φ is the 6×6 state transition matrix, from the final state on the quasi-periodic orbit, $\vec{x}_0$, propagated in reverse time to the manifold trajectory connection "step off", and $\vec{v}$ is a 6×1 stable eigenvector direction at $\vec{x}_0$. The partial derivative of $\vec{x}_M$ with respect to the propagation time along the quasi-periodic, τ, is defined,

$$\frac{\partial \vec{x}_M}{\partial \tau} = \dot{\vec{x}}_{\text{QPO}} + \delta \left(\frac{\dot{\Phi} \vec{v}}{(\vec{v}^T \Phi^T \Phi \vec{v})^{\frac{1}{2}}} - \Phi \vec{v} \frac{\vec{v}^T \Phi^T \dot{\Phi} \vec{v} + \vec{v}^T \dot{\Phi}^T \Phi \vec{v}}{2(\vec{v}^T \Phi^T \Phi \vec{v})^{\frac{2}{3}}} \right) \tag{4.24}$$

where $\dot{\Phi}$ is the time derivative of the state transition matrix and $\dot{\vec{x}}_{\text{QPO}}$ is the time derivative of the state on the quasi-periodic orbit before the "step off". The derivative of the state vector with respect to the latitudinal angle, θ_1, is defined,

$$\frac{\partial \vec{x}_M}{\partial \theta_1} = \Phi \frac{\partial \vec{x}_0}{\partial \theta_1} + \delta \frac{\partial \left(\Phi \vec{v} (\vec{v}^T \Phi^T \Phi \vec{v})^{-\frac{1}{2}} \right)}{\partial \theta_1} \tag{4.25}$$

where $\frac{\partial \vec{x}_0}{\partial \theta_1}$ is defined,

$$\frac{\partial \vec{x}_0}{\partial \theta_1} = \mathrm{i} e^{\mathrm{i} \theta_1 \vec{k}} \text{diag}[\vec{k}] \boldsymbol{C}_0 \tag{4.26}$$

where $\boldsymbol{C}_0$ is defined in Equation (3.15). The second term in Equation (4.25) defined,

$$\frac{\partial\left(\Phi\vec{v}(\vec{v}^T\Phi^T\Phi\vec{v})^{-\frac{1}{2}}\right)}{\partial\theta_1}=\frac{\frac{\partial\Phi}{\partial\theta_1}\vec{v}+\Phi\frac{\partial\vec{v}}{\partial\theta_1}}{(\vec{v}^T\Phi^T\Phi\vec{v})^{\frac{1}{2}}}-\Phi\vec{v}\frac{\frac{\partial\vec{v}}{\partial\theta_1}^T\Phi^T\Phi\vec{v}+\vec{v}^T\frac{\partial\Phi}{\partial\theta_1}^T\Phi\vec{v}+\vec{v}^T\Phi^T\frac{\partial\Phi}{\partial\theta_1}\vec{v}+\vec{v}^T\Phi^T\Phi\frac{\partial\vec{v}}{\partial\theta_1}}{2\left(\vec{v}^T\Phi^T\Phi\vec{v}\right)^{\frac{3}{2}}} \tag{4.27}$$

where the term $\frac{\partial\Phi}{\partial\theta_1}$ is evaluated numerically via finite differencing and the term $\frac{\partial\vec{v}}{\partial\theta_1}$ is defined using a Fourier series to represent the stable eigenvector directions on the invariant curve,

$$\frac{\partial\vec{v}}{\partial\theta_1}=\mathrm{i}e^{\mathrm{i}\theta_1\vec{k}}\mathrm{diag}[\vec{k}]\boldsymbol{C}_s \tag{4.28}$$

where $\boldsymbol{C}_s$ is the matrix of Fourier coefficients that is constructed from the stable eigenvector directions on the invariant curve. To compute the matrix $\boldsymbol{C}_s$, the stable eigenvectors computed in Equation (3.81) are rearranged into an $N\times 6$ matrix, $\boldsymbol{V}_s$, such that the i^{th} row represents the stable eigenvector direction for the i^{th} state along the invariant curve,

$$\boldsymbol{C}_s=\boldsymbol{D}\boldsymbol{V}_s \tag{4.29}$$

where $\boldsymbol{D}$ is the discrete Fourier transform defined in Equation (3.17). This free-variable and constraint method is used to generate ballistic lunar transfers to quasi-periodic orbits in the BCR4BP.

Using an initial guess obtained from the Poincaré map in Figure 4.16a, a family of ballistic lunar transfer trajectories to an L_2 quasi-halo orbit is computed and rendered as a blue surface in 4.21 in the Earth-Moon rotating frame. The family of transfes in Figure 4.21 exists as a closed surface, which is further evidenced by the closed curve Figure 4.22b, where time-of-flight is plotted as a function of Sun angle at TLI. Note that the gold dot in Figure 4.22b corresponds to the gold trajectory in Figure 4.21. Additionally, it is useful to know where along the torus each transfer arrives. Thus, the transfer arrival locations are plotted as a blue curve on the quasi-halo torus (grey) in configuation space in Figure 4.22a. The arrival location of the gold trajectory in Figure 4.21 is indicated by the red arrow on Figure 4.22a. Constructing the family of transfers demonstrates the expanded solution space that exists by leveraging quasi-periodic orbits. By departing the Earth at any location on

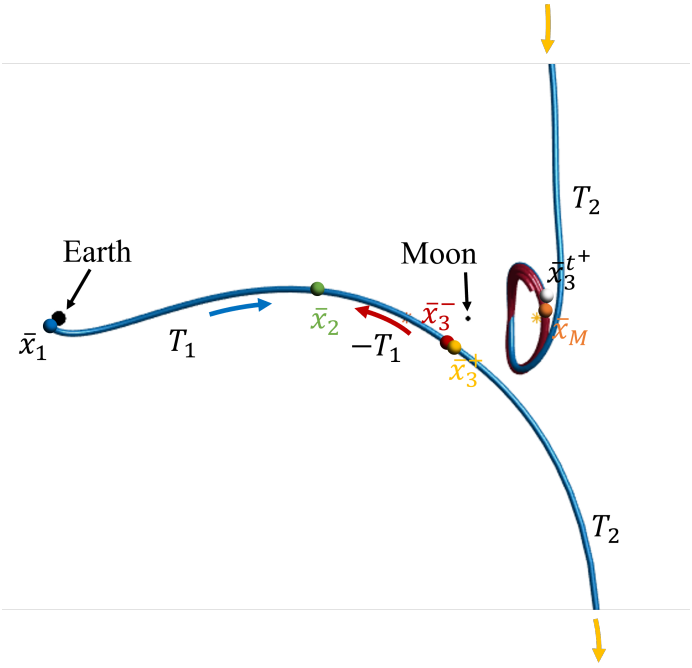

Figure 4.20. Transfer targeting illustration in the BCR4BP. The arrows indicate the direction along the shooting leg for the differential corrector. Note the trajectory segments near the cislunar region are displayed. The blue arc indicates.

the surface in Figure 4.21 at the proper epoch, the path flows (maneuver-free) into the L_2 quasi-halo orbit.

A family of transfer solutions is also generated to an L_1 quasi-halo orbit using an initial guess produced from a stable manifold periapsis map. The same targeting scheme yields a family of solutions that arrives onto an L_1 quasi-halo orbit. The complete family of solutions is difficult to visualize, since members intersect in configuration space, so only a few members of the family are plotted in Figure 4.23 in the Sun-B_1 rotating frame. Additionally, the departure location from Earth and the arrival locations along the quasi-halo surface are plotted in the Earth-Moon rotating frame in Figures 4.24a and 4.24b, respectively. The discrete points representing arrival locations along the torus in Figure 4.24b appears to represent a jagged curve; however, the points represent a smooth curve, indicating it is a single, continuous family of solutions.

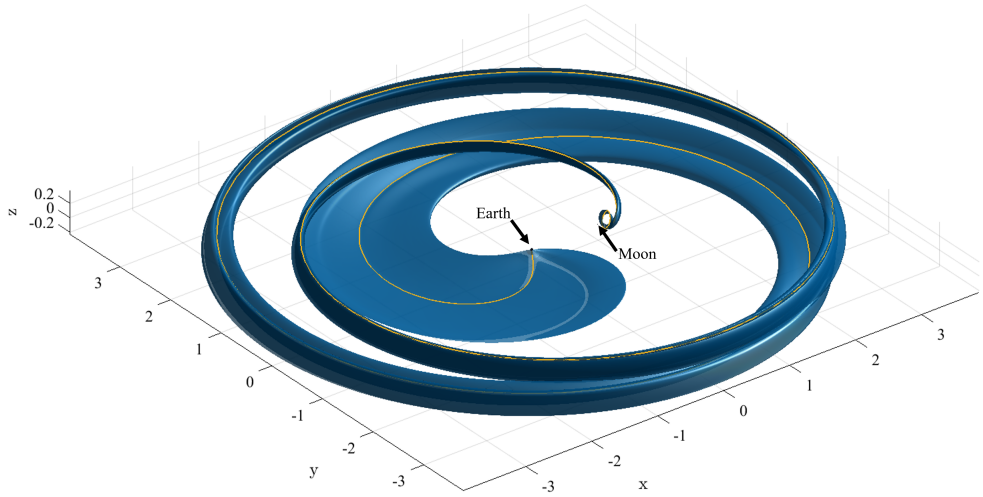

Figure 4.21. Family of maneuver-free ballistic lunar transfers to an L_2 quasi-halo orbit. A single trajectory from the family is represented in gold.

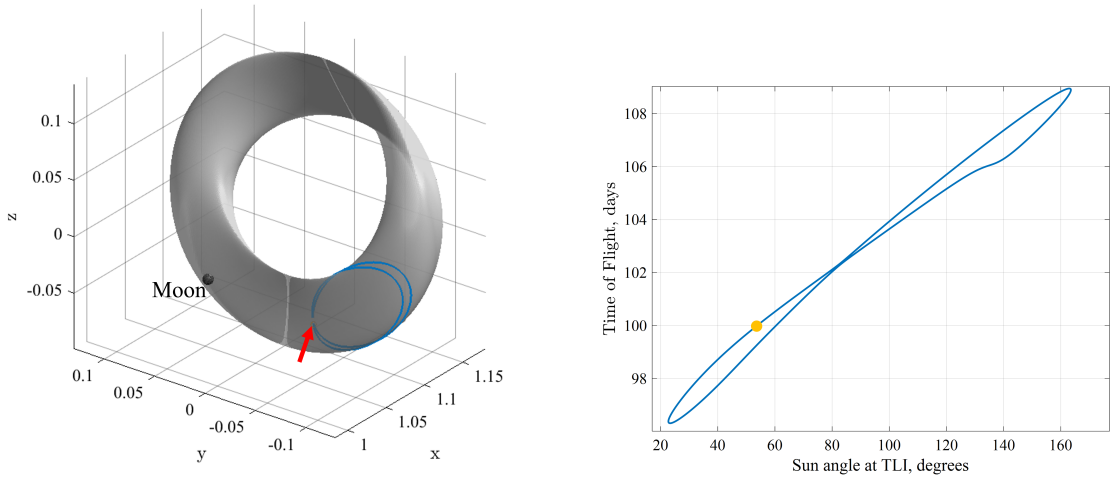

a b

Figure 4.22. (a) The destination L_2 quasi-halo orbit (grey) with the transfer arrival locations (blue) plotted in the Earth-Moon rotating frame. The red arrow corresponds to the arrival location of the gold trajectory from Figure 4.21 (b) Time of flight as a function of the Sun angle at TLI; the small gold circle represents the gold trajectory from the family in Figure 4.21.

Transfers that possess no maneuver along the transfer path are most fuel efficient to reach a particular destination. However, introducing maneuvers along the path expands the solution space and the accessibility to a particular orbit. Consider a family of BLTs to an

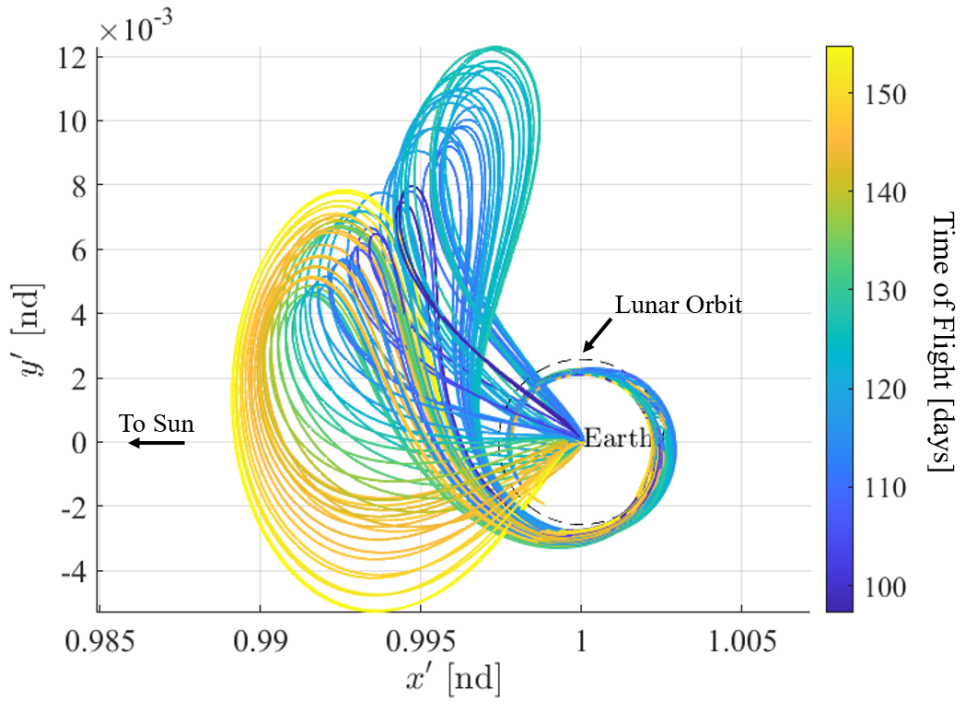

Figure 4.23. Members of a transfer family to an L_1 quasi-halo orbit in the Sun-B_1 rotating frame colored by time of flight.

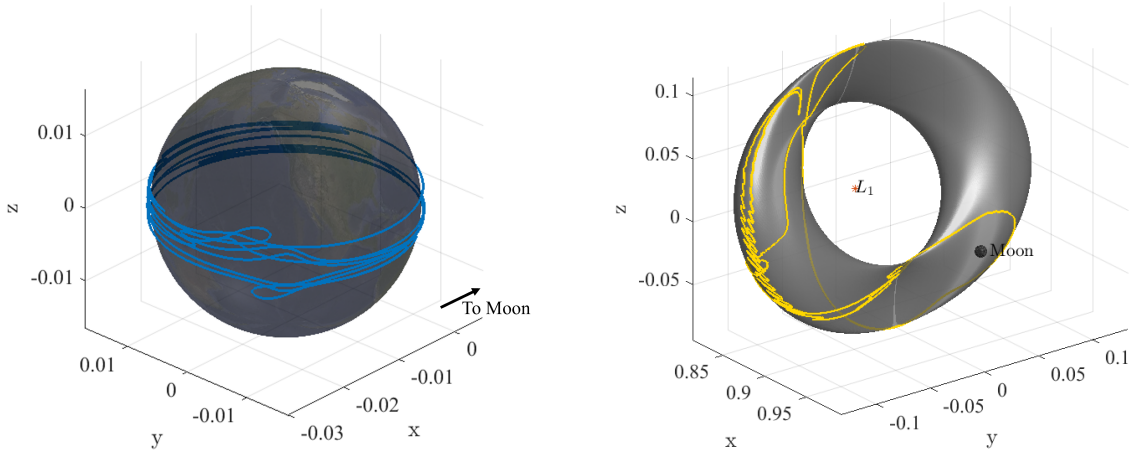

a b

Figure 4.24. (a) Departure locations from Earth for the family of transfers to an L_1 quasi-halo orbit. (b) Arrival locations (gold) on the L_1 quasi-halo orbit for the family of ballistic transfers.

L_2 quasi-vertical orbit, rendered as the blue surface in Figure 4.25a. Lunar flyby altitude is plotted as a function of the arrival Sun angle in Figure 4.25b as well. Note that the surface representing the flow on the family collapses to a tighter set of paths in configuration space after the flyby. To expand this solution space, a maneuver is introduced at the lunar encounter and the altitude is constraint to be equal to 2000 km. The constraint vector in Equation (4.9) is modified such $\Delta v = 0$ is replaced with an altitude constraint, defined,

$$F_{\text{alt}} = |\vec{r_3^-}|^2 - (a + R_M)^2 = 0 \tag{4.30}$$

where $\vec{r_3^-}$ is the position vector relative to the Moon at Node 3, a is the desired altitude (i.e., 2000 km), and $R_M = 1737$ km is the nominal radius of the Moon. Segments along a member of the family are represented in Figure 4.26a. The maneuver at the flyby is equal to $\Delta v = 150$ m/s for this transfer. The Δv is plotted as a function of the arrival Sun angle for the family of solutions with a constrained 2000 km flyby altitude in Figure 4.26b. Note that there are two zero-Δv solutions in this family that correspond to the two solutions in Figure 4.25a that possess a precisely 2000 km flyby altitude. Leveraging a powered flyby expands the available transfer options for a particular destination orbit.

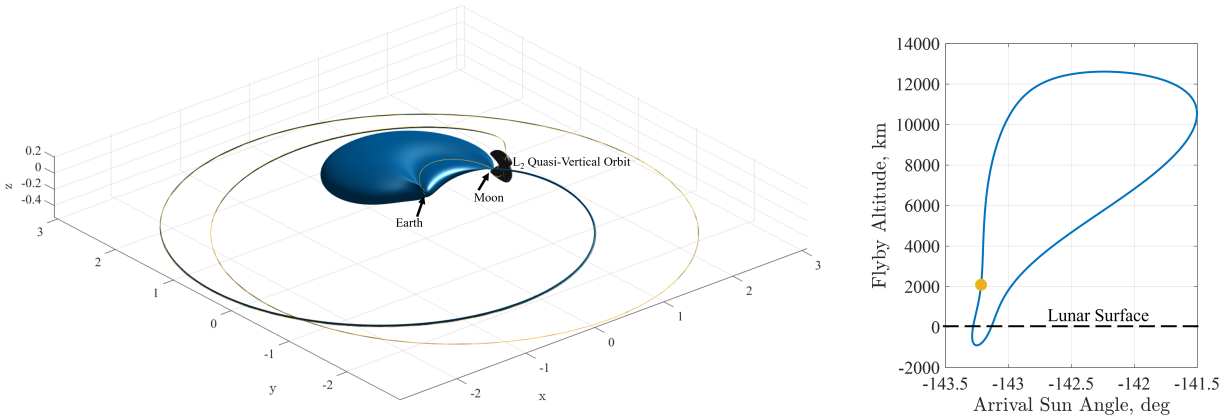

a b

Figure 4.25. (a) Family of solutions to an L_2 quasi-vertical orbit (blue surface). A single trajectory from the family is represented by in gold and the destination quasi-vertical orbit (grey surface). (b) The flyby altitude is plotted as a function of arrival Sun angle. The gold point corresponds to the gold trajectory in (a).

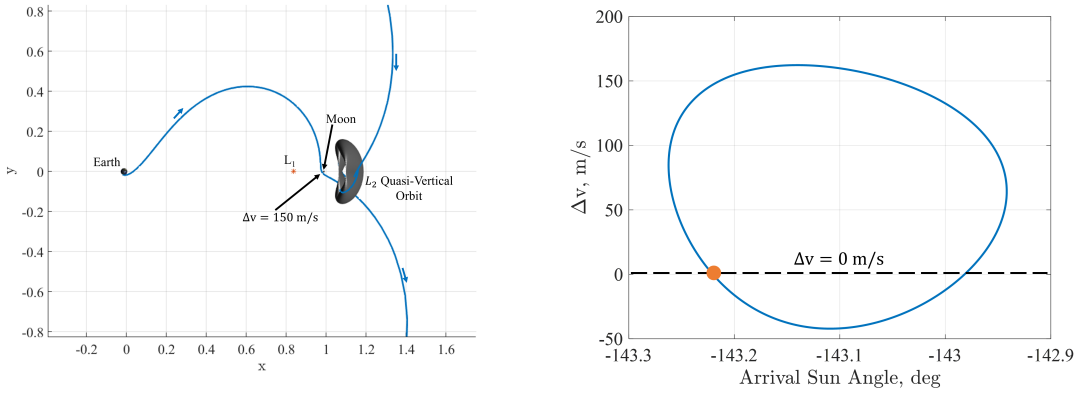

a b

Figure 4.26. (a) A member of the 2000 km altitude transfer family to an L_2 quasi-vertical orbit (grey surface) that leverages a powered flyby. (b) The magnitude of the Δv maneuver as a function of arrival Sun angle for the family of solutions constrained to have a 2000 km outbound lunar flyby. The zero-Δv transfer highlighted in orange corresponds to the gold trajectory in Figure 4.25a.

4.4.3 Families of Transfers to Various Destinations

Families of transfers to a particular destination orbit are useful for certain mission profiles; however, if the destination orbit changes, flexibility in the design process is critical to effectively produce a new path. Subsequently, it is also important to understand transfer solutions to nearby destination orbits. Consider the family of transfers to the L_2 quasi-halo orbit represented in Figure 4.21. One property of this family that it is bounded by the surface represented in Figure 4.21. When the time-of-flight is plotted as a function of the initial Sun angle, a closed curve is also formed. Effectively, the family of transfers repeats on itself after the continuation scheme has completed. To visual represent this phenomenon more clearly, the same family of transfers to the L_2 quasi-halo orbit is rendered in the Sun-B_1 rotating frame in Figure 4.27. The surface is "sliced" at a particular time to show a cross section of the surface. Thus, it is apparent that the transfer family in Figure 4.27 forms a closed "tube" that originates at Earth departure and flows into to the destination orbit. Exploring this phenomenon further and understand the motion inside of the "tube", the destination orbit is changed to a different L_2 quasi-halo orbit and a family of transfers is recomputed for that

orbit. This process is repeated for several orbits in the quasi-halo family and the sections of the surfaces of transfer families are rendered in Figure 4.28a. The outermost surface in Figure 4.28a is the same family rendered in Figure 4.27. Note that transfer families to a different destination quasi-halo orbits are represented as a blue-shaded surfaces and occupy space inside of the initial transfer family. The time-of-flight as a function of Sun angle at TLI is also plotted in Figure 4.28b. Each curve corresponds to a transfer family associated with a different destination L_2 quasi-halo orbit. Some of the tori of the destination quasi-halo orbits are rendered on the right side of Figure 4.28b. Also note that when the destination quasi-halo orbit collapses to the periodic 2:1 L_2 resonant halo orbit, a single point ballistic transfer solution remains. This point solution is represented by the red star in Figure 4.28b. By generating families of transfers to various destinations, a transfer "corridor" is illustrated to reach quasi-halo motion in the vicinity of the L_2 libration point. For this transfer geometry, when the spacecraft is inserted at the proper Sun-Earth-Moon orientation in the flow, it falls into quasi-halo motion in the vicinity of L_2.

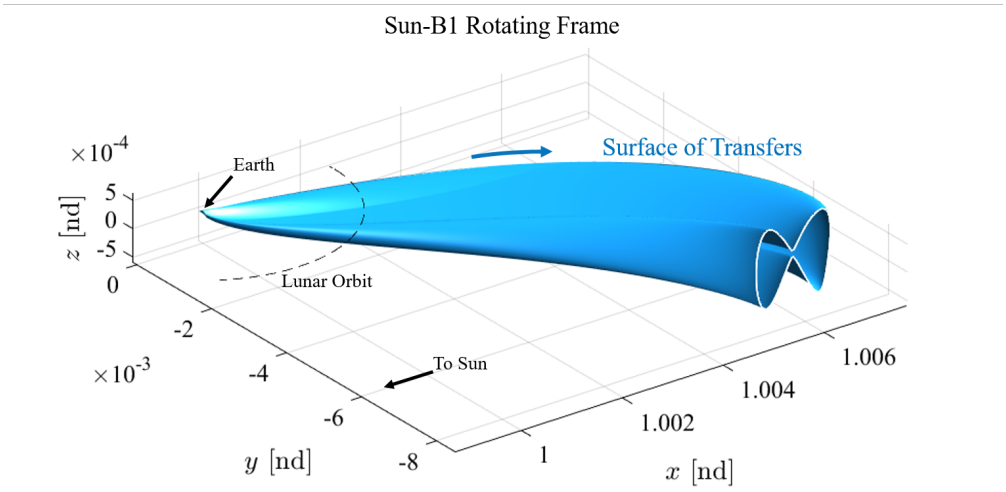

Figure 4.27. Surface representing the family of transfers to the L_2 quasi-halo orbit in Figure 4.22a in the Sun-B_1 rotating frame. The trajectories representing the family are propagated for 50 days to show the cross section of the surface. The blue arrow indicates the direction of motion.

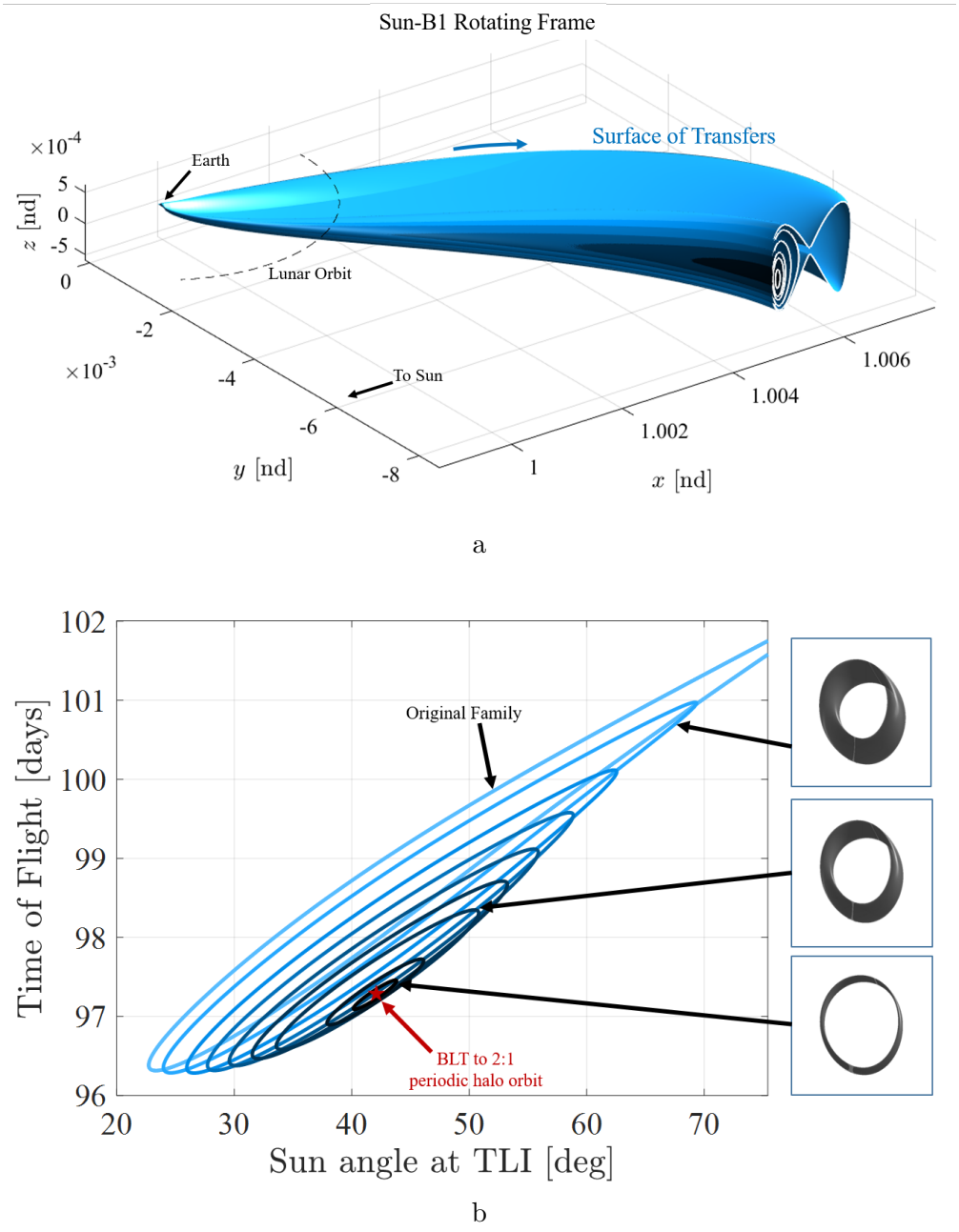

Figure 4.28. (a) Surfaces representing transfer families to various Type A L_2 quasi-halo orbit destinations. The blue arrow indicates the direction of motion. (b) Time of flight as a function of the Sun angle at TLI for families of transfers to other quasi-halo destinations in the quasi-halo Type A family. The outermost curve is the same curve from Figure 4.22b

4.4.4 Ephemeris Validation

The BCR4BP offers a good approximation for the dynamical behavior associated with low-energy transfers that rely on the coupled motion of the Earth, Moon, and Sun; however, validation of the solutions in a higher-fidelity ephemeris model is also important in the design process. Two steps are generally employed to transition a solution from the BCR4BP to an ephemeris model. The first step is the selection of an appropriate Julian date that corresponds to the Sun-Earth-Moon geometry from the BCR4BP solution. The second step employs a specific multiple shooting differential corrections strategy to successfully transition a solution into an ephemeris force model and simultaneously retain the desirable characteristics.

Step 1: Julian Date Selection

The first step to transition a trajectory design concept to an ephemeris model involves the selection of a Julian date that best aligns with the Sun-Earth-Moon geometry from the BCR4BP solution. As noted in Section 2.2, an assumption in this formulation of the BCR4BP is that the Sun, Earth, and Moon are in the same plane of motion, i.e., $\hat{z} = \hat{z}'$. However, the true motion is not coplanar. The inclination of the lunar orbit relative to the ecliptic plane is approximately 5.16 degrees [102]. To accommodate for this discrepancy, an approximate Julian date is selected to seed a search for the appropriate Sun-Earth-Moon orientation that is associated with the particular Sun angle, θ_S. The search uses a bisection method to determine a Julian date such that the angle between Sun-Earth line and the projection of the Moon's location into the ecliptic plane is equal to $\pi - \theta_S$. The search is implemented in both forward and backward time; the final selected Julian date is one that is closest to the original Julian date employed to seed the search. The angle definition and the geometry of the lunar position as projected into the ecliptic plane is illustrated in Figure 4.29. The result of the search supplies a good initial guess for the Sun-Earth-Moon geometry in the ephemeris model for transition of a state from the BCR4BP. The framework for the search algorithm is leveraged for each discretized node as described later in Step 2. Additionally,

the actual epoch for mission considerations is accomplished later via a continuation in the ephemeris model.

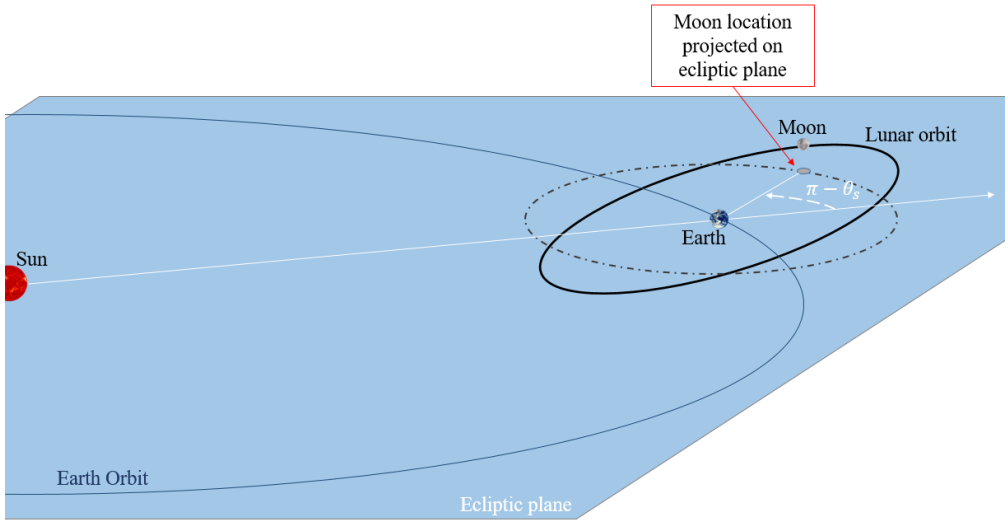

Figure 4.29. Diagram of Julian date selection from Sun angle, θ_S.

Step 2: Multiple Shooting Differential Corrections

A free-variable/constraint differential corrections approach is constructed to transition a trajectory from the BCR4BP to the ephemeris model. First, the BCR4BP trajectory is discretized into a set of nodes, or patch points. Each node is associated with a 6-element state vector, a Sun angle, and a propagation time. Next, the Julian date is selected for the first node along the trajectory using the search strategy from Step 1. The search is seeded with a user-selected Julian date. For subsequent nodes, the search is seeded with the Julian date corresponding to the previous node and advanced by the corresponding change in time from the previous node; the initial guess is seeded in this manner so the search algorithm converges on the nearest Sun-Earth-Moon geometry in forward time. Additionally, a number of nodes for several revolutions along the destination orbit are included in the differential corrections formulation. Finally, the state vector associated with each node is transformed from the barycentered Earth-Moon rotating frame to a primary-centered J2000 inertial frame. The free variable vector is constructed using the elements of the state

vector, the times of flight, and the epoch times associated with each node. State and epoch time continuity are constrained between successive nodes; additionally, the initial state is constrained to a 150-km altitude perigee to represent a post-translunar injection state.

Using one of the ballistic lunar transfers to an L_2 quasi-halo orbit that possesses a leading side flyby from Figure 4.19b, the initial guess from the BCR4BP is converged into a Sun-Earth-Moon point mass ephemeris model and the resulting ephemeris trajectory (blue) is rendered in the Earth-Moon rotating frame in Figure 4.30a along with the initial BCR4BP initial guess (orange). A close view of the encounter with the Moon and the arrival along the quasi-halo orbit are also rendered in Figure 4.30b. The resulting trajectory possesses an initial epoch of Dec 26 2023 12:11:50. The trajectory remains purely ballistic in the ephemeris model and the general geometry associated with the transfer is consistent with the original design that delivered the initial guess from the BCR4BP. Additionally, a similar result in geometry consistency is present when transitioning a ballistic lunar transfer to the quasi-halo orbit that possesses a trailing side lunar flyby. The BCR4BP solution (blue) and associated ephemeris solution (orange) of one of the members from family of transfer computed from the initial guess provided in Figure 4.19b is rendered in the Earth-Moon rotating frame in Figure 4.31.

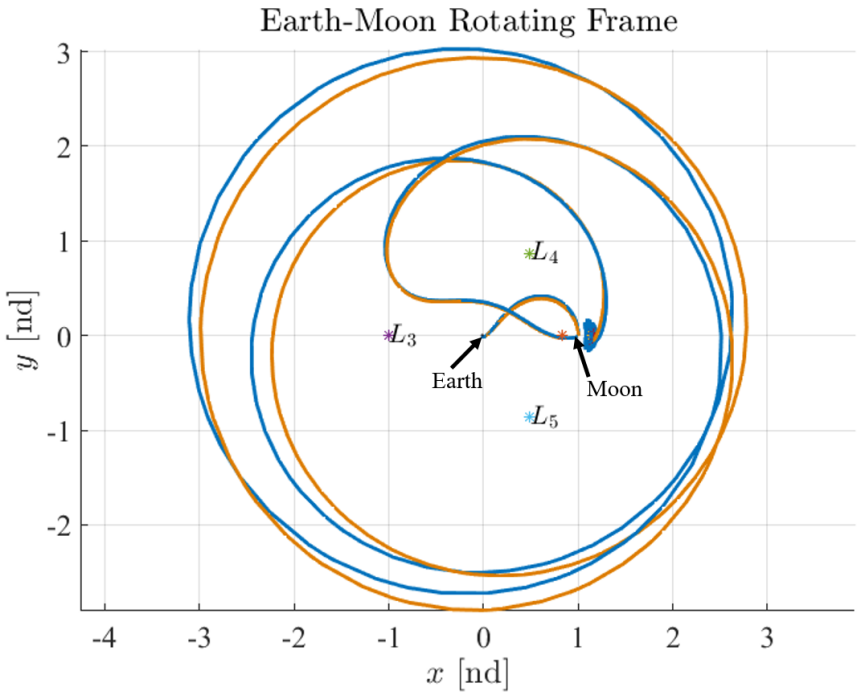

a

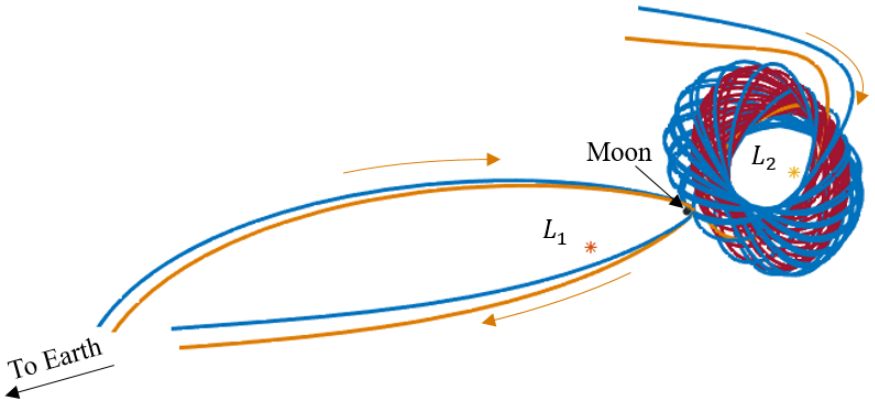

b

Figure 4.30. (a) Ballistic lunar transfer to an L_2 quasi-halo orbit converged in Sun-Earth-Moon point mass ephemeris model (blue) and the BCR4BP as an initial guess (orange). The trajectory is plotted in the Earth-Moon rotating frame. (b) Zoomed view of the lunar encounter and the arrival on the quasi-halo orbit in the Earth-Moon rotating frame. The ephemeris solution is plotted in blue and the BCR4BP initial guess is plotted in orange with the destination quasi-halo orbit from the BCR4BP in red. The orange arrows indicate the direction of motion.

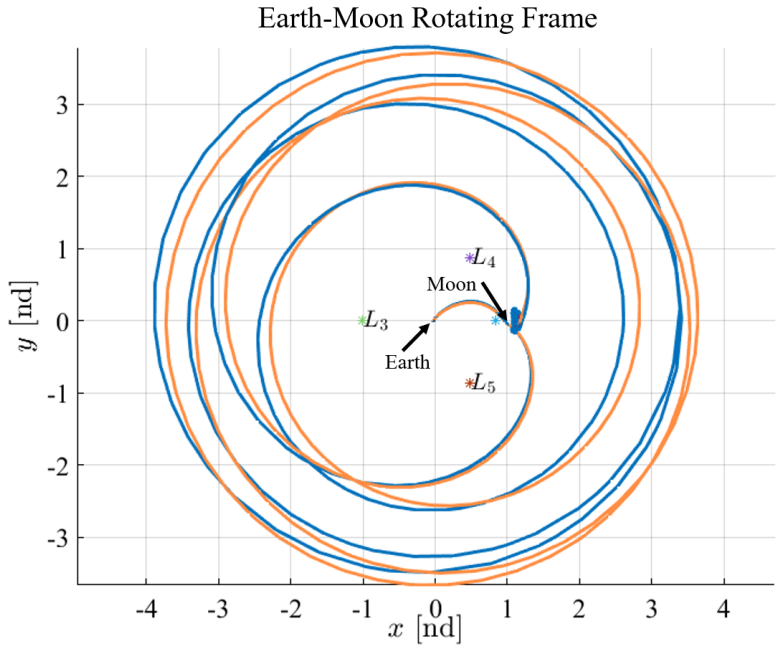

Figure 4.31. Ballistic lunar transfer possessing a trailing side outbound flyby to an L_2 quasi-halo orbit converged in Sun-Earth-Moon point mass ephemeris model (blue) and the BCR4BP as an initial guess (orange). The trajectory is plotted in the Earth-Moon rotating frame.

5. CONCLUDING REMARKS

As missions to cislunar space leverage more multi-body dynamical structures, an effective strategy to incorporate these structures into the design process is required. This investigation provides a framework to incorporate a broad class of these dynamical structures: quasi-periodic orbits. An efficient method to compute quasi-periodic orbits in two multi-body models is presented. Then, a series of relevant cislunar applications are presented to demonstrate the utility of quasi-periodic motion. The methodologies presented in this investigation leverage several dynamical systems theory techniques to identify and construct desired paths. The results of the investigation are summarized below.

5.1 Computation of Quasi-Periodic Orbits

A computational framework for construction of quasi-periodic orbits in the CR3BP and the BCR4BP is outlined leveraging a differential corrections process formulated by four previous authors [25], [26]. An invariance constraint is summarized that provides the foundation for the computation algorithm. This algorithm is extended to the BCR4BP to examine motion in the Sun-perturbed Earth-Moon neighborhood. The invariance constraint is also extended to computation of 3-dimensional tori in the CR3BP and BCR4BP, which proves to be computationally intensive. Subsequently, the computational framework in this investigation provides a means to explore a wide range of quasi-periodic motion within cislunar space.

Families of two- and three-dimensional quasi-periodic tori in the CR3BP are presented. Three types of quasi-periodic orbit families are characterized in the CR3BP. In the BCR4BP, two methods are presented to provide an initial guess to compute quasi-periodic orbits. The first method relies on leveraging the center subspace of a periodic orbit from the BCR4BP, similar to how initial guesses are constructed in the CR3BP. A second method is presented that transitions periodic orbits from the CR3BP to quasi-periodic orbits in the BCR4BP. To perform this transition, the BCR4BP is formulated into a periodically perturbed Earth-Moon CR3BP that possesses a single parameter to scale the mass of the Sun into the model. Both of these techniques provide an understanding of how the solar gravity affects the motion in

cislunar space; in particular, how structures computed in the BCR4BP relate to structures found in the Earth-Moon CR3BP.

Finally, linear stability of quasi-periodic orbits is summarized and a stability metric is defined to conveniently characterize stable and unstable quasi-periodic orbits. For orbits characterized as unstable, the process to compute trajectories that represent the stable and unstable manifolds is detailed. These manifold trajectories provide maneuver-free paths into and out of their associated orbit and provide the foundation for the transfer trajectory applications in this investigation.

5.2 Novel Transfer Design Techniques

This investigation also summarizes methods to construct transfer trajectories throughout cislunar space that leverage quasi-periodic motion. Several applications are initially examined to perform transfers in the vicinity of the Moon. First, a simple transfer application between two periodic L_2 NRHOs is explored. A single trajectory arc from a quasi-periodic orbit is leveraged as an initial guess to transfer between the orbits. Second, a more complex scenario is examined which leverages several arcs to transfer between a planar periodic orbit and an out-of-plane NRHO. The first geometry is constructed leveraging trajectory arcs associated with quasi-periodic orbit in the vicinity to "slide" up from the planar orbit to the NRHO. The second transfer geometry is constructed from an arc from a quasi-periodic orbit and an associated manifold trajectory. Poincaré mapping is also employed to aid in identification of a suitable initial guess for a differential corrections process to construct an end-to-end transfer. Lastly, a heteroclinic transfer scenario between two quasi-periodic orbits is examined in the vicinity of the Moon. By constraining the Jacobi Constant between the departing and destination orbit to be equal, families of heteroclinic connections are constructed using a differential corrections process coupled with natural parameter continuation. To validate that each of these transfer solutions is applicable to a higher fidelity space environment, the Lyapunov orbit to NRHO transfers and an example heteroclinic transfer are transitioned into a Sun-Earth-Moon ephemeris model and the geometry characteristics are maintained.

Applications to construct and characterize ballistic lunar transfers to quasi-periodic orbits are also examined within the BCR4BP. First, periapsis Poincaré maps are exploited to isolate point solutions of interest. Depending on the type of transfer characteristics desired, i.e., shorter time of flight, or incorporating a lunar flyby, the points on the map are colored identify those transfer characteristics. Using initial guesses obtained from the periapsis maps, two types of families of ballistic lunar transfers are constructed to a desired destination orbit. First, maneuver-free families are constructed to demonstrate that no deterministic Δv is required for a wide range of Sun-Earth-Moon geometries. Second, families of transfer that include a powered lunar flyby are constructed to expand the solution space further. Families of transfers are constructed for spatial orbits in the vicinity of L_1 and L_2 to demonstrate the flexibility of the strategy. While it is useful to have a family of solutions to a particular destination orbit, a strategy to generate a continuum of transfers to a type of desired motion was investigated. Subsequently, a "corridor" of transfers was generated by computing a family of transfers to various destination orbits within the L_2 quasi-halo family. When the destination quasi-periodic orbit collapses to the underlying periodic orbit, a point transfer solution associated with that transfer geometry emerges. Using a two-step transition process, two solutions from the BCR4BP are transitioned to the Sun-Earth-Moon ephemeris model to validate their existence in a higher fidelity model. The framework to construct end-to-end ballistic lunar transfers demonstrates that the BCR4BP is a useful model to capture the fundamental motion that is simultaneously influenced by the Sun, Earth, and Moon.

5.3 Recommendations for Future Work

Several areas of future work are recommended that could augment this investigation. The areas are summarized as follows:

- *Further explore the relationship between quasi-periodic orbits in the BCR4BP and how they relate to periodic solutions in the CR3BP*

  While the relationships between quasi-periodic orbits in the CR3BP have been studied, less is understood about quasi-periodic orbit families in the BCR4BP. This investigation provides a cursory look into the types of motion that exist, but a more extensive

investigation would provide more insight into the Sun-perturbed Earth-Moon neighborhood. By providing a robust bifurcation detection process across a family in the BCR4P, relationships to other families will become more apparent. This investigation also did not encompass motion in the vicinity of L_3, L_4, and L_5, which would be of interest to examine. Additionally, this investigation formulates the equations of motion for the BCR4BP as a Sun-perturbed Earth-Moon CR3BP using a parameter to scale the Sun mass. However, this investigation does not extensively explore the transition process. Further exploring the transition between the CR3BP and the BCR4BP would provide insight into how solar gravity affects the motion in cislunar space.

- *Explore quasi-periodic orbits and applications in other formulations of the four-body problem*

  The BCR4BP was the primary four-body model for this investigation; however, other four-body models may provide additional insight into regions where the assumptions of the BCR4BP break down. For example, the quasi-bicircular four-body problem attempts to more accurate represent the Sun-perturbed Earth-Moon motion. Andreu examined the quasi-bicircular problem extensively and the framework for computing ballistic lunar transfers presented in this investigation could be extended into the quasi-bicircular model [48]. An analysis of transitioning ballistic lunar transfer computed in the quasi-bicircular model would be insightful. Lastly, extending computation and applications to a planet-moon-moon-spacecraft four-body problem could provide insight for path planning in other planetary systems.

- *Characterizing families of heteroclinic connections in the CR3BP and BCR4BP*

  This investigation summarized a Poincaré mapping technique and a differential corrections process to compute families of heteroclinic connections between quasi-periodic orbits in the CR3BP. One of the difficulties associated with this process was computation of partial derivatives associated when the departing and/or destination orbit is allowed to vary. A more extensive investigation would allow for a more effective computation algorithm and provide insight into more types of heteroclinic transfer ge-

ometries. Lastly, extending this strategy to the BCR4BP would provide insight into how heteroclinic connections behave in the Sun-perturbed cislunar region.

- *Incorporating low thrust into quasi-periodic orbit applications*

  Impulsive maneuvers were only considered for constructing ballistic lunar transfer in this investigation. However, low thrust propulsion capabilities could provide more efficient mission profiles to reach the Moon while leveraging solar gravity. Additionally, a low thrust spacecraft could be used to change the Jacobi Constant when considering a connection between two quasi-periodic orbits in the CR3BP. By including low thrust control, more transfer geometries could be considered.

REFERENCES

[1] T. Bayer, B. Cooke, I. Gontijo, and K. Kirby, "Europa Clipper mission: the habitability of an icy moon," in *IEEE Aerospace Conference*, Big Sky, Montana, Jun. 2015.

[2] K. Norton, "NASA's Dragonfly Will Fly Around Titan Looking for Origin, Signs of Life," *web*, Jun. 2019, https://www.nasa.gov/press-release/nasas-dragonfly-will-fly-around-titan-looking-for-origins-signs-of-life. [Online]. Available: https://www.nasa.gov/feature/nasa-outlines-lunar-surface-sustainability-concept.

[3] K. Hambleton, "Deep Space Gateway to Open Opportunities for Distant Destinations," *web*, Mar. 2017, https://www.nasa.gov/feature/deep-space-gateway-to-open-opportunities-for-distant-destinations. [Online]. Available: https://www.nasa.gov/feature/deep-space-gateway-to-open-opportunities-for-distant-destinations.

[4] National Aeronautics and Space Administration, "NASA's Lunar Exploration Program Overview," Sep. 2020.

[5] D. E. Lee, "Gateway Destination Orbit Model: A Continuous 15 Year NRHO Reference Trajectory," National Aeronautics and Space Administration, Houston, Texas, Tech. Rep. JSC-E-DAA-TN72594, Aug. 2019.

[6] K. K. Boudad, D. C. Davis, and K. C. Howell, "Disposal Trajectories From Near Rectilinear Halo Orbits," in *AAS/AIAA Astrodynamics Specialist Conference*, Snowbird, Utah, Aug. 2018.

[7] N. L. Parrish, E. Kayser, S. Udupa, J. S. Parker, B. W. Cheetham, and D. C. Davis, "Survey of Ballistic Lunar Transfers to Near Rectilinear Halo Orbit," in *AAS/AIAA Astrodynamics Specialist Conference*, Portland, Maine, Aug. 2019.

[8] I. Newton, *The Principia: Mathematical Principles of Natural Philosophy*, I. B. Cohen and A. Whitman, Eds. University of California Press, 1999.

[9] L. Euler, "De motu rectilineo trium corporum se mutuo attrahentium," *Novi Commentarii academiae scientiarum Petropolitanae*, vol. 11, pp. 144–151, 1767.

[10] J.-L. Lagrange, "Essai sur le problème des trois corps," *Oeuvres de Lagrange*, vol. 6, pp. 229–332, 1772.

[11] C. G. J. Jacobi, "Sur le movement d'un point et sur un cas particulier du problème des trois corps," *Comptes Rendus de l'Académie des Sciences de Paris*, vol. 3, pp. 59–61, 1836.

[12] G. W. Hill, "Researches in the Lunar Theory," *American Journal of Mathematics*, vol. 1, no. 1, pp. 5–26, 1878.

[13] J. H. Poincaré, *Les Méthodes Nouvelles de la Mécanique Céleste*. 1892-1899, vol. 1-3, Republished by Blanchard, Paris, 1987.

[14] A. N. Kolmogorov, "On the conservation of conditionally periodic motions uner small perturbations of the hamiltonian," *Dokl. Akad. Nauk, SSSR*, vol. 98, pp. 527–530, 1954.

[15] J. Moser, "On invariant curves of area-preserving mappings of an annulus," *Nachr. Akad. Wiss., Göttingen, Math. Phys. Kl.*, pp. 1–20, 1962.

[16] V. I. Arnold, "Proof of a theorem of A. N. Kolmogorov on the preservation of conditionally periodic motions under a small perturbation of the Hamiltonian," *Uspehi Mat. Nauk*, vol. 18, no. 5, pp. 13–40, 1963.

[17] V. Szebehely, *The Theory of Orbits: The Restricted Problem of Three Bodies*. New York, New York: Academic Press, Inc, 1967.

[18] R. W. Farquhar and A. A. Kamel, "Quasi-Periodic Orbits About the Translunar Libration Point," *Celestial Mechanics*, vol. 7, no. 4, pp. 458–473, Jun. 1973.

[19] D. L. Richardson and N. D. Cary, "A Uniformly Valid Solution for Motion About the Interior Libration Point of the Perturbed Elliptic-Restricted Problem," in *AAS/AIAA Astrodynamics Specialist Conference*, Nassau, Bahamas, Jul. 1975.

[20] G. Gómez, J. Masdemont, and C. Simó, "Quasihalo Orbits Associated with Libration Points," *Journal of the Astronautical Sciences*, vol. 46, pp. 135–176, Mar. 1999.

[21] G. Gomez and M. Noguera, "Some manifolds of periodic orbits in the restricted three-body problem," *Celestial Mechanics and Dynamical Astronomy*, vol. 35, no. 3, pp. 235–255, Jan. 1985.

[22] K. C. Howell and H. J. Pernicka, "Numerical Determination of Lissajous Trajectories in the Circular Restricted Three-Body Problem," *Celestial Mechanics*, vol. 41, no. 1-4, pp. 107–124, 1988.

[23] F. Schilder, H. M. Osinga, and W. Vogt, "Continuation of Quasi-periodic Invariant Tori," *SIAM Journal on Applied Dynamical Systems*, vol. 4, no. 3, pp. 459–488, 2005.

[24] A. Jorba and E. Olmeda, "On The Computation of Reducible Invariant Tori on a Parallel Computer," *SIAM Journal on Applied Dynamical Systems*, vol. 8, pp. 1382–1404, Jan. 2009.

[25] G. Gomez and J. M. Mondelo, "The Dynamics Around the Collinear Equilibrium Points of the RTBP," *Physica D: Nonlinear Phenomena*, vol. 157, no. 4, pp. 283–321, Oct. 2001.

[26] Z. P. Olikara and D. J. Scheeres, "Numerical Methods for Computing Quasi-Periodic Orbits and Their Stability in the Circular Restricted Three-Body Problem," in *IAA Conference on Dynamics and Control of Space Systems*, Porto, Portugal, Mar. 2012.

[27] Z. Olikara, "Computation of Quasi-Periodic Tori and Heteroclinic Connections in Astrodynamics Using Collocation Techniques," Ph.D. Dissertation, University of Colorado, Boulder, Boulder, Colorado, Jan. 2016.

[28] N. Baresi, Z. P. Olikara, and D. J. Scheeres, "Fully Numerical Methods for Continuing Families of Quasi-Periodic Invariant Tori in Astrodynamics," *Journal of Astronautical Sciences*, vol. 65, no. 2, Jun. 2018.

[29] Á. Haro, M. Canadell, J.-L. Figueras, A. Luque, and J. M. Mondelo, *The Parameterization Method for Invariant Manifolds*. Springer International Publishing, 2016, vol. 195, ISBN: 978-3-319-29660-9.

[30] R. L. Anderson, R. W. Easton, and M. W. Lo, "Computing libration point isolated invariant sets using isolating blocks," *Physica D: Nonlinear Phenomena*, vol. 405, Apr. 2020.

[31] B. Kumar, R. Anderson, and R. de la Llave, "Rapid and Accurate Methods for Computing Whiskered Tori and Their Manifolds in Periodically Perturbed Planar Circular Restricted 3-Body Problems," *Celestial Mechanics and Dynamical Astronomy*, vol. 134, no. 3, Jan. 2022.

[32] R. Farquhar, D. Muhonen, and L. C. Church, "Trajectories and Orbital Maneuvers for the ISEE-3/ICE Comet Mission," *Journal of the Astronautical Sciences*, vol. 33, no. 3, pp. 235–254, 1985.

[33] C. E. Roberts, "Long Term Missions at the Sun-Earth Libration Point L1: ACE, WIND, and SOHO," in *AAS/AIAA Astrodynamics Specialist Conference*, Girdwood, Alaska, Aug. 2011.

[34] C. Roberts, S. Case, J. Reagoso, and C. Webster, "Early Mission Maneuver Operations for the Deep Space Climate Observatory Sun-Earth L1 Libration Point Mission," in *AAS/AIAA Astrodynamics Specialist Conference*, Vail, Colorado, Aug. 2015.

[35] J. Peterson, "L2 Station Keeping Maneuver Strategy for the James Webb Space Telescope," in *AAS/AIAA Astrodynamics Specialist Conference*, Portland, Maine, Aug. 2019.

[36] R. L. Restrepo, R. P. Russell, and M. W. Lo, "Europa Lander Trajectory Design Using Lissajous Staging Orbits," in *AAS/AIAA Astrodynamics Specialist Conference*, Snowbird, Utah, Aug. 2018.

[37] N. Baresi and D. J. Scheeres, "Quasi-Periodic Invariant Tori of Time-Periodic Dynamical Systems: Applications to Small Body Exploration," in *International Astronautical Congress*, Guadalajara, Mexico, Sep. 2016.

[38] B. Barden and K. C. Howell, "Fundamental Motions Near Collinear Libration Points and Their Transitions," *Journal of the Astronautical Sciences*, vol. 46, no. 4, pp. 361–378, Dec. 1998.

[39] N. Baresi, "Spacecraft Formation Flight on Quasi-Periodic Invariant Tori," Ph.D. Dissertation, University of Colorado, Boulder, Boulder, Colorado, Jan. 2017.

[40] D. B. Henry and D. J. Scheeres, "Generalized Spacecraft Formation Design through Exploitation of Quasi-Periodic Tori Families," in *AIAA SciTech 2020 Forum*, Orlando, Florida, Jan. 2020.

[41] D. Guzzetti, R. Sood, L. Chappaz, and H. Baoyin, "Stationkeeping Analysis for Solar Sailing the L4 Region of Binary Asteroid Systems," *Journal of Guidance, Control, and Dynamics*, vol. 42, no. 6, Jun. 2019.

[42] A. F. Mora and J. Heiligers, "Solar Sail Quasi-Periodic Orbits in the Sun-Earth System," *Journal of Guidance, Control, and Dynamics*, vol. 43, no. 9, Sep. 2020.

[43] A. Farres and A. Jorba, "Periodic and Quasi-Periodic Motions of Solar Sail Close SL1 in the Earth-Sun System," *Celestial Mechanics and Dynamical Astronomy*, no. 107, pp. 233–253, May 2010.

[44] B. P. McCarthy, "Characterization of Quasi-Periodic Orbits for Applications in the Sun-Earth and Earth-Moon Systems," MS Thesis, Purdue University, West Lafayette, Indiana, Dec. 2018.

[45] A. E. Roy, *Orbital Motion*, 4th. Institute of Physics Publishing Ltd, 2005.

[46] S. S. Huang, "Very Restricted Four-Body Problem," NASA Goddard Space Flight Center, Tech. Rep. NASA TN D-501, Sep. 1960.

[47] P. Musen and L. Carpenter, "On the General Planetary Perturbations in Rectangular Coordinates," *Journal of Geophysical Research*, vol. 68, pp. 2727–2734, May 1963.

[48] M. A. Andreu, "The Quasi-Bicircular Problem," Ph.D. dissertation, Universitat de Barcelona, Barcelona, Spain, 1998.

[49] S. Scheuerle, "Construction of Ballistic Lunar Transfers in the Earth-Moon-Sun System," M.S. thesis, Purdue University, West Lafayette, Indiana, May 2021.

[50] K. K. Boudad, "Disposal Dynamics From the Vicinity of Near Rectilinear Halo Orbits in the Earth-Moon-Sun System," MS Thesis, Purdue University, West Lafayette, Indiana, Dec. 2018.

[51] C. H. Action, *Ancillary Data Services of NASA's Navigation and Ancillary Information Facility*, https://naif.jpl.nasa.gov/naif/, Jan. 1996.

[52] C. Spreen, "Automated Patch Point Placement Capability for Hybrid Trajectory Targeting," Ph.D. dissertation, Purdue University, West Lafayette, Indiana, Dec. 2017.

[53] N. Bosanac, "Leveraging Natural Dynamical Structures to Explore Multi-Body Systems," Ph.D. Dissertation, Purdue University, West Lafayette, Indiana, 2016.

[54] A. E. Roy and M. W. Ovenden, "On the Occurrence of Commensurable Mean Motions in the Solar System, the Mirror Theorem," *Monthly Notices of the Royal Astronomical Society*, vol. 115, no. 3, pp. 296–309, Dec. 1955.

[55] K. K. Boudad, K. C. Howell, and D. C. Davis, "Dynamics of Synodic Resonant Near Rectilinear Halo Orbits in the Bicircular Four-Body Problem," *Advances in Space Research*, vol. 66, no. 9, pp. 2194–2214, Jul. 2020.

[56] B. A. Steves, A. J. Maciejewski, and M. Hendry, Eds., *Chaotic Worlds: From Order to Disorder in Gravitational N-Body Dynamical Systems* (NATO Science). Springer, 2006, vol. II. Mathematics, Physics, and Chemistry - Vol 227.

[57] H. B. Keller, *Numerical Methods for Two-Point Boundary-Value Problems*. Dover Publications, 1992.

[58] E. L. Allgower and K. Georg, *Introduction to Numerical Continuation*. Society for Industrial and Applied Mathematics, 1987.

[59] E. J. Doedel, V. A. Romanov, R. C. Paffenroth, *et al.*, "Elemental Periodic Orbits Associated with the Libration Points in the Circular Restricted 3-Body Problem," *International Journal of Bifurcation and Chaos*, vol. 17, no. 8, pp. 2625–2677, 2007.

[60] B. P. McCarthy and K. C. Howell, "Leveraging Quasi-Periodic Orbits for Trajectory Design in Cislunar Space," *Astrodynamics*, vol. 5, pp. 139–165, Jun. 2021, Issue 2.

[61] N. Bosanac, "Bounded Motions Near Resonant Orbits in the Earth-Moon and Sun-Earth Systems," in *AAS/AIAA Astrodynamics Specialist Conference*, Snowbird, Utah, Aug. 2018.

[62] À. Jorba and J. Villanueva, "On the Persistence of Lower Dimensional Invariant Tori Under Quasi-Periodic Perturbations," *Journal of Nonlinear Science*, vol. 7, no. 5, pp. 427–473, 1997.

[63] À. Jorba, M. Jorba-Cuscó, and J. Rosales, "The vicinity of the Earth-Moon L1 point in the Bicircular Problem," *Celestial Mechanics and Dynamical Astronomy*, vol. 132, no. 11, Feb. 2020.

[64] J. J. Rosales, "On the Effect of the Sun's Gravity Around the Earth-Moon L_1 and L_2 Libration Points," Ph.D. Dissertation, Universitat de Barcelona, Barcelona, Spain, Jun. 2020.

[65] A. Jorba, "Numerical Computation of the Normal Behavior of Invariant Curves of n-Dimensional Maps," *Nonlinearity*, vol. 14, no. 5, pp. 943–976, Sep. 2001.

[66] R. A. Bate, D. D. Mueller, and J. E. White, *Fundamentals of Astrodynamics*. Mineola, New York: Dover Publications, Inc, 1971.

[67] M. Vaquero and K. C. Howell, "Leveraging Resonant-Orbit Manifolds to Design Transfers Between Libration-Point Orbits," *Journal of Guidance, Control, and Dynamics*, vol. 37, no. 4, pp. 1143–1157, Jul. 2014.

[68] L. A. Hilday-Johnston and K. C. Howell, "Impulsive Time-Free Transfers Between Halo Orbits," *Celestial Mechanics and Dynamical Astronomy*, vol. 64, pp. 281–303, May 1996.

[69] A. Haapala and K. C. Howell, "A Framework for Construction of Transfers Linking Periodic Libration Point Orbits in the Earth-Moon Spatial Circular Restricted Three-Body Problem," *Journal of Bifurcations and Chaos*, vol. 26, no. 5, pp. 1630013-1–1630013-40, May 2016.

[70] L. R. Capdevila and K. C. Howell, "Transfer Network Linking Earth, Moon, and the Triangular Libration Point Regions in the Earth-Moon System," *Advances in Space Research*, vol. 62, no. 7, pp. 1826–1852, Oct. 2018.

[71] A. Das-Stuart, K. Howell, and D. Folta, "Rapid Trajectory Design in Complex Environments Enabled by Reinforcement Learning and Graph Search Strategies," *Acta Astronautica*, vol. 171, pp. 172–195, Jun. 2020.

[72] D. C. Davis, S. M. Phillips, K. C. Howell, S. Vutukuri, and B. P. McCarthy, "Station-keeping and Transfer Trajectory Design for Spacecraft in Cislunar Space," in *AAS/AIAA Astrodynamics Specialist Conference*, Stevenson, Washington, Aug. 2017.

[73] L. Capdevila, D. Guzzetti, and K. C. Howell, "Various Transfer Options from Earth into Distant Retrograde Orbits in the Vicinity of the Moon," in *AAS/AIAA Space Flight Mechanics Meeting*, Santa Fe, New Mexico, Jan. 2014.

[74] B. P. McCarthy and K. C. Howell, "Trajectory Design using Quasi-Periodic Orbits in the Multi-Body Problem," in *29th AAS/AIAA Space Flight Mechanics Meeting*, Ka'anapali, Hawaii, Jan. 2019.

[75] R. Whitley and R. Martinez, "Options for Staging Orbits in Cislunar Space," in *IEEE Aerospace 2015*, Big Sky, Montana, Mar. 2015.

[76] R. J. Whitley, D. C. Davis, L. M. Burke, *et al.*, "Earth-Moon Near Rectilinear Halo and Butterfly Orbits for Lunar Surface Exploration," in *AAS/AIAA Astrodynamics Specialist Conference*, Snowbird, Utah, Aug. 2018.

[77] E. M. Zimovan-Spreen, K. C. Howell, and D. C. Davis, "Near Rectilinear Halo Orbits and Nearby Higher-Period Dynamical Structures," *Celestial Mechanics and Dynamical Astronomy*, vol. 496, no. 2, Aug. 2020.

[78] R. C. Calleja, E. J. Doedel, A. R. Humphries, A. Lemus-Rodriquez, and B. E. Oldeman, "Boundary Value Problem Formulations for Computing Invariant Manifolds and Connecting Orbits in the Circular Restricted Three Body Problem," *Celestial Mechanics and Dynamical Astronomy*, vol. 114, no. 1-2, pp. 77–106, Oct. 2012.

[79] G. Gómez, W. S. Koon, M. W. Lo, J. E. Marsden, J. Masdemont, and S. D. Ross, "Connecting Orbits and Invariant Manifolds in the Spatial Restricted Three-Body Problem," *Nonlinearity*, vol. 17, no. 5, pp. 1571–1606, 2004.

[80] T. Pavlak, "Trajectory Design and Orbit Maintenance Strategies in Multi-Body Dynamical Regimes," Ph.D. dissertation, Purdue University, West Lafayette, Indiana, May 2013.

[81] E. A. Belbruno and J. K. Miller, "Sun-Perturbed Earth-to-Moon Transfers with Ballistic Capture," *Journal of Guidance, Control, and Dynamics*, vol. 16, no. 4, pp. 770–775, 1993.

[82] R. B. Roncoli and K. K. Fujii, "Mission Design Overview for the Gravity Recovery and Interior Laboraotry (GRAIL) Mission," in *AAA/AIAA Astrodynamics Specialist Conference*, Toronto, Ontario, Aug. 2010.

[83] T. Gardner, B. Cheetham, A. Forsman, *et al.*, "CAPSTONE: A CubeSat Pathfinder for the Lunar Gateway Ecosystem," in *AIAA/USU Small Satellite Conference*, North Logan, Utah, Jul. 2021.

[84] K. Oguri, K. Oshima, S. Campagnola, *et al.*, "EQUULEUS Trajectory Design," *Journal of the Astronautical Sciences*, vol. 67, pp. 950–976, Jan. 2020.

[85] D. C. Folta, N. Bosanac, A. Cox, and K. C. Howell, "The Lunar IceCube Mission Design: Construction of Feasible Transfer Trajectories with a Constrained Departure," in *26th AAS/AIAA Space Flight Mechanics Meeting*, Napa, California, Feb. 2016.

[86] B. Tucker, "Lunar Flight Study Series Volume 1: Earth-Moon Transit Studies Based on Ephemeris Data and Using Best Available Computer Program," NASA Marshal Spaceflight Center, Huntsville, Alabama, Tech. Rep., Sep. 1962.

[87] J. S. Parker and R. L. Anderson, *Low-Energy Lunar Trajectory Design* (Deep Space Communications and Navigation Series), J. H. Yuen, Ed. Pasadena, California: Jet Propulsion Laboratory, Jul. 2013.

[88] S. T. Scheuerle, B. P. McCarthy, and K. C. Howell, "Construction of Ballistic Lunar Transfers Leveraging Dynamical Systems Techniques," in *AAS/AIAA Astrodynamics Specialist Virtual Conference*, Lake Tahoe, California, Aug. 2020.

[89] S. T. Scheuerle and K. C. Howell, "Characteristics and Analysis of Families of Low-Energy Ballistic Lunar Transfers," in *AAS/AIAA Astrodynamics Specialist Conference*, Big Sky, Montana, Aug. 2021.

[90] J. J. Rosales, A. Jorba, and M. Jorba, "Families of Halo-like invariant tori around L2 in the Earth-Moon Bicircular Problem," *Celestial Mechanics and Dynamical Astronomy*, vol. 133, no. 16, Apr. 2021.

[91] B. P. McCarthy and K. C. Howell, "Cislunar Transfer Design Exploiting Periodic and Quasi-Periodic Orbital Structures in the Four-Body Problem," in *71st International Astronautical Congress*, Virtual, Oct. 2020.

[92] B. P. McCarthy and K. C. Howell, "Ballistic lunar transfer design to access cislunar periodic and quasi-periodic orbits leveraging flybys of the moon," in *72nd International Astronautical Congress*, Dubai, United Arab Emirates, Oct. 2021.

[93] B. McCarthy and K. Howell, "Characterization of Families of Low-Energy Transfers to Cislunar Four-Body Quasi-Periodic Orbits," in *AIAA SciTech Forum*, San Diego, California, Jan. 2022.

[94] K. Oshima, F. Topputo, and T. Yanao, "Low-energy transfers to the Moon with long transfer time," *Celestial Mechanics and Dynamical Astronomy*, vol. 131, no. 4, 2019.

[95] D. C. Davis, "Multi-Body Trajectory Design Strategies Based on Periapsis Poincaré Maps," Ph.D. Dissertation, Purdue University, West Lafayette, Indiana, Aug. 2011.

[96] A. Haapala and K. Howell, "Trajectory Design Using Periapse Poincaré Maps and Invariant Manifolds," in *21st AAS/AIAA Spaceflight Mechanics Meeting*, New Orleans, Louisiana, Feb. 2011.

[97] A. Haapala and K. Howell, "Representations of Higher-Dimensional Poincaré Maps with Application to Spacecraft Trajectory Design," *Acta Astronautica*, vol. 96, pp. 23–41, Apr. 2014.

[98] M. E. Paskowitz and D. J. Scheeres, "Robust Capture and Transfer Trajectories for Planetary Satellite Orbiters," *Journal of Guidance, Control, and Dynamics*, vol. 29, no. 2, Mar. 2006.

[99] M. E. Paskowitz and D. J. Scheeres, "Design of Science Orbits About Planetary Satellites: Application to Europa," *Journal of Guidance, Control, and Dynamics*, vol. 29, no. 5, pp. 1147–1158, 2006.

[100] D. C. Davis, S. M. Phillips, and B. P. McCarthy, "Trajectory Design for Saturnian Ocean Worlds Orbiters Using Multidimensional Poincaré Maps," *Acta Astronautica*, vol. 143, pp. 16–28, Feb. 2018.

[101] J. A. O. Romero and K. C. Howell, "Ridesharing Options From Geosynchronous Transfer Orbits in the Sun-Earth System," in *AAS/AIAA Astrodynamics Specialist Conference*, Big Sky, Montana, Aug. 2021.

[102] E. M. Sandish, "Approximate Mean Ecliptic Elements of the Lunar Orbit," Jet Propulsion Laboratory, Pasadena, California, Tech. Rep. 312.F-01-004, 2001.

A. Circular Restricted Three-Body Problem Derivation

From Newton's Second Law, the motion of P_3 is modeled in terms of the following second-order, vector differential equation

$$m_3 \frac{^I d^2\vec{r}_3}{dt^2} = m_3 \vec{r}_3'' = -\frac{\tilde{G} m_3 m_1}{r_{13}^3}\vec{r}_{13} - \frac{\tilde{G} m_3 m_2}{r_{23}^3}\vec{r}_{23} \tag{A.1}$$

where $\vec{r}_{ij}$ is the location of body j relative to body i, $\vec{r}_i''$ is the inertial acceleration vector for body i as viewed in the inertial reference frame, and $\tilde{G}$ is the universal gravitational constant. Since P_1 and P_2 move in circular orbits, they rotate at a constant rate $\dot{\theta}$ about their mutual barycenter. Subsequently, a new rotating coordinate frame, R, ($\hat{x}$-$\hat{y}$-$\hat{z}$) is defined and appears in Figure 2.1. The position vectors are rewritten in terms of the rotating frame. The location of the P_3 relative to the barycenter is defined as $\vec{P}$, and the location of P_3 relative to P_1 and P_2 in the rotating frame are defined as $\vec{D}$ and $\vec{R}$, respectively. Additionally, the distances from the barycenter to P_1 and P_2 are denoted as the magnitudes D_1 and D_2, respectively. Consequently, the vector differential equation in Equation (A.1) is rewritten as

$$\vec{P}'' = -\frac{\tilde{G} m_1}{D^3}\vec{D} - \frac{\tilde{G} m_2}{R^3}\vec{R} \tag{A.2}$$

where this differential equation governs the three-dimensional motion.

Typically, in applications to spacecraft trajectory design and analysis, position and velocity values differ significantly in terms of magnitude. When the state variables display wide variations in magnitude and rates of change, the implementation of numerical processes is sometimes challenging. Nondimensionalization is an effective strategy to mitigate some numerical difficulties and allows a broader range of applications. Nondimensionalization is based on the definition of characteristic quanitities. For application to the CR3BP, the characteristic length, mass and time are defined as

$$l^* = D_1 + D_2 \tag{A.3}$$

$$m^* = m_1 + m_2 \tag{A.4}$$

$$t^* = \sqrt{\frac{l^{*3}}{\tilde{G}m^*}} \tag{A.5}$$

where the characteristic time quantity is defined such that the nondimensional mean motion, n, of P_1 and P_2 is equal to unity. The nondimensional mean motion is defined

$$n = Nt^* = \sqrt{\frac{\tilde{G}m^*}{l^{*3}}}\sqrt{\frac{l^{*3}}{\tilde{G}m^*}} = 1 \tag{A.6}$$

where N is the dimensional mean motion of P_1 and P_2 in their Keplerian orbits. The nondimensional mass of P_2 or mass parameter, μ, is defined using the characteristic mass

$$\mu = \frac{m_2}{m^*} \tag{A.7}$$

Additionally, the nondimensional mass of P_1 is defined

$$1 - \mu = \frac{m_1}{m^*} \tag{A.8}$$

The distances from the barycenter to the primaries are evaluated via the definition of the center of mass

$$(m_1 + m_2)\vec{r}_{1,B} = m_2\vec{r}_{1,2} \tag{A.9}$$

where $\vec{r}_{1,B}$ is the location of P_1 relative to the barycenter, and $\vec{r}_{1,2}$ is the location of P_1 relative to P_2. Since l^* is defined as the distance between the primaries and the mass parameter is defined in Equation (A.7), Equation (A.9) is rewritten

$$r_{1,B} = D_1 = \mu l^* \tag{A.10}$$

where the distance D_1 is the distance between P_1 and the barycenter. Similarly, by evaluating the center of mass relative to P_2 yields the definition of the distance between the barycenter and P_2

$$r_{2,B} = D_2 = (1 - \mu)l^* \tag{A.11}$$

Some characteristic quantities for systems in this investigation are found in Table A.1. Using

Table A.1. Non-dimensional quantities for the Earth-Moon, Jupiter-Europa, and Sun-Earth CR3BP systems.

	Length [km]	Time [s]	Mass [kg]	μ
Earth-Moon	384747.9920	375699.859	6.0456444×10^{24}	0.012150584
Sun-Earth	149649952	5025263.006	1.9884182×10^{30}	3.003486×10^{-6}
Jupiter-Europa	671100.0	48843.878	1.8981783×10^{27}	2.52802×10^{-5}

the characteristic quantities, the dimensional second order vector differential equation in Equation (A.2) is rewritten,

$$\ddot{\vec{\rho}} = -\frac{1-\mu}{d^3}\vec{d} - \frac{\mu}{r^3}\vec{r} \tag{A.12}$$

where $\vec{\rho} = \frac{\vec{P}}{l^*}$, $\vec{d} = \frac{\vec{D}}{l^*}$, $\vec{r} = \frac{\vec{R}}{l^*}$. The variables d and r represent the magnitude of the nondimensional vectors $\vec{d}$ and $\vec{r}$, respectively. The vectors $\dot{\vec{\rho}}$ and $\ddot{\vec{\rho}}$ represent the first and second derivatives of the position vector as view by an inertial observer with respect to nondimensional time, τ. The nondimensional position vector of P_3 relative to the barycenter, ρ, is defined in terms of components in the rotating frame, i.e.,

$$\vec{\rho} = x\hat{x} + y\hat{y} + z\hat{z} \tag{A.13}$$

The derivatives of Equation (A.13) with respect to nondimensional time, τ, as seen by an inertial observer, are expanded using the the basic kinematic equation

$$\frac{{}^I d\vec{\rho}}{d\tau} = \dot{\vec{\rho}} = \frac{{}^R d\vec{\rho}}{d\tau} + {}^I\vec{\omega}^R \times \vec{\rho} \tag{A.14}$$

$$\frac{{}^I d^2\vec{\rho}}{d\tau^2} = \ddot{\vec{\rho}} = \frac{{}^R d\dot{\vec{\rho}}}{d\tau} + {}^I\vec{\omega}^R \times \dot{\vec{\rho}} \tag{A.15}$$

where ${}^I\vec{\omega}^R$ represents nondimensional angular velocity of the rotating frame, R, relative to the inertial frame. Recall that the angular velocity of the rotating frame is constant at the rate $\dot{\theta}$ with respect to the inertial frame. Furthermore, $\dot{\theta} = n$, since the primaries rotate in the circular orbits about their mutual barycenter. The angular velocity vector of the rotating

frame is in the $\hat{z}$-direction, aligned with the nondimensional angular velocity vector of the rotating frame with respect to the inertial frame and is defined

$$ {}^{I}\vec{\omega}^{R} = \dot{\theta}\hat{z} = n\hat{z} \tag{A.16} $$

By substituting Equation (A.13) and Equation (A.16) into Equation (A.14), the expression for $\dot{\vec{\rho}}$ is obtained as expressed in terms of rotating coordinates,

$$ \dot{\vec{\rho}} = (\dot{x} - ny)\hat{x} + (\dot{y} + nx)\hat{y} + \dot{z}\hat{z} \tag{A.17} $$

Similarly, the following kinematic expansion applies to the acceleration vector

$$ \ddot{\vec{\rho}} = (\ddot{x} - 2n\dot{y} - n^2x)\hat{x} + (\ddot{y} + 2n\dot{x} - n^2y)\hat{y} + \ddot{z}\hat{z} \tag{A.18} $$

Equation (A.18) supplies the kinematic expression for the left side of the vector Equation (A.12). The vector expressions for $\vec{d}$ and $\vec{r}$ are defined in terms of components

$$ \vec{d} = (x + \mu)\hat{x} + y\hat{y} + z\hat{z} \tag{A.19} $$

$$ \vec{r} = (x - 1 + \mu)\hat{x} + y\hat{y} + z\hat{z} \tag{A.20} $$

Substituting Equations (A.19), and (A.20) into the single vector differential equation in Equation (A.12) and exploiting the kinematic expansion in Equation (A.18) yields the three second order scalar differential equations of motion for the CR3BP

$$ \ddot{x} - 2n\dot{y} - n^2x = -\frac{(1-\mu)(x+\mu)}{d^3} - \frac{\mu(x-1+\mu)}{r^3} \tag{A.21} $$

$$ \ddot{y} + 2n\dot{x} - n^2y = -\frac{(1-\mu)y}{d^3} - \frac{\mu y}{r^3} \tag{A.22} $$

$$ \ddot{z} = -\frac{(1-\mu)z}{d^3} - \frac{\mu z}{r^3} \tag{A.23} $$

where $\ddot{x}$, $\ddot{y}$, and $\ddot{y}$ are the acceleration components in the rotating frame, and $\dot{x}$, $\dot{y}$, and $\dot{z}$ are the velocity components in the rotating frame, all derivatives with respect to nondimensional time. Alternatively the equations of motion can be rewritten in terms of a pseudo-potential, U^*,

$$\ddot{x} - 2n\dot{y} = \frac{\partial U^*}{\partial x} \tag{A.24}$$

$$\ddot{y} + 2n\dot{x} = \frac{\partial U^*}{\partial y} \tag{A.25}$$

$$\ddot{z} = \frac{\partial U^*}{\partial z} \tag{A.26}$$

where U^* is defined

$$U^* = \frac{1-\mu}{d} + \frac{\mu}{r} + \frac{n^2(x^2+y^2)}{2} \tag{A.27}$$

No analytical solutions is known for the equations of motion in either form, Equations (A.21)-(A.23) or the differential equations (A.24)-(A.26). Numerical integration of Equations (A.21)-(A.23) determines the time history of the path for a given set of initial states.

A.0.1 First Order Linear Variations about Equilibrium Points

The differential equations that govern the behavior in the CR3BP are nonlinear, but understanding the linear motion in the vicinity of the equilibrium points offers some initial insight into the dynamical flow throughout the space. One approach to organize the dynamical behavior in the CR3BP is collection of the solutions into four types: equilibrium points, periodic orbits, quasi-periodic trajectories, and chaotic motion. Understanding all types of fundamental motion is necessary for successful path planning in this regime.

First Order Linear Periodic Motion

The construction of periodic solutions originates with linear variational equations in the vicinity of a particular solution. Consider the nonlinear vector differential equations of motion expressed as $\dot{\vec{x}} = \vec{f}(\vec{x}, t)$, where $\vec{x} = \begin{bmatrix} x & y & z & \dot{x} & \dot{y} & \dot{z} \end{bmatrix}^T$ and $\dot{\vec{x}} = \begin{bmatrix} \dot{x} & \dot{y} & \dot{z} & \ddot{x} & \ddot{y} & \ddot{z} \end{bmatrix}^T$

and let a particular solution be defined as $\vec{x}^*$. The particular, or reference, solution satisfies the nonlinear differential equations. Let the variations from the reference be defined

$$\delta\vec{x} = \begin{bmatrix} \delta x(t) & \delta y(t) & \delta z(t) & \delta\dot{x}(t) & \delta\dot{y}(t) & \delta\dot{z}(t) \end{bmatrix}^T = \vec{x}(t) - \vec{x}^*(t) \tag{A.28}$$

By substituting the above equations into $\vec{f}(\vec{x}, t)$ and expanding in a first-order Taylor series about $\vec{x}^*(t)$ yields

$$\dot{\vec{x}}^*(t) + \delta\dot{\vec{x}} = \vec{f}(\vec{x}^*, t) + \mathsf{Eval}\frac{\partial\vec{f}}{\partial\vec{x}}_{\vec{x}^*}\delta\vec{x} + \text{Higher Order Terms} \tag{A.29}$$

Since $\dot{\vec{x}}^*(t) = \vec{f}(\vec{x}^*, t)$, and the higher order terms are neglected, then the Taylor series reduces to

$$\delta\dot{\vec{x}} = \left.\frac{\partial\vec{f}}{\partial\vec{x}}\right|_{\vec{x}^*}\delta\vec{x} = \mathbf{A}(t)\delta\vec{x} \tag{A.30}$$

where $\mathbf{A}(t)$ is a matrix, evaluated on the reference solution. Using the definition of the variations with respect to a reference in Equation (A.30), the variational equations of motion in the CR3BP are written in scalar form as

$$\delta\ddot{x} - 2\delta\dot{y} = \frac{\partial U^*}{\partial x\partial x}\delta x + \frac{\partial U^*}{\partial x\partial y}\delta y + \frac{\partial U^*}{\partial x\partial z}\delta z \tag{A.31}$$

$$\delta\ddot{y} + 2\delta\dot{x} = \frac{\partial U^*}{\partial y\partial x}\delta x + \frac{\partial U^*}{\partial y\partial y}\delta y + \frac{\partial U^*}{\partial y\partial z}\delta z \tag{A.32}$$

$$\delta\ddot{z} = \frac{\partial U^*}{\partial z\partial x}\delta x + \frac{\partial U^*}{\partial z\partial y}\delta y + \frac{\partial U^*}{\partial z\partial z}\delta z \tag{A.33}$$

Expressing the equations of motion in matrix form, $\delta\dot{\vec{x}} = \mathbf{A}(t)\delta\vec{x}$, yields

$$\begin{bmatrix} \delta\dot{x} \\ \delta\dot{y} \\ \delta\dot{z} \\ \delta\ddot{x} \\ \delta\ddot{y} \\ \delta\ddot{z} \end{bmatrix} = \begin{bmatrix} 0 & 0 & 0 & 1 & 0 & 0 \\ 0 & 0 & 0 & 0 & 1 & 0 \\ 0 & 0 & 0 & 0 & 0 & 1 \\ U^*_{xx} & U^*_{xy} & U^*_{xz} & 0 & 2 & 0 \\ U^*_{yx} & U^*_{yy} & U^*_{yz} & -2 & 0 & 0 \\ U^*_{zx} & U^*_{zy} & U^*_{zz} & 0 & 0 & 0 \end{bmatrix} \begin{bmatrix} \delta x \\ \delta y \\ \delta z \\ \delta\dot{x} \\ \delta\dot{y} \\ \delta\dot{z} \end{bmatrix} \tag{A.34}$$

where the notation for the pseudo-potential partial derivatives is $\frac{\partial U^*}{\partial \mathrm{i} \partial \mathrm{j}} = U^*_{\mathrm{ij}}$. If the reference solution is defined as an equilibrium solution, the libration points are constant solutions in the CR3BP. Thus, when the second order partial derivatives of the pseudo-potential, U^*, are evaluated at any of the equilibrium points, with $z = 0$, the variational equations of motion reduce to

$$\delta\ddot{x} - 2\delta\dot{y} = U^*_{xx}\Big|_{eq} \delta x + U^*_{xy}\Big|_{eq} \delta y \tag{A.35}$$

$$\delta\ddot{y} + 2\delta\dot{x} = U^*_{yx}\Big|_{eq} \delta x + U^*_{yy}\Big|_{eq} \delta y \tag{A.36}$$

$$\delta\ddot{z} = U^*_{zz}\Big|_{eq} \delta z \tag{A.37}$$

where the second order partial derivatives of the pseudo-potential function is evaluated at the equilibrium point. Note that the motion in the $\hat{x}\hat{y}$-plane is decoupled from the out-of-plane motion. The out-of-plane motion is simple harmonic oscillatory motion with a frequency $s_{\delta z} = \sqrt{|U_{zz}\Big|_{eq}|}$. Considering the in-plane motion, Equation (A.34) is rewritten in matrix form, $\delta\vec{x}_{\text{planar}} = \mathbf{A}_{\text{planar}}\delta\vec{x}_{\text{planar}}$,

$$\delta\vec{x}_{\text{planar}} = \begin{bmatrix} \delta x & \delta y & \delta\dot{x} & \delta\dot{y} \end{bmatrix}^T \tag{A.38}$$

$$\mathbf{A}_{\text{planar}} = \begin{bmatrix} 0 & 0 & 1 & 0 \\ 0 & 0 & 0 & 1 \\ U^*_{xx}\Big|_{eq} & U^*_{xy}\Big|_{eq} & 0 & 2 \\ U^*_{yx}\Big|_{eq} & U^*_{yy}\Big|_{eq} & -2 & 0 \end{bmatrix} \tag{A.39}$$

The $\mathbf{A}_{\text{planar}}$ is constant for a given libration point and $\mathbf{A}_{\text{planar}}\delta\vec{x}_{\text{planar}}$ is assessed as a linear system. The eigenvalues of the $\mathbf{A}_{\text{planar}}$ matrix are determined to yield information about the motion in the vicinity of the equilibrium points. Constructing the characteristic polynomial of the $\mathbf{A}_{\text{planar}}$ matrix results in a fourth order polynomial

$$\lambda^4 + (4 - U^*_{xx} - U^*_{yy})\lambda^2 + (-2U^*_{xy} - 2U^*_{yx})\lambda + (U^*_{xx}U^*_{yy} - U^*_{yx}U^*_{xy}) = 0 \tag{A.40}$$

where λ is an eigenvalue of $\mathbf{A}_{\text{planar}}$. The type of planar motion in the vicinity of the five equilibrium solutions is characterized by roots of the characteristic polynomial in Equation (A.40). Consider the characteristic polynomial for the collinear points, which lie on the $\hat{x}$-axis of the rotating coordinate frame. Equation (A.40) is then simplified to a quadratic polynomial

$$\Lambda^2 + 2\beta_1\Lambda - \beta_2^2 = 0 \tag{A.41}$$

since $y_{eq} = 0$ and $z_{eq} = 0$, making $U^*_{xy} = 0$, $U^*_{xx} > 0$, and $U^*_{yy} < 0$, where

$$\beta_1 = 2 - \frac{U^*_{xx} + U^*_{yy}}{2} \tag{A.42}$$

$$\beta_2^2 = -U^*_{xx}U^*_{yy} \tag{A.43}$$

$$\lambda = \pm\sqrt{\Lambda} \tag{A.44}$$

Using the quadratic equation, Equation (A.41) is solved,

$$\Lambda_1 = -\beta_1 + \sqrt{\beta_1^2 + \beta_2^2} > 0 \tag{A.45}$$

$$\Lambda_2 = -\beta_1 - \sqrt{\beta_1^2 + \beta_2^2} < 0 \tag{A.46}$$

where Λ_1 and Λ_2 are the two solutions to the quadratic polynomial in Equation (A.41). Substituting Λ_1 and Λ_2 back into Equation (A.44), the four eigenvalues are determined. Two real eigenvalues (λ_1 and λ_2) and two imaginary eigenvalues (λ_3 and λ_4) result and the general solution to $\delta\dot{\vec{x}}_{\text{planar}} = \mathbf{A}_{\text{planar}}\delta\vec{x}_{\text{planar}}$ near the collinear equilibrium points becomes

$$\delta x(t)_{eq} = A_1 e^{\lambda_1 t} + A_2 e^{\lambda_2 t} + A_3 e^{\lambda_3 t} + A_4 e^{\lambda_4 t} \tag{A.47}$$

$$\delta \dot{x}(t)_{eq} = \lambda_1 A_1 e^{\lambda_1 t} + \lambda_2 A_2 e^{\lambda_2 t} + \lambda_3 A_3 e^{\lambda_3 t} + \lambda_4 A_4 e^{\lambda_4 t} \tag{A.48}$$

$$\delta y(t)_{eq} = B_1 e^{\lambda_1 t} + B_2 e^{\lambda_2 t} + B_3 e^{\lambda_3 t} + B_4 e^{\lambda_4 t} \tag{A.49}$$

$$\delta \dot{y}(t)_{eq} = \lambda_1 B_1 e^{\lambda_1 t} + \lambda_2 B_2 e^{\lambda_2 t} + \lambda_3 B_3 e^{\lambda_3 t} + \lambda_4 B_4 e^{\lambda_4 t} \tag{A.50}$$

where A_{i} and B_{i} are coefficients of the general solution. The coefficients A_{i} and B_{i} in Equations (A.47)-(A.50) are dependent on each other and are computed,

$$B_{\mathrm{i}} = \frac{\lambda_{\mathrm{i}} - U_{xx}\Big|_{eq}}{2\lambda_{\mathrm{i}}} A_{\mathrm{i}} \tag{A.51}$$

Thus, the variational equations offer information concerning behavior in the vicinity of the collinear equilibrium solutions. The eigenvalues associated with the collinear points and the form of the linear solutions in Equations (A.47)-(A.50) reflect the existence of unstable (λ_1), stable (λ_1), and center (λ_3 and λ_4) modes in the vicinity of these points.

Exciting only the modes associated with the imaginary eigenvalues results in periodic motion near the collinear equilibrium points. The modes associated with exponential increase and decay are removed in the differential equations by exploring solutions that yield coefficient values $A_1 = 0$ and $A_2 = 0$, resulting purely in periodic behavior

$$\delta y(t)_{eq} = \delta y_{0,eq} \cos s(t - t_0) + \frac{\delta x_{0,eq}}{\beta_3} \sin s(t - t_0) \tag{A.52}$$

$$\delta \dot{y}(t)_{eq} = -s\delta y_{0,eq} \sin s(t - t_0) + \frac{s\delta x_{0,eq}}{\beta_3} \cos s(t - t_0) \tag{A.53}$$

$$\delta x(t)_{eq} = \delta x_{0,eq} \cos s(t - t_0) - \beta_3 \delta y_{0,eq} \sin s(t - t_0) \tag{A.54}$$

$$\delta \dot{x}(t)_{eq} = -s\delta x_{0,eq} \sin s(t - t_0) - \beta_3 \delta y_{0,eq} s \cos s(t - t_0) \tag{A.55}$$

where s and β_3 are defined

$$s = \sqrt{\beta_1 + (\beta_2^2 + \beta_1)^{\frac{1}{2}}} \tag{A.56}$$

$$\beta_3 = \frac{s^2 + U_{xx}}{2s} \tag{A.57}$$

A similar linear analysis demonstrates that two types of planar periodic motion exist in the vicinity of the triangular equilibrium points as well. Examining the eigenvalues from the linear variations in the vicinity of the equilibrium solutions provides insight into the nonlinear dynamics that region.

First Order Linear Quasi-Periodic Motion

In Section A.0.1, the in-plane linear variations near the collinear equilibrium points is decoupled from the out-of-plane variations. An example of the out-of-plane (blue) and in-plane (red) linear variations from the L_1 point are illustrated in Figure A.1 in the Earth-Moon system. However, introducing initial conditions that include both the in-plane oscillatory motion coupled with the harmonic out-of-plane variations yields a quasi-periodic Lissajous motion around the collinear equilibrium solutions. By isolating and exciting the oscillatory out-of-plane motion, the linear variations for a Lissajous path are defined

$$\delta y(t)_{eq} = \delta y_{0,eq} \cos s(t-t_0) + \frac{\delta x_{0,eq}}{\beta_3} \sin s(t-t_0) \tag{A.58}$$

$$\delta \dot{y}(t)_{eq} = -s\delta y_{0,eq} \sin s(t-t_0) + \frac{s\delta x_{0,eq}}{\beta_3} \cos s(t-t_0) \tag{A.59}$$

$$\delta x(t)_{eq} = \delta x_{0,eq} \cos s(t-t_0) - \beta_3 \delta y_{0,eq} \sin s(t-t_0) \tag{A.60}$$

$$\delta \dot{x}(t)_{eq} = -s\delta x_{0,eq} \sin s(t-t_0) - \beta_3 \delta y_{0,eq} s \cos s(t-t_0) \tag{A.61}$$

$$\delta z(t)_{eq} = \delta z_{0,eq} \cos s_{\delta z}(t-t_0) + s_{\delta z}\delta \dot{z}_{0,eq} \sin s_{\delta z}(t-t_0) \tag{A.62}$$

$$\delta \dot{z}(t)_{eq} = -\delta z_{0,eq} s_{\delta z} \sin s_{\delta z}(t-t_0) + s_{\delta z}^2 \delta \dot{z}_{0,eq} \cos s_{\delta z}(t-t_0) \tag{A.63}$$

Note that Equations (A.58)-(A.61) are the same as Equations (A.52)-(A.55). The frequency of the out-of-plane motion is defined as $s_{\delta z} = \sqrt{|U_{zz}|_{eq}|}$. The initial out-of-plane position, δz_0, initial out-of-plane velocity, $\delta \dot{z}_0$, in addition to the initial in-plane positions, δx_0 and δy_0, are specified to define the Lissajous path. The quasi-periodic Lissajous motion around L_1 in the Earth-Moon system is depicted in Figure A.2. The linear periodic variations exist in both the planar case and the out-of-plane case, however, the motion can be coupled to demonstrate quasi-periodic variations around the collinear points as well.

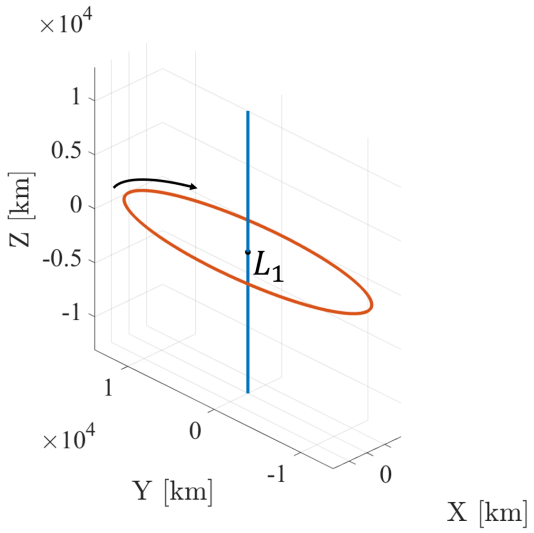

Figure A.1. Decoupled out-of-plane (blue) and in-plane (red) variations from the L_1 point in the Earth-Moon system

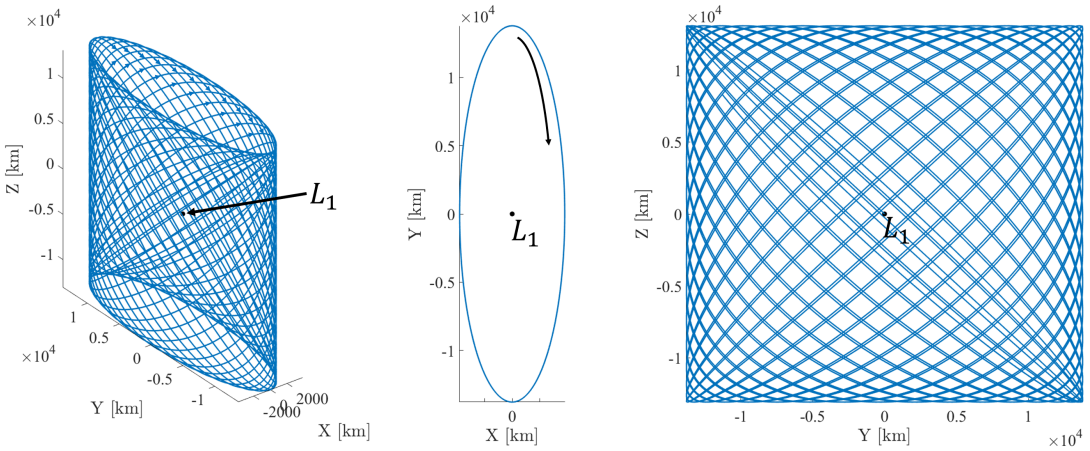

Figure A.2. (a) 3D View, (b) $\hat{x}\hat{y}$ plane projection and (c) $\hat{y}\hat{z}$ plane projection of linearized Lissajous motion around the Earth-Moon L_1 equilibrium point.

B. Bicircular Restricted Four-Body Problem Derivation

Given the assumptions from Section 2.2, the equations of motion are derived for the BCR4BP. An inertial reference frame, I, denoted $\hat{X}$-$\hat{Y}$-$\hat{Z}$, is defined with a base point at B_2, as illustrated in Figure B.1. From Newton's second law of motion, the motion of P_3 is modeled in terms of the following second-order, vector differential equation,

$$M_3\vec{R}_3'' = -\frac{\tilde{G}M_3M_1}{R_{13}^3}\vec{R}_{13} - \frac{\tilde{G}M_3M_2}{R_{23}^3}\vec{R}_{23} - \frac{\tilde{G}M_3M_4}{R_{43}^3}\vec{R}_{43} \tag{B.1}$$

where R_{ij} is the position of object j relative to object i and M_{i} is the mass of object i, and $\tilde{G}$ is the Universal Gravitational Constant. For this derivation, an assumption is made that B_2, the barycenter between B_1 and the Sun, is assumed to be an inertially fixed point. Subsequently, the acceleration of P_3 relative to B_2, as expressed in an inertial frame is defined,

$$\vec{R}_{B_23}'' = -\frac{\tilde{G}M_1}{R_{13}^3}\vec{R}_{13} - \frac{\tilde{G}M_2}{R_{23}^3}\vec{R}_{23} - \frac{\tilde{G}M_4}{R_{43}^3}\vec{R}_{43} \tag{B.2}$$

Note that the mass M_3 is factored out of the differential equation. Subsequently, the position vectors of each body are defined relative to B_2,

$$\vec{R}_{B_21} = \vec{R}_{B_2B_1} - R_{B_11}\left(\cos\beta_2\hat{X} + \sin\beta_2\hat{Y}\right) \tag{B.3}$$

$$\vec{R}_{B_22} = \vec{R}_{B_2B_1} + R_{B_12}\left(\cos\beta_2\hat{X} + \sin\beta_2\hat{Y}\right) \tag{B.4}$$

$$\vec{R}_{B_2B_1} = R_{B_2B_1}\left(\cos\beta_1\hat{X} + \sin\beta_1\hat{Y}\right) \tag{B.5}$$

$$\vec{R}_{B_24} = -R_{B_24}\left(\cos\beta_1\hat{X} + \sin\beta_1\hat{Y}\right) \tag{B.6}$$

where β_1 is the angle defined clockwise from the positive $\hat{X}$ axis to the B_2-B_1 line, β_2 the angle between the $\hat{X}$ axis and the direction from B_1 to P_2, $R_{B_2B_1}$ is the position magnitude between B_1 and B_2. The assumptions of the BCR4BP state that the distance between the Earth-Moon barycenter and B_2 remains constant and the distance between P_1 and P_2 remains constant. To examine trajectories in the vicinity of the Earth and Moon, it is also

often useful to describe the motion relative to B_1. Thus the position of P_3 with respect to B_1 is defined,

$$\vec{R}_{B_1 3} = \vec{R}_{B_2 3} - \vec{R}_{B_2 B_1} \tag{B.7}$$

and the acceleration is thus defined by taking two time derivatives,

$$\vec{R}''_{B_1 3} = \vec{R}''_{B_2 3} - \vec{R}''_{B_2 B_1} \tag{B.8}$$

where $\vec{R}_{B_1 3}$ is the inertial acceleration of P_3 with respect to B_1. The term $\vec{R}''_{B_2 B_1}$ is computed by taking the time derivative of Equation (B.5),

$$\vec{R}''_{B_2 B_1} = R_{B_2 B_1} {\beta_1}'^2 (-\cos\beta_1 \hat{X} - \sin\beta_1 \hat{Y}) \tag{B.9}$$

where β'_1 is the time derivative of the angle β_1, which is assumed to be constant. The acceleration term $\vec{R}''_{B_2 3}$ is defined in Equation (B.2). Thus, the inertial acceleration of P_3 with respect to B_1, is defined,

$$\vec{R}''_{B_1 3} = -\frac{\tilde{G}M_1}{R_{13}^3}\vec{R}_{13} - \frac{\tilde{G}M_2}{R_{23}^3}\vec{R}_{23} - \frac{\tilde{G}M_4}{R_{43}^3}\vec{R}_{43} - R_{B_2 B_1} {\beta_1}'^2 (-\cos\beta_1 \hat{X} - \sin\beta_1 \hat{Y}) \tag{B.10}$$

This dimensional second order vector differential equation describes the inertial acceleration motion of P_3; however, there is no analytic solution to this differential equation. Subsequently, numerical integration is required to obtain a trajectory path in this model. To avoid numerical challenges, it is advantageous to non-dimensionalize the quantities. Similar to the CR3BP, the P_1-P_2 mass parameter, μ, is defined,

$$\mu = \frac{M_2}{M_1 + M_2} = 1 - \frac{M_1}{M_1 + M_2} \tag{B.11}$$

where M_{i} is the mass of body i. The non-dimensional quantities for mass, length and time are defined similar to the CR3bP as well,

$$m^* = M_1 + M_2 \tag{B.12}$$

$$l^* = R_{12} \tag{B.13}$$

$$t^* = \sqrt{\frac{{l^*}^3}{Gm^*}} \tag{B.14}$$

where G is the Universal Gravitational Constant and R_{12} is the dimensional distance between P_1 and P_2. In the BCR4BP, there are several additional parameters that are defined using these non-dimensional quantities,

$$m_s = \frac{M_4}{\mu} \tag{B.15}$$

$$a_s = \frac{R_{B_14}}{l^*} \tag{B.16}$$

where m_s is the non-dimensional mass of the Sun and a_s is the non-dimensional distance between B_1 and the Sun. Using these non-dimensional definitions, the non-dimensional inertial acceleration is thus defined,

$$\ddot{\vec{r}}_{B_13} = -\frac{1-\mu}{r_{13}^3}\vec{r}_{13} - \frac{\mu}{r_{23}^3}\vec{r}_{23} - \frac{m_s}{r_{43}^3}\vec{r}_{43} - \frac{a_s m_s}{m_s+1}n_{4B_1}^2(-\cos\beta_1\hat{X} - \sin\beta_1\hat{Y}) \tag{B.17}$$

where n_{4B_1} is the non-dimensional mean motion, ${\beta_1}'^2$, of the Sun and B_1, the dots above the vectors indicate the non-dimensional time derivative, and the lower case position vectors, $\vec{r}_{\text{ij}}$ are the non-dimensional counterparts to the upper case position vectors, $\vec{R}_{\text{ij}}$. The non-dimensional mean motion is also defined,

$$n_{4B_1} = \sqrt{\frac{m_s+1}{a_s^3}} \tag{B.18}$$

which is substituted into Equation B.17 and simplifies,

$$\ddot{\vec{r}}_{B_13} = -\frac{1-\mu}{r_{13}^3}\vec{r}_{13} - \frac{\mu}{r_{23}^3}\vec{r}_{23} - \frac{m_s}{r_{43}^3}\vec{r}_{43} - \frac{m_s}{a_s^3}\vec{r}_{B_14} \tag{B.19}$$

where $\vec{r}_{B_14}$ is the non-dimensional position of the Sun with respect to B_1. Lastly, to obtain the relative acceleration in the rotating frame, the kinematic expansion of $\ddot{\vec{r}}_{B_13}$ is defined similar to Equation (A.18). The kinematic expansion using the notation for the BCR4BP is defined,

$$\ddot{\vec{r}}_{B_13} = (\ddot{x} - 2n_{12}\dot{y} - n_{12}^2 x)\hat{x} + (\ddot{y} + 2n_{12}\dot{x} - n12^2 y)\hat{y} + \ddot{z}\hat{z} \tag{B.20}$$

where $n_12 = 1$ is the non-dimensional mean motion of P_1-P_2, x, y, and z are the non-dimensional position components of P_3 relative to B_1 in the P_1-P_2 rotating frame, and $\dot{x}$, $\dot{y}$, and $\dot{z}$ are the non-dimensional relative velocity components of P_3 in the P_1-P_2 rotating frame. Substituting the kinematic expansion into Equation (B.19) yields the following scalar second order differential equations that describe the relative acceleration of P_3 in the P_1-P_2 rotating frame,

$$\ddot{x} - 2\dot{y} - x = -\frac{(1-\mu)(x+\mu)}{r_{13}^3} - \frac{\mu(x-1+\mu)}{r_{23}^3} - \frac{m_s x_{34}}{r_{34}^3} - \frac{m_s \cos\theta_s}{a_s^2} \tag{B.21}$$

$$\ddot{y} + 2\dot{x} - y = -\frac{(1-\mu)y}{r_{13}^3} - \frac{\mu y}{r_{23}^3} - \frac{m_s y_{34}}{r_{34}^3} - \frac{m_s \sin\theta_s}{a_s^2} \tag{B.22}$$

$$\ddot{z} = -\frac{(1-\mu)z}{r_{13}^3} - \frac{\mu z}{r_{23}^3} - \frac{m_4 z}{r_{43}^3} \tag{B.23}$$

where x_{43} and y_{43} are the position components of the Sun relative to P_3 and θ_s is the angle between the vector from P_1 to P_2 and $\vec{r}_{B_14}$. Numerical integration of Equations (B.21)-(B.23) determines the time history of the path for a given set of initial conditions and initial Sun angle, θ_s.

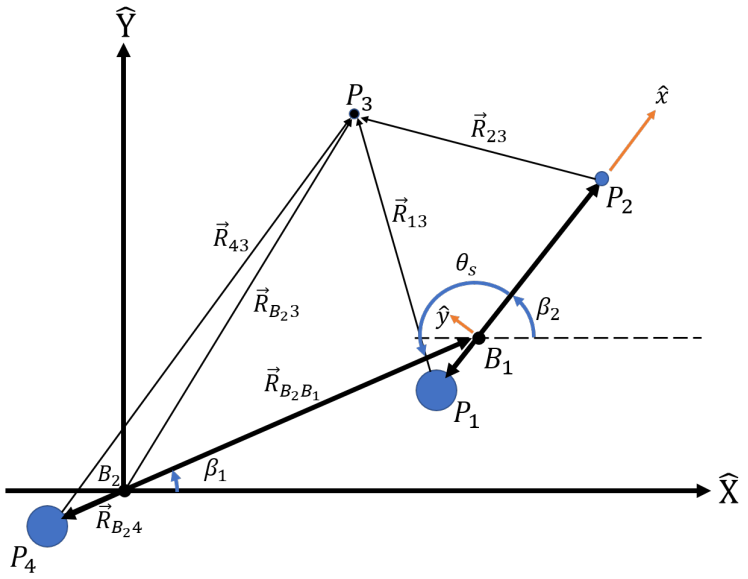

Figure B.1. Geometry in the four-body system; definition of inertial and rotating reference frames.

C. State Transition Matrix

The STM is an essential element of trajectory analysis. Not only is it useful in differential corrections strategies, it crucial for many spacecraft guidance, navigation and control strategies as well. For a given reference solution, the STM offers information on the impact of the deviations of an initial state to the deviations in a final state downstream. In the variational equations in Equation (A.34), the $\mathbf{A}$ matrix remains constant for equilibrium solutions. However, in the general case, $\mathbf{A}$ is time varying and is exploited to compute the differential equations associated with the STM. First consider the variations from reference path at time t_0, denoted $\delta\vec{x}(t_0)$. Further consider the variations from the same reference path at some time t, denoted $\delta\vec{x}(t)$. A linear mapping between initial variations at t_0 and the final variations at time t is defined by partial derivatives of the final state variations with respect to the initial state variations,

$$\delta\vec{x}(t) = \frac{\partial\vec{x}(t)}{\partial\vec{x}(t_0)}\delta\vec{x}(t_0) = \mathbf{\Phi}(t,t_0)\delta\vec{x}(t_0) \tag{C.1}$$

where $\frac{\partial\vec{x}(t)}{\partial\vec{x}(t_0)}$ is the linear mapping and is equal to $\mathbf{\Phi}(t,t_0)$ or the STM from time t_0 to t. This matrix supplies information on the sensitivity of the final state at time t relative to the initial state at time t_0. The equations of motion for the elements of the STM are derived via the time derivative of the STM in Equation (C.1)

$$\dot{\mathbf{\Phi}} = \frac{\partial}{\partial t}\frac{\partial\vec{x}(t)}{\partial\vec{x}(t_0)} = \frac{\partial\dot{\vec{x}}(t)}{\partial\vec{x}(t_0)} \tag{C.2}$$

Recall $\delta\dot{\vec{x}}(t) = \mathbf{A}(t)\delta\vec{x}(t)$ from Equation (A.30), Equation (C.2) is rewritten

$$\dot{\mathbf{\Phi}} = \frac{\mathbf{A}(t)\partial\vec{x}(t)}{\partial\vec{x}(t_0)} = \mathbf{A}(t)\frac{\partial\vec{x}(t)}{\partial\vec{x}(t_0)} \tag{C.3}$$

Noticing that $\frac{\partial\vec{x}(t)}{\partial\vec{x}(t_0)}$ is the definition of the STM, the equations of motion for the STM become

$$\dot{\mathbf{\Phi}} = \mathbf{A}(t)\mathbf{\Phi} \tag{C.4}$$

The STM is a 6×6 matrix, whose elements are evaluated as

$$\mathbf{\Phi}(t,t_0) = \begin{bmatrix} \frac{\partial x(t)}{\partial x(t_0)} & \frac{\partial x(t)}{\partial y(t_0)} & \frac{\partial x(t)}{\partial z(t_0)} & \frac{\partial x(t)}{\partial \dot{x}(t_0)} & \frac{\partial x(t)}{\partial \dot{y}(t_0)} & \frac{\partial x(t)}{\partial \dot{z}(t_0)} \\ \frac{\partial y(t)}{\partial x(t_0)} & \frac{\partial y(t)}{\partial y(t_0)} & \frac{\partial y(t)}{\partial z(t_0)} & \frac{\partial y(t)}{\partial \dot{x}(t_0)} & \frac{\partial y(t)}{\partial \dot{y}(t_0)} & \frac{\partial y(t)}{\partial \dot{z}(t_0)} \\ \frac{\partial z(t)}{\partial x(t_0)} & \frac{\partial z(t)}{\partial y(t_0)} & \frac{\partial z(t)}{\partial z(t_0)} & \frac{\partial z(t)}{\partial \dot{x}(t_0)} & \frac{\partial z(t)}{\partial \dot{y}(t_0)} & \frac{\partial z(t)}{\partial \dot{z}(t_0)} \\ \frac{\partial \dot{x}(t)}{\partial x(t_0)} & \frac{\partial \dot{x}(t)}{\partial y(t_0)} & \frac{\partial \dot{x}(t)}{\partial z(t_0)} & \frac{\partial \dot{x}(t)}{\partial \dot{x}(t_0)} & \frac{\partial \dot{x}(t)}{\partial \dot{y}(t_0)} & \frac{\partial \dot{x}(t)}{\partial \dot{z}(t_0)} \\ \frac{\partial \dot{y}(t)}{\partial x(t_0)} & \frac{\partial \dot{y}(t)}{\partial y(t_0)} & \frac{\partial \dot{y}(t)}{\partial z(t_0)} & \frac{\partial \dot{y}(t)}{\partial \dot{x}(t_0)} & \frac{\partial \dot{y}(t)}{\partial \dot{y}(t_0)} & \frac{\partial \dot{y}(t)}{\partial \dot{z}(t_0)} \\ \frac{\partial \dot{z}(t)}{\partial x(t_0)} & \frac{\partial \dot{z}(t)}{\partial y(t_0)} & \frac{\partial \dot{z}(t)}{\partial z(t_0)} & \frac{\partial \dot{z}(t)}{\partial \dot{x}(t_0)} & \frac{\partial \dot{z}(t)}{\partial \dot{y}(t_0)} & \frac{\partial \dot{z}(t)}{\partial \dot{z}(t_0)} \end{bmatrix} = \begin{bmatrix} \mathbf{\Phi_{r,r}} & \mathbf{\Phi_{r,v}} \\ \mathbf{\Phi_{v,r}} & \mathbf{\Phi_{v,v}} \end{bmatrix} \tag{C.5}$$

Examining the submatrices of the STM, the upper left 3×3 quadrant is the sensitivity of the final position to variations in the initial position; the upper right 3×3 quadrant reflects the sensitivity of the final position to variations in the initial velocity; the lower left and right quadrants 3×3 represent the variations in the final velocity due to perturbations in the initial position and initial velocity, respectively. Some useful properties of the STM include

$$\mathbf{\Phi}(t_0,t) = \mathbf{\Phi}^{-1}(t,t_0) \tag{C.6}$$

$$\mathbf{\Phi}(t_2,t_0) = \mathbf{\Phi}(t_2,t_1)\mathbf{\Phi}(t_1,t_0) \tag{C.7}$$

$$\mathbf{\Phi}(t_0,t_0) = \mathbf{I}_{6\times 6} \tag{C.8}$$

$$\det \mathbf{\Phi}(t,t_0) = 1 \tag{C.9}$$

In all of the multi-body models in this investigation, no analytical solutions exists for the elements of the STM. Along with the state equations of motion, the equations of motion for the elements of the STM are also numerically integrated. Generally, the STM supplies sensitivity information for many applications in dynamical systems analysis as well as problems in guidance and control. One type of design problem that exploits STMs are targeting scenarios.

VITA

Brian Patrick McCarthy was born in Washington, D.C., and raised in northern Virginia. After graduating from Gonzaga College High School, he attended Virginia Tech where he double majored in Aerospace and Ocean Engineering in 2014. He then worked as a flight dynamics analyst for a.i. solutions in Greenbelt, Maryland at NASA Goddard Space Flight Center on the Aqua, Aura, Terra, and TRMM missions. During his time as a flight dynamics analyst, Brian had the opportunity to work on several other projects including development of flight dynamics tools for the ISS and a multi-body astrodynamics tool for internal research and development. In August of 2016, he started graduate school at Purdue University and joined Professor Howell's Multi-Body Dynamics Research Group. Brian completed his MS in December of 2018, conducting research on computation and applications of quasi-periodic orbits in the three-body problem. He continued this area of research for his Ph.D., expanding to computation and applications in the four-body problem. Brian completed four internships with the Flight Mechanics and Trajectory Design Branch at NASA Johnson Space Center (JSC), working on the Gateway, Artemis and HLS programs. He also had the opportunity to intern at the Johns Hopkins Applied Physics Lab where he worked on the Dragonfly and Europa Clipper missions as well as national security space programs. Brian will continue his career at NASA JSC as a trajectory designer for the Gateway and Artemis programs.